BULLETIN OF THE GEOLOGICAL SOCIETY OF GREECE

ΔΕΛΤΙΟ ΤΗΣ ΕΛΛΗΝΙΚΗΣ ΓΕΩΛΟΓΙΚΗΣ ΕΤΑΙΡΙΑΣ

ejournals.epublishing.ekt.gr/index.php/geosociety

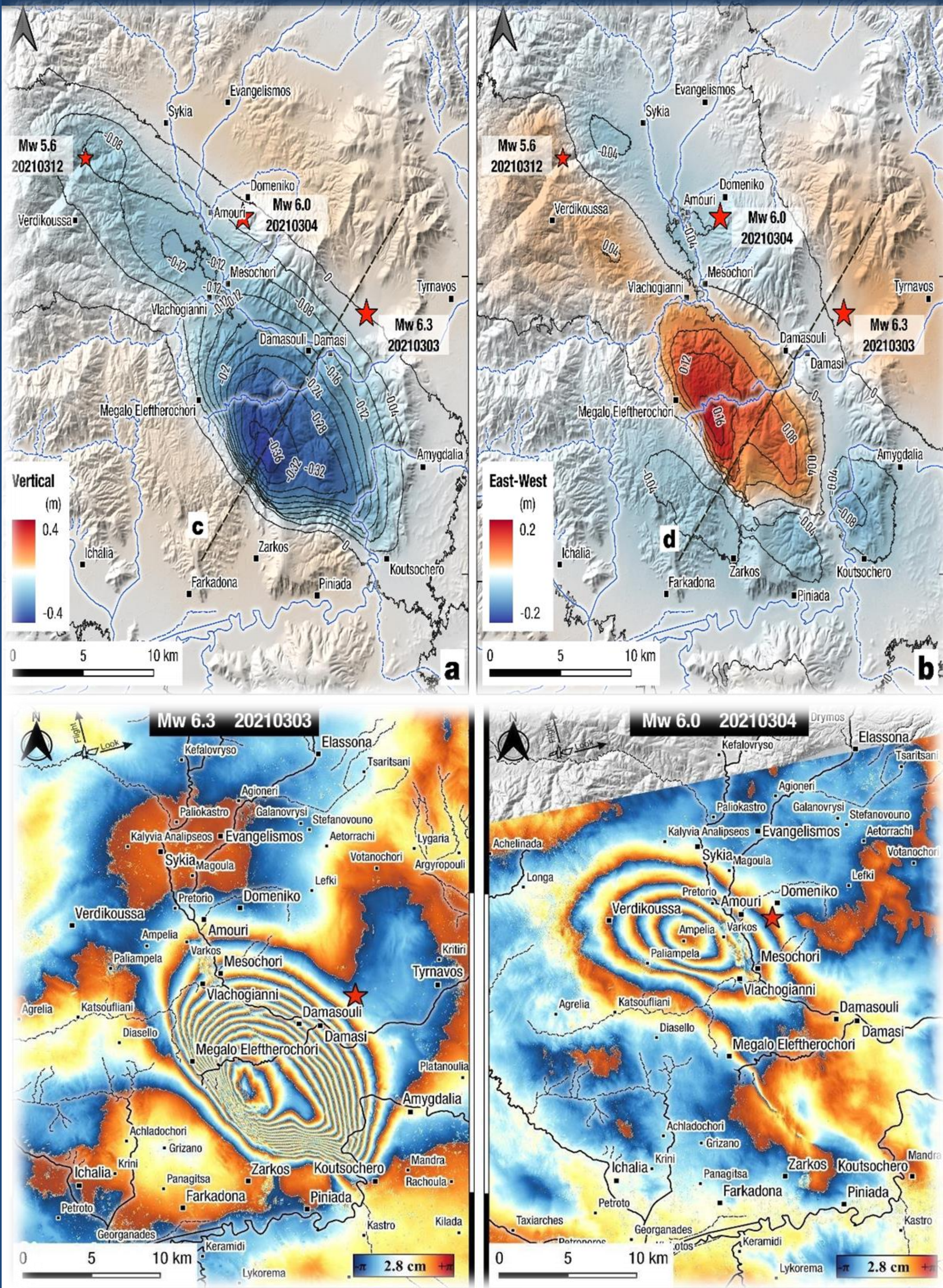

B
G
S
G

Τόμος 58
Volume 58
2021

ΕΘΝΙΚΟ ΚΕΝΤΡΟ ΤΕΚΜΗΡΙΩΣΗΣ
NATIONAL DOCUMENTATION CENTRE

ePublishing
eJournals

ISSN: 2529-1718

ΔΙΟΙΚΗΤΙΚΟ ΣΥΜΒΟΥΛΙΟ
ΤΗΣ ΕΛΛΗΝΙΚΗΣ ΓΕΩΛΟΓΙΚΗΣ ΕΤΑΙΡΙΑΣ
ΠΕΡΙΟΔΟΣ 2021-2023

GEOLOGICAL SOCIETY OF GREECE
EXECUTIVE BOARD

BGSG Editorial Board

Editor in chief

Athanassios Ganas, Institute of Geodynamics National Observatory of Athens, Greece, aganas@noa.gr

Editors

Assimina Antonarakou, National and Kapodistrian University of Athens, Greece, aantonar@geol.uoa.gr
Apostolos Arvanitis, Institute of Geology and Mineral Exploration-I.G.M.E, arvanitis@igme.gr
Hara Drinia, National and Kapodistrian University of Athens, Greece, cntrinia@geol.uoa.gr
Haralambos Kranis, National and Kapodistrian University of Athens, Greece, hkranis@geol.uoa.gr

Section Editors

Apostolos Alexopoulos, National and Kapodistrian University of Athens, Greece, aalexopoulos@geol.uoa.gr
Assimina Antonarakou, National and Kapodistrian University of Athens, Greece, aantonar@geol.uoa.gr
Pierre Briole, Centre National de la Recherche Scientifique, Paris, France, briole@ens.fr
Riccardo Caputo, University of Ferrara, Italy, rcaputo@unife.it
Kimon Christanis, University of Patras Department of Geology, Greece, christan@upatras.gr
Vasileios G. Christaras, Aristotle University of Thessaloniki, Greece, christar@geo.auth.gr
Hara Drinia, National and Kapodistrian University of Athens, Greece, cntrinia@geol.uoa.gr
George C. Ferentinos, University of Patras, Greece, gferen@upatras.gr
Athanassios Ganas, Institute of Geodynamics National Observatory of Athens, Greece, aganas@noa.gr
Antonis Giannopoulos, The University of Edinburgh, UK A. Giannopoulos@ed.ac.uk
Dimitrios Kostopoulos, National and Kapodistrian University of Athens, Greece, dikostop@geol.uoa.gr
George Koukis, University of Patras Department of Geology, Greece, G.Koukis@upatras.gr
Ioannis K. Koukouvelas, University of Patras Department of Geology, Greece, iannis@upatras.gr
Konstantinos N. Laskaridis, Institute of Geology and Mineral Exploration, Greece, laskaridis@igme.gr
Jan Mrlina, Institute of Geophysics CAS Prague, Czech Republic, jan@ig.cas.cz
Spiros Pagiatakis, York University Lassonde School of Engineering, Canada, spiros@yorku.ca
Gerassimos Papadopoulos, National Observatory of Athens, Greece, papadop@noa.gr
Costas Papazachos, Aristotle University of Thessaloniki, Greece, kpapaza@geo.auth.gr
Georgia Pe-Piper, Saint Mary's University, Canada, georgia.pe-piper@smu.ca
David J.W. Piper, Geological Survey of Canada Atlantic, Canada, david.piper@canada.ca
Gerald Patrick Roberts, Birkbeck, University of London, UK, gerald.roberts@ucl.ac.uk
George Syrides, Aristotle University of Thessaloniki, Greece, syrides@geo.auth.gr
Maria Triantaphyllou, National and Kapodistrian University of Athens, Greece, mtriant@geol.uoa.gr
George Tsiambaos, National Technical University of Athens, Greece, gktsiamb@central.ntua.gr
Konstantinos S. Voudouris, Aristotle University of Thessaloniki, Greece, kvoudour@geo.auth.gr
Alexandra Zampetakis-Lekkas, National and Kapodistrian University of Athens, Greece, zambetaki@geol.uoa.gr

Journal Managers

Assimina Antonarakou, National and Kapodistrian University of Athens, Greece, aantonar@geol.uoa.gr
Georgia Gkaniatsa, National and Kapodistrian University of Athens, Greece, gorgiagkan@gmail.com

B
G
S
G

Cover Photo1: InSAR displacement maps
Cover photo2: Coseismic interferograms Ganas et al., 2021, this volume

ISSN: 2529-1718

TABLE OF CONTENTS – ΠΕΡΙΕΧΟΜΕΝΑ

Editorial Note

Natural Hazards

Remote Sensing and GIS

Editorial Note

On March 3, and March 4, 2021, the region of northern Thessaly was struck by the largest earthquakes to occur in the region in the last 80 years. The M_w=6.3 and M_w=6.0 earthquakes occurred ~25 km NW of Larissa city, because of (roughly speaking) north–south extension of the Earth's crust. The two events generated severe ground shaking in several towns and the greater northern Thessaly area causing serious damage to old buildings, with economic and social impacts on the local population. Unravelling the characteristics of the sequence and the geodynamics of the area is the crucial point of this special issue of Bulletin of Geological Society of Greece, aimed at gathering a set of articles on detailed investigations and syntheses in all phases of scientific and engineering work about the Thessaly earthquakes, as well as papers on post-earthquake response and public policy matters.

The issue includes papers on the aftershock evolution and the properties of the activated fault network employing aftershock relocations using the double-difference and cross-correlation techniques; inversion of teleseismic and strong motion waveforms to derive slip models; Coulomb stress calculations highlighting increased positive stress changes at the locations of most of the aftershocks and activation of neighbouring fault segments by stress transfer; map of the deformation field caused by the earthquakes using InSAR & GNSS; Use of InSAR displacement data from Sentinel-1 interferograms, to invert for the fault parameters; geodetic measurements of permanent uplift and ground subsidence; maps of effects of the earthquakes, including field observations on liquefaction, rock falls, rock slides, road cracks all due to the strong ground motion and associated near-surface mobilization of soil cover and loose sediments.

This issue would not have been possible without the contribution of our fellow guest editors: Christophe Gruetzner, Alexandros Chatzipetros and Haris Kranis. Understanding the mechanism and recurrence of earthquakes such as the March 2021 events is extremely important for regional seismic hazard assessment, to help reduce the risk of people being subjected to future earthquakes, and for tectonics since little is known about the link between deep tectonic processes and upper crustal deformation in this key region.

The Editor-in-chief of BGSG

Dr. Athanassios Ganas

Research Director NOA

aganas@noa.gr

BGSG Vol. 58

The March 2021 Thessaly Earthquake Sequence

Alexandros Chatzipetros[1], Christoph Grützner[2], Haris Kranis[3]

1 (ac@geo.auth.gr)
2 Friedrich-Schiller-Universität Jena, Institute of Geosciences, Burgweg 11, 07749 Jena, Germany (christoph.gruetzner@uni-jena.de)
3 (hkranis@geol.uoa.gr)

Keywords: Greece, Thessaly, Earthquake, Special Issue

Introduction

Greece, the seismically most active country in Europe, has a longstanding tradition of earthquake research. Fundamental insights into earthquake physics and fault behaviour came from the study of Greek earthquakes and many modern concepts of earthquake geology have been developed here. Among the many strong earthquakes that hit Greece throughout its long history, perhaps the 1981 Gulf of Corinth earthquake series (Jackson et al., 1982; Vita-Finzi & King, 1985; Collier et al., 1998) had the largest impact on modern earthquake science. The deadly 1999 Athens Earthquake (Papadopoulos et al., 2000; Tselentis & Zahradník, 2000; Pavlides et al., 2002) triggered renewed efforts to map the active faults of Greece and to collect data on their slip rates and earthquake recurrence intervals. This was done by various means. Large-scale studies used geomorphological observations to better understand the distributed deformation of the crust both on mainland Greece and on the islands (e.g., Goldsworthy et al., 2002; Tzanis et al., 2010; Chatzipetros et al., 2013). Paleoseismic studies and tectonic geomorphology techniques were applied to many faults throughout the country (e.g., Benedetti et al., 2002; Chatzipetros et al., 2005; Kokkalas et al., 2007; Palyvos et al., 2010; Grützner et al., 2016, Koukouvelas et al., 2017; Copley et al., 2018). These data were used to build databases for active faults in Greece (Pavlides et al., 2010; Caputo et al., 2012, Ganas et al., 2013). In addition to these efforts, new methods have been developed to translate the fault data into better seismic hazard estimates (e.g., Papanikolaou et al., 2013; Deligiannakis et al., 2018).

Despite all these efforts, the 2021 Thessaly Earthquake Sequence occurred on faults that were previously unknown. The sequence included a M6.3 mainshock on March 3 and a M6.0 event 32 hours later. An M5.6 event on March 12 followed as well as thousands of smaller aftershocks. This was the most significant earthquake sequence in Thessaly in 41 years, and the largest event in this area of Greece since the major upgrades of the seismological, strong motions and geodetic networks. The sequence raised numerous questions related to fault interactions, blind faulting, near- and far-field ground motions, damage distribution, earthquake triggering, liquefaction phenomena and seismic hazard and seismotectonics of the Northern Thessaly. Today, remote-sensing data are available from several satellites and other platforms. Seismological and geodetic networks have improved significantly in the last decades. These new data allow investigating the Thessaly Earthquakes in detail. This Special Issue contains several papers that deal with such new data to characterise the seismogenic structures that ruptured in March 2021. Other studies deal with potential precursor phenomena and with disaster relief efforts. The Thessaly Earthquake sequence helps to better understand the regional tectonic setting, but it also sheds light on knowledge gaps that still exist despite many years of active tectonics research in Greece. As such, the Thessaly Earthquakes teach us how to save lives in the future.

Papers in the Special Volume

Mavroulis et al. focus on the disaster management. Since the earthquake series damaged many of the old houses without reinforcements in Thessaly, provisional shelters needed to be provided for hundreds of people. The earthquakes, however, happened during the third wave of the COVID-19 pandemic, which lead to a challenge: the emergency housing had to also comply with the anti-virus measures such as distancing and testing. This was amongst other measures achieved by providing more and different shelters than usual, by innovative approaches to supply distribution, and by isolation of infected people. The authors show that the infection rate in the area affected by the earthquake did not increase compared to other areas. Thus, this approach can be used as good practice in similar situations.

The paper by **Ganas et al.** deals with a wide range of methods that allow identifying the sources of the three main shocks. Geodetical (InSAR and GNSS) and seismological (aftershock distribution and p-wave arrivals) data show that normal motion occurred on (W)NW-(E)SE striking faults. The first two earthquakes ruptured NE-dipping faults; the third earthquake ruptured a SW-dipping structure. InSAR data allowed to map the ground deformation of the individual events and revealed that no significant postseismic deformation occurred on the previously unknown faults. The authors furthermore document several coseismic phenomena such as dilatational cracks and widespread liquefaction. With their paper the authors demonstrate the advantages of combing seismological data with geodetic information, especially when it comes to disentangling the deformation during three events close in time.

The Acceleration Deformation Method was tested by **Chatzopoulos** using the Thessaly Earthquake example. This method analyses the seismicity patterns preceding large earthquakes. Chatzopoulos uses the Tsallis Entropy approach to test if there was a spatio-temporal significant increase of seismicity before the Thessaly main shock. He shows that two different approaches of data processing, symmetrical and non-symmetrical, both indicate a significant increase of seismicity preceding the 3rd of March, 2021, main shock.

Karakostas et al. report on seismic monitoring of the Thessaly Earthquakes with a regional seismological network and a local network installed after the main shock. Aftershock distribution and focal mechanisms point to almost pure dip-slip faulting with an NNE–SSW direction of extension. Using regionally recorded seismic waveforms, the authors compute finite–fault slip inversions for the two largest earthquakes of the sequence and report rather low rupture velocities. The largest earthquake (M_W6.3) had more than 1 m of slip at depths between 3 and 7 kilometres, although the fault rupture did not reach the surface. The second main (M_W6.0) shock still had more than 20 cm of slip in ca. 5 km depth. Using the finite slip models, synthetic shake maps were produced for the two strongest earthquakes and compared to macroseismic data. This study sheds light on the source parameters of the Thessaly Earthquakes and the strong motion caused by them.

Spingos et al. investigate the problem of Earthquake Early Warning Systems (EEWS) using the data from the Thessaly Earthquakes. They estimate the integral of the squared velocity from the first few seconds of the wave train after the P-wave arrival at local permanent stations. These data are used to establish scaling relationships for the peak ground accelerations that occur when later, and more energetic, seismic phases arrive. Such scaling relationships are needed to automatically compute the expected shaking from initial earthquake data to achieve a meaningful EEWS. The few seconds of potential warning time between the alarm and the strongest shaking can save lives. A special emphasis is put on local site effects that can significantly modify the shaking.

The Neogene-Quaternary tectonic regime of the Thessaly region is in the focus of the paper by **Galanakis et al**. The authors provide background on the geological setting and document abundant coseismic effects such as cracks, liquefaction, and mass movements.

They furthermore provide data on the mechanism and location of the main shocks. In their paper, Galanakis et al. show that the causative fault of the main shock manifests as the boundary between the Alpidic basement and the alluvial deposits. Although the faults that ruptured were not previously identified as active, geological data point to long-lived activity. These findings may inform future hazard assessments and provide a useful case study for neighbouring regions.

The paper by **Kouli et al.** deals with a remote sensing approach to study possible precursors of the Thessaly Earthquake series. Using a 10 years' time series of land surface temperature data from the MODIS sensor (Moderate Resolution Imaging Spectroradiometer), the authors analyse the epicentral area adopting the Robust Satellite Technique. They interpret preseismic, coseismic and post seismic thermal anomalies as being related to the seismogenic faults that ruptured in March 2021.

References

Benedetti, L., Finkel, R., Papanastassiou, D., King, G., Armijo, R., Ryerson, F., Farber, D., & Flerit, F. (2002). Post-glacial slip history of the Sparta fault (Greece) determined by 36Cl cosmogenic dating: Evidence for non-periodic earthquakes. Geophysical Research Letters, 29(8), 87-1. doi: https://doi.org/10.1029/2001GL014510.

Caputo, R., Chatzipetros, A., Pavlides, S., & Sboras, S. (2012). The Greek Database of Seismogenic Sources (GreDaSS): state-of-the-art for northern Greece. Annals of Geophysics, 55(5).doi: https://doi.org/10.4401/ag-5168 .

Chatzipetros, A., Kokkalas, S., Pavlides, S., & Koukouvelas, I. (2005). Palaeoseismic data and their implication for active deformation in Greece. Journal of Geodynamics, 40(2-3), 170-188. doi: https://doi.org/10.1016/j.jog.2005.07.005.

Chatzipetros, A., Kiratzi, A., Sboras, S., Zouros, N., & Pavlides, S. (2013). Active faulting in the north-eastern Aegean Sea Islands. Tectonophysics, 597, 106-122. doi: https://doi.org/10.1016/j.tecto.2012.11.026.

Chatzopoulos, G. (2021). Accelerating deformation seismicity patterns before the March 3, 2021 Thessaly strong earthquake. First results. Bulletin of the Geological Society of Greece, 58, 87-104. doi:https://doi.org/10.12681/bgsg.27155.

Collier, R. E., Pantosti, D., D'addezio, G., De Martini, P. M., Masana, E., & Sakellariou, D. (1998). Paleoseismicity of the 1981 Corinth earthquake fault: Seismic contribution to extensional strain in central Greece and implications for seismic hazard. Journal of

Geophysical Research: Solid Earth, 103(B12), 30001-30019. doi: https://doi.org/10.1029/98JB02643.

Copley, A., Grützner, C., Howell, A., Jackson, J., Penney, C., & Wimpenny, S. (2018). Unexpected earthquake hazard revealed by Holocene rupture on the Kenchreai Fault (central Greece): Implications for weak sub-fault shear zones. Earth and Planetary Science Letters, 486, 141-154.doi: https://doi.org/10.1016/j.epsl.2018.01.014.

Deligiannakis, G., Papanikolaou, I. D., & Roberts, G. (2018). Fault specific GIS based seismic hazard maps for the Attica region, Greece. Geomorphology, 306, 264-282. doi: https://doi.org/10.1016/j.geomorph.2016.12.005.

Galanakis, D., Sboras, S., Konstantopoulou, G., & Xenakis, M. (2021). Neogene-Quaternary tectonic regime and macroseismic observations in the Tyrnavos-Elassona broader epicentral area of the March 2021, intense earthquake sequence. Bulletin of the Geological Society of Greece, 58, 200-221. doi:https://doi.org/10.12681/bgsg.27196.

Ganas, A., Oikonomou, I. A., & Tsimi, C. (2013). NOAfaults: a digital database for active faults in Greece. Bulletin of the Geological Society of Greece, 47, Proceedings of the 13th International Congress, Chania, Sept. 2013, 518-530. doi: https://doi.org/10.12681/bgsg.11079

Ganas, A., Valkaniotis, S., Briole, P., Serpetsidaki, A., Kapetanidis, V., Karasante, I., Kassaras, I., Papathanassiou, G., Karamitros, I., Tsironi, V., Elias, P., Sarhosis, V., Karakonstantis, A., Konstantakopoulou, E., Papadimitriou, P., & Sokos, E. (2021). Domino-style earthquakes along blind normal faults in Northern Thessaly (Greece): kinematic evidence from field observations, seismology, SAR interferometry and GNSS. Bulletin of the Geological Society of Greece, 58, 37-86. doi:https://doi.org/10.12681/bgsg.27102.

Goldsworthy, M., Jackson, J., & Haines, J. (2002). The continuity of active fault systems in Greece. Geophysical Journal International, 148(3), 596-618. doi: https://doi.org/10.1016/S0191-8141(00)00121-8.

Grützner, C., Schneiderwind, S., Papanikolaou, I., Deligiannakis, G., Pallikarakis, A., & Reicherter, K. (2016). New constraints on extensional tectonics and seismic hazard in northern Attica, Greece: the case of the Milesi Fault. Geophysical Journal International, 204(1), 180-199. doi:https://doi.org/10.1093/gji/ggv443.

Jackson, J. A., Gagnepain, J., Houseman, G., King, G. C. P., Papadimitriou, P., Soufleris, C., & Virieux, J. (1982). Seismicity, normal faulting, and the geomorphological development of the Gulf of Corinth (Greece): the Corinth earthquakes of February and March 1981. Earth and Planetary Science Letters, 57(2), 377-397. doi:https://doi.org/10.1016/0012-821X(82)90158-3.

Karakostas, V., Papazachos, C., Papadimitriou, E., Foumelis, M., Kiratzi, A., Pikridas, C., Kostoglou, A., Kkallas, C., Chatzis, N., Bitharis, S., Chatzipetros, A., Fotiou, A., Ventouzi, C., Karagianni, E., Bonatis, P., Kourouklas, C., Paradisopoulou, P., Scordilis, E., Vamvakaris, D., Grendas, I., Kementzetzidou, D., Panou, A., Karakaisis, G., Karagianni, I., Hatzidimitriou, P., & Galanis, O. (2021). The March 2021 Tyrnavos, central Greece, doublet (Mw6.3 and Mw6.0): Aftershock relocation, faulting details, coseismic slip and deformation. Bulletin of the Geological Society of Greece, 58, 131-178. doi:https://doi.org/10.12681/bgsg.27237.

Kokkalas, S., Pavlides, S., Koukouvelas, I., Ganas, A., & Stamatopoulos, L. (2007). Paleoseismicity of the Kaparelli fault (eastern Corinth Gulf): evidence for earthquake recurrence and fault behavior. Bollettino Societa Geologica Italiana, 126(2), 387.

Koukouvelas, I. K., Zygouri, V., Papadopoulos, G. A., & Verroios, S. (2017). Holocene record of slip-predictable earthquakes on the Kenchreai Fault, Gulf of Corinth, Greece. Journal of Structural Geology, 94, 258-274. doi: https://doi.org/10.1016/j.jsg.2016.12.001.

Kouli, M., Peleli, S., Saltas, V., Makris, J. P., & Vallianatos, F. (2021). Robust Satellite Techniques for mapping thermal anomalies possibly related to seismic activity of March 2021, Thessaly Earthquakes. Bulletin of the Geological Society of Greece, 58, 105-130. doi: https://doi.org/10.12681/bgsg.27058.

Mavroulis, S., Mavrouli, M., Carydis, P., Agorastos, K., & Lekkas, E. (2021). The March 2021 Thessaly earthquakes and their impact through the prism of a multi-hazard approach in disaster management. Bulletin of the Geological Society of Greece, 58, 1-36. doi:https://doi.org/10.12681/bgsg.26852.

Mechernich, S., Schneiderwind, S., Mason, J., Papanikolaou, I. D., Deligiannakis, G., Pallikarakis, A., Binnie, S. A., Dunai, T. J., & Reicherter, K. (2018). The seismic history of the Pisia fault (eastern Corinth rift, Greece) from fault plane weathering features and cosmogenic 36Cl dating. Journal of Geophysical Research: Solid Earth, 123(5), 4266-4284. doi: https://doi.org/10.1029/2017JB014600.

Palyvos, N., Pavlopoulos, K., Froussou, E., Kranis, H., Pustovoytov, K., Forman, S.L., & Minos-Minopoulos, D. (2010). Paleoseismological investigation of the oblique-normal Ekkara ground rupture zone accompanying the M 6.7–7.0 earthquake on 30 April 1954 in Thessaly, Greece: Archaeological and geochronological constraints on ground rupture recurrence. J. Geophys. Res. 115, B06301. doi:https://doi.org/10.1029/2009JB006374.

Papadopoulos, G. A., Drakatos, G., Papanastassiou, D., Kalogeras, I., & Stavrakakis, G. (2000). Preliminary results about the catastrophic earthquake of 7 September 1999 in Athens, Greece. Seismological Research Letters, 71(3), 318-329. doi:

https://doi.org/10.1785/gssrl.71.3.318.

Papanikolaou, I. D., Roberts, G. P., Deligiannakis, G., Sakellariou, A., & Vassilakis, E. (2013). The Sparta Fault, Southern Greece: From segmentation and tectonic geomorphology to seismic hazard mapping and time dependent probabilities. Tectonophysics, 597, 85-105. doi: https://doi.org/10.1016/j.tecto.2012.08.031.

Pavlides, S. B., Papadopoulos, G., & Ganas, A. (2002). The fault that caused the Athens September 1999 Ms= 5.9 earthquake: Field observations. Natural Hazards, 27(1), 61-84. doi:https://doi.org/10.1023/A:1019927302304.

Pavlides, S., Caputo, R., Sboras, S., Chatzipetros, A., Papathanasiou, G., & Valkaniotis, S. (2010). The Greek catalogue of active faults and database of seismogenic sources. Bulletin of the Geological Society of Greece, 43(1), 486-494. doi: https://doi.org/10.12681/bgsg.11199.

Spingos, I., Vallianatos, F., & Kaviris, G. (2021). The scaling of PGA with IV2p and its potential for Earthquake Early Warning in Thessaly (Central Greece). Bulletin of the Geological Society of Greece, 58, 179-199. doi:https://doi.org/10.12681/bgsg.27062.

Tselentis, G. A., & Zahradnik, J. (2000). The Athens earthquake of 7 September 1999. Bulletin of the Seismological Society of America, 90(5), 1143-1160. doi: https://doi.org/10.1785/0119990168.

Tzanis, A., Kranis, H., & Chailas, S. (2010). An investigation of the active tectonics in central-eastern mainland Greece with imaging and decomposition of topographic and aeromagnetic data. Journal of Geodynamics, 49(2), 55-67. doi: https://doi.org/10.1016/j.jog.2009.09.042.

Vita-Finzi, C., & King, G. C. P. (1985). The seismicity, geomorphology and structural evolution of the Corinth area of Greece. Philosophical Transactions of the Royal Society of London. Series A, Mathematical and Physical Sciences, 314(1530), 379-407. doi: https://doi.org/10.1098/rsta.1985.0024.

BGSG

Volume 58

Research Paper

Correspondence to:
Spyridon Mavroulis
smavroulis@geol.uoa.gr

DOI number:
http://dx.doi.org/10.12681/bgsg.26852

Keywords:
Thessaly, earthquake emergency, COVID-19 pandemic, compound emergencies, multi-hazard management

Citation:
Mavroulis S., Mavrouli M., Carydis P., Agorastos K. and Lekkas E. (2021), The March 2021 Thessaly Earthquakes and Their Impact Through the Prism of A Multi-Hazard Approach in Disaster Management. Bulletin Geological Society of Greece, 58, 1-36.

Publication History:
Received: 23/04/2021
Accepted: 29/06/2021
Accepted article online: 08/07/2021

The Editor wishes to thank two anonymous reviewers for their work with the scientific reviewing of the manuscript and Ms Emmanouela Konstantakopoulou for editorial assistance.

THE MARCH 2021 THESSALY EARTHQUAKES AND THEIR IMPACT THROUGH THE PRISM OF A MULTI-HAZARD APPROACH IN DISASTER MANAGEMENT

Spyridon Mavroulis [1,*], Maria Mavrouli [2], Panayotis Carydis [3], Konstantinos Agorastos [4], Efthymis Lekkas [1]

[1] **Department of Dynamic Tectonic Applied Geology, Faculty of Geology and Geoenvironment, National and Kapodistrian University of Athens, 15784 Athens, Greece, smavroulis@geol.uoa.gr**

[2] **Department of Microbiology, Medical School, National and Kapodistrian University of Athens, 11527 Athens, Greece, mmavrouli@med.uoa.gr**

[3] **European Academy of Sciences and Arts, A-5020 Salzburg, Austria, pkary@tee.gr**

[4.] **Region of Thessaly, 41110 Larissa, Greece, periferiarxis@thessaly.gov.gr**

Abstract

In early March 2021, when Greece was struggling with the evolving third wave of the COVID-19 pandemic with the highest numbers of daily cases and fatalities from its initiation, Thessaly was struck by a seismic sequence, which included the 3 March, Mw = 6.3 mainshock, its strongest Mw = 6.1 aftershock the following day and numerous large aftershocks. The mainshock caused extensive damage to houses and infrastructure, while the aftershock aggravated damage and caused widespread concern among residents. Based on post-event field surveys in the affected area, it is concluded that the old unreinforced houses with load-bearing masonry walls in the northeastern part of the Thessaly basin suffered the most, while the recent constructions remained intact. As a result, hundreds of homeless were in need of immediate temporary sheltering, which immediately mobilized the Civil Protection authorities to manage the emergency situation. This emergency had something unique, which made its management a challenge: the implementation of the earthquake emergency response actions was incompatible with the measures to limit the further spread of the SARS-CoV-2 virus in the community during the evolving third pandemic wave. Many of the actions have been adapted to the unprecedented conditions through a prism of a multi-hazard approach to disaster management and their impact. Among others, more and different types of emergency shelters were used to prevent overcrowding, emergency supplies distribution processes were modified to prevent transmission through hands *and surfaces, places for the identification and isolation of suspected COVID-19 cases were designated in emergency shelters and extensive and regular screening testing of the local population was conducted for the detection of SARS-CoV-2 virus. From the analysis of the daily reported COVID-19 cases in the earthquake-affected area during the pre- and post- disaster periods as well as from results of rapid testing during the post-disaster period, it was found that the viral load of the earthquake-affected villages was not increased, despite the difficult and unprecedented conditions. It can be suggested that the adaptation of the measures to the new conditions has worked beneficially to reduce the spread of the new virus among those affected and the involved staff. For this reason, this approach could be considered as good practice and important lesson learned, which can be applied to similar future compound emergencies in areas with similar geoenvironmental and epidemiological characteristics.*

Keywords: *Thessaly; earthquake emergency; COVID-19 pandemic; compound emergencies; multi-hazard management*

Περίληψη

Στις αρχές Μαρτίου 2021, όταν η Ελλάδα πάλευε με το εξελισσόμενο τρίτο κύμα της πανδημίας COVID-19 με τους υψηλότερους αριθμούς ημερήσιων κρουσμάτων και απωλειών από την έναρξή της, η Θεσσαλία επλήγη από μια σεισμική ακολουθία, που περιλάμβανε τον κύριο σεισμό μεγέθους $M_w = 6.3$ *στις 3 Μαρτίου, τον ισχυρότερο μετασεισμό με μέγεθος* $M_w = 6.1$ *την επόμενη ημέρα και πολλούς μεγάλους μετασεισμούς στη συνέχεια. Ο κύριος σεισμός προκάλεσε εκτεταμένες βλάβες σε κατοικίες και υποδομές, ενώ ο μετασεισμός επιβάρυνε τα ήδη πληγέντα κτήρια και επέτεινε την ανησυχία του τοπικού πληθυσμού. Με βάση έρευνες πεδίου στην πληγείσα περιοχή διαπιστώθηκε ότι οι παλαιές μη ενισχυμένες κατοικίες με φέρουσα τοιχοποιία στο βορειοανατολικό τμήμα της Θεσσαλικής πεδιάδας επλήγησαν περισσότερο από τις σύγχρονες κατασκευές, που παρέμειναν ανέπαφες. Αποτέλεσμα ήταν να προκύψουν εκατοντάδες άστεγοι και χιλιάδες πληγέντες, γεγονός που κινητοποίησε άμεσα τις υπηρεσίες Πολιτικής Προστασίας για τη διαχείριση της έκτακτης ανάγκης. Αυτή η έκτακτη ανάγκη είχε μια ιδιαιτερότητα, που καθιστούσε τη διαχείρισή της πρόκληση: η εκπόνηση των απαιτούμενων δράσεων για τη διαχείριση των επιπτώσεων του σεισμού ήταν ασύμβατες με τα μέτρα περιορισμού περαιτέρω διασποράς του ιού SARS-CoV-2 στην κοινότητα κατά τη διάρκεια του τρίτου πανδημικού κύματος. Πολλές από τις δράσεις προσαρμόστηκαν στις πρωτόγνωρες συνθήκες υπό το πρίσμα πολυκινδυνικής προσέγγισης στη διαχείριση του κινδύνου καταστροφών και των επιπτώσεών τους.*

Μεταξύ άλλων, χρησιμοποιήθηκαν περισσότεροι και διαφορετικού τύπου χώροι φιλοξενίας σεισμόπληκτων για την αποφυγή συνωστισμού, τροποποιήθηκαν οι διαδικασίες διανομής ειδών έκτακτης ανάγκης για την αποφυγή της μετάδοσης μέσω χεριών και επιφανειών, προβλέφθηκαν χώροι για την αναγνώριση και απομόνωση ύποπτων κρουσμάτων με λοίμωξη COVID-19 σε χώρους φιλοξενίας σεισμοπλήκτων και εκπονήθηκε μαζικός και τακτικός έλεγχος πληγέντων για την ανίχνευση πιθανών κρουσμάτων. Από τη ανάλυση των ημερήσιων κρουσμάτων COVID-19 στη σεισμόπληκτη περιοχή κατά την προ- και μετα- καταστροφική περίοδο, αλλά και των αποτελεσμάτων του προγράμματος μαζικού και τακτικού ελέγχου των σεισμόπληκτων με τη μέθοδο των ταχέων τεστ κατά τη μετακαταστροφική περίοδο, διαπιστώθηκε ότι το ιικό φορτίο της σεισμόπληκτης περιοχής δεν αυξήθηκε, παρά τις δύσκολες και πρωτόγνωρες συνθήκες. Μπορεί να ειπωθεί ότι η προσαρμογή των μέτρων στις νέες συνθήκες λειτούργησε ευεργετικά για τον περιορισμό της διασποράς του νέου ιού μεταξύ των πληγέντων και του προσωπικού των αρμόδιων υπηρεσιών. Για το λόγο αυτό μπορούν να θεωρηθούν ως καλή πρακτική και σημαντικό μάθημα, που μπορεί να εφαρμοστεί και σε παρόμοιες μελλοντικές σύνθετες έκτακτες ανάγκες σε περιοχές με παρόμοια γεωπεριβαλλοντικά και επιδημιολογικά χαρακτηριστικά.

Λέξεις – Κλειδιά

Θεσσαλία, έκτακτη ανάγκη από σεισμό, πανδημία COVID-19, σύνθετη έκτακτη ανάγκη, πολυκινδυνική διαχείριση

1. INTRODUCTION

On 3 March 2021 (10:16:10 UTC) an earthquake struck the Region of Thessaly located in the central part of Greece (Fig. 1). The earthquake occurred in an area characterized mainly by normal faulting along NW-SE striking faults that belong to the Northern Thessaly fault zone (Caputo and Pavlides, 1993) (Fig. 1). Based on the Seismological Laboratory of the Department of Geology and Geoenvironment of the National and Kapodistrian University of Athens (SL-NKUA), the magnitude has been assessed as Mw = 6.3 and its focal depth as 19 km. Based on the provided focal plane solution (SL-NKUA) (Fig. 1), the 3 March event was generated by the activation of an NW-SE striking normal fault.

The main shock was felt in Thessaly basin and its surroundings, from Athens in the south to the northern borders of Greece. Fortunately, it caused no fatalities, while only 3 people were slightly injured due to partially collapsed buildings with load-bearing masonry walls in Damassi village. The Disaster Management Special Units (EMAK in

Greek) of the Hellenic Fire Service managed to rescue 6 people from the rubbles in the earthquake-affected villages of Mesochori and Magoula. On 4 March 2021, (18:38:19 UTC), another earthquake struck the same area with magnitude Mw = 6.1 and focal depth of 15 km (SL-NKUA) (Fig. 1). Based on the provided focal plane solutions, the parameters of the second earthquake were similar to those of the first earthquake (Fig. 1). More specifically, it was also generated by the rupture of a NW-SE striking normal fault.

The mainshock induced extensive secondary environmental effects comprising mainly liquefaction phenomena in river beds, lateral spreading along river banks, slope failures including rockfalls and landslides along abrupt slopes and ground cracks mainly in areas with preexisting instability (Lekkas et al., 2021; Valkaniotis et al., 2021). Moreover, it caused damage to buildings in many residential areas of the northern part of Thessaly Basin (Lekkas et al., 2021).

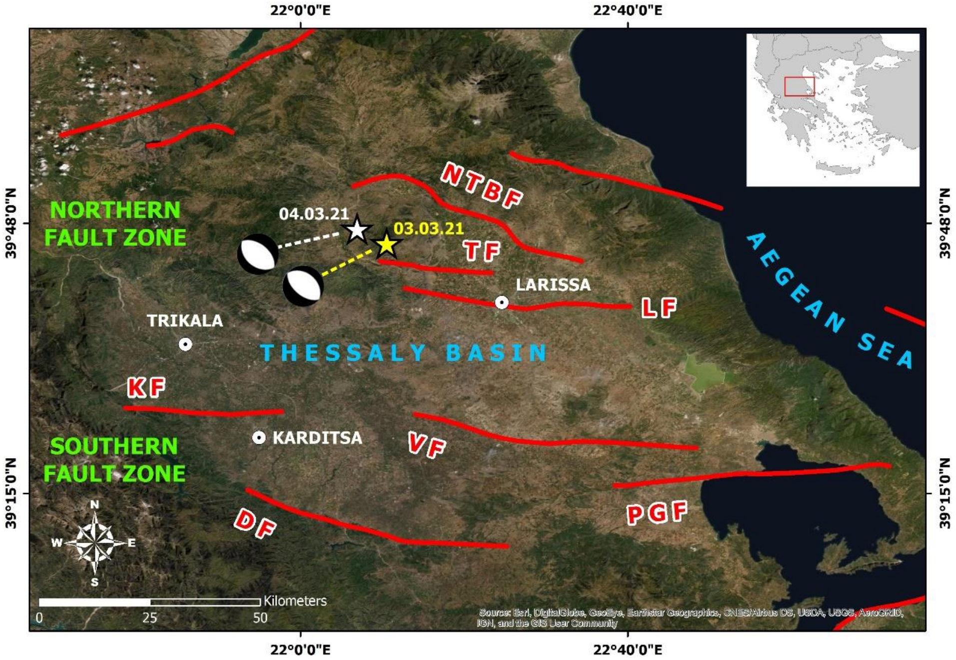

Fig. 1: The seismogenic sources of Thessaly Basin based on the Greek database of seismogenic sources (Caputo et al., 2012). Its northern fault zone comprises the North Tyrnavos Basin fault (NTBF), the Tyrnanos fault (TF), the Larissa fault (LF), while the southern fault zone includes the Karditsa fault (KF), the Vasilika fault (VF), the Pagasitikos Gulf fault (PGF) and the Domokos fault (DF). The yellow star corresponds to the 3 March 2021, Mw = 6.3 earthquake epicenter and the white star to the 4 March 2021, Mw = 6.1 earthquake epicenter. The focal plane solutions for both earthquakes were provided by SL-NKUA.

This seismic sequence raises many questions on several scientific issues, including the causative fault, the earthquake triggering process and fault interactions, surface fault expression and blind faulting, type and distribution of earthquake environmental effects and building damage, among other important questions on the seismic hazard of the earthquake-affected area. The significance of this seismic sequence lies not only in these questions about geological hazards, but also in its occurrence amid an evolving biological hazard, which is the COVID-19 pandemic.

The COVID-19 pandemic knocked on the door of Greece in late February 2020 (Fig. 2), affecting activities in all sectors of the daily life including the disaster risk reduction and management among others. Until early March 2021, when the mainshock struck Thessaly, Greece counted 198271 laboratory-confirmed COVID-19 cases and 6592 fatalities according to the official daily reports of COVID-19 epidemiological surveillance of the National Public Health Organization (NPHO), which are freely available online in the NPHO (2021) website. The early March 2021 Thessaly seismic sequence was not the first, which tested the readiness and effectiveness of the state mechanism in managing the effects of an earthquake disaster amid the pandemic. It was preceded by the 21 March 2020, Mw = 5.7 Epirus (Northwestern Greece) earthquake (e.g., Lekkas et al., 2020a), which coincided with the initiation of the pandemic in the country (Fig. 2), and the 30 October 2020, Mw = 7.0 Samos (Eastern Aegean Sea) earthquake (e.g., Lekkas et al., 2020b; Papadimitriou et al., 2020; Cetin et al., 2021), which was generated within the second wave of the pandemic (Fig. 2). The seismic sequence of Thessaly occurred amid the evolving third pandemic wave (Fig. 2).

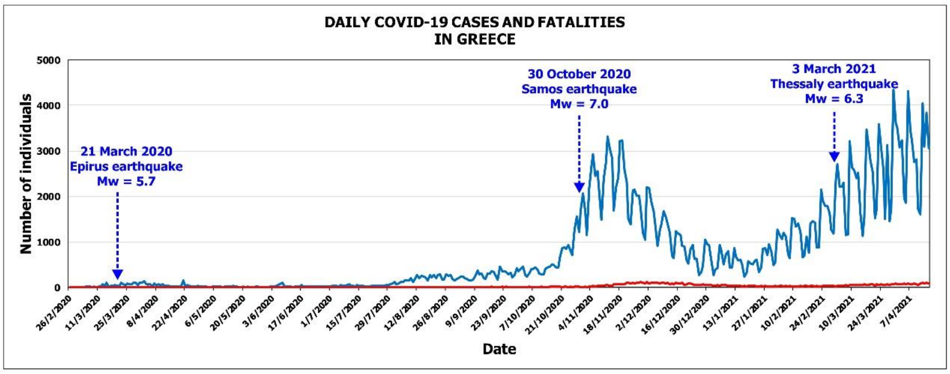

Fig. 2: The evolution of the pandemic in Greece through the daily COVID-19 cases and fatalities. The Epirus earthquake occurred in the first wave of the pandemic, the Samos earthquake in the second wave and the early March 2021 Thessaly seismic sequence in the third wave (Data for daily COVID-19 cases and fatalities from the daily reports of COVID-19 epidemiological surveillance of the National Public Health Organization, which are available in the NPHO (2021) website.

The main element of the third pandemic wave in Greece is the highest numbers of daily confirmed COVID-19 cases, intensive care unit (ICU) patients and fatalities since the pandemic initiation in the country. Since the completion of the second wave in mid-January 2021, the above daily numbers have never reached the low levels of the first wave. This fact shows that there is a great viral load in the community, which has a strong potential to cause, if not drastically reduced, a resurgence of the pandemic with adverse effects on public health and the proper functioning of society. Recent viral mutations, which tend to prevail in the community and make the spread of the virus easier, may also contribute to this resurgence.

The epidemiological characteristics that prevail in Greece at the beginning of spring 2021 made the response to the earthquake emergency and the management of the induced effects a challenge. This is attributed to the fact that many actions planned and effectively applied to pre-pandemic disasters related to natural hazards are now incompatible with the pandemic mitigation measures. In particular, each action of the earthquake emergency response, described in detail by Lekkas et al. (2020c) and Mavroulis et al. (2021), requires cooperation between the Civil Protection authorities as well as interaction and close contact with the earthquake-affected local population, which is incompatible with the preventive measures to limit the spread of the SARS-CoV-2 virus and its recent mutations.

Taking into account the above data and the unprecedented conditions, which have been formed not only in Greece, but also worldwide, this paper deals with the early March 2021 Thessaly earthquake and its impacts through the prism of a multi-hazard approach of disaster risk reduction and management. We initially present the effects of the seismic sequence on the building stock of the earthquake-affected area based on our post-event field surveys, which resulted in an extended mobilization of Civil Protection authorities. Moreover, we examined the trend that prevailed in the evolution of the pandemic in the earthquake-affected area during the pre- and the post- disaster phase in order to detect possible changes (increase, decrease) or stability and to identify possible factors affecting the detected trends. Emphasis is also placed on response actions during the emergency phase, adapted to the newly introduced conditions, which require the implementation of a multi-risk approach for the effective simultaneous management of geological and biological hazards. These actions can be used as a guide for managing the effects of disasters related to geological hazards amid evolving biological hazards, not only in Greece, but also in other regions and countries, characterized by respective geoenvironmental characteristics and epidemiological properties.

2. IMPACT OF THE EARLY MARCH 2021 SEISMIC SEQUENCE IN THESSALY REGION

The earthquake-induced damage on the built environment was assessed during post-event field surveys conducted by the authors in the Elassona, Tyrnavos and Larissa Municipalities of the Larissa Regional Unit, the Palamas Municipality of the Karditsa Regional Unit and the Farkadona Municipality of the Trikala Regional Unit (Fig. 3). Based on the post-earthquake first building inspection conducted by the General Directorate of Natural Disaster Recovery (GDAEFK in Greek), damage was also detected in a smaller scale in Kalampaka and Trikala Municipalities of the Trikala Regional Unit and in Tempi, Kileler and Ayia Municipalities of the Larissa Regional Unit (Fig. 3).

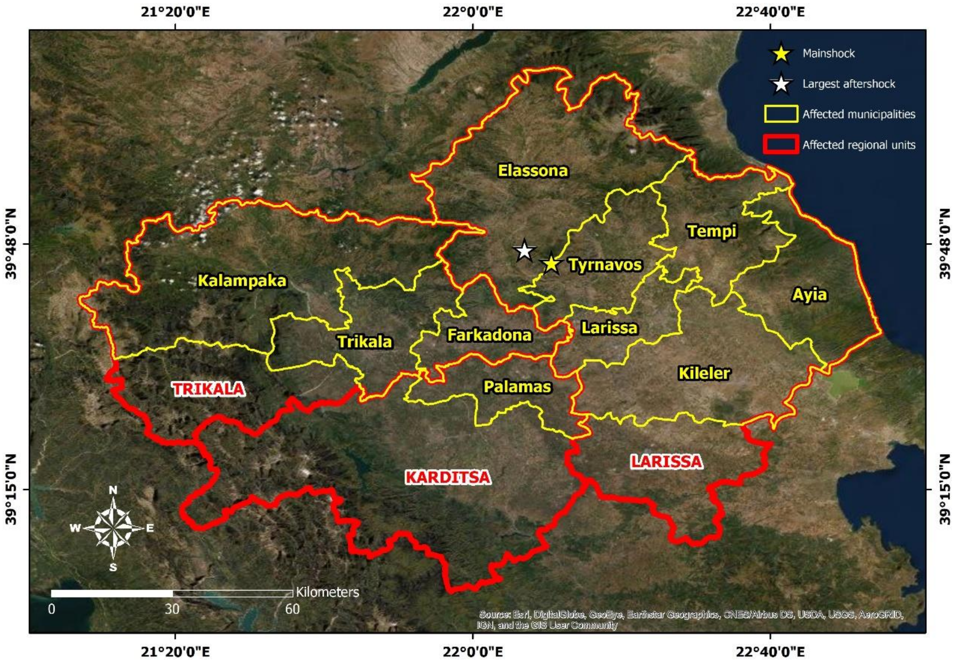

Fig. 3: The regional units (red polygons and names) and the municipalities (yellow polygons and names) of Thessaly Region affected by the early March 2021 Thessaly sequence. The earthquake epicenters of the mainshock (yellow star) and the largest aftershock (white star) are also presented.

2.1. Dominant building types in the earthquake-affected area

Based on post-event field surveys conducted by the authors in the earthquake-affected area shortly after the 3 March mainshock and according to the data provided by the

2011 Building Census of Greece (Hellenic Statistical Authority, 2011), it is concluded that the dominant building types in the affected municipalities comprise buildings with reinforced concrete frame and infill walls and buildings with load-bearing masonry walls composed of bricks and stone (Fig. 4a). Other types of buildings were also recorded comprising buildings of metal, wood and other construction material including plasterboards (Fig. 4b).

Regarding the construction period of the buildings, over two-thirds of the buildings in the affected municipalities have been constructed before 1980 (Fig. 5). This information is very important, as it highlights that the majority of the buildings in the affected area was built according to the first code for seismic-resistant design for Greece published in 1959 (Royal Decree 19-2-1959, Government Gazette 36A/26-2-1959). This code continued to be applied for about 20 years until the large destructive earthquakes that affected the largest urban centers of Greece, the 1978 Thessaloniki (Northern Greece) and the early 1981 Athens earthquakes.

Moreover, the affected area belongs to two zones of the current Greek Building Code (EAK, 2003). Its northern part belongs to **Zone I** characterized by a Peak Ground Acceleration (PGA) value of 0.16 g for a return period of 475 years, while its southern part to **Zone II** with a PGA value of 0.24 g for the same return period.

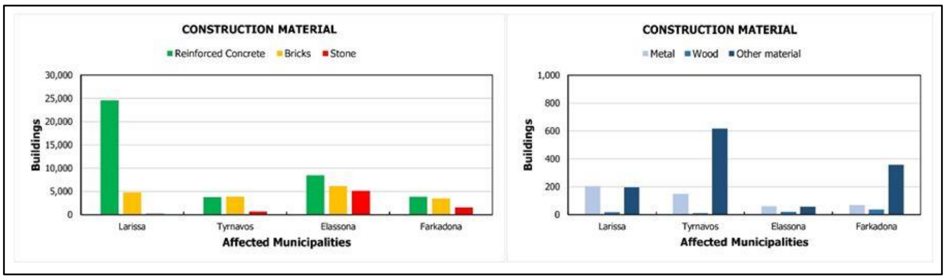

Fig. 4: (**a**) Dominant building types in the most-earthquake affected municipalities of the Thessaly Region [data from the 2011 Building Census of Greece (Hellenic Statistical Authority, 2011)]. (**b**) Buildings constructed with metal, wood and other construction materials including plasterboards were also observed.

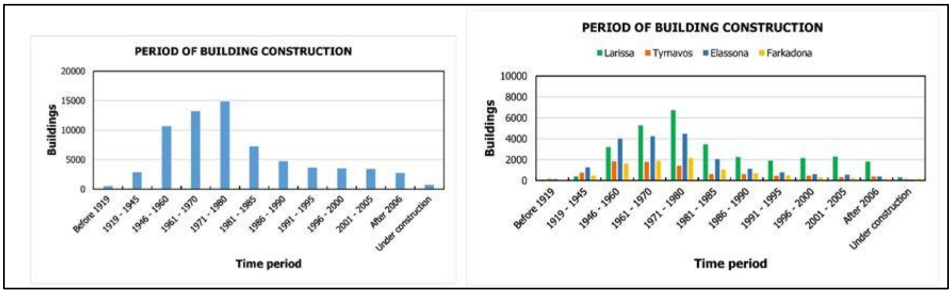

Fig. 5. (a) Over two-thirds of the buildings in the earthquake-affected municipalities have been constructed before 1980 [data from the 2011 Building Census of Greece (Hellenic Statistical Authority, 2011)].

2.2. Building damage induced by the 3 March 2021, Mw = 6.3 Thessaly earthquake

The earthquake-induced building damage was mainly observed in villages founded on recent deposits of the Titarissios and Pineios Rivers' beds (Fig. 6).

The most affected residential areas are located on the alluvial plains comprising recent deposits of Titarissios River and its main tributaries, comprising from north to south the Palaeokastro, Evangelismos, Sykia, Magoula, Domeniko, Praetorio, Amouri, Mesochori, Vlachogianni and Damassi villages (Fig. 6). Damage was also induced in villages of Pineios River plain including from west to east the Grizano, Farkadona, Zarkos and Koutsochero villages (Fig. 6). Limited damage was observed in other villages located outside the Titarissios and Pineios River alluvial plains including Verdikoussa among others (Fig. 6). The 4 March 4 2021, Mw = 6.1 earthquake aggravated damage induced by the first earthquake.

The worst affected building type is the old unreinforced buildings with load-bearing masonry walls (Figs 7, 8). These buildings suffered mainly heavy damage on their structural elements comprising vertical cracks at wall intersections due to the lack of horizontal band beams (Figs 7a-b), out-of-plane failures of the upper part of the walls attributed to the interaction between roof structure and perimeter walls and to lack of building integrity (Figs 7c-d) as well as partial or total collapse due to poor quality mortar and poor workmanship, resulting in disintegration of masonry units and loss of support to floors (Figs 7e-f).

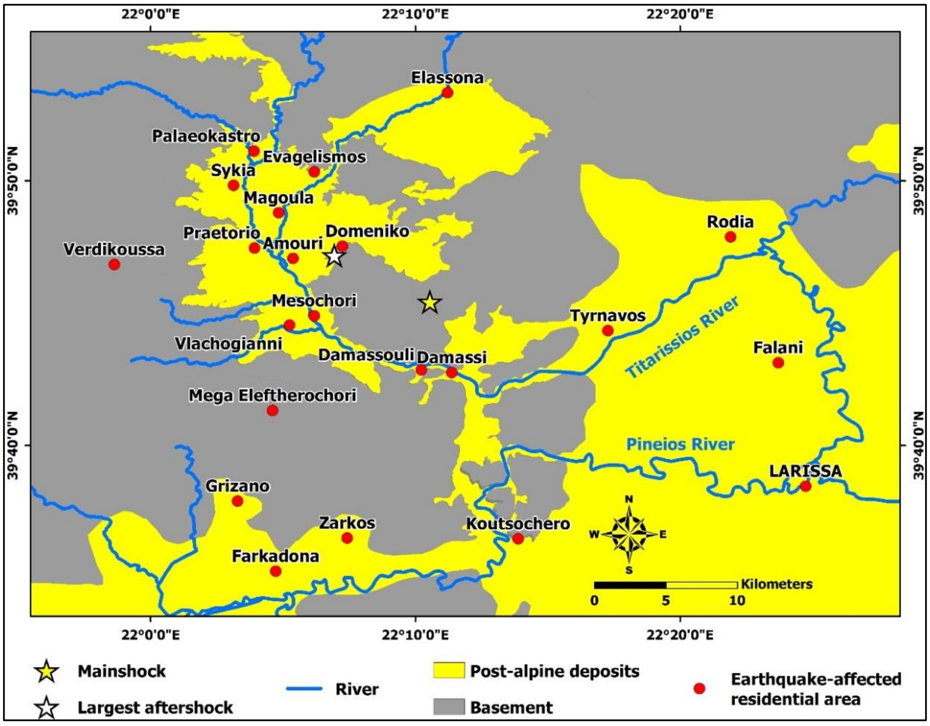

Fig. 6. Simplified geological map illustrating post-alpine deposits and their basement along with the distribution of the residential areas affected by the early March 2021 Thessaly earthquakes. The epicenters of the 3 and 4 March earthquakes (yellow and white stars respectively) in the northern part of Thessaly Basin are also presented.

Similar damage was generated in special structures, including schools, and monumental buildings, comprising churches (Fig. 8). Churches suffered damage to their load-bearing masonry walls, arches, roofs, plasters and their bell towers. Their seismic performance depended on their strengthening with longitudinal steel tie rods and on the soil foundation. A characteristic example comprises the churches in Mesochori and Vlachogianni villages located only 1.5 km away from each other. The Mesochori church founded on recent river deposits suffered partial collapse (Fig. 8a), while the Vlachogianni church founded on alpine formations and recently reinforced with steel tie rods remained intact by the earthquakes (Figs 8b-c).

Based on the results of the first building inspection conducted by GDAEFK and published on 12 March 2021, 67 school units with 142 buildings were inspected in the earthquake-affected municipalities and 47 of them needed repair before reopening. Characteristic example of a heavily affected old school building in the earthquake-affected area is the Elementary School of Damassi village, which was an over-80-year-old building with load-bearing masonry. It suffered severe structural damage by the mainshock comprising extensive cracking and partial collapse of its masonry walls (Figs 8d-f) and consequently was later demolished. It is significant to note that 63 students and 10 teachers were in the building when the earthquake struck the area. They immediately evacuated the buildings and were all safe.

Regarding the recently constructed buildings with reinforced concrete frame and infill walls, they remained intact by the earthquake in general. They suffered damage on their non-structural elements comprising detachment of plasters from infill walls, detachment of infill walls from the surrounding reinforced concrete frame and detachment of tiles from roofs and of cladding from walls (Fig. 9a-b). However, limited cases of reinforced concrete buildings that suffered structural damage including damage to columns of the ground floor were also detected (Fig. 9c).

Fig. 7: (**a**, **b**) Vertical cracks and gaps were frequently formed and propagated along the height of the bearing wall intersections. This damage is attributed to the absence of horizontal banding means, which could provide structural integrity. Examples from Mesochori village. (**c**, **d**) Failures of the upper part of the walls were also attributed to the interaction of roof structure and perimeter walls. Examples from Mesochori (**c**) and Damassi (**d**) villages. (**e**, **f**) Damage were also attributed to poor mortar and poor workmanship resulting in partial or total collapse. Views from Mesochori village.

Fig. 8: (**a**) The Ayios Dimitrios church in Mesochori village, which has been founded on recent deposits, suffered damage to its walls and bell towers by the 3 March earthquake. The 4 March earthquake aggravated damage. (**b**, **c**) The Ayia Triada church in Vlachogianni village has been founded on alpine deposits and has been recently reinforced with steel ties in the bell tower and in the other parts of the construction. It remained intact by the early March earthquakes. (**d**, **e**, **f**) Damage to the old masonry elementary school of Damassi village. It suffered heavy structural damage including partial collapse of the walls.

Fig. 9. Few earthquake-affected reinforced concrete buildings suffered non-structural damage varying from slight detachment of the infill walls from the surrounding reinforced concrete frame (**a**) and cracking in the infill walls (**b**) to partial collapse of the infill walls (**c**).

2.3. Results from the first-degree inspection of buildings

Shortly after a destructive earthquake in Greece with impact on the built environment, engineers involved in disaster management in order to conduct building inspections and assess the earthquake-induced damage. The rapid visual inspections, performed immediately after the earthquake last ten up to twenty days, depending on the intensity and the damage extent and aim primarily to protect the local population, to contribute to the continuation of the basic functions of the affected community and to identify and define the earthquake-affected area.

The post-earthquake assessment procedure consists of two degrees of inspections (Lekkas et al., 2020c; Cetin et al., 2021):

(a) the first-degree inspection is a rapid visual inspection that evaluates the buildings and classifies them into two categories: usable or unusable (should not be used until re-inspection is performed) and

(b) the second-degree inspection (reinspection) that is performed only to the buildings characterized unusable during the first stage. The buildings that are reinspected, are classified in three categories regarding their usability and damage: buildings suitable for use, buildings temporarily unsuitable for use or buildings dangerous for use, depending on the observed damage. The duration of the secondary inspection is proportional to the intensity of the earthquake and the extent of the induced damage.
The results of the first-degree inspection in the earthquake-affected area in Thessaly basin were announced on 12 March 2021 by the GDAEFK (Table 1):

- A total of 5079 buildings were inspected. 4533 of them are residential. 1820 were deemed temporarily unusable and would be reinspected during the second-degree inspection.

- 148 business premises have been inspected. 49 of them were temporarily unusable and would be reinspected during the second-degree inspection.

- 66 of 132 special structures including temples and public buildings were characterized unusable. 211 of 247 warehouses were characterized temporarily unusable until the second inspection.

Based on the aforementioned, it is clear that the early March 2021 seismic sequence was destructive and had the potential for leaving thousands of residents with heavily affected properties and hundreds homeless in need of immediate temporary sheltering.

Table 1. Total buildings based on the Buildings Census of the Hellenic Statistical Authority (2011), buildings inspected by GDAEFK during the first post-earthquake building inspection and percentage of buildings inspected for the municipalities affected by the early March 2021 Thessaly sequence.

Municipality	Regional Unit	Buildings in Municipality	Inspected buildings in Municipality	Percentage of buildings inspected in Municipality (%)
Tyrnavos	Larissa	9026	1311	14.52
Farkadona	Trikala	9374	1308	13.95
Elassona	Larissa	19847	1558	7.85
Palamas	Karditsa	11085	275	2.48
Larissa	Larissa	30006	392	1.31
Tempi	Larissa	10378	62	0.60
Kalampaka	Trikala	18309	84	0.46
Kileler	Larissa	14921	46	0.31
Ayia	Larissa	10631	19	0.18
Trikala	Trikala	30135	24	0.08
Total		163712	5079	3.10

3. IMPACT OF THE COVID-19 PANDEMIC IN THE EARTHQUAKE-AFFECTED REGION OF THESSALY

The studied Thessaly earthquakes occurred within the third wave of the COVID-19 pandemic in Greece. From the third wave initiation in mid-January 2021 until the earthquake occurrence on 3 March, 49477 laboratory-confirmed COVID-19 cases and 1156 fatalities were reported throughout Greece based on the official reports of the NPHO. As regards its evolution in Thessaly Region, 2333 cases were laboratory-confirmed in the same period. Data on fatalities in Thessaly Region are not available, as they are officially announced at national level and not at regional or local level.

In early March 2021, a high viral load was detected in the community, as shown by the corresponding graph (Fig. 10). This viral load, in combination with the mutations that occurred later, had, as it turned out, the potential to cause a resurgence of the pandemic in Greece.

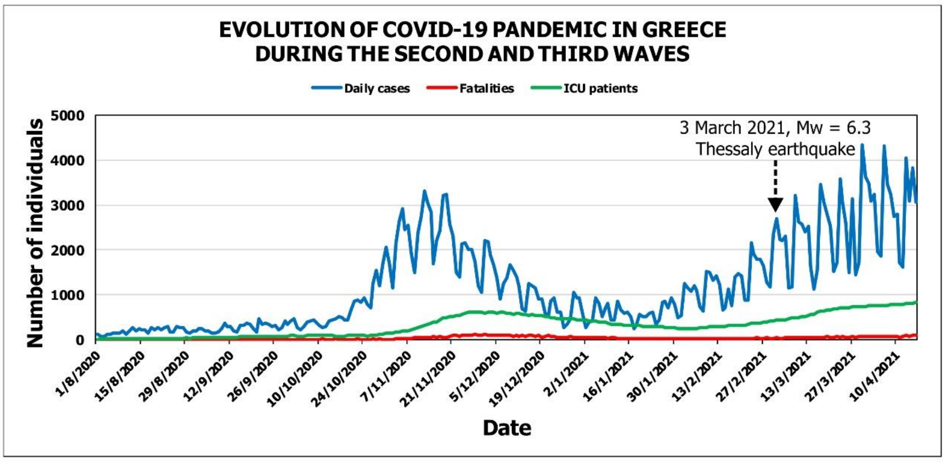

Fig. 10: The second and the third waves of the COVID-19 pandemic in Greece. The second wave lasted from the early August 2020 until mid-January 2021 and the third one started in mid-January and is evolving with the highest numbers of daily reported COVID-19 cases and related ICU patients and fatalities since the pandemic initiation (Data of daily COVID-19 cases, ICU patients and fatalities from the NPHO).

3.1. The evolution of the covid-19 pandemic in the earthquake-affected Thessaly region in the pre- and post- disaster period

We present the results of our study on the evolution of the pandemic in the earthquake-affected Thessaly Region. The analysis is based on laboratory-confirmed, daily-recorded COVID-19 cases in the earthquake-affected Karditsa, Larissa, Magnesia, and Trikala regional units of the Thessaly Region (Fig. 11) derived from the daily reports of COVID-19 epidemiological surveillance of the NPHO (2021) available on its website. These reports include the daily reported number of laboratory-confirmed COVID-19 cases, fatalities and ICU patients, their geographic and age distribution and the total number of cases, fatalities and intubations since the initiation of the COVID-19 pandemic in Greece. The number of samples, which have been tested by laboratories and Health Units of NPHO performing tests for the detection of SARS-CoV-2 virus, are also presented in these daily reports of the NPHO. All data are freely accessible to public on the respective website mentioned above.

We followed the methodology applied by Mavroulis et al. (2021) for studying the post-disaster trends and factors affecting the evolution of COVID-19 pandemic in areas affected by geological and hydrometeorological hazards in Greece. They take into account that the estimated incubation period of SARS-CoV-2, the time between exposure to the virus and emergence of symptoms ranges from 2 to 14 days (Lauer et al., 2020; WHO, 2020b) with the median incubation being 5 days (Lauer et al., 2020; WHO, 2020b) and the SARS-CoV-2 detection up to 21 days after onset of symptoms by PCR in infected patients (La Scola et al., 2020; García et al., 2020). In order to study the viral load and the infection rate in each affected regional unit before the disaster occurrence, they considered appropriate to monitor the number of daily confirmed cases in the 7 days (1 week) that preceded the disaster. In this way, any pre-existing outbreak of the novel virus in the affected areas will be perceived and the evolution of this outbreak will be possible to correlate or not with the disaster generated amid this outbreak. Taking into account all the aforementioned data, the number of daily COVID-19 cases in the present study has been tracked from 24 February to 24 March, 2021 for the Thessaly earthquake generated on 3 March 2021.

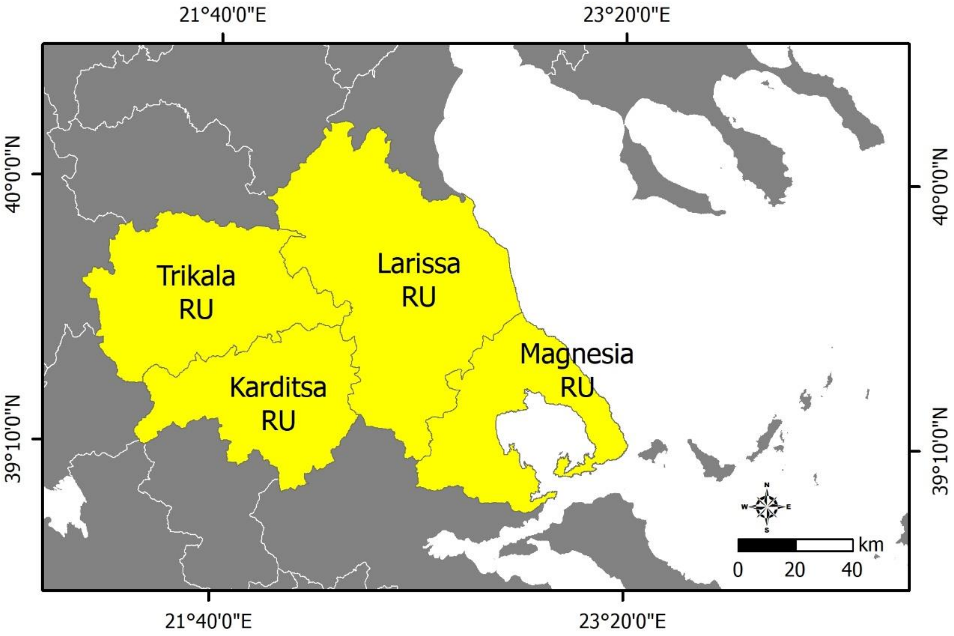

Fig. 11. The regional units (RU) of the Region of Thessaly used in our study in order to detect the evolution of the COVID-19 pandemic in the Thessaly Region.

3.1.1. Results for the affected Karditsa regional unit

In the graph for the affected Karditsa regional unit, the confirmed COVID-19 cases are presented for the week before the earthquake and for the following 3 weeks (Fig. 12). More specifically, 73 confirmed COVID-19 cases were reported during the selected pre-earthquake period. During the post-earthquake period, 338 COVID-19 cases were recorded. In particular, 79 cases were recorded during the first week after the earthquake, 114 cases during the second and 145 cases during the third. Based on this case distribution, it is concluded that the pandemic evolution in Karditsa regional unit is characterized by an increase in the daily confirmed COVID-19 cases during the studied post-disaster period. More specifically:

- the total cases of the first week following the earthquake were 6 more than those of the week before the earthquake,
- the total cases of the second week following the earthquake were 35 more than those of the first week following the earthquake,
- the total cases of the third week following the earthquake were 31 more than those of the second week following the earthquake.

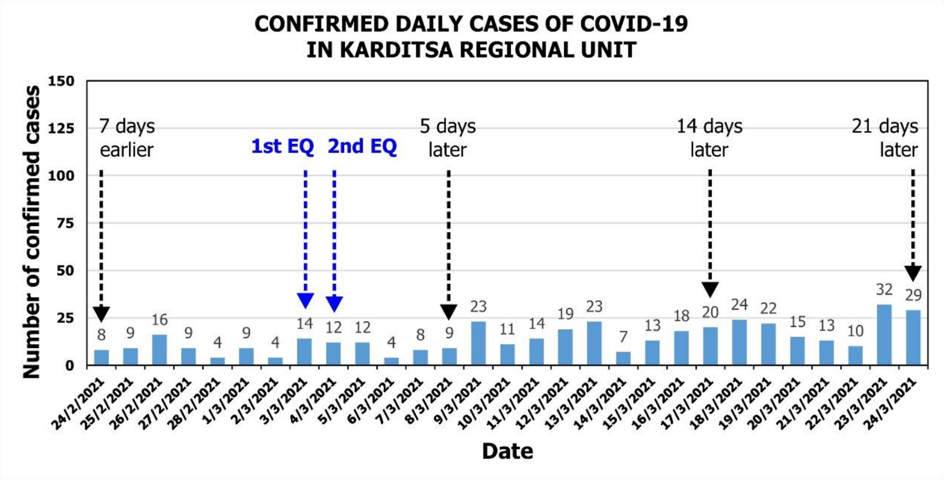

Fig. 12. Graph of the daily confirmed COVID-19 cases in the local population of Karditsa regional unit of Thessaly Region, which was affected by the destructive 3 and 4 March 2021 earthquakes. The highlighted dates refer to the 3 March 2021 earthquake.

3.1.2. Results for the affected Larissa regional unit

In the graph for the affected Larissa regional unit, the confirmed COVID-19 cases are presented for the week before the earthquake and for the following 3 weeks (Fig. 13). More specifically, 462 laboratory-confirmed COVID-19 cases was reported during the selected pre-earthquake period. During the post-earthquake period, 1592 COVID-19 cases were recorded. In particular, 477 cases were recorded during the first week after the earthquake, 514 cases during the second and 601 cases during the third. Based on this case distribution, it is concluded that the pandemic evolution in Larissa regional unit is characterized by an increase in the daily confirmed COVID-19 cases during the studied post-disaster period. More specifically:

- the total cases of the first week following the earthquake were 15 more than those of the week before the earthquake,
- the total cases of the second week following the earthquake were 37 more than those of the first week following the earthquake,
- the total cases of the third week following the earthquake were 87 more than those of the second week following the earthquake.

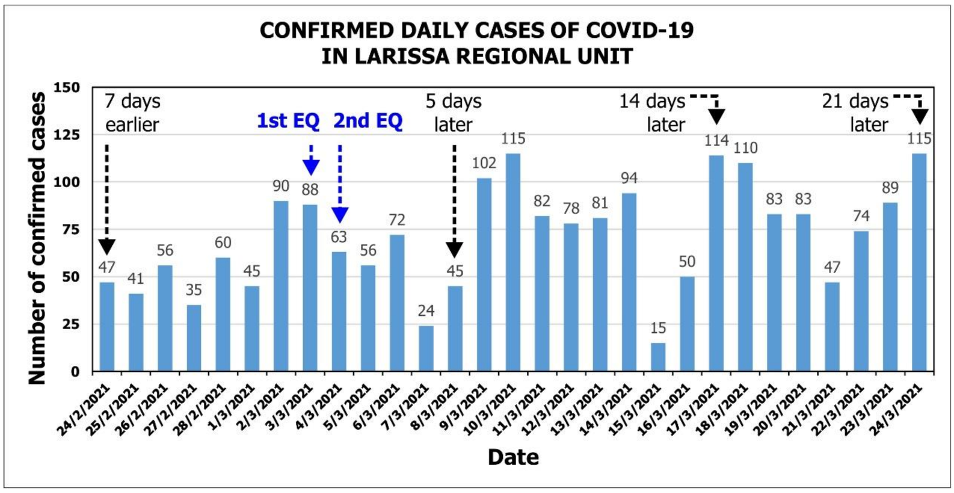

Fig. 13. Graph of the daily confirmed COVID-19 cases in the local population of Larissa regional unit of Thessaly Region, which was affected by the destructive 3 and 4 March 2021 earthquakes. The highlighted dates refer to the 3 March 2021 earthquake.

3.1.3. Results for the affected Magnesia regional unit

In the graph for the affected Magnesia regional unit, the confirmed COVID-19 cases are presented for the week before the earthquake and for the following 3 weeks (Fig. 14). More specifically, 119 confirmed COVID-19 cases were reported during the selected pre-earthquake period. During the post-earthquake period, 464 COVID-19 cases were recorded. In particular, 113 cases were recorded during the first week after the earthquake, 145 cases during the second and 206 cases during the third. Based on this case distribution, it is concluded that the pandemic evolution in Magnesia regional unit is characterized by an increase in the daily confirmed COVID-19 cases during the studied post-disaster period. More specifically:

- the total cases of the first week following the earthquake were 6 less than those of the week before the earthquake,

- the total cases of the second week following the earthquake were 32 more than those of the first week following the earthquake,
- the total cases of the third week following the earthquake were 61 more than those of the second week following the earthquake.

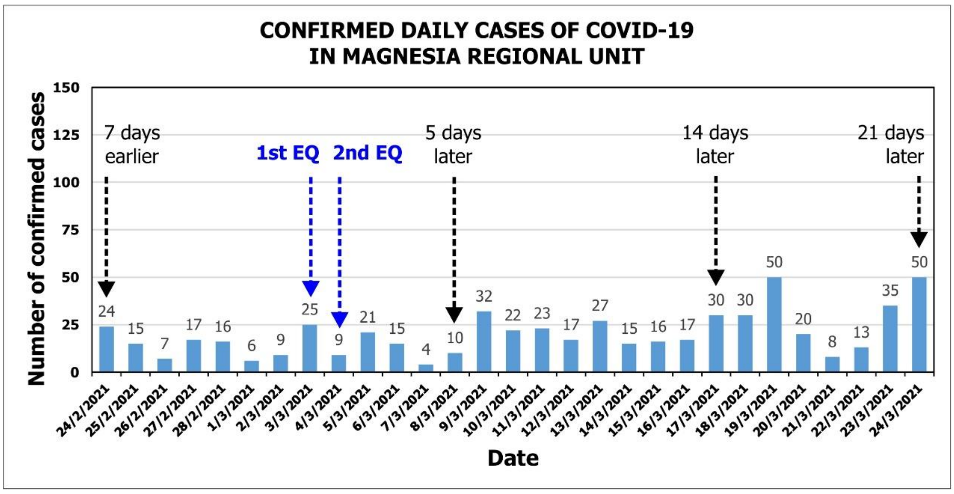

Fig. 14. Graph of the daily confirmed COVID-19 cases in the local population of Magnesia regional unit of Thessaly Region, which was affected by the destructive 3 and 4 March 2021 earthquakes. The highlighted dates refer to the 3 March 2021 earthquake.

3.1.4. Results for the affected Trikala regional unit

In the graph for the affected Trikala regional unit, the confirmed COVID-19 cases are presented for the week before the earthquake and for the following 3 weeks (Fig. 15). More specifically, 45 confirmed COVID-19 cases were reported during the selected pre-earthquake period. During the post-earthquake period, 190 COVID-19 cases were recorded. In particular, 39 cases were recorded during the first week after the earthquake, 61 cases during the second and 90 cases during the third. Based on this distribution of cases, it is concluded that the pandemic evolution in Trikala regional unit is characterized by an increase in the daily confirmed COVID-19 cases during the selected post-disaster period. More specifically:

- the total cases of the first week following the earthquake were 6 less than those of the week before the earthquake,
- the total cases of the second week following the earthquake were 22 more than those of the first week following the earthquake,
- the total cases of the third week following the earthquake were 90 more than those of the second week following the earthquake.

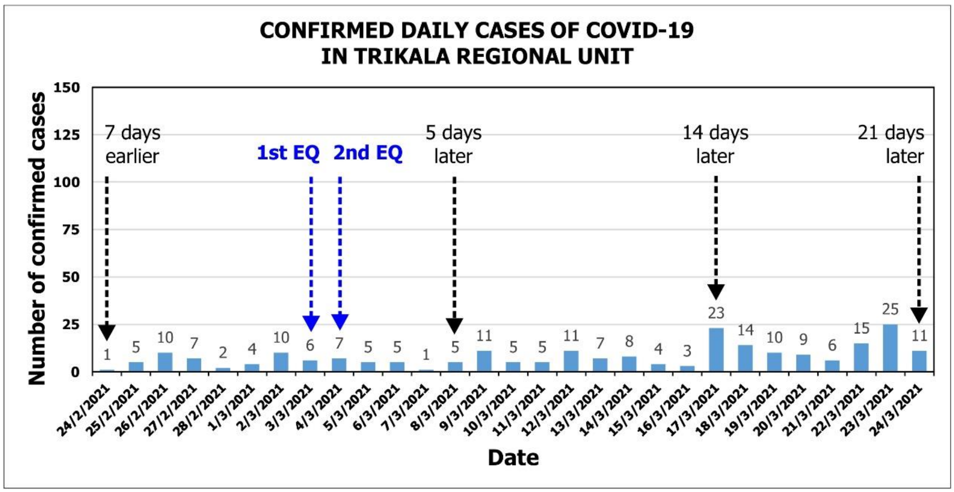

Fig. 15. Graph of the daily confirmed COVID-19 cases in the local population of Trikala regional unit of Thessaly Region, which was affected by the destructive 3 and 4 March 2021 earthquakes. The highlighted dates refer to the 3 March 2021 earthquake.

3.1.5. Results for all affected regional units

The daily cases in Karditsa, Larissa, Magnesia and Trikala regional units (Fig. 16) showed a stability from the beginning of the third wave in mid-January until 2 March. During this period, the total confirmed cases on a daily base in all studied regional units never exceeded 90. However, from 3 to 24 March, an increase is detected in the number of totally confirmed cases in the above regional units. This new trend starts with a total of 133 cases on the mainshock occurrence day, continues with a total of 153 daily cases within a week from the earthquake, with a total of 187 daily cases within two weeks from the earthquake and reaches a total of 205 daily cases within three weeks from the mainshock (Fig. 16).

This increasing trend is detected in the cases per week in all the regional units. In the week following the earthquake, the total recorded cases in all regions are 685, in the second week after the earthquake they amounted to 834 and in the third week to 1042 (Fig. 16).

Based on the above records and taking into account the median incubation period of the virus, which is 5 days (Lauer et al., 2020; WHO, 2020), the increasing trend observed in the first week after the earthquake is not attributed to the earthquake impact on the natural and built environment in the northern part of Thessaly.

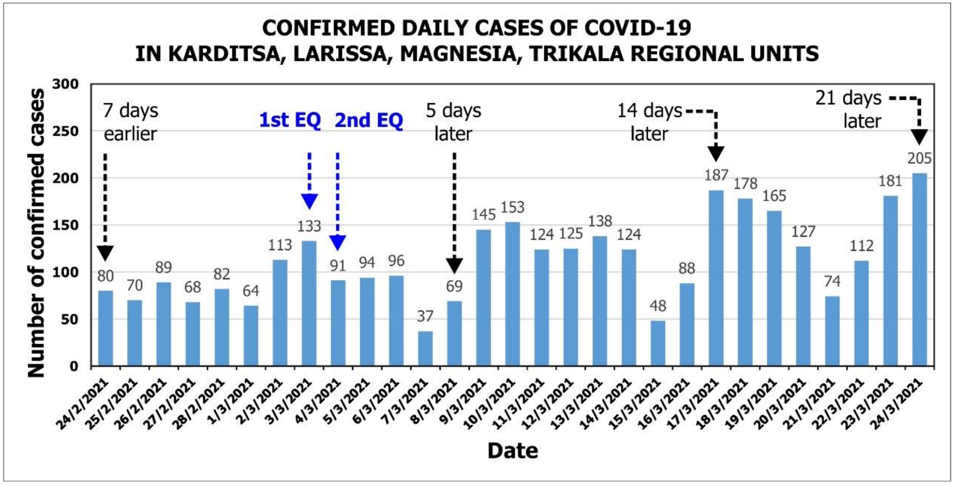

Fig. 16. Graph of the daily confirmed COVID-19 cases in the local population of the studied regional units of Thessaly Region, which were affected by the destructive 3 and 4 March 2021 earthquakes. The highlighted dates refer to the 3 March 2021 earthquake.

4. MULTI-HAZARD EMERGENCY RESPONSE AFTER THE EARLY MARCH THESSALY EARTHQUAKES

4.1. Difficulties in dealing with the compound emergency – geological hazard amid an evolving biological hazard

As it emerged from the above, the 3 March 2021 Thessaly earthquake was destructive resulting in severe structural and non-structural damage to old and unreinforced masonry buildings in the earthquake-affected villages (Fig. 9) and subsequently in dozens of homeless and more than 300 affected people, whose properties were severely damaged. This fact resulted in the mobilization of all Civil Protection authorities to deal with the emergency and the immediate management of the earthquake effects. This mobilization was the first for a compound emergency in 2021 and the first during the third wave of the COVID-19 pandemic in Greece.

The Civil Protection authorities were also mobilized and involved in the emergency operations after the 30 October 2020, Mw = 7.0 Samos earthquake generated during the second pandemic wave. Details on the emergency response actions for management of the geological hazard amid the pandemic are presented by Mavroulis et al. (2021) on the study of post-disaster factors affecting the pandemic evolution in the disaster-affected area of the North Aegean Region among others. The points that make this compound emergency unique are the following:

- Thessaly was hit by the earthquake amid the third pandemic wave, which began in mid-January and is evolving since then. The third wave in Greece is characterized by the highest numbers of daily-confirmed COVID-19 cases, ICU patients and fatalities from the initiation of the pandemic in Greece. During this phase, SARS-CoV-2 has mutated in a variety of ways since it first began spreading in humans in 2019. In the past few months, several SARS-CoV-2 variants, which were first detected in the United Kingdom, South Africa, Brazil and California, presented with mutations that have changed the virus enough to alter its impact on people, as they are more contagious than the strain commonly circulating in Europe and the United States (Liu et al., 2021; Khan et al., 2021; van Dorp et al., 2021).
- The pre-disaster viral load in the regional units of Thessaly Region was large and of high potential for resulting in an outbreak of COVID-19 cases during the post-earthquake period with adverse effects not only on the public health but also to the earthquake emergency response actions and recovery.
- The earthquake-affected mainland area of Thessaly was easily accessible and close to large urban centers with higher viral load and infectious rates.
- The population density in Thessaly is higher than those other areas affected by earthquakes so far amid the COVID-19 pandemic.
- Thessaly was hit amid the third pandemic period, but with a powerful weapon to deal with its adverse effects. Widespread testing and COVID-19 vaccines have provided an opportunity to slow the SARS-CoV-2 spread and reduce chances of developing severe infection and mortality. Trials confirm that COVID-19 vaccines drastically reduce the severity of COVID-19 infections, prevent deaths and curb the spread of the pandemic (Rutkowski et al., 2021; Levine-Tiefenbrun et al., 2021).

All these issues made the case of the earthquake-affected Thessaly more difficult in terms of selecting appropriate measures to manage the earthquake effects, which at the same time should be compatible with the applied pandemic mitigation measures.

4.2. Multi-hazard emergency response actions

The Directorate of Civil Protection of the Region of Thessaly activated the mechanism in accordance with the “Enceladus” plan published by the General Secretariat for Civil Protection for dealing with the earthquake emergency and earthquake effects. This plan was issued on February 2020 before the initiation of the pandemic in Greece and it is characterized by a single hazard approach to manage earthquake emergencies and related effects, in which hazards are treated as isolated and independent phenomena.

The Directorate of Civil Protection of the Region of Thessaly was in full cooperation and constant communication with the Ministry of Citizen Protection and the relevant Ministries during the first hours and days of the post-disaster phase in order to effectively respond to the emergency situation.

The on-site operations coordination center was established in an open space (camp) with the participation of all involved Civil Protection authorities and services, and in constant communication with the Deputy Minister for Civil Protection and Crisis Management, and the Secretary General for Civil Protection. In these spaces, the participants were not only safe from the ongoing aftershocks, but also from further transmission of the new virus. These facilities provided continuous ventilation and space for maintaining physical distancing among participants.

Moreover, specially designed places for information and coordination meetings were designated in the emergency shelter set up in an open football field of the earthquake-affected Damassi village. This shelter was set up for the accommodation of homeless and affected people with areas designated for emergency supplies distribution, medical care, health screening and monitoring, psychological support of the accommodated as well as for voluntary services (Fig. 17).

During the earthquake emergency, several actions were conducted comprising search and rescue operations, first-aid treatment and medical care, provision of emergency supplies, provision of emergency shelters, building inspections and assessment of damage extent.

Many of these actions are characterized by continuous interaction and close contact of the Civil Protection staff with the local population of the earthquake-affected area. This interaction amid the COVID-19 pandemic is incompatible with its mitigation measures. For this reason, many of the actions, which are characterized by high transmission risk among the affected population, have been adjusted to the new conditions of a multi-risk approach to disaster risk reduction and management. This adjustment comprised:

- Organization of camp sites with tents in many earthquake-affected villages including Damassi (Fig. 17), Mesochori, Amouri and Vlachogianni.
- Temporary sheltering of homeless and affected in hotels in nearby urban centers. Three hotels in Trikala and two in Larissa were leased by the Region of Thessaly in cooperation with the municipalities of the area for the residents who did not want to spend the night in their homes after the earthquake. It is important to mention

that the hotels in Trikala hosted about 300 residents during the first days of the emergency response.

- Various types of sheltering were also used shortly after the earthquake for the immediate temporary accommodation of the affected people, including semi-permanent container-type structures (Fig. 17a) and camper vans (Figs 17a-b).

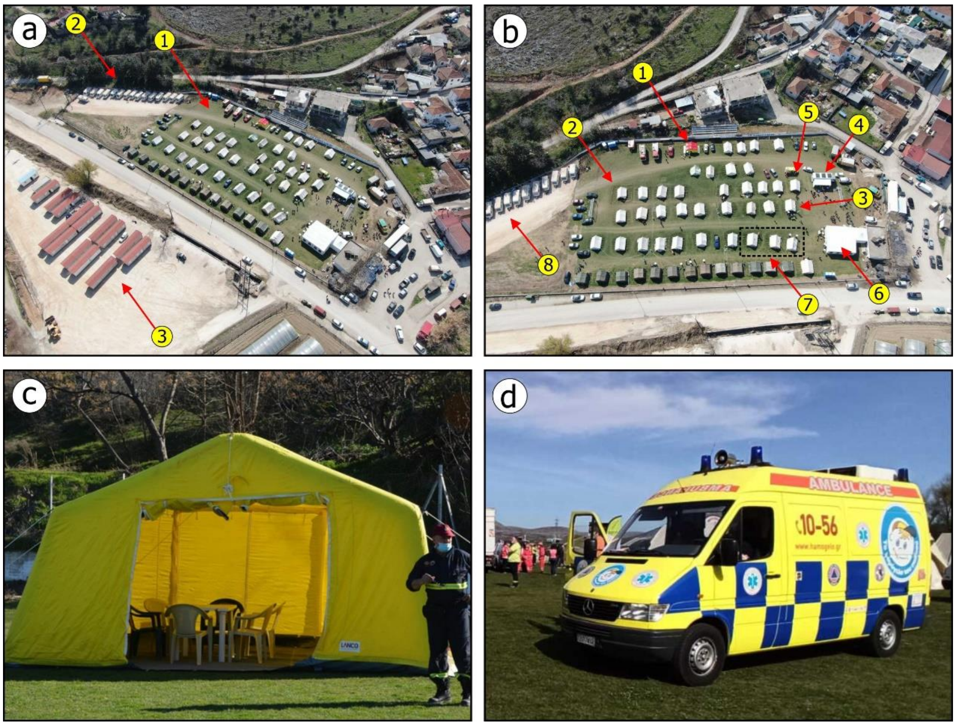

Fig. 17. (**a**) Drone view of the emergency shelter (**1**) in the earthquake-affected Damassi village. In addition to the tents, camper vans were used (**2**). They were installed in a specially designed municipal area (**2**). Few days later, container-type houses (**3**) were also set up for the temporary sheltering of the affected people who lost their properties. (**b**) Drone view of the Damassi emergency shelter with its facilities. **1**: Operations coordination center; **2**: Isolation tent intended for separating suspected COVID-19 cases and managing mild COVID-19 patients; **3**: Tent of the National Public Health Organization staff; **4**: Mobile facility staffed by specialized personnel comprising psychologist, social worker, volunteer doctor, in order to provide medical, social, psychological and material support to adults and kids; **5**: Mobile Intensive Care Unit. The mobile facility with the specialized personnel and the mobile Intensive Care Unit was provided by the volunteer organization "The Smile of the Child"; **6**: Food distribution facilities; **7**: Tents for involved voluntary teams; **8**: Camper vans area. (**c**) Close view of the Operational Coordination Center. (**d**) The aforementioned Mobile Intensive Care Unit.

The organization of many temporary shelters for the affected population, the use of hotels to accommodate homeless, and the immediate use of various means of accommodation contributed substantially to avoid overcrowding in a single emergency shelter, to maintain the physical distance between the accommodated people and to limit the transmission risk among the affected population and the staff involved in disaster management.

On late March 2021, tents were gradually removed from the Damassi emergency shelter. Most of residents were transferred to adjacent container-type structures in Damassi village and Elassona town as well as in camper vans, while others stayed in hotels in Trikala and in intact houses of their close family and friendly environment. Some of the affected people rent houses using the provided financial support comprising rent allowance.

The modification of food distribution process in the emergency shelters in Thessaly was considered mandatory amid the COVID-19 pandemic. In the pre-pandemic period, food in emergency shelters were served buffet style and self-service. Amid the COVID-19 pandemic, meals in the Damassi emergency shelter were packaged and served by staff, which wore masks and disposable gloves throughout the preparation and serving of meals (Fig. 18). Similar modifications were also applied in the provision of emergency supplies from individuals and voluntary teams.

Fig. 18. (**a**) The Damassi emergency shelter had specially designed area for food and emergency supplies distribution. (**b**) Modification of the food distribution was mandatory amid the COVID-19 pandemic. Meals were served by staff wearing masks and disposable gloves throughout the preparation and the distribution process.

Temporary isolation facilities for separating suspected COVID-19 cases and managing mild COVID-19 patients, who do not require hospitalization, but ample medical support, were designated in the emergency shelters (Fig. 19a). These facilities were intended for residents (a) tested positive for COVID-19 and having mild symptoms, (b) waiting on a test or test results and having mild symptoms and (c) having no symptoms, but having been told to self-isolate. Moreover, beds, oxygen cylinders and equipment for monitoring oxygen levels were also available, while access to health assessment, medical care and counseling were available any time and kindly provided not only by the state authorities but also from specially trained volunteers (Fig. 17). This approach was essential for further prevention of transmission in case of detection of a suspected COVID-19 case.

Moreover, the involved staff of the Civil Protection authorities applied pandemic mitigation measures for their own safety and the safety of the affected community. These measures comprised mandatory use of face mask indoors and outdoors as well as regular hand washing and using of hand sanitizers according to the guidelines of the NPHO.

One of the most important actions carried out during the emergency response in the earthquake-affected area was the massive and regular screening tests in order to give the possibility to the authorities to detect virus circulation within the affected community and to further isolate the COVID-19 cases in order to prevent virus transmission among the local population of the tested earthquake-affected villages. This action took place after consultation of the Region of Thessaly with the earthquake-affected municipalities and the NPHO and was carried out by the Mobile Health Units (MHU) of the NPHO (Figs 19b-d). The action included free rapid screening tests targeted in the affected Koutsochero, Damassi, Vlachogianni, Mesochori, Amouri, Domeniko, Praetorio, Sykia, Magoula and Evagelismos villages and in Elassona and Tyrnavos towns. It began shortly after 3 March and continued during the emergency and recovery phase (4-20 March).

The screening tests showed that the majority of residents tested in the aforementioned earthquake-affected villages were negative (Table S1). This means that the viral load within the earthquake-affected villages was low at the initiation of the emergency situation and remained at the same level for many days. Due to the fact that there was no virus transmission among local population in the affected villages, the infection rate also remained very low. The results of the massive and regular screening tests showed that the earthquake-affected villages remained safe from virus transmission at least for the critical studied period (3-24 March 2021) and confirmed that the adopted response actions for dealing with the earthquake emergency amid the evolving pandemic were effective.

Fig. 19. (**a**) Isolation tent intended for separating suspected COVID-19 cases and managing mild COVID-19 patients in Damassi emergency shelter. (**b**, **c**) Mobile Health Units of the NPHO were available and properly equipped in the earthquake-affected villages for conducting mass rapid screening tests for the detection of COVID-19 cases among the affected population. (b) A unit in Mesochori village and (**c**, **d**) in Damassi emergency shelter. The Civil Protection staff was also screened for COVID-19 (**d**).

However, there are several factors that can affect the evolution of the pandemic in an area during the post-disaster period, including the demographic characteristics and the ease of access to the affected area and the epidemiological characteristics of the neighboring areas (Mavroulis et al., 2021). As regards the meizoseismal area in Thessaly, its proximity to urban centers with high population density and higher numbers of daily reported COVID-19 cases, including Larissa city, could make the earthquake-affected area more vulnerable to transmission of the new virus and its mutations, especially during the first days of the emergency. However, restrictions of non-essential movements into or out of the municipalities imposed throughout Greece in early March 2021 constituted a measure that also contributed to keep the earthquake-affected area safe from SARS-CoV-2 emergence and transmission.

5. DISCUSSION – CONCLUSIONS

Based on the aforementioned, it can be concluded that in early March 2021 an increasing trend is detected in the COVID-19 pandemic evolution in the Region of Thessaly. This trend resulted from the continuous increase of laboratory-confirmed daily-recorded COVID-19 cases in the region and coincided with the occurrence of the seismic sequence, which included the mainshock on 3 March and the aftershock the following day.

Despite the extensive impact on the built environment induced by the first earthquake and aggravated by the second, and the hundreds of homeless and in need of immediate sheltering, there was no increase in daily cases in the earthquake affected villages. This fact is demonstrated by the results of the massive screening testing targeted in the affected villages and towns by NPHO throughout the duration of the earthquake emergency and especially in the first critical phase of the post-disaster period, which we analyzed in the frame of this study. Moreover, despite the high viral load recorded in the nearby major urban centers (mainly in the adjacent Larissa city and secondarily in smaller cities), the earthquake-affected villages were characterized by different epidemiological characteristics comprising very low to negligible viral load from early to late March.

In order to prevent SARS-CoV-2 transmission in the earthquake-affected community, the involved authorities had to adapt response actions, already included in the existing disaster management plans, to the new conditions formed by the earthquake occurrence amid the pandemic. This adaptation was mandatory due to the fact that the response actions to the earthquake emergency were incompatible to the pandemic mitigation measures announced by both the NPHO and the WHO.

More specifically:

- Gathering of many affected people in a small number of emergency shelters would lead to overcrowded conditions in small spaces, which is incompatible with maintaining physical distance to limit further spread of SARS-CoV-2 virus within the community.
- The distribution of emergency supplies was done with bare hands and with participation of many people, who used and exchanged objects and equipment and often touched the same surfaces. This action is incompatible with pandemic control

measures and in particular with regular hand washing, continuous disinfection of surfaces, use of personal items and avoidance of common items and equipment use.
- In the emergency shelters, some guests may not report fever or any of the signs and symptoms of a respiratory infection, because they believe that their symptoms do not require medical attention. This is incompatible with the temporary isolation that should be followed in the case of people who have tested positive for the novel virus and have mild symptoms, are waiting for test results and have mild symptoms, and have no symptoms but have come into contact with a COVID-19 case.

The above contradicting issues, which arose from the single-hazard approach to disaster management, require the adjustment of actions in the light of a multi-hazard approach. The main goal of earthquake response actions amid an evolving biological hazard, the COVID-19 pandemic, is not only to support those affected by the earthquake and its related hazards, but also to protect those affected by the adverse effects of an uncontrolled transmission of the novel virus in the community, attributed to neglecting design and implementation of immediate response actions.

In the case of the Thessaly seismic sequence, the actions adapted to the new conditions shaped by the collided geological and biological hazards, concerned the provision of emergency shelters, the distribution of emergency supplies to the earthquake-affected population and the provision of medical care to people accommodated in emergency shelters.

The adapted measures comprised:

- Increase of the number of the emergency shelters in the earthquake-affected villages and the adjacent cities for avoiding overcrowding in limited emergency shelters.
- Inclusion of different types of emergency shelters for temporary sheltering of the affected people (hotels, intact houses of the close family and friend environment, container-type houses shortly after the earthquake, camper vans) for maintaining physical distancing between earthquake-affected families.
- Designation of isolation facilities in the emergency shelters in order to prevent further transmission in the facilities and the community in case of detection of COVID-19 cases.
- Screening tests in the earthquake-affected residential areas for detecting cases as quick as possible and preventing further transmission.

- Modification of the process followed for the distribution of emergency supplies to the earthquake-affected people for avoiding further transmission by items and surfaces.

The above-mentioned conflicting issues and the measures adopted to resolve them highlights the urgent need of a multi-hazard approach to disaster risk reduction and disaster management. This approach is widely encouraged in international frameworks and national policies for action on the disaster risk reduction. For example, the Sendai Framework for Disaster Risk Reduction 2015-2030 clearly stated that "disaster risk reduction needs to be multi-hazard". This statement seems to be the most effective approach as interactions between hazards have been already identified (e.g., Gill and Malamud, 2014, 2016) and have high potential to generate impacts which are more severe than the sum of the single impacts.

In the case of the earthquake-affected villages, it seems that the synergy of pandemic mitigation measures and actions adapted to manage the effects of the earthquake amid the COVID-19 pandemic was effective, as the majority of the tested residents in the earthquake-affected villages were negative throughout the response phase for the earthquake emergency. The proximity of the earthquake-affected villages to large urban centers with higher viral load does not seem to affect the villages as at that time, there were restrictions of non-essential movements into or out of the municipalities.

Taking into account the above adapted measures and their positive results, it can be said that they constitute a good practice and an important lesson for disaster management and disaster risk reduction amid the evolving pandemic. This multi-hazard approach could be also adopted and applied in respective collisions of geological and biological hazards and related disasters not only in Greece, but also in other countries with respective geoenvironmental characteristics and similar epidemiological features.

Acknowledgements

Several information provided in this manuscript are compiled from publicly available, open-access data provided by the relevant agencies, the authors of which are acknowledged. The Post-Graduate Program "Environmental, Disaster, and Crises Management Strategies" of the National and Kapodistrian University of Athens, Greece, is also acknowledged for supporting the post-event field surveys.

6. REFERENCES

Caputo, R., Chatzipetros, A., Pavlides, S., Sboras, S., 2012. The Greek Database of Seismogenic Sources (GreDaSS): State-of-the-art for northern Greece. *Annals of Geophysics*, 55, 859-894.

Caputo, R., Pavlides, S., 1993. Late Cainozoic geodynamic evolution of Thessaly and surroundings (central-northern Greece). *Tectonophysics*, 223, 339-362.

Cetin, K.O., Mylonakis, G., Sextos, A., Stewart, J.P., et al., 2021. Seismological and Engineering Effects of the M 7.0 Samos Island (Aegean Sea) Earthquake. Report GEER-069; Geotechnical Extreme Events Reconnaissance Association: Alameda County, CA, USA, http://dx.doi.org/10.18118/G6H088.

García Garmendia, J.L., Ramírez Arcos, M., Barrero Almodóvar, A.E., Chávez Caballero, M., Jorge Amigo, V., Serrano Martino, M.C., 2020. Detección viral y respuesta serológica en pacientes críticos intubados con SARS-CoV-2. Implicaciones para retirada de aislamiento [Viral detection and serological response in critically ill patients with SARS-CoV-2. Implications for isolation withdrawal]. *Medicina Intensiva*, 44 (9), 586-588, https://doi.org/10.1016/j.medin.2020.04.014

Gill, J.C., Malamud, B.D. 2014. Reviewing and visualizing the interactions of natural hazards. *Reviews of Geophysics*, 52, doi:10.1002/2013RG000445.

Gill, J.C., Malamud, B.D. 2016. Hazard Interactions and Interaction Networks (Cascades) within Multi-Hazard Methodologies. *Earth Syst. Dynam.*, 7, 659-679, https://doi.org/10.5194/esd-7-659-2016

Hellenic Statistical Authority (2011). 2011 Building Census of Greece. Available at: https://www.statistics.gr/en/2011-census-pop-hous

La Scola, B., Le Bideau, M., Andreani, J., Hoang, V.T., Grimaldier, C., Colson, P., Gautret, P., Raoult, D., 2020. Viral RNA load as determined by cell culture as a management tool for discharge of SARS-CoV-2 patients from infectious disease wards. *European Journal of Clinical Microbiology & Infectious Diseases*. 39 (6), 1059-1061, https://doi.org/10.1007/s10096-020-03913-9

Lauer, S.A., Grantz, K.H., Bi, Q., Jones, F.K., Zheng, Q., Meredith, H.R., Azman, A.S., Reich, N.G., Lessler, J., 2020. The incubation period of coronavirus disease 2019

(COVID-19) from publicly reported confirmed cases: estimation and application. *Annals of Internal Medicine*. 172 (9), 577-582, https://doi.org/10.7326/M20-0504.

Lekkas, E., Agorastos, K., Mavroulis, S., Kranis, Ch., Skourtsos, Emm., Carydis, P., Gogou, M., Katsetsiadou, K.-N., Papadopoulos, G., Triantafyllou, I., Agalos, A., Moraitis, S., Stamati, E., Psarris, D., Kaviris, G., Kapetanidis, V., Papadimitriou, P., Karakonstantis, A., Spingos, I., Kouskouna, V., Kassaras, I., Pavlou, K., Voulgaris, N., Mavrouli, M., Pavlides, S., Chatzipetros, A., Sboras, S., Kremastas, E., Chatziioannou, A., Kiratzi, A., Papazachos, C., Chatzis, N., Karakostas, V., Papadimitriou, E., Koukouvelas, I., Nikolakopoulos, K., Kyriou, A., Apostolopoulos, D., Zygouri, V., Verroios, S., Belesis, A., Tsentzos, I., Krassakis, P., Lymperopoulos, K., Karavias, A., Bafi, D., Gatsios, T., Karatzia, M., Gkougkoustamos, I., Falaras, T., Parcharidis, I., Papathanassiou, G., Evangelidis, C.P., Karastathis,V., Tselentis, G-A., Ganas, A., Tsironi, V., Karasante, I., Valkaniotis, S., Galanakis, D., Kostantopoulou, G., Theodoulidis, N., Karakostas, Ch., Lekidis,V., Makra, K., Margaris, V., Morfidis, K., Papaioannou, Ch., Rovithis, M., Salonikios, Th., Papadopoulos, N., Kourou, A., Manousaki, M., Thoma, T., 2021. The early March 2021 Thessaly earthquake sequence. *Newsletter of Environmental, Disaster and Crises Management Strategies*, 22, 195 p., ISSN 2653-9454, http://dx.doi.org/10.13140/RG.2.2.34803.04644

Lekkas, E., Mavroulis, S., Carydis, P., Skourtsos, E., Kaviris, G., Paschos, P., Ganas, A., Kazantzidou-Firtinidou, D., Parcharidis, I., Gatsios, T., Angelou, D., Karavias, A., Bafi, D., Markogiannaki, O., 2020a. The March 21, 2020, Mw 5.7 Epirus (Greece) Earthquake. *Newsletter of Environmental, Disaster and Crises Management Strategies*, 17, 75 p, ISSN 2653-9454, http://dx.doi.org/10.13140/RG.2.2.16251.54561

Lekkas, E., Mavroulis, S., Gogou, M., Papadopoulos, G.A., Triantafyllou, I., Katsetsiadou, K.-N., Kranis, H., Skourtsos, E., Carydis, P., Voulgaris, N., Papadimitriou, P., Kapetanidis, V., Karakonstantis, A., Spingos, I., Kouskouna, V., Kassaras, I., Kaviris, G., Pavlou, K., Sakkas, V., Karatzetzou, A. Evelpidou, N. Karkani, E. Kampolis, I., Nomikou, P., Lambridou, D., Krassakis, P., Foumelis, M., Papazachos, C., Karavias, A., Bafi, D., Gatsios, T., Markogiannaki, O., Parcharidis, I., Ganas, A., Tsironi, V., Karasante, I., Galanakis, D., Kontodimos, K., Sakellariou, D., Theodoulidis, N., Karakostas, C., Lekidis, V., Makra, K., Margaris, V., Morfidis, K., Papaioannou, C., Rovithis, E., Salonikios, T., Kourou, A., Manousaki, M., Thoma, T., Karveleas, N., 2020b. The October 30, 2020 Mw 6.9 Samos (Greece) earthquake. *Newsletter of Environmental, Disaster and Crises Management Strategies*, 21, 156 p., ISSN 2653-9454, http://dx.doi.org/10.13140/RG.2.2.13630.10561

Lekkas, E., Mavroulis, S., Kourou, A., Manousaki, M., Thoma, T., Karveleas, N., 2020c. The October 30, 2020, Mw=6.9, Samos (Eastern Aegean Sea, Greece) Earthquake: Preparedness and Emergency Response for Effective Disaster Management. Joint Report of National and Kapodistrian University of Athens and Earthquake Planning and Protection Organization, p. 53, ISSN 2653-9454, http://dx.doi.org/10.13140/RG.2.2.25478.60482

Levine-Tiefenbrun, M., Yelin, I., Katz, R., Herzel, E., Golan, Z., Schreiber, L., Wolf, T., Nadler, V., Ben-Tov, A., Kuint, J., Gazit, S., Patalon, T., Chodick, G., Kishony, R., 2021. Initial report of decreased SARS-CoV-2 viral load after inoculation with the BNT162b2 vaccine. *Nature Medicine*, https://doi.org/10.1038/s41591-021-01316-7.

Mavroulis, S., Mavrouli, M., Lekkas, E., 2021. Geological and hydrometeorological hazards and related disasters amid COVID-19 pandemic in Greece: Post-disaster trends and factors affecting the COVID-19 evolution in affected areas. *Safety Science*, 138, 105236. https://doi.org/10.1016/j.ssci.2021.105236

National Public Health Organization 2021. COVID-19 Daily Reports. Available at: https://eody.gov.gr/epidimiologika-statistika-dedomena/ektheseis-covid-19/

Papadimitriou, P., Kapetanidis, V., Karakonstantis, A., Spingos, I., Kassaras, I., Sakkas, V., Kouskouna, V., Karatzetzou, A., Pavlou, K., Kaviris, G., Voulgaris, N., 2020. First results on the Mw = 6.9 Samos Earthquake of 30 October 2020. *Bulletin of the Geological Society of Greece*, 56, 251-279.

Rutkowski, K., Mirakian, R., Till, S., Rutkowski, R., Wagner, A., 2021. Adverse reactions to COVID-19 vaccines: A practical approach. *Clinical & Experimental Allergy*. https://doi.org/10.1111/cea.13880

Valkaniotis, S., Papathanassiou, G., Ganas, A., Kremastas, E., Caputo, R., 2021. Preliminary report of liquefaction phenomena triggered by the March 2021 earthquakes in Central Thessaly, Greece. DOI: 10.5281/zenodo.4608365

WHO 2020. Coronavirus disease (COVID-19). Available at: https://www.who.int/emergencies/diseases/novel-coronavirus-2019/question-and-answers-hub/q-adetail/coronavirus-disease-covid-19.

Table S1. Results of the massive rapid screening tests for COVID-19 detection in the earthquake-affected area of the Region of Thessaly. Data derived from official reports of the NPHO and announcements of the Region of Thessaly.

Massive Rapid Screening Tests for COVID-19 Detection in the earthquake-affected area of the Region of Thessaly				
Date	**Area**	**Total conducted rapid tests**	**Negative**	**Positive**
4 March 2021	Damassi	19	19	0
	Mesochori	27	27	0
	Falani	156	155	1
	Kileler	76	73	3
	Tempi	29	29	0
	Larissa	456	448	8
5 March 2021	Damassi	10	10	0
	Mesochori	8	8	0
	Amouri	11	11	0
	Ayia	96	95	1
	Stomio	84	84	0
	Larissa	690	678	12
6 March 2021	Larissa	444	434	10
7 March 2021	Damassi	23	23	0
	Mesochori	7	7	0
	Magoula	36	36	0
	Domeniko	20	20	0
	Praetorio	41	41	0
	Vlachogianni	61	61	0
8 March 2021	Koutsochero	42	42	0
	Amygdalea	5	5	0
	Mandra	51	51	0
	Amouri	9	9	0
	Damassi	10	10	0
	Tyrnavos	32	31	1
	Mesochori	7	5	2
9 March 2021	Domeniko	10	10	0
	Vlachogianni	23	23	0
	Praetorio	25	25	0
	Magoula	31	31	0
	Mesochori	11	11	0
	Amouri	7	7	0

	Damassi	10	10	0
	Elassona	81	81	0
	Farsala	209	209	0
	Larissa	660	635	25
10 March 2021	Koutsochero	3	3	0
	Mandra	19	19	0
	Damassi	14	14	0
	Mesochori	10	10	0
	Amouri	11	11	0
	Tyrnavos	38	36	2
	Larissa	453	440	13
11 March 2021	Larissa	326	319	7
	Ayios Antonios	134	133	1
	Damassi	13	13	0
	Evagelismos	59	59	0
	Kileler	114	114	0
	Mesochori	4	4	0
	Palaeokastro	22	22	0
	Tempi	25	25	0
	Sykia	10	10	0
12 March 2021	Larissa	687	674	13
	Ayia	82	82	0
	Mesochori	7	7	0
	Vlachogianni	21	21	0
	Damassi	15	15	0
	Tyrnavos	31	31	0
13 March 2021	Larissa	434	0	5
	Rachoula	17	17	0
	Elassona	146	146	0
	Magoula	11	11	0
	Mesochori	5	5	0
	Vlachogianni	5	5	0
	Amouri	8	8	0
	Praetorio	5	5	0
	Damassi	17	17	0
17 March 2021	Larissa	574	565	9
	Domeniko	2	2	0
	Mesochori	14	14	0
	Amouri	11	11	0
	Milaea	86	83	3

	Damassi	19	19	0
	Palaeokastro	17	17	0
20 March 2021	Larissa	175	171	4
	Amouri	5	5	0
	Magoula	58	57	1
	Damassi	13	13	0
	Mesochori	13	12	1

BGSG

Volume 58

Research Paper

Correspondence to:
Athanasios Ganas
aganas@noa.gr
DOI number:
http://dx.doi.org/10.12681/bgsg.27102

Keywords:
Thessaly; earthquake; InSAR; relocation; GNSS; stress transfer; blind fault; extension

Citation:
Ganas, A., Valkaniotis, S., Briole, P., Serpetsidaki, A., Kapetanidis, V., Karasante, I., Kassaras, I., Papathanassiou, G., Karamitros, I., Tsironi, V., Elias, P., Sarhosis, V., Karakonstantis, A., Konstantakopoulou, E., Papadimitriou, P. and Sokos, E. (2019), Domino-Style Earthquakes Along Blind Normal Faults in Northern Thessaly (Greece): Kinematic Evidence from Field Observations, Seismology, Sar Interferometry and GNSS. Bulletin Geological Society of Greece, 58, 37-86.

Publication History:
Received: 20/05/2021
Accepted: 07/07/2021
Accepted article online: 09/07/2021

The Editor wishes to thank Prof. V. Karakostas and Prof. R. Caputo for their work with the scientific reviewing of the manuscript and Ms Emmanouela Konstantakopoulou for editorial assistance.

DOMINO-STYLE EARTHQUAKES ALONG BLIND NORMAL FAULTS IN NORTHERN THESSALY (GREECE): KINEMATIC EVIDENCE FROM FIELD OBSERVATIONS, SEISMOLOGY, SAR INTERFEROMETRY AND GNSS

Athanassios Ganas[1], Sotiris Valkaniotis[2], Pierre Briole[3], Anna Serpetsidaki[4], Vasilis Kapetanidis[5], Ilektra Karasante[1], Ioannis Kassaras[5], George Papathanassiou[2], Ioannis Karamitros[1], Varvara Tsironi[1,4], Panagiotis Elias[6], Vasilis Sarhosis[7], Andreas Karakonstantis[5], Emmanouela Konstantakopoulou[1,5], Panagiotis Papadimitriou[5], and Efthimios Sokos[4]

[1]National Observatory of Athens, Institute of Geodynamics, Lofos Nymfon, Thission, 11810 Athens, Greece
aganas@noa.gr, vtsironi@noa.gr, hlekara@hotmail.com, jkaram@noa.gr, emma.kon97@gmail.com,
[2]Department of Civil Engineering, Democritus University of Thrace, 67100 Xanthi, Greece
valkaniotis@yahoo.com, gpapatha@civil.duth.gr,
[3]Ecole Normale Supérieure de Paris, PSL Research University, Laboratoire de Géologie - UMR CNRS 8538, 24 rue Lhomond, 75005 Paris – France
briole@ens.fr,
[4]Seismological Laboratory, Department of Geology, University of Patras, 26504 Rio, Greece
annaserp@upatras.gr, esokos@upatras.gr,
[5]Seismological Laboratory, Department of Geology and Geoenvironment, National and Kapodistrian University of Athens, Greece
ppapadim@geol.uoa.gr, vkapetan@geol.uoa.gr, kassaras@geol.uoa.gr, akarakon@geol.uoa.gr,
[6]National Observatory of Athens, Institute of Astronomy, Astrophysics, Space Applications and Remote Sensing, Vas. Pavlou and I. Metaxa, GR-15 236 Penteli, Greece;
pelias@noa.gr,
[7]School of Civil Engineering, University of Leeds, UK
v.sarhosis@leeds.ac.uk,
***Correspondence: aganas@noa.gr, Tel.: +30 210 3490186 (A.G.)**

Abstract

Here we present a joint analysis of the geodetic, seismological and geological data of the March 2021 Northern Thessaly seismic sequence, that were gathered and processed as of April 30, 2021. First, we relocated seismicity data from regional and local networks and inferred the dip-direction (NE) and dip-angle (38°) of the March 3, 2021 rupture plane. Furthermore, we used ascending and descending SAR images acquired by the Sentinel-1 satellites to map the co-seismic displacement field. Our results indicate that the March 3, 2021 Mw=6.3 rupture occurred on a NE-dipping, 39° normal fault located between the villages Zarko (Trikala) and Damasi (Larissa). The event of March 4, 2021 occurred northwest of Damasi, along a fault oriented WNW-ESE and produced less deformation than the event of the previous day. The third event occurred on March 12, 2021 along a south-dipping normal fault. We computed 22 focal mechanisms of aftershocks with M≥4.0 using P-wave first motion polarities. Nearly all focal mechanisms exhibit normal kinematics or have a dominant normal dip-slip component. The use of InSAR was crucial to differentiate the ground deformation between the ruptures. The majority of deformation occurs in the vertical component, with a maximum of 0.39 m of subsidence over the Mw=6.3 rupture plane, south and west of Damasi. A total amount of 0.3 m horizontal displacement (E-W) was measured. We also used GNSS data (at 30-s sampling interval) from twelve permanent stations near the epicentres to obtain 3D seismic offsets of station positions. Only the first event produces significant displacement at the GNSS stations (as predicted by the fault models, themselves very well constrained by InSAR). We calculated several post-seismic interferograms, yet we have observed that there is almost no post-seismic deformation, except in the footwall area (Zarkos mountain). This post-seismic deformation is below the 7 mm level (quarter of a fringe) in the near field and below the 1 mm level at the GNSS sites. The cascading activation of the three events in a SE to NW direction points to a pattern of domino-style earthquakes, along neighbouring fault segments. The kinematics of the ruptures point to a counter-clockwise change in the extension direction of the upper crust (from NE-SW near Damasi to N-S towards northwest, near Verdikoussa).

Keywords: Thessaly; earthquake; InSAR; relocation; GNSS; stress transfer; blind fault; extension

Περίληψη

Μέσω της εργασίας αυτής, παρουσιάζουμε μια πολύπλευρη ανάλυση γεωδαιτικών, σεισμολογικών και γεωλογικών δεδομένων της σεισμικής ακολουθίας του Μαρτίου 2021 στη Βόρεια Θεσσαλία. Για την ανάλυση αυτή, χρησιμοποιήθηκαν δεδομένα έως και τις 30 Απριλίου 2021. Πρώτα, έγινε ο επαναπροσδιορισμός των σεισμικών επικέντρων των σεισμολογικών δεδομένων με την παροχή δεδομένων από τοπικά σεισμολογικά δίκτυα και βρέθηκε η φορά κλίσης (ΒΑ) και η γωνία κλίσης (38°) του σεισμικού ρήγματος του σεισμού της 3ης Μαρτίου 2021. Στη συνέχεια, χρησιμοποιήθηκαν δεδομένα εικόνων ραντάρ ανοδικής και καθοδικής τροχιάς από τους δορυφόρους Sentinel-1 της ESA για την χαρτογράφηση της συν-σεισμικής παραμόρφωσης που προκλήθηκε από τους σεισμούς. Τα αποτελέσματα μας υποδεικνύουν ότι η κύρια διάρρηξη του σεισμικού γεγονότος στις 3 Μαρτίου μεγέθους Mw=6.3 ενεργοποίησε ένα κανονικού τύπου «τυφλό» ρήγμα, που κλίνει προς τα ΒΑ με 39 μοίρες κλίση και βρίσκεται μεταξύ των χωριών Ζάρκο (Τρίκαλα) και Δαμάσι (Λάρισα). Το σεισμικό γεγονός της 4ης Μαρτίου 2021, που έγινε βορειοδυτικά του Δαμασίου, διέρρηξε ένα ρήγμα με μέση διεύθυνση ΔΒΔ-ΑΝΑ και παρήγαγε λιγότερη εδαφική παραμόρφωση σε σχέση με το πρώτο. Το τρίτο σεισμικό γεγονός έλαβε χώρα στις 12 Μαρτίου 2021, κατά μήκος ενός κανονικού ρήγματος που κλίνει προς το νότο. Στη συνέχεια, ο υπολογισμός 22 μηχανισμών γένεσης από μετασεισμούς μεγέθους M>4.0 έγινε με βάση την μέθοδο των πρώτων αποκλίσεων των P σεισμικών κυμάτων. Σχεδόν όλοι οι μηχανισμοί γένεσης δείχνουν κινηματική κανονικών ρηγμάτων ή ότι η κανονική κινηματική των ρηγμάτων είναι η επικρατούσα. Η χρήση της Συμβολομετρίας Ραντάρ είναι καθοριστική στην ερμηνεία των σεισμών αυτών καθότι με αυτή μπορέσαμε να προσδιορίσουμε χωρικά την διαφοροποίηση της παραμόρφωσης του εδάφους μεταξύ των σεισμικών διαρρήξεων από τον εκάστοτε σεισμό. Το μεγαλύτερο ποσοστό της παραμόρφωσης παρατηρήθηκε στη κατακόρυφη συνιστώσα της κίνησης, με μέγιστη καθίζηση 0.39 m στην περιοχή πάνω από το ρήγμα του πρώτου σεισμού Mw=6.3, νότια του χωριού Δαμάσι. Επίσης, μετρήθηκε μία συνολική κίνηση της τάξεως των 0.3 m στην οριζόντια συνιστώσα Α-Δ. Επιπρόσθετα, χρησιμοποιήθηκαν δεδομένα GNSS (με ρυθμό δειγματοληψίας σήματος τα 30 s) από 12 μόνιμους σταθμούς της Θεσσαλίας έτσι ώστε να μετρηθεί το τρισδιάστατο άνυσμα της σεισμικής κίνησης του εκάστοτε σταθμού. Μόνο ο πρώτος σεισμός παρήγαγε σημαντικές μετατοπίσεις της θέσης των γεωδαιτικών σταθμών GNSS (όπως το είχαν προβλέψει και τα μοντέλα σεισμικών ρηγμάτων, που παρήχθησαν από τα δεδομένα της συμβολομετρίας ραντάρ). Επίσης, δεν παρατηρήθηκε κάποια μετασεισμική παραμόρφωση στα συμβολογράμματα ραντάρ, εκτός από την περιοχή που είναι το ανερχόμενο τέμαχος του ρήγματος του πρώτου σεισμού, στο βουνό Ζάρκο. Αυτή η μετασεισμική παραμόρφωση βρίσκεται κάτω από το όριο των 7 mm και κάτω από 1 mm σε περιοχές κοντά σε GNSS σταθμούς. Η διαδοχική ενεργοποίηση των τριών

σεισμών με διεύθυνση από τα ΝΑ προς τα ΒΔ δείχνει ένα χαρακτηριστικό τύπο ντόμινο διάρρηξης, κατά μήκος γειτονικών ρηγμάτων. Η κινηματική των διαρρήξεων που παρήγαγαν αυτούς τους σεισμούς δείχνουν μια αριστερόστροφη αλλαγή στην διεύθυνση του εφελκυσμού του άνω φλοιού (από ΒΑ-ΝΔ κοντά στο χωριό Δαμάσι σε Β-Ν προς βορειοδυτικά, κοντά στο χωριό Βερδικούσσα).

Λέξεις – Κλειδιά: Θεσσαλία, σεισμός, InSAR, επαναπροσδιορισμός σεισμών, GNSS, μεταφορά τάσης, «τυφλό» ρήγμα, εφελκυσμός.

1. INTRODUCTION

The region of Thessaly, in Central Greece is part of the Pelagonian zone which forms the western Internal Hellenides. It is characterised by abundant occurrences of crystalline basement, predominantly pre-Alpine in age. The Pelagonian is defined as a NW-SE trending zone consisting of thrust sheets that record Alpine orogenic events and is bordered by the Neotethys/Vardar oceanic suture zone in the NE and the external Hellenides (Pindos and Adria) in the SW (Mountrakis, 1984; Kilias and Mountrakis, 1989). The basement of the Thessaly region comprises a complexly deformed assemblage of quartzo-feldspathic gneiss and schist, mid-Mesozoic ultramafic ophiolite fragments, late Palaeozoic to Mesozoic marble and early Paleogene flysch, as well as mafic and calcareous schists.

Thessaly is located at the western end of the North Anatolian Fault Zone (NAFZ; a large transcurrent structure in the East Mediterranean), where the right-lateral strike slip ends and crustal extension prevails in mainland Greece (Fig. 1; Kiratzi et al. 1991; Taymaz et al. 1991; Hatzfeld et al. 1999; Papadimitriou and Karakostas, 2003; Müller et al., 2013; Konstantinou, 2017; Briole et al. 2021). The most prominent structural and geomorphic features strike NW-SE, such as the coastal and interior mountain ranges, their bounding faults and the late Tertiary sedimentary basins (Caputo and Pavlides, 1993). However, the Middle-Late Quaternary-to-present tectonic regime has formed WNW-ESE and E-W high angle, normal and oblique-slip faults (Mountrakis et al., 1993; Caputo and Pavlides, 1993; Caputo, 1995; 1996; Pavlides et al. 2004; Palyvos et al., 2010; Mantovani et al. 2018). The recent activity of these structures is confirmed by the location of both moderate and large magnitude earthquakes during the 20th century (Papazachos et al., 1983, 1993; Papastamatiou and Mouyaris, 1986; Pavlides, 1993; Hatzfeld et al., 1999), and by paleoseismological data (e.g., Caputo et al., 2004; Caputo and Helly, 2005; Palyvos et al., 2010; Tsodoulos et al. 2016). In northern

Thessaly, the strike of the active structures acquires a WNW-ESE orientation (Caputo and Pavlides, 1993; Ganas, 2020). This orientation of crustal stretching is probably a kinematic response to a change in the orientation of the regional stress field with respect to the NW-SE extension across the neighbouring rift systems of western and central Macedonia (Konstantinou et al. 2016). For example, the 1995 earthquake of Grevena - Kozani ruptured an ENE-WSW striking normal fault (Rigo et al. 2004). New strain rate data for west-central Macedonia and Thessaly (D'Agostino et al. 2020) also show a rotation of the dilatational strain axis from NW-SE to N-S across north Thessaly.

The epicentral area of the March 2021 earthquakes is characterised by low seismicity and low strain rates (~30 ns/yr; D'Agostino et al. 2020) while this area is located within the, Pindos crustal block as defined by kinematic criteria by Briole et al. (2021). The crustal thickness is about 35 km with the Moho dipping towards the west beneath the Pindos range (Grigoriadis et al. 2016). The March 3, 2021 10:16 UTC (Mw=6.3) shallow earthquake occurred near Damasi, about 20 km to the northwest of Larissa (Fig. 1; Lekkas et al. 2021; Ganas et al. 2021a; Valkaniotis et al. 2021; Tolomei et al. 2021). Then, a Mw=6.0 shallow earthquake occurred on March 4, 2021 18:38 UTC beneath the sedimentary basin of the Titarissios river. On March 12, 2021 12:57 UTC a third event of Mw=5.6 occurred near the NW edge of the Titarissios basin. The PGA due to the first event was measured as ~0.14 g at one strong-motion instrument in Larissa (Karakostas, 2021; Fig. 1).

In Table 1 we summarize the focal parameters of the three largest shocks of the sequence, as they have been determined by international agencies from moment tensor (MT) inversions. We observe that the events are located in the upper crust, with median depth ranging between 10 and 11 km. Some discrepancies occur, i.e., the shallow centroid depth obtained for the event on March 3, 2021 by NOA (4 km) compared to the solution by UOA (19 km); and for the centroid depth of March 4, 2021 by UOA (15 km) and GFZ (17 km), likely the result of unmodelled velocity structure. Both Mw and nodal planes of the GFZ solution for the event of 4 March 2021 diverge from the solutions provided by UOA, NOA and AUTH, likely the result of the poor data quality, the latter being likely the reason that MT is available from only four institutes for this event, despite its large size. In particular, the teleseismic inversions for the March 4, 2021 18:38 UTC event might be affected by the Kermadec Island event of Mw=7.4 (USGS), on 17:41 UTC since teleseismic inversions based mainly on surface waves are more vulnerable to this wave interference compared to local/regional body-wave inversions. The median values of the dip-angles of the MTs indicate shallow, intermediate-dipping normal faulting (≤40°), in agreement with the preliminary results from the inversion of geodesy data and field observations that indicated the activation of three previously unknown normal faults (Ganas et al., 2021a). In addition, when considering the dip direction of the median nodal planes in Table 1, a counterclockwise rotation of ~30° is observed between the strike of the event on March 3, 2021 and the events on the 4th and 12th of March.

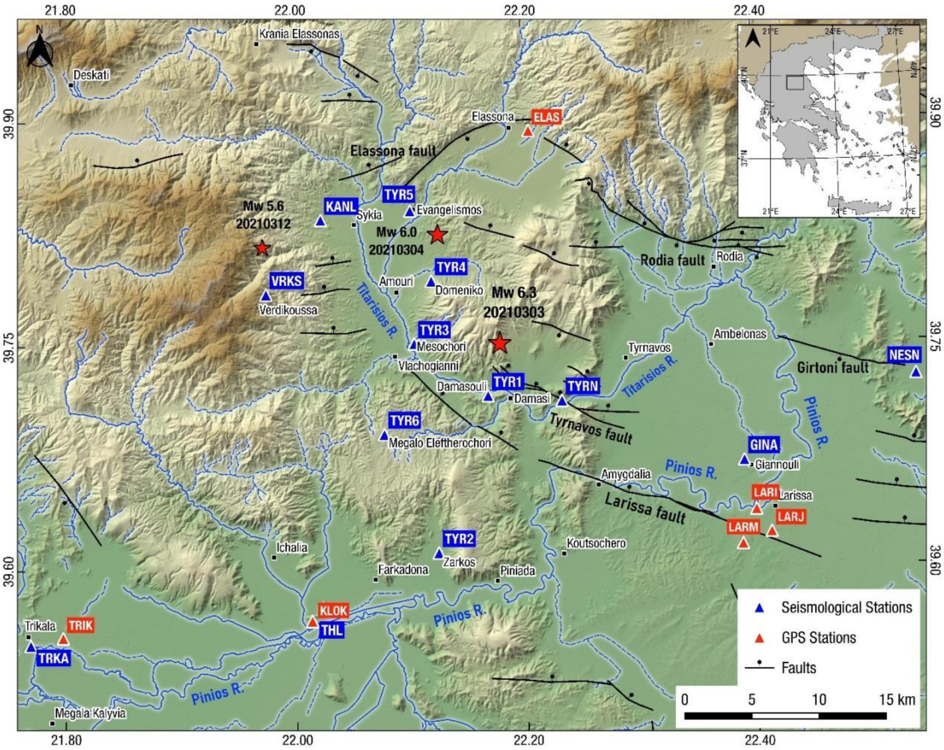

Fig. 1: Shaded relief map of the northern Thessaly 2021 earthquake area. Solid stars indicate relocated mainshock epicentres (this study). Blue triangles indicate the locations of the seismological stations. Red triangles represent permanent GNSS stations. Inset box at upper right shows study area within Greece. Black lines are active faults from the NOAFAULTs database http://doi.org/10.5281/zenodo.3483136 (with ticks at the downthrown side; modified from Caputo, 1990; 1995) and faults determined by our field work (this study). *A high-resolution version of this figure is provided in the supplement section of this article*.

In this study we present an analysis of seismological, geological and geodetic data that constrain the location and geometry of the activated faults. We relocated hundreds of aftershocks and computed the focal mechanisms for events with M≥4.0. Due to the shallow depth of the earthquakes (ranging from 5 to 15 km) and the good coherence of the area, it was possible to accurately map the surface deformation using InSAR. The interferograms show three main lobes of subsidence, partially overlapping, with a NW-SE orientation. We then processed GNSS data from twelve permanent stations located at distances ranging from 15 to 40 km. The displacement data were inverted to model the dislocation sources assuming a homogeneous elastic half space. The inversion modelling confirms the activation of three normal faults, previously unknown. The earthquakes generated numerous secondary phenomena with vast areas of alluvial deposits exhibiting spectacular liquefaction features. No tectonic surface ruptures were found in the field, in agreement with the modelled faults. However, several NW-SE surface breaks were observed north of village Zarko (Fig. 1), aligned with the vanishing gradient of the interferometric phase of the first event (March 3, 2021). We interpret those as tensional cracks related to the dilatational strain of the rupture. Our study highlights the rotation of the stress field in this key region of central Greece and the particular type of strain release, that is by clustering of earthquakes along blind normal faults that ruptured in an unprecedented domino pattern involving three mainshocks.

2. ANALYSIS OF SEISMOLOGICAL DATA

2.1. Relocation of Seismicity

The mainshocks and aftershocks of the sequence were recorded by the broad-band and strong motion stations of the Hellenic Unified Seismological Network (HUSN; http://eida.gein.noa.gr/); moreover, seven (7) temporary stations were installed on March 5, 2021 in the epicentral area by AUTH (Department of Geophysics of the Aristotle University of Thessaloniki; HT network; doi:10.7914/SN/HT). These stations were named as TYR1-6 (Fig. 1) and they were equipped with Nanometrics hardware i.e., Trillium Compact (TC120) seismometers and Centaur recorders. Two (2) more temporary stations were installed on March 14, 2021 by the University of Patras Seismology Lab (UPSL; HP network; doi:10.7914/SN/HP), with GEOBIT-instruments equipment, i.e., the Geotiny Seismometer (KANL; Analipsi site; Fig. 1) and the GEOsix datalogger combined with GEOfba200 accelerometer and TC120 Seismometer (VRKS; Verdikoussa site; Fig. 1). The manually picked events by Institute of Geodynamics of the National Observatory of Athens NOA, during the first 30 days, were used for the initial location. Several velocity models were examined during the location procedure such as Hatzfeld et al., (1997), Drakatos et al., (1998), Novotny et al., (2001), Karastathis et al., (2011); the comparison was initially performed on the HYPOINVERSE location errors and the hypocentres' distribution. The crustal model suggested by Hatzfeld et al., (1997) was finally selected since it yielded the lowest errors (i.e., mean RMS ~ 0.13 s) with a Vp/Vs ratio value of 1.76, as also suggested by Hatzfeld et al. (1997).

Table 1 (next page). Source parameters of the three mainshocks from various agencies (https://www.seismicportal.eu/mtws/). (*) GFZ solution excluded (see text for discussion).

Origin time (UTC) YYYYMMDD	Lat. (°)	Lon. (°)	Source	Mw	Z (km)	Strike (°)	Dip (°)	Rake (°)
2021-03-03 10:16:08.3	39.76	22.21	USGS	6.3	12	307	36	-100
			GCMT	6.3	12	324	48	-72
			CPPT	6.3	12	321	36	-77
			GFZ	6.3	10	310	44	-89
			UOA	6.3	19	309	36	-91
			ERD	6.2	7	332	43	-85
			IPGP	6.2	10	321	33	-78
			KOERI	6.3	10	323	53	-79
			OCA	6.2	7	315	45	-90
			INGV	6.3	10	327	53	-70
			NOA	6.3	4	305	33	-108
			AUTH	6.2	6	314	36	-88
			Median	**6.3**	**10**	**318**	**39**	**-87**
			Stdev	**0.05**	**4**	**9**	**7**	**11**
2021-03-04 18:38:17.1	39.78	22.12	UOA	6.1	15	308	50	-92
			GFZ	6.3	17	329	41	-88
			NOA	6	8	287	31	-95
			AUTH	5.9	7	287	30	-92
			Median	**6.1**	**11**	**298**	**36**	**-92**
			Stdev	**0.2**	**5**	**20**	**9**	**3**
			Median*	**6.0**	**8**	**287**	**31**	**-92**
			Stdev*	**0.1**	**4**	**12**	**11**	**2**
2021-03-12 12:57:50.7	39.84	22.01	CPPT	5.5	18	109	41	-92
			INGV	5.6	10	96	37	-133
			GFZ	5.5	10	120	40	-85
			KOERI	5.5	10	108	38	-108
			GCMT	5.6	12	87	42	-109
			Median	**5.5**	**10**	**108**	**40**	**-108**
			Stdev	**0.1**	**4**	**13**	**2**	**19**

Subsequently, the double difference relocation HYPODD (Waldhauser, 2001) procedure was performed for two time periods, i.e., before and after the installation of the local stations. The relocation combined the P- and S- wave arrival times from 66007 phase picks in total, derived from fourteen (14) stations within 90 km from the mainshocks epicentral area for the first period and ten (10) stations within 30 km for the operation period of the local stations (Fig. 1) including data from three strong motion stations in the near field (TRKA, GINA and SOFA). HYPODD determines relative locations within clusters, using the double difference algorithm, developed by

Waldhauser and Ellsworth (2000). It improves relative location accuracy by strongly reducing the influence of the velocity structure on locations. The double-difference residuals for the pairs of earthquakes at each station were minimized by weighted least-squares, using the method of conjugate gradient (LSQR). The velocity model used in the relocation was the same with the model used in the initial location process. In total, 855 events were relocated and clustered in the area of interest with magnitude M_L between 0.8 and 6.0 (see Fig. S1; see Table S1 for a list of the relocated epicentres of the three main events). The HYPODD final results include the 89.2% of the initial dataset. The relocated hypocentres have an estimated mean rms residual of 4 ms and the mean location formal uncertainties x, y, z and t were 24 m, 25 m, 27 m and 11 ms, respectively for both periods. The relocated events are densely distributed, in three major clusters (Fig. 2 shown in boxes), activated in diverse times. The main activity is concentrated at the central area during the first 2-day period, March 3-4, 2021 (Fig. 3; cross section B_1B_2) where the distribution of the hypocentres indicates a NE-dipping structure. After the addition of the portable network (Fig. 2), we can infer the position of the fault plane dipping 38° towards northeast (Fig. 3d). The inferred dip-angle is similar to the dip-angle of the northeast-dipping nodal plane of the moment tensor solutions (median value 39°; see Table 1). The northern cluster (Fig. 3; cross section A_1A_2) was activated one week after the M_w=6.3 event and the distribution of the events is not conclusive on the dip-direction of the seismic fault. The southern cluster (Fig. 3c; section C_1C_2) was active during the whole period, depicting a steeply dipping structure.

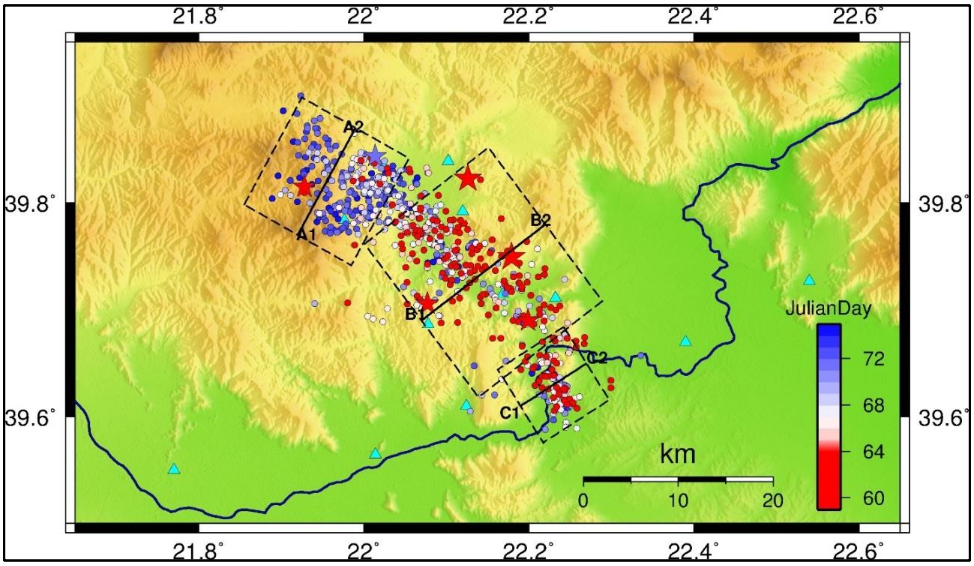

Fig. 2: Map of relocated seismicity. Epicentre colours are according to Julian date of occurrence. Sections A_1A_2, B_1B_2 and C_1C_2 are shown in Fig. 3. Cyan triangles indicate station locations.

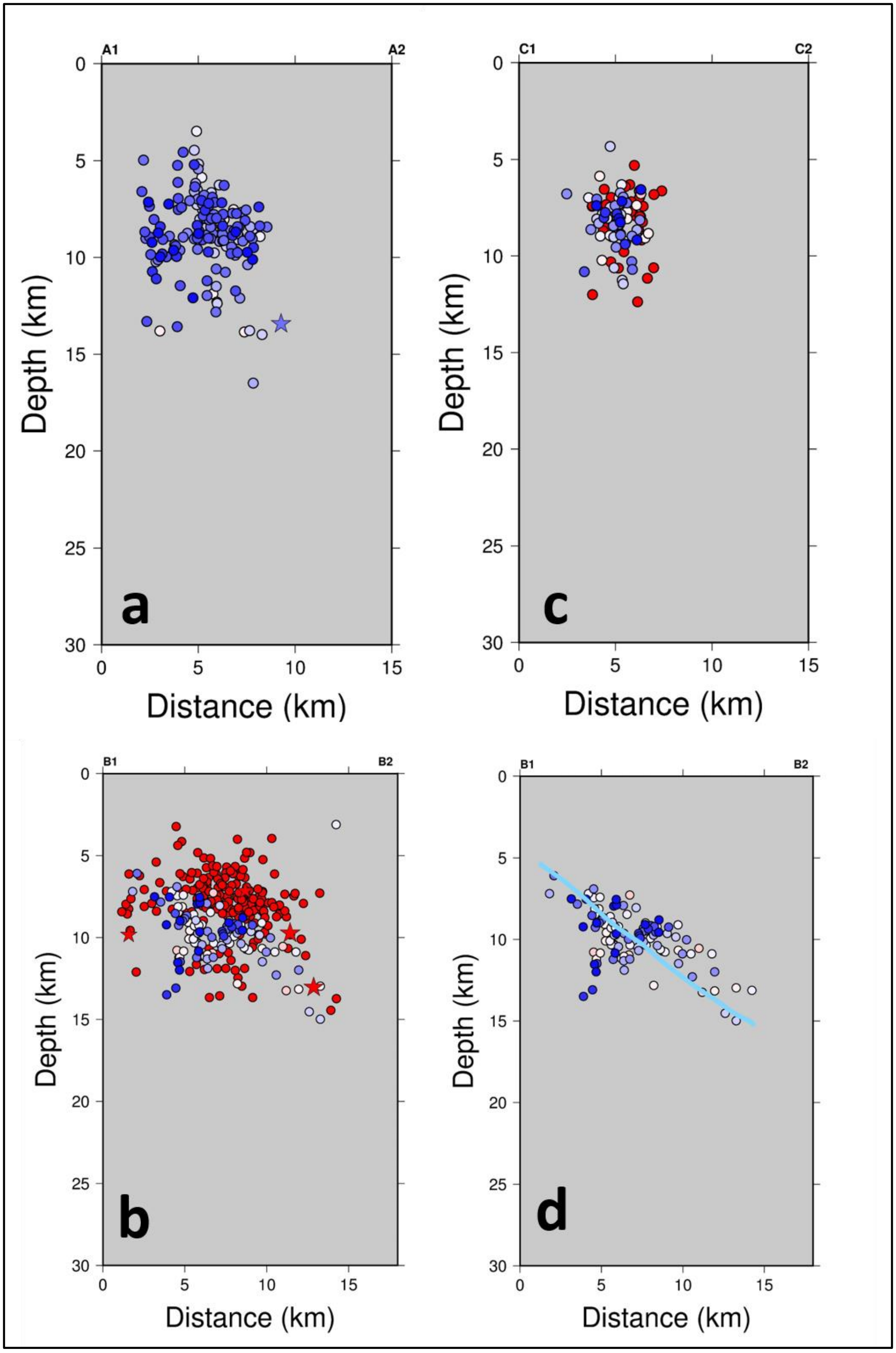

Fig. 3: Cross sections of relocated seismicity (a) to (c) corresponding to profiles A_1A_2, B_1B_2 and C_1C_2 respectively (see Fig. 2 for locations). Foci colours are according to Julian date of occurrence. Panel (d) displays the blue foci of (b) indicating aftershock

hypocentres from day 065 (March 6, 2021) onwards, together with an imaginary line showing the projection of the inferred fault plane with a dip-angle of 38°.

2.2. Computation of Focal mechanisms

The configuration of the regional HUSN seismic stations and accelerographs, allowed the computation of a large number of focal mechanisms using *P*-wave first motion polarities. This was possible especially after March 6, 2021 when the temporary local network was installed (Fig. 4). 5180 *P*-wave first-motion polarities were manually picked using Seisgram2K (Lomax, 2014). A total number of 408 focal mechanisms were determined using a grid search method applied on the first motion polarities (Kapetanidis, 2017). Out of the 408 solutions, herein, we present 22 focal mechanisms for events with M ≥ 4.0 as most representative of the rupture processes and afterslip. The stations positions on the stereo-net for the determination of the fault plane solutions by first motion polarities were determined using relocated hypocentres (where available) and the velocity model of Hatzfeld et al. (1997) by applying the TauP code (Crotwell et al., 1999). These focal mechanisms are shown in Fig. 4 according to their day of occurrence, indicating that 16 out 22 events with M ≥ 4.0 occurred with the first 48 hours from the first mainshock. Nearly all focal mechanisms exhibit normal kinematics or have a dominant normal dip-slip component. Oblique-normal and strike-slip focal mechanisms are also resolved, some being less constrained due to the unavailability of an adequate number of local stations until March 6, 2021. The parameters of 22 aftershocks are shown in Table 2 (and Table S2).

Table 2. Parameters of aftershocks with M≥4.0 determined with first polarities. See Table S1 for full parameters.

Year	Mo	Day	Hr	Min	Sec	Depth (km)	Mag	Strike (°)	Dip (°)	Rake (°)
2021	3	3	10	20	45.93	9.4	4.7	178.8	49.5	-43.8
2021	3	3	10	23	8.12	10.4	4.1	267.5	47.0	-139.7
2021	3	3	10	26	18.33	9.7	4.1	2.8	52.9	-37.8
2021	3	3	10	34	7.54	11.7	4.9	283.0	56.1	-148.8
2021	3	3	11	12	23.08	10.3	4.3	327.1	50.8	-41.6
2021	3	3	11	35	56.66	10.2	4.8	344.4	44.7	-87.5
2021	3	3	18	24	8.06	11.6	5.2	328.6	54.0	-34.7
2021	3	3	18	49	48.25	12.4	4.2	77.7	33.7	-92.0
2021	3	3	21	0	54.67	10.2	4.0	278.3	43.7	-145.3
2021	3	4	2	43	37.77	11.6	4.0	349.1	36.7	-71.0
2021	3	4	9	36	15.37	13.2	4.4	130.9	48.0	-35.9
2021	3	4	18	45	26.58	11.9	4.1	242.0	51.4	-150.8
2021	3	4	19	23	50.99	11.6	5.0	248.8	41.9	-101.6
2021	3	4	19	31	31.96	11.5	4.2	125.0	52.7	-38.4

2021	3	4	20	3	8.11	11.1	4.2	331.7	53.5	-29.4
2021	3	5	9	59	58.96	15.1	4.2	86.0	41.7	-85.4
2021	3	5	10	1	14.49	10.3	4.2	294.8	36.0	-84.3
2021	3	6	16	36	17.51	11.6	4.1	356.0	65.3	-22.9
2021	3	6	19	47	39.76	9.6	4.1	3.7	47.9	-34.6
2021	3	11	14	19	40.4	6.3	4.0	124.4	46.9	-42.0
2021	3	15	15	43	37.71	8.0	4.3	263.2	24.5	-86.2
2021	3	21	17	15	54.04	8.8	4.1	287.5	42.3	-69.4

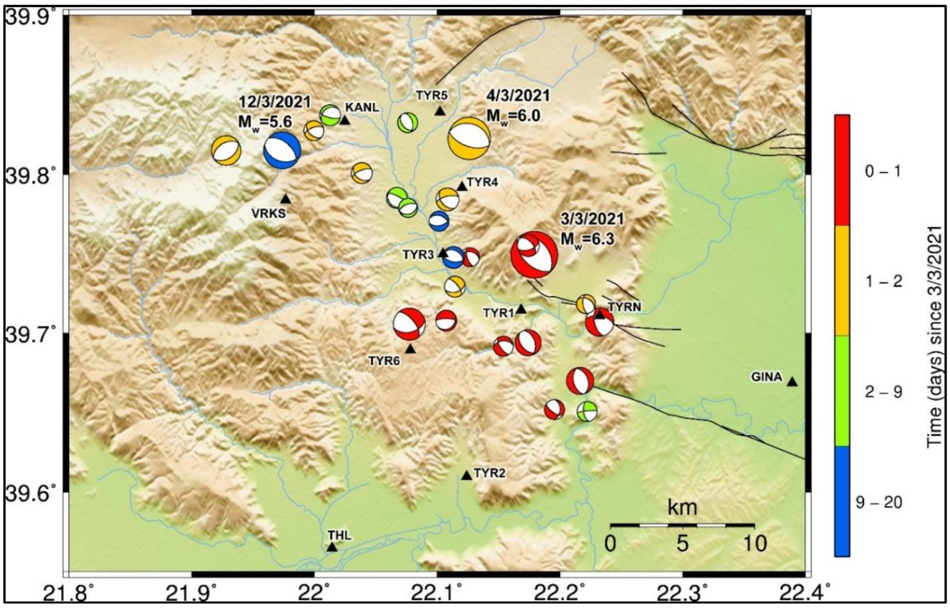

Fig. 4: Map showing the focal mechanisms of the three mainshocks (Moment Tensor solutions; median values from Table 1) and twenty-two major aftershocks with M≥4.0 (computed with the method of first motion polarities). Compressional quadrants are coloured according to the day of occurrence since 3 March 2021. Solid triangles indicate locations of the seismic instruments.

3. PROCESSING OF INSAR DATA - ANALYSIS OF INTERFEROGRAMS

InSAR is a technique of side-looking imagery collected by repeating passes of a radar satellite over an area. Since 1992, the technique it has been used to measure how much the ground surface has moved along the line-of-sight (LOS) between each pass of a satellite and can give vital information as to how much slip occurred on a fault. In the case of the Thessaly 2021 earthquakes preliminary field data indicate that the ruptured faults are “blind”, i.e., they have no surface expression in terms of fault scarps (Ganas et al. 2021a; Valkaniotis et al. 2021). We used the ascending images acquired by the European Copernicus satellites Sentinel-1 (S1; C-band data) on the ascending tracks 102 and 175 and on the descending tracks 7 and 80. The area of interest for InSAR is included within 21.7-22.5° in longitude and 39.5-39.9° in latitude. The geometrical characteristics of the S1 tracks are given in Table 3. Due to acquisition schedule and track geometry, the M_w=6.3 and M_w=6.0 earthquakes were captured only in ascending track interferograms as separate deformation events (Fig. 5; Fig. 6).

Table 3. Parameters of the four available S1 tracks.

Orbit	**Ascending**	**Ascending**	**Descending**	**Descending**
Track	102	175	7	80
Acq. time (UTC)	16:24	16:32	04:31	04:38
Incidence angle (°)	33.7274	41.5527	41.5469	36.8476
Incidence vector east, north, up	-0.537 -0.126 +0.832	-0.646 -0.151 +0.748	+0.646 -0.151 +0.748	+0.584 -0.137 +0.800

The interferograms (Fig. 5) were made using the SNAP v8.0 software (Veci et al. 2014). The digital elevation model (DEM) used for the processing is the Shuttle Radar Topography Mission (SRTM) 1 Arc-Second Global (doi: /10.5066/F7PR7TFT). During processing, the interferogram was formed by cross-multiplying the master image (the pre-event acquisition image) with the complex conjugate of the slave (the post-event image). The resulting phase represents the difference between the two images. Through the interferometric processing, we eliminate sources of noise, as much as possible, to isolate the remaining signal that is likely to be related to the ground displacement. We also enhanced the signal-to-noise ratio by applying the adaptive power spectrum filter of Goldstein and Werner (1998) with a coherence threshold of 0.4. For this sequence, the quality of the interferograms is good, both in terms of coherence and tropospheric noise.

The interferogram of the first event shows 13 fringes corresponding to ground deformation in the Damasi area (Fig. 5 left panel; see location of Damasi in Fig. 1). The interferogram of the second event shows 4 fringes corresponding to ground deformation in the Amouri area, about 10 km to the northwest (Fig. 6, middle panel; see location of Amouri in Fig. 1). All fringes correspond to motion away from the satellite (increase in the line-of-sight distance). The subsidence pattern is interpreted as result of co-seismic motion along two normal faults, running NW-SE and dipping to the northeast. The third event created a fringe pattern consistent with subsidence due to a south-dipping fault according to the shape and density of fringes (denser closer to fault’s trace; Fig. 5 right panel). The InSAR results show that the Titarissios river valley and large areas to the west and SW of Tyrnavos moved roughly downwards.

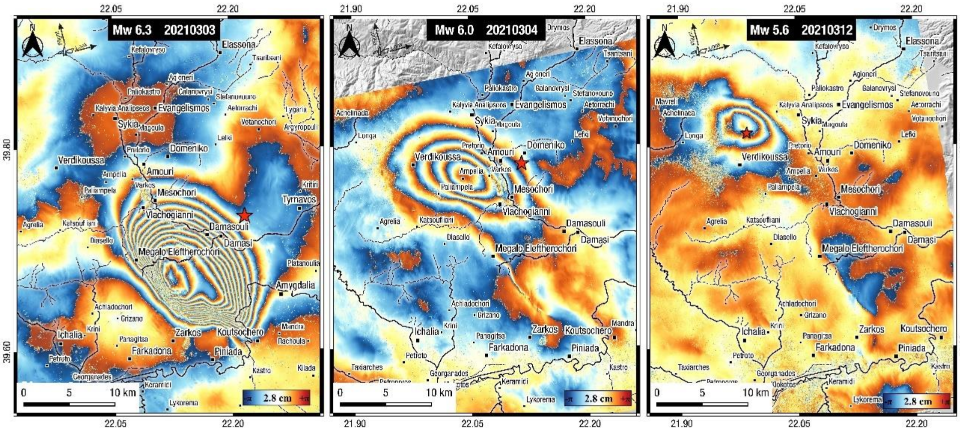

Fig. 5: Coseismic interferograms (wrapped phase; cropped swath) from Sentinel-1 SAR imagery pairs, for the three main events of the earthquake sequence. Left) Ascending track 102, February 25 – March 3, 2021. Middle panel) Ascending track 102, March 3 – March 9, 2021. Right panel) Ascending track 175, March 8 – March 26, 2021. The interferograms are draped over shaded relief. Red stars indicate epicentres of the three earthquakes. *A high-resolution version of this figure is provided in the supplement section of this article*.

We also used the LOS displacements from track 80 & 175 interferograms (March 2 – March 14, 2021) for decomposition into horizontal (East-West) and vertical displacement components. Decomposition processing combines the ascending and descending unwrapped interferograms (neglecting the contribution of the North-South displacement), using simplified geometry and the Sentinel-1 acquisition incidence angles (Wright et al. 2004; Dalla Via et al. 2012). These interferograms contain the cumulative deformation from all three main events (Fig. 6). Later interferograms show no significant deformation in the area. The majority of deformation occurs in the vertical component, with a maximum of 0.39 m of subsidence over the M_w=6.3 rupture plane, south of Damasi (Fig. 6 a & c). A small amount of uplift is observed in the area NE of Farkadona (Fig. 6a; up to 4 cm). The uplift might be attributed to the relative motion of the two fault blocks either side of the fault surface. In normal faulting the maximum surface displacement is manifested as subsidence of the hanging wall, with the footwall being uplifted but with less amounts (e.g., King et al. 1988). The small cumulative uplift of the Thessaly earthquakes is probably due to the blind character and intermediate dip-angle of the normal fault ruptures. A significant amount of E-W horizontal displacement (from +0.19 m to –0.1 m) is observed (Fig. 6 b & d), that is attributed to the crustal extension due to the normal fault ruptures.

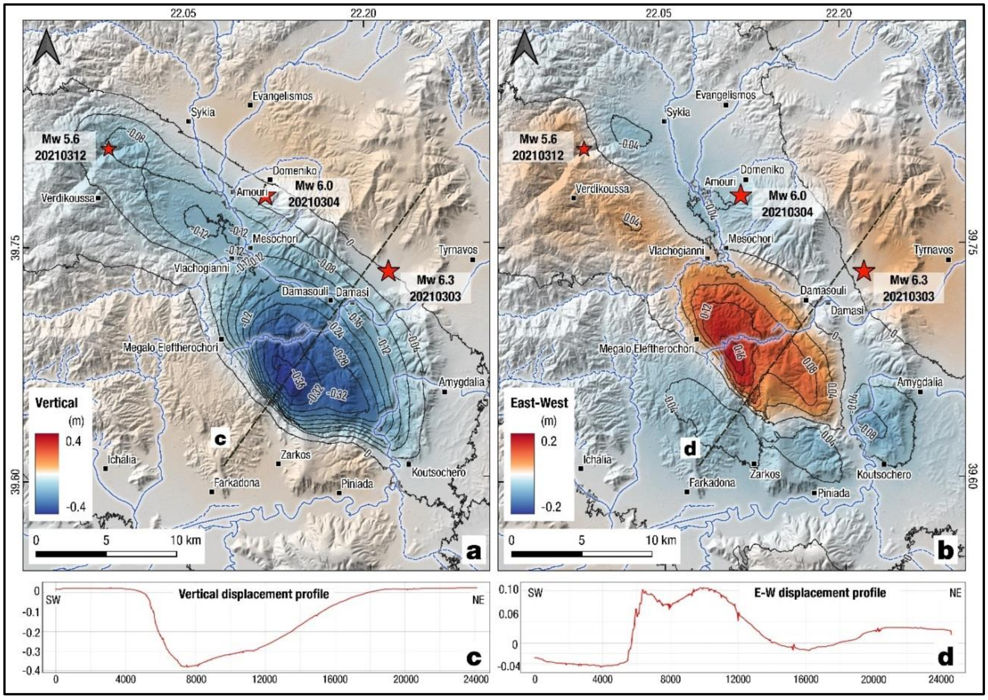

Fig. 6: InSAR displacement maps from the decomposition of Track 80 & 175 interferograms (2 March – 14 March 2021) a) vertical component b) east-west component with NE-SW oriented profiles in c) and d) respectively. Positive values (red colours) of E-W displacement show movement towards east. *A high-resolution version of this figure is provided in the supplement section of this article*.

4. CO-SEISMIC MOTION OF THE GNSS STATIONS

We analyzed dual-frequency GPS data of twelve (12) GNSS stations, all located in Thessaly. One station (KLOK) belongs to both NOANET (Ganas et al. 2008) and INGV (Fig. 1). It is equipped with a choke-ring antenna and its 10-yr long time-series analysis indicates a very stable behavior (Argyrakis et al. 2020). Two GNSS stations belong to AUTH-HERMES network (code name ELAS and LARM), five stations belong to Tree-URANUS (FAR2, KARD, LARI, PIRG and TRIK), two stations to METRICA- HxGN Smartnet (BELE, MURG) and two stations to JGC-net (KARJ and LARJ). The data (rinex v2.11 files) were processed with the Gipsy version 6.0 software of the JPL/NASA (Bertiger et al., 2010). For Tree-URANUS stations we processed data until April 25, 2021 while for METRICA-HxGN SmartNET stations until the March 31, 2021. Unfortunately, there were no data available for ELAS after March 5, 2021. The sampling interval was 30 s, and the data were collected on a 24-hour basis. We used the JPL final satellite orbits (flinnR) and clocks, absolute antenna calibration, random walk troposphere estimation and the FES2004 ocean loading model. We calculated the static offsets (and their uncertainties) for the three events (Table 4; Fig. 7 and

Fig. 8). The offsets indicate cm size motion mainly along the NE-SW direction. Station KLOK (Fig. 7) registered the largest displacements, as it moved 4.2 cm towards south and 3.1 cm towards west. In terms of Up-Down (vertical) displacement, we obtained no clear trends of co-seismic motion for the three events. We also processed in kinematic mode the high-rate data (1s sampling interval) of several stations, including station KLOK, using the CSRS-PPP SPARK, an online GNSS service developed by the Geodetic Survey Division of Natural Resources Canada. We present the results of the data processing for the March 4, 2021 shock in supplementary Fig. S2. Unfortunately, for the day of the March 3, 2021 earthquake station KLOK has a duration of observations of only 2:54:30 (hh:mm:ss), starting from 21:05:00.00 GMT.

The six best-constrained displacements of GNSS stations are shown in Fig. 7**.** The events of March 4, and March 12, 2021 are much smaller in size and do not contribute (they produce local InSAR fringes as seen in Fig. 5, but minor offsets were recorded in the intermediate and far field). The uncertainties on the displacements are (on average) 3 mm in east and north (~10% of a fringe). These values were used for assigning the zero of the interferograms. They were also used for the control of the prediction of the fault models. For modelling the fault parameters, InSAR is adequate for this seismic sequence while GNSS cannot constrain the models. There is no evidence of significant post-seismic displacement except some small displacements (below ¼ of a fringe) in the near field of the faults. Note that the co-seismic offsets on Fig. 7 appear smooth because we applied a Gaussian filter on the position time series; this filter reduces by a factor of two the signal-to-noise ratio of the time series, which is useful in case of small displacements.

In addition, in the time series of E, N coordinates plotted in Fig. 7, the secular velocities of the stations from Briole et al. (2021) have been subtracted. The station offsets are reported in Table 3 together with their modelled displacements according to the derived fault models (see section 5 below). The map of the horizontal displacement pattern is shown in Fig. 8. The horizontal displacement pattern is in agreement with the normal dip-slip kinematics of the rupture, i.e., axis of extension oriented ~NE-SW. We note that several stations located along strike (i.e., NW-SE), such as LARJ and LARM, recorded smaller displacements than stations such as KARD and TRIK, despite the latter being further to the epicentral area. This effect is due to the asymmetric elastic response of the crust during seismic faulting and it was also observed in the case of the Samos 2020 earthquake (Ganas et al. 2021b).

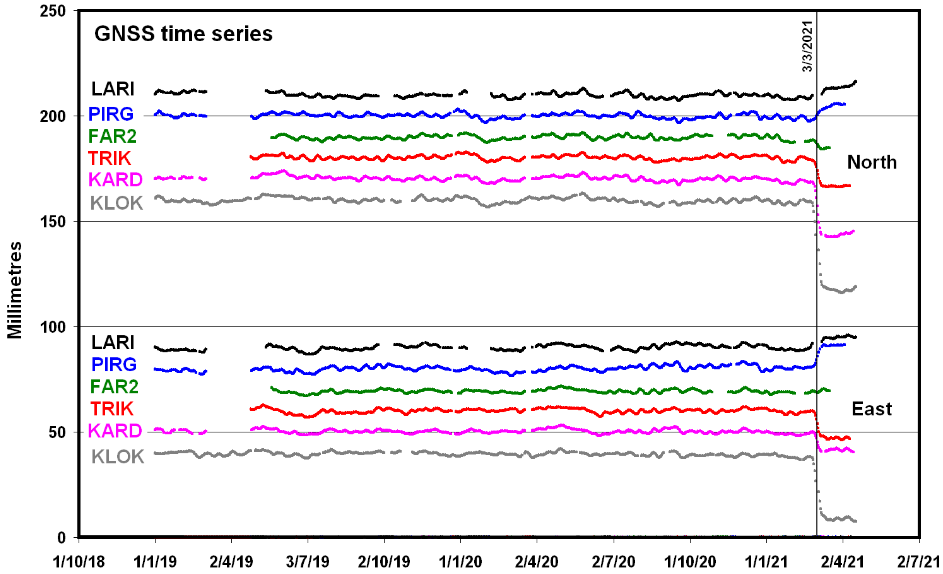

Fig. 7: Graphs showing position time series of GNSS stations in Thessaly (north and east components). The time-series have been offset for clarity on the Y-axis. Vertical line indicates the day of the 3 March 2021 event and marks the co-seismic displacements on six stations having the lowest uncertainties on the estimation of the co-seismic displacements. Station locations are in Fig. 8**.**

Table 4. Coordinates of the 12 GNSS stations, secular velocities (Briole et al. 2021), total displacement values (in mm; all three main shocks), total model values. The mean difference between observations and model is 0.8 cm, -1.6 cm, and -0.4 cm in east, north and up respectively. See Fig. 8 for station locations.

Station		**Coordinates**		**Velocity ITRF2014**		**Total co-seismic motion**			**Model**		
Code	**Owner**	**Long.**	**Lat.**	**vE**	**vN**	**East**	**North**	**Up**	**East**	**North**	**Up**
		°	°	mm yr^{-1}	mm yr^{-1}	mm	mm	mm	mm	mm	mm
BELE	Metrica	23.133	39.295	18.8 ± 0.5	0.3 ± 0.6	1 ± 1	0 ± 1	0 ± 3	0	0	0
ELAS	AUTH	22.206	39.892	22.7 ± 0.5	6.1 ± 0.6	12 ± 5	34 ± 5	0 ± 15	18	33	8
FAR2	Uranus	22.384	39.296	19.5 ± 0.8	3.1 ± 0.8	1 ± 1	-5 ± 1	8 ± 3	-1	-1	1
KARD	Uranus	22.082	39.470	20.4 ± 0.4	6.1 ± 0.5	-9 ± 1	-26 ± 1	3 ± 3	-10	-22	0
KARJ	JCG	21.745	39.355	n/a	n/a	0 ± 5	-5 ± 5	0 ± 15	-7	-8	2
KLOK	NOA/INGV	22.014	39.565	21.1 ± 0.2	6.6 ± 0.2	-31 ± 1	-42 ± 1	-2 ± 3	-32	-38	6
LARI	Uranus	22.400	39.637	20.5 ± 0.4	4.7 ± 0.4	5 ± 1	4 ± 1	3 ± 3	5	5	4
LARJ	JCG	22.413	39.622	n/a	n/a	3 ± 5	1 ± 5	1 ± 15	3	4	4
LARM	AUTH	22.388	39.614	21.3 ± 0.2	5.3 ± 0.3	-1 ± 2	3 ± 2	6 ± 6	0	6	3
MURG	Metrica	21.554	39.739	21.7 ± 0.4	7.9 ± 0.4	-1 ± 2	1 ± 2	0 ± 6	-4	-2	1
PIRG	Uranus	22.589	39.919	22.4 ± 0.4	6.0 ± 0.4	11 ± 1	5 ± 1	1 ± 3	11	8	0
TRIK	Uranus	21.798	39.555	20.0 ± 0.6	7.4 ± 0.8	-13 ± 1	-13 ± 1	5 ± 3	-14	-12	0

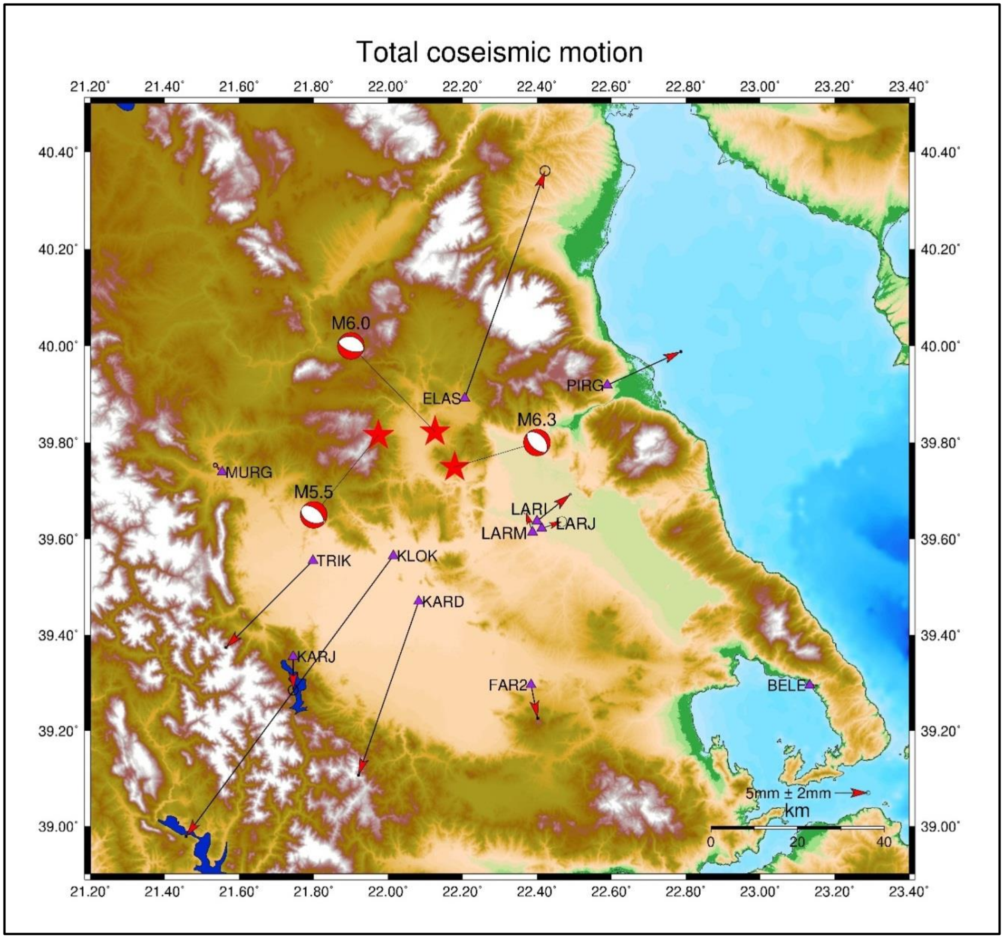

Fig. 8: GNSS total displacement map showing also topography/bathymetry, the focal mechanisms (beachballs; compressional quadrants in red) and the epicentres of the Thessaly 2021 earthquakes. Triangles indicate permanent GNSS station locations. Vectors indicate the horizontal displacement of GNSS stations with 67% confidence scaling. Notice the large displacements obtained for stations located normal to the strike of the seismic faults.

5. INSAR DATA INVERSION - FAULT MODELS

In the Damasi earthquake sequence there are three main events, that occurred on March 3 (M_w =6.3), March 4 (M_w=6.0) and March 12, 2021 (M_w=5.6). In our inversion models, we use as initial values for the angles (azimuth, dip) the median angles of the available focal mechanisms (Table 1). The choice of the dip-angle is also justified by the results of seismicity relocation, as we infer a 38°-dipping fault plane towards the NE (Fig. 3d). Ten (10) interferograms are used and inverted to estimate the parameters of the faults responsible for the earthquakes (Table 4). The coherence of those interferograms is, on average, outstanding. Weather during the period of interest was most of the time cold and dry and therefore the tropospheric effects are very small. The ground surfaces are partly rocky, which also greatly contributes to the overall coherence. In each of the ten interferograms, we pick the fringes where they are visible and unambiguous. The fringe number zero (0) is accurately determined on the basis of the displacements recorded at the GNSS stations (see section GNSS above). Then, this zero is controlled and fine-tuned during the modelling/minimisation process. We also made several post-seismic interferograms, until May 1, 2021, and we have seen that there is almost no post-seismic deformation, even in the near field. The post-seismic displacements are below the 7 mm level (quarter of fringe) in the near field and below the 1 mm level at the GNSS sites.

Table 5. Interferograms used for the modelling of the faults. Events: 1 is for March 3 (M_w =6.3), 2 if for March 4 (M_w=6.0), 3 is for March 12, 2021 (M_w=5.6). The bias is the value (in mm) of the offset applied to the picked fringes to minimize the residuals in the modelling. Tracks A102 and A175 are ascending, D007 and D080 descending.

Track	**Start**		**End**		**Picked points**	**r.m.s. fit**	**bias**	**Event**
	Date	***Orbit***	***Date***	***Orbit***		***mm***	***mm***	
A102	19/02/21	25678	03/03/21	25853	453	40.6	6	1
A102	03/03/21	25853	09/03/21	36924	106	7.4	14	2
A102	25/02/21	36749	09/03/03	36924	783	41.9	7	1+2
A175	24/02/21	25751	08/03/21	25926	834	42.4	6	1+2
D007	03/03/21	36829	09/03/21	25933	376	42.1	-9	1+2
D080	24/02/21	36727	08/03/21	36902	490	37.2	-5	1+2
A102	09/03/21	36924	15/03/21	26028	45	7.7	9	3
A175	08/03/21	25926	14/03/21	36997	31	4.3	-15	3
D007	09/03/21	25933	15/03/21	37004	48	5.1	3	3
D080	08/03/21	36902	14/03/21	26006	51	6.2	0	3

Each earthquake is supposed to correspond to a homogeneous dislocation on a rectangular fault buried in an elastic half-space. The formalism used is the one established by Okada (1992). The inversion is made with the method developed by Briole et al. (1986) using the code *Inverse6* (Briole, 2017). For the first and second events, only track A102 contains those earthquakes separated from the others. We inverted the corresponding interferograms (parameters in Table 5) to estimate a first model for each of those events. Then, we combined the two events and made a joint inversion of the four interferograms available on the four tracks to fine-tune the parameters of the two faults. Although mixing the two faults in one single inversion may reduce the discrimination potential of the inversion, this is balanced by the fact that the combination of the four tracks allows to assess in a more robust manner the zero bias of the four sets of picked fringes (column bias in Table 5). This robustness is enhanced by the fact that there are ascending and descending data which greatly stabilizes the inversion and provides robustness.

The parameters of the best-fitting models are in Table 6. The modelled fault sources are shown in Fig. 9 as shaded rectangles. The fault sizes are: 9.6 km long by 10.5 km wide (March 3 event), 11.9 km by 4.0 km (March 4 event) and 4.3 km by 5.5 km (March 12 event), respectively. The longer fault size of the March 4 event is due to the particular rupture characteristics; the March 3 event occupied a larger rupture area due to most slip occurring down-dip of the fault plane.

Table 6. Source Parameters of the fault models based on the inversion of geodetic data.

Parameter		**Unit**	**March 3 event**	**March 4 event**	**March 12 event**	**Notes**
Centre of upper edge	Longitude	°	22.134 ± 0.010	22.066 ± 0.010	22.002 ± 0.010	
	Latitude	°	39.665 ± 0.010	39.760 ± 0.010	39.827 ± 0.010	
	Up	km	3.0 ± 1.0	4.2 ± 1.5	1.3 ± 1.0	
Azimuth		°	318	298	108	Not inverted (used values from seismology)
Dip angle		°	39	36	40	
Length		km	9.6 ± 1.0	11.9 ± 1.5	4.3 ± 1.0	
Width		km	10.5 ± 2.0	4.0 ± 1.0	5.5 ± 1.0	
Strike slip		m	0.082	-0.021	0. (not inverted)	Positive = left lateral
Dip slip		m	1.173	0.591	0.25	Positive = normal
Geodetic moment		N m	3.56 10^{18}	0.84 10^{18}	0.18 10^{18}	

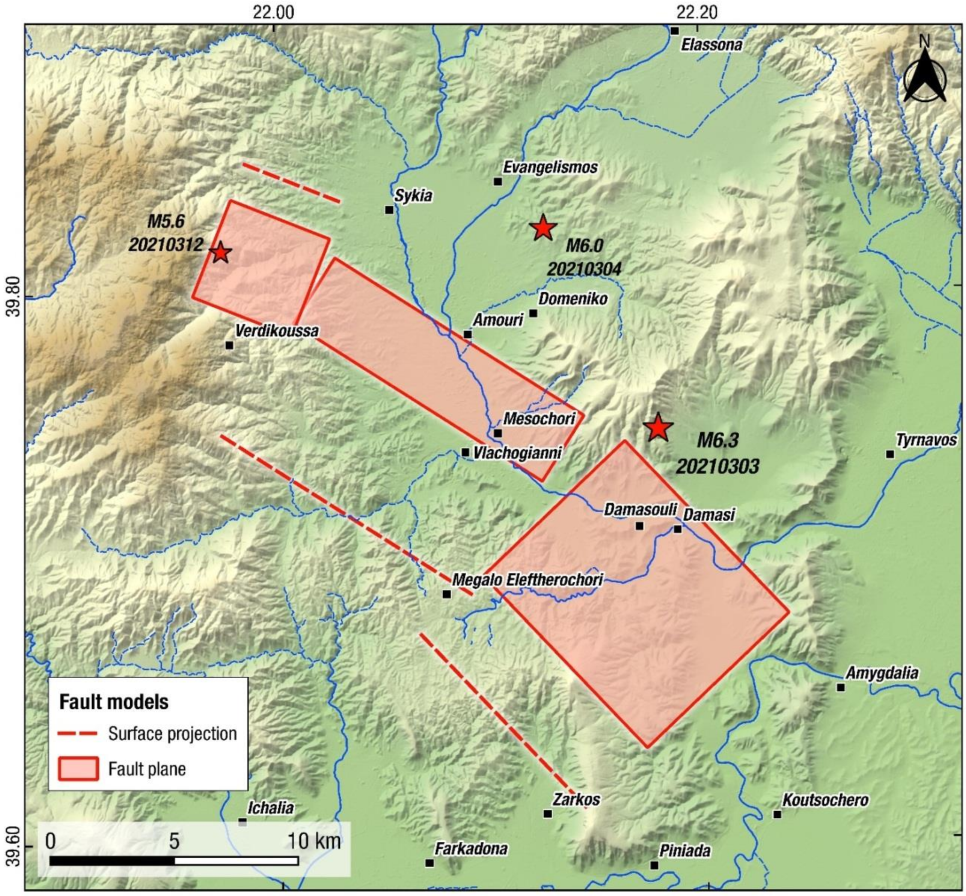

Fig. 9: Surface projection of the faults (shaded rectangles) of the three events. Dashed red line is the intersection of the fault plane at the surface (when projected up-dip). *A high-resolution version of this figure is provided in the supplement section of this article*.

6. GEOLOGICAL AND MACROSEISMIC OBSERVATIONS

6.1 Geological effects

Following the M_w=6.3 earthquake of March 3, 2021 the most prominent earthquake environmental effects were the widespread liquefaction phenomena and lateral spreading that was triggered over Titarissios and Pinios river valleys (Fig. 10; Valkaniotis et al. 2021). The Titarissios and Pinios basins have Pliocene-Quaternary fluvial and lacustrine sediments deposited directly on the metamorphic basement (Caputo et al. 2021). During post-earthquake surveys, we mapped more than 500 sites with liquefaction fissures and craters and lateral spreading deformation/cracks. A number of sites with high density of liquefaction fissures were surveyed by the UAS (Unmanned Aircraft System) model DJI 4 Pro V2.0. Co-seismic interferograms revealed two large areas, along the Titarissios river valley to the north and Pinios river valley to the south (orange-shaded polygons in Fig. 10), with very low to no coherence. We suggest that lack of coherence in those areas is related to widespread surface deformation and change due to liquefaction. In addition, low InSAR coherence over Titarissios valley suggests repeated liquefaction and lateral spreading during the second (M_w=6.0) earthquake on March 4, 2021. Careful examination of post-earthquake Sentinel-2 optical imagery (10-m ground resolution) revealed a number of sites with evidence of liquefaction fissures and craters. Our field survey lasted during the period March 3 – 15, 2021 and validated these satellite observations. The vast majority of liquefaction and lateral spreading surveyed sites are found along the Titarissios valley from Amouri to Damasouli villages (Fig. 9 & 10), and Pinios river valley from Farkadona to Koutsochero (Fig. 9 & 10). Liquefaction fissures and craters were more prominent inside the Pinios river valley, due to the presence of finer fluvial sediments, while the Titarissios valley has a dominance of coarser-grained material deposited on the flood plain (gravels, coarse sand). Preliminary examination of local palaeogeography and surficial geology revealed a possible correlation between liquefaction manifestations and fluvial geomorphology – palaeochannels (Valkaniotis et al. 2021). Witness reports from local residents describe the strong manifestation of sand and water ejection immediately after the M_w=6.3 earthquake. We suggest that localised ground deformation and displacement due to lateral spreading is responsible for a large number of geotechnical failures, mostly related to bridge and road embankments.

Landslides from the March 2021 earthquake sequence were rather limited, despite the magnitude and shallow crustal depth of the events. We mapped about 40 sites of landslides and rockfalls around the epicentral area (Fig. 10), from field observations and post-earthquake Sentinel-2 optical imagery (March 4 and March 14, 2021 acquisitions). Apart from a series of debris and avalanches in the steep gorge of Pinios west of village Amygdalea (Fig. 9 & 10), and a number of large boulders uphill the Zarko village, most locations involved landslides and rockfalls of small extent and size. A small number of ground cracks were also surveyed around the epicentral area (Fig. 10). Most of those might be related to local gravitational phenomena but without solid evidence to suggest a clear relation with larger slides or lateral spreading. We found two localities that deserve more attention. First, ground cracks were observed and surveyed at two locations along the western sector of the Tyrnavos fault trace (red triangles in Fig. 10; Caputo, 1993), north of village Damasi, immediately after the M6.3 earthquake (on the afternoon of March 3, 2021). The cracks are oriented approx. N308°E and show an opening of less than 1 cm. However, these cracks show no vertical offset. Therefore, the cracks may be related to triggered shallow slip along a section of the Tyrnavos fault by the March 3 rupture or to ground failure due to strong ground motion as this locality is situated above the rupture plane (see its extent in Fig. 9). More importantly, two sets of ground fractures were surveyed north of village Zarko, with an average orientation of N355°E. These tensional cracks coincide with a zone of co-seismic and post-seismic secondary slip mapped with InSAR (location 4 in Fig. 10; Fig. 14d). This deformation zone possibly coincides with the surface projection of the M_w=6.3 rupture plane (see dashed red line in Fig. 9) and we examine the data in section 7.3 below.

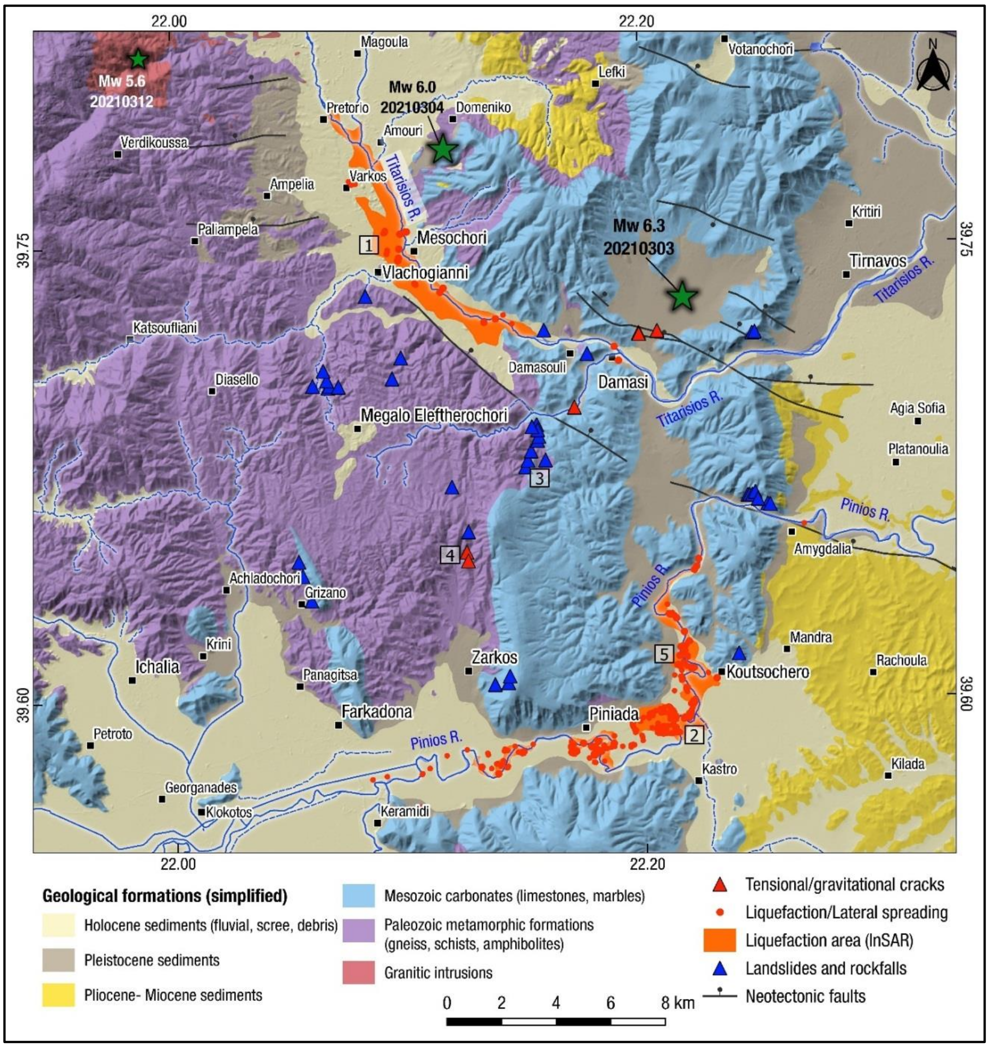

Fig. 10: Overview of field observations of the geological/environmental effects from the March 2021 earthquake sequence. The majority of earthquake effects are found within an area of approximately 20 km x 20 km. Epicentres of the main three events are shown with green star symbols (source AUTH). Simplified geological map is based on IGME maps. All field data were collected by SV, GP and AG during March 3-15, 2021. Simplified geology from the IGME map sheets compiled by Migiros (1985), Plastiras (1985), Stamatis (1987), Triantafillis (1987) and Vidakis (1998).

Fig. 11: Field photographs showing a & b) Liquefaction fissures with ejected sand in Titarissios river valley c & d) Liquefaction fissures with ejected sand in Pinios river (Piniada valley) e & f) Large sand boil craters in Pinios river sediments g) distributed deformation and ground cracks from lateral spreading in Pinios river terrace near Piniada h) localised graben structure in the head scarp of a lateral spreading (Pinios river valley north of Koutsochero). See village locations in Fig. 10.

Fig. 12: Field photographs showing a) Upthrown rocks in a gentle slope near Tsouma Monastery (Location 3 in Fig. 10) b) Rockfalls and debris along a mountainous road south of Damasi c) Rockfalls and wedge chips in a road cut north of Grizano d) Tension cracks north of Zarko, possibly along the surface projection of the M6.3 rupture plane (Location 4 in Fig. 10) e) Lateral spreading phenomena along the Pinios river valley, north of Koutsochero. f) Liquefaction at the base of the bridge pillars. Larissa – Trikala new highway bridge over Pinios river, west of Koutsochero (location 5 in Fig. 10).

6.2 Macroseismic observations and structural damage

The strong earthquakes and aftershocks of March 2021 revealed the seismic vulnerability of the critical infrastructure (e.g., bridges) and building stock in Thessaly. A summary of the structural damage observations obtained from the earthquake engineering field survey are presented below.

Bridges: Damage to bridges was reported and observed after the first earthquake on Wednesday 3 March 2021. Operation of the bridges that suffered damages around the epicentral area was suspended for a few hours after the earthquake, until an evaluation of their structural performance was performed by state engineer teams. The majority of the bridges suffered only surficial or minor structural damages, rapidly repaired during the first days after the main earthquake. The Titarissios bridge near Mesochori (Fig. 10) suffered moderate damage, due to extensive lateral spreading and liquefaction on its embankment, and remained closed to traffic (as of 30 June 2021). Most of the damage in bridges encountered in the epicentral area can be attributed to foundation and large displacements of their structural components due to lateral spreading / liquefaction along Pinios and Titarisios rivers (Fig. 11; Fig. 12).

Reinforced concrete (RC) buildings: The response of reinforced concrete buildings when subjected to earthquakes is highly dependent on the distribution of stiffness and mass in both the horizontal and vertical direction. RC buildings designed as per the more recent Greek seismic codes and the Eurocodes didn’t experience any significant damage. Some damage occurred mainly to non-structural elements of RC buildings such as in-plane and out-of-plane failure of infill panels (Fig. 13a). In some cases, damages were observed in open ground floors (*pilotes*) in RC buildings designed and constructed before 1985.

The lack of shear reinforcement accompanied with loss of stiffness due to open ground floors led to shear failures of columns and beam to column joints. Lack of appropriate shear links resulted in buckling of the longitudinal rebars of the columns. The strong beams remained undamaged while severe damage and plastic hinges developed at the top of the columns (Fig. 13b). In other cases, and where not enough reinforcement was installed in shear walls, diagonal shear cracking occurred.

Masonry buildings: A significant amount of unreinforced masonry buildings can be found in the villages of the epicentral area. Such buildings can be grouped into three main categories: a) residential; b) schools; and c) churches. Masonry is a brittle and anisotropic material which is strong in compression and weak in tension. Masonry buildings were made of masonry units (e.g., bricks, stones, concrete blocks, adobe) bonded together with or without mortar joints. At low levels of stress, masonry is behaving as a linear elastic matter. Its behaviour is becoming highly non-linear with the development of cracks and the redistribution of stresses in the uncracked regions during ground vibrations. Cracks in masonry buildings may open and close according to the type of stresses applied to them. Typically, cracks greater than 0.2 mm in width are visible to the naked eye. If such cracks open and propagate through the structure, they may reduce its load-carrying capacity and could lead to collapse. The preliminary damage assessment presented here is based on the patterns of cracks and dislocation observed on the exterior of the buildings, since access to the interior was not allowed at the time of the visit.

Residential masonry buildings: Typical domestic masonry buildings in rural areas of Thessaly are single- or two-story ones. These were constructed with uncoarsed rubble (irregularly shaped) unreinforced stone masonry and multi-leaf walls. The thickness of the walls is usually 0.5 m, but in some cases, it can be larger and even up to 1 m. Also, residential buildings in the region are characterised by large openings with or without lintels above them. In most cases, such buildings were constructed before 1959 and thus without any seismic provision. Since these buildings were not built using modern building codes, they suffered significant damage and even collapse. The extent of damage varies from one building to the other and from region to region.

Field investigations carried out after the earthquake demonstrated that poor construction techniques, poor material quality of multi-leaf masonry walls and lack of maintenance was the main reason for their structural damage, which in cases led to complete collapse. In particular, pounding, diagonal shear cracking in piers between window openings, delamination of the outer leaf of the walls as well as out-of-plane partial or complete collapse of walls observed in most of the residential unreinforced masonry buildings in Damasi and Mesochori (see Fig. 13d - 13f). In such places, walls were constructed with mud mortar, which is of very low strength and has very low resistance to humidity.

Another reason for the development of such out-of-plane failures are the absence of horizontal binding elements and, inadequate connections at wall intersections. Also, many of the buildings in the region lacked stiff in plane diaphragms at the floor and roof level. So, during earthquake, each of the load bearing walls acted independently in the in-plane and out-of-plane direction under the which led the buildings to collapse (See Fig. 13f).

Schools: Damages observed in school buildings made of masonry in Thessaly follow the typical damage typology of the masonry residential buildings. Significant damage occurred at the exterior and interior walls of the school of Damasi which was built in 1938 and is shown in Fig. 13g. During the earthquake, parts of the load bearing walls of the building failed in the out-of-plane direction while some in-plane diagonal and bi-diagonal shear cracks and out-of-plane failure occurred at the piers. In the interior of the building, major diagonal shear cracks at the masonry walls as well as non-structural damages such as delamination of coating and overturning of chairs, desks and equipment occurred. The structure has been characterised as unsuitable and has been demolished.

Churches: The earthquake of March 3, 2021 proved to be particularly devastating for religious buildings made of masonry in Thessaly. Although religious buildings usually consist of well-constructed material, many of them do not meet any seismic standards since they were constructed over 80 years ago and were eventually deemed dangerous or unsuitable for immediate use. The damages in churches that were observed are typical for stone constructions and include: damage at their upper part in the system of arches and domes which are anyhow vulnerable to earthquake action, cracks in the corners of the windows and doors openings, cracking and rotation of bell towers which in cases led to their collapse (Fig. 13h). Temporary measures were installed in many churches with damages a few days after the earthquake to avoid further damage and collapse due to aftershock activity.

Fig. 13: a) Detachment of infill wall from RC frame in Damasi; b) Lack of proper detailing in an open ground floor in Damasi; c) Cross-section of a typical multi-leaf wall; d) Delamination of the outer leaf of the wall in a domestic building in Damasi; e) Out-of-plane collapse of masonry walls in Damasi; f) Out-of-plane collapse due to poor connection between the roof and masonry walls in Damasi; g) Damages in the School of Damasi; h) Out of plain failure of St Nickolas Church in Koutchochero.

7. DISCUSSION

7.1. Domino-style Faulting and Coulomb stress Transfer

Static stress changes due to the mainshock have been computed using the Coulomb failure criterion (CFF or Coulomb failure function; King et al., 1994; Ganas et al. 2006b; Toda et al., 2011; Taymaz et al. 2021), assuming the source parameters listed in Table 6 and effective coefficient of friction μ'=0.4. Most active faults in the north Thessaly area strike ±30° with respect to the seismic fault of the 3 March 2021 event (Fig. 1 and Table 1), so it is reasonable to model static stress transfer on receiver faults with similar kinematics as those of the first two events (Fig. 14)**,** but also on faults optimally oriented to the regional stress field (~N184°E; Kapetanidis and Kassaras, 2019; see Fig. S3 for a map of static stress transfer on optimal fault planes). As in section 5, we assume that failure of the crust occurs by shear, so that the mechanics of the process can be approximated by the Okada (1992) expressions for the displacement and strain fields due to a finite rectangular source inside an elastic, homogeneous and isotropic half-space. The ΔCFF results presented in Fig. 14 at depth of 9 km, i.e., the average depth of aftershocks (see Fig. 3; also Fig. S4) show: a) positive stress changes (loading) along strike of the March 3, 4 and 12, 2021 seismic faults, of the order of several bar and b) negative stress changes (stress shadows) across the strike of faults. Therefore, it is suggested that this stress transfer model explains well the on- and mainly off-plane distribution of aftershocks at that depth.

Moreover, this sequence increased Coulomb stress on segments to the northwest and southeast of the ruptures, which are potential sites of future earthquakes (with similar kinematics), and decreased Coulomb stress orthogonally to the rupture plane. We suggest that the M_w=6.3 earthquake promoted failure at the crustal volume of the M_w=6.0 earthquake which struck 32 hours later. It is notable the absence of aftershocks inside the area of the northern shadow (blue lobe), around the town of Elassona. We also find that the stress transfer results explain the cascade-type triggering of the three shocks in a domino-model of earthquake occurrence, from SE (Damasi area) towards the NW. The triggering pattern is probably influenced by the rupture kinematics of the first event, with a large slip patch located close to the SE tip of the second fault. A SE to NW directivity could have possibly resulted in a cascading (domino) rupture of the neighbouring segment (March 4 fault) which in turn triggered slip on the isolated segment of the March 12, 2021 event (see Fig. 15 for a faut segment map).

We note that the Larissa active fault has been loaded with stress transferred (red lobe in Fig. 14a) after the first event; therefore, it has been brought closer to failure (see the map in Fig. S3). Furthermore, a small cluster of aftershocks is observed directly SE of the main rupture, within the ΔCFF +1.0 bar lobe; however, this activity lies on the footwall of NNE-dipping Larissa fault. We interpret that this indicates a likely smaller, unmapped structure. It is also very interesting, that there is no activity along the Larissa fault proper which is located in ΔCFF red (stress-loaded) areas (Fig. 14).

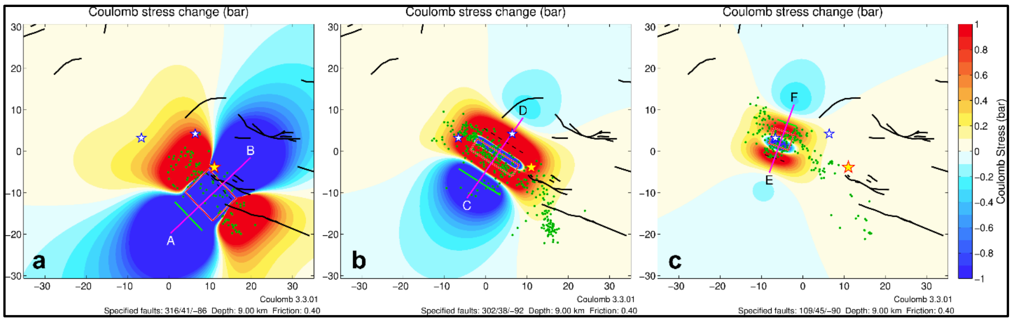

Fig. 14: Coulomb stress changes (ΔCFF) at 9-km depth (roughly corresponding to the average depth of aftershocks) associated with the northern Thessaly earthquakes a) after the 1st event, b) after the 2nd event and c) after the 3rd event, respectively. The palette of Coulomb stress values is linear in the range −1 to +1 bar. The stress change has been computed for receiver faults with the same kinematics as the source models (see Table 6). Red rectangle is the surface projection of the rupture plane, and green line is its surface trace (projected up-dip). Green circles are relocated aftershocks for the periods of a) March 3 - March 4, 2021 17:41 UTC b) 4 March, 18:38 UTC – 12 March, 12:57 UTC and c) 12 March, 12:57 – 16 March 2021. Profiles A-B, C-D and E-F are used for the ΔCFF cross-sections of Fig. S4. Colour scale in bar (1 bar = 0.1 MPa); blue areas: ΔCFF unloading (relaxed); red areas: ΔCFF loading.

7.2 Active faulting in northern Thessaly and the 2021 seismic faults

Clustering of earthquakes along neighboring fault segments in Greece that ruptured in a domino pattern involving two or three mainshocks has been observed in 1894 (Atalanti; Ganas et al. 2006), 1978 (Mygdonia; Soufleris et al. 1982; Tranos et al. 2003), 1981 (Alkyonides; Jackson et al. 1982), 2014 (Cephalonia; Valkaniotis et al. 2014; Lekkas and Mavroulis, 2016) among other cases. In Thessaly, there was a cluster of strong events during the period 1954-1957 (Pavlides, 1993; Papadimitriou and Karakostas, 2003) along normal faults, oriented ~E-W. In Northern Thessaly there are no data (at least instrumental) indicating earthquake clustering, so the 2021 seismic sequence was unprecedented.

The activation of three blind faults during the March 2021 seismic sequence indicates the continuity of active structures west of the known active faults of Northern Thessaly, i.e., the Rodia, Tyrnavos and Larissa faults (Fig. 15). The inversion modelling of InSAR data suggests the activation of intermediate-angle normal faults, previously unknown, or likely exploiting crustal structures inherited from previous events (Tolomei et al., 2021). The lack of fault characterisation in this area in Greek active fault databases (Caputo and Pavlides, 2013; Ganas, 2020) probably reflects the subtle nature of surface deformation without the development of large basins and well-defined erosional features. The intermediate-angle rupture planes of the 2021 seismic faults also do not contribute to the considerable build-up of footwall topography, either. This intermediate-angle geometry of the 2021 seismic sources probably continues towards the west (i.e., between Trikala and Deskati; Fig. 1; Antihassia mountains) as the subdued landscape is dominant; however, the strain rates are comparable (~30 ns/yr). Early InSAR studies (Salvi et al., 2004; Ganas et al. 2006) mapped surface deformation on the mountains west of Elassona and Tyrnavos, however, no GNSS stations were in operation at that time, so as to validate the SAR results.

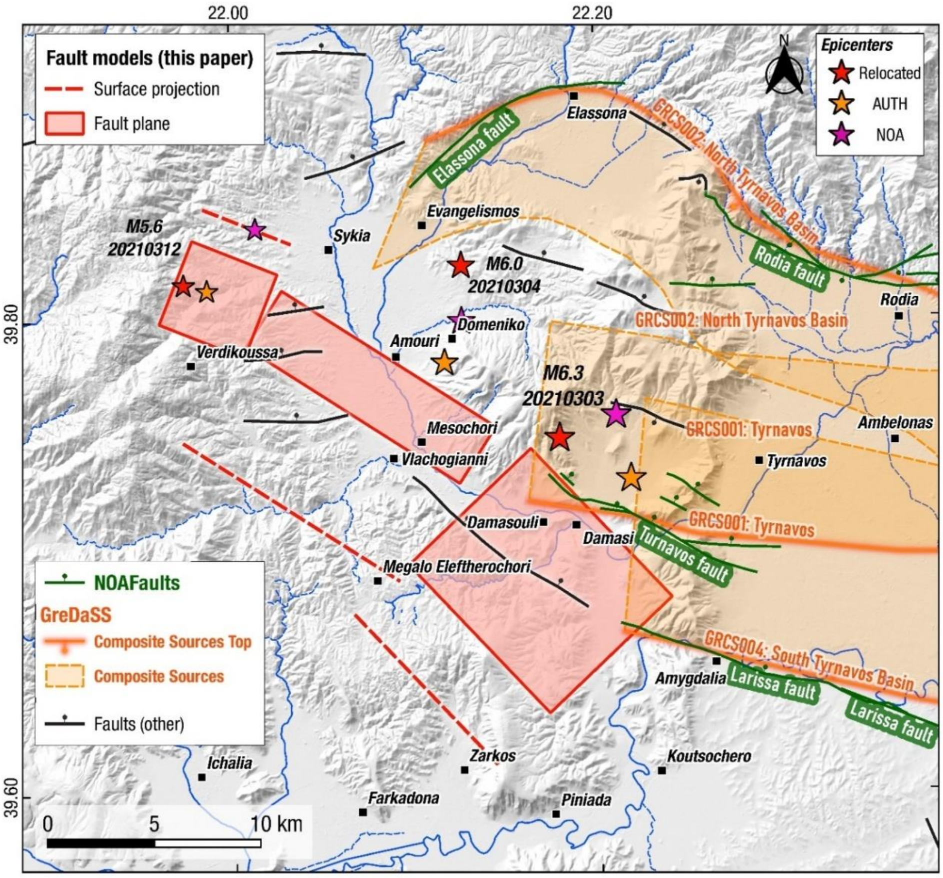

Fig. 15: Shaded relief map showing active faults according to the GreDASS (orange lines and shaded areas; Caputo and Pavlides, 2013) and NOAFAULTs databases (with ticks on the downthrown side). Solid stars indicate epicentres of the three main shocks. Rectangles indicate the surface projection of seismic faults (this study). *A high-resolution version of this figure is provided in the supplement section of this article*.

7.3 Ground cracks marking localized co-seismic and post-seismic deformation

On March 13, 2021 we mapped ground cracks at two locations north of village Zarko (Fig. 10 locality 4; Fig. 12d); about 4 km north of the village inside the Pelagonian basement rocks (schists and gneisses). At the second location (Fig. 12d; approx. 39.6460°N - 22.1251°E) we found two fracture traces, roughly oriented N-S. The fracture length is 15 m (Fig. 16). Then, each fracture trace was mapped in detail by means of a DEM created by close-range photogrammetric data (Fig. 16a). We used a camera Lenovo Tab M8 FHD and the Agisoft Photoscan 1.6.4 to process the data. The terrain model (cell-size 2 mm) was imported in ArcGIS Pro where the fracture trace was analysed for its spatial characteristics (orientation). In order to accurately measure the fracture's strike, we created 12 segments with a relatively homogeneous strike (Fig. 16b). Each fracture segment had its strike computed by the software using the entirety of its length.

We measured at 20 points the direction of fracture opening (the tension axis) using photogrammetry and we compared the findings with our field measurements (7 points; by use of a compass) at nearly identical sites. The measurements were imported in WinTensor v5.9.2 (Delvaux and Sperner, 2003) and rose diagrams were created showing the tensile axes azimuths (Fig. 16a) of both field and photogrammetry measurements. The azimuth of the mean tensile axis (Fig. 16a) is N75°E. In addition, detailed measurements of the fracture's azimuth were also taken, both photogrammetrically (12) and on site (7; Fig. 16b). The mean strike of the fracture is N343°E (a secondary strike is N320°E; Fig. 16b). The mean aperture (opening) of the cracks is 0.018 m (20 measurements).

Moreover, the Zarko ground cracks were mapped where we have observed a vanishing gradient on both the co-seismic and post-seismic interferograms of the 1st event (March 3, 2021 10:16 UTC; Fig. 6 and Fig. 17). This evidence suggests that the cracks are due to primary tectonic motion along the fault and they are not due to ground shaking. We attribute their formation to dilatational strains that develop at the tip of the rupture plane which we infer that it is located very close to the ground surface, perhaps a few hundred metres deep (see dashed red-line in Fig. 15). Other than this locality, we observed a lack of significant post-seismic deformation on our geodetic data. This is something different than the recent Aegean and Ionian Sea earthquakes (see a compilation in Briole et al. 2021; also, Ganas et al. 2021b). This lack of detectability of post-seismic deformation may be due to a combination of factors such as a) lack of GNSS stations near to the seismic faults (for example, in the Samos earthquake case the nearest GNSS station was located 4 km from the top-fault edge; Ganas et al. 2021b), b) the moderate magnitudes of the events ($5.6 \leq M \leq 6.3$) and c) the intermediate-angle of fault dip (ranging from 36° to 40°).

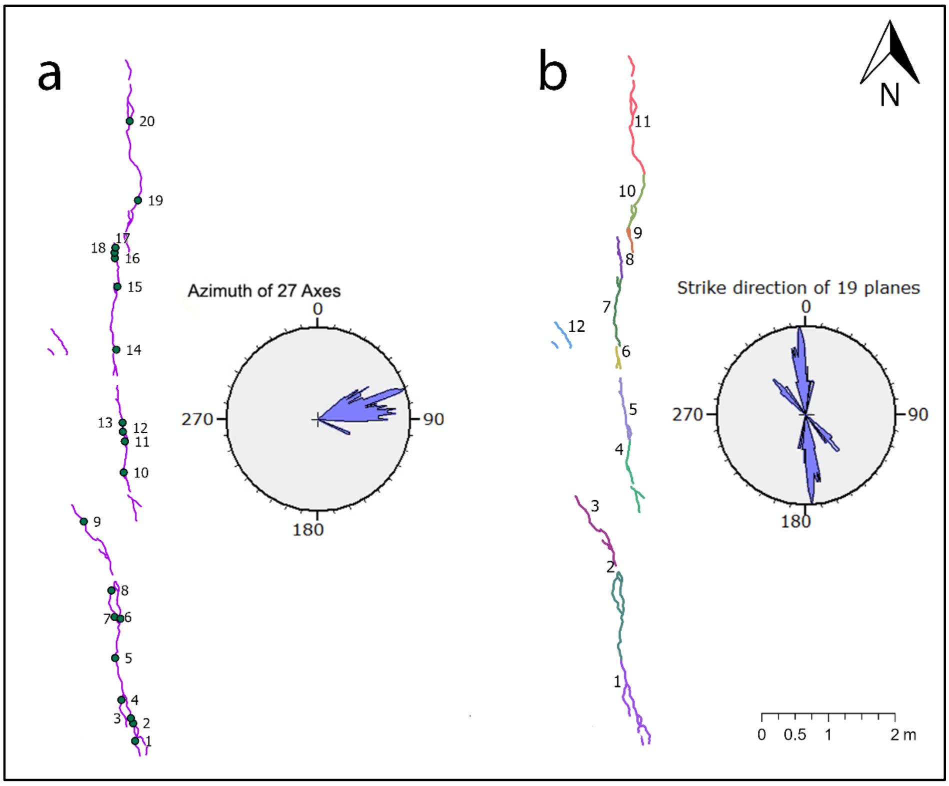

Fig. 16: Surface break data north of village Zarko a) the fracture trace consisting of two segments (thin purple lines) with points (green dots) where the tension axis was measured. The rose diagram (10° interval) shows the azimuths of the individual tensile axes (27 measurements in total) b) the fracture trace showing the 12 segment groups that were used for the calculation of the strike (19 measurements in total). See Fig. 12d for a field photograph. See Fig. 17 for location.

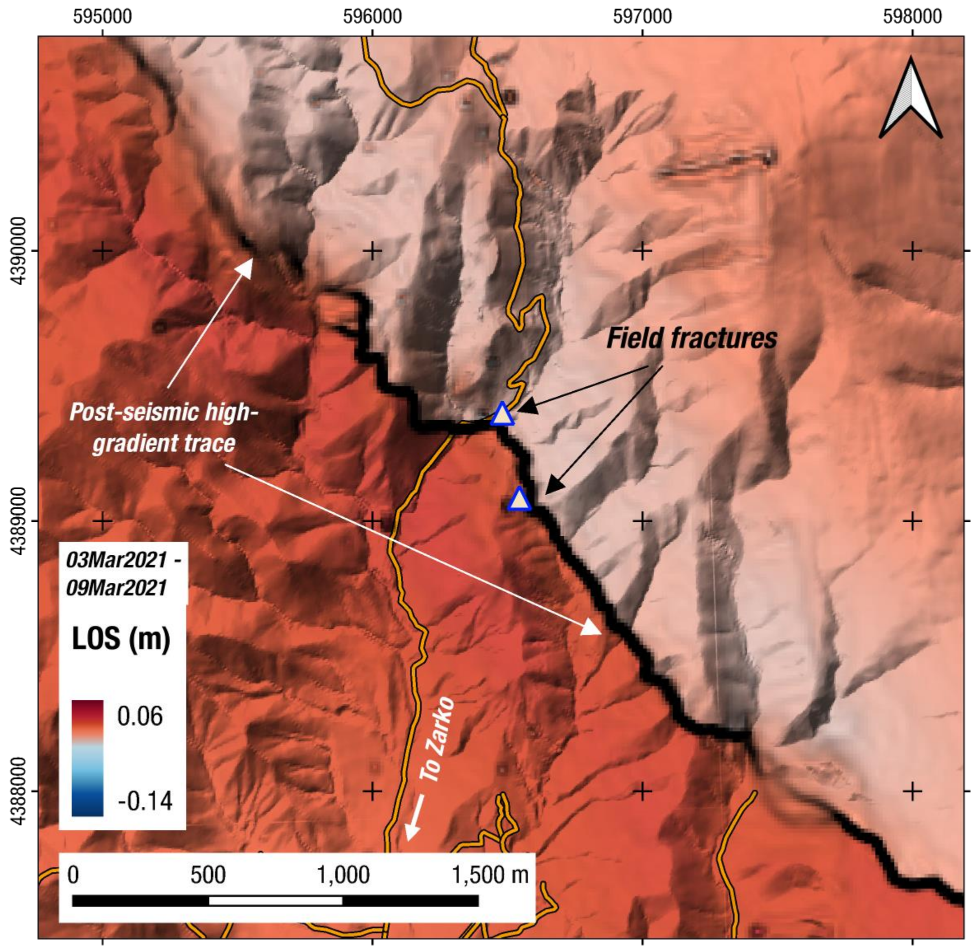

Fig. 17: Post-seismic interferogram (track 102, ascending orbit) showing alignment of phase gradient (thick black line) with location of surface cracks observed in the field (see Fig. 12d for a field photograph).

8. CONCLUSIONS

1. Our results indicate that the March 3, 2021 M_w=6.3 rupture occurred on a northeast-dipping, intermediate-angle normal fault located between the villages Zarko (Trikala) and Damasi (Larissa).
2. The event of March 4, 2021 M_w=6.0 occurred northwest of Damasi, along a fault oriented WNW-ESE and produced less deformation than the event of the previous day.
3. The third event (M_w=5.6) occurred on March 12, 2021 along a south-dipping normal fault.
4. The use of InSAR was crucial to differentiate the ground deformation between the ruptures. The majority of deformation occurs in the vertical component, with a maximum

of 0.39 m of subsidence over the M_w=6.3 rupture plane, south of Damasi. A total amount of 0.3 m horizontal displacement (E-W) was measured in the same region.

5. The inversion modelling of InSAR data indicates the activation of intermediate-angle normal faults, previously unknown.
6. No tectonic ruptures with lateral displacement were found in the field, in agreement with the modelled faults as blind structures.
7. We mapped two fracture sets to the north of village Zarko which comprise tensile cracks. We attribute their formation to dilatational strains that develop at the tip of the rupture plane which we infer that it is located very close to the ground surface,
8. Only the March 3, 2021 M_w=6.3 event produced significant displacement at the GNSS stations.
9. We made several post-seismic interferograms, but we have seen that there is almost no post-seismic deformation, except in the footwall area (Zarkos mountain; Fig. 17). In general, it is below the 7 mm level (quarter of fringe) in the near field and below the 1 mm level at the GNSS sites.
10. The March 2021 earthquakes generated numerous secondary phenomena with vast areas of alluvial deposits (mainly along the Piniada valley) exhibiting spectacular liquefaction features.

9. ACKNOWLEDGEMENTS

We are indebted to ESA and Copernicus for providing access to SAR images. We acknowledge the constructive reviews of Vassilis Karakostas, Ritsa Papadimitriou and Riccardo Caputo. We thank Efthimios Lekkas, Costas Papazachos, Ritsa Papadimitriou, Vasillis Karakostas, Spiros Pavlides, Ioannis Koukouvelas, Alekos Belesis and Dimitris Galanakis for comments and discussions in the field. GNSS data were provided by INGV, NOANET, HxGN Smartnet, AUTH-Hermes and Tree-Uranus networks. We are indebted to the local authorities of Tyrnavos, Elassona, Piniada and Zarko for their help. We used seismological data from the following seismic networks, HL (Institute of Geodynamics, National Observatory of Athens, doi: 10.7914/SN/HL), HP (University of Patras, doi: 10.7914/SN/HP), HT (Aristotle University of Thessaloniki, doi: 10.7914/SN/HT), HA (National and Kapodistrian University of Athens, doi: 10.7914/SN/HA), and HI Institute of Engineering Seismology and Earthquake Engineering, doi: 10.7914/SN/HI) networks. We thank the staff of the National Observatory of Athens, Institute of Geodynamics, for phase picking. Several figures were created by use of GMT (Wessel et al. 2019) and the QGIS Geographic Information System http://www.qgis.org .

10. REFERENCES

Argyrakis, P., Ganas, A., Valkaniotis, S., Tsioumas, V., Sagias, N., Psiloglou, B., 2020. Anthropogenically induced subsidence in Thessaly, central Greece: new evidence from GNSS data. *Nat. Hazards*, 102, 179–200. https://doi.org/10.1007/s11069-020-03917-w

Bertiger, W., Desai, S.D., Haines, B., Harvey, N., Moore, A.W., Owen, S., Weiss, J.P., 2010. Single receiver phase ambiguity resolution with GPS data. *J Geod*, 84, 327–337 https://doi.org/10.1007/s00190-010-0371-9

Briole, P., De Natale, G., Gaulon, R., Pingue, F., Scarpa, R., 1986. Inversion of geodetic data and seismicity associated with the Friuli earthquake sequence (1976-1977), *Annales Geophysicae*, 4(B4), 481-492.

Briole, P., 2017. Modelling of earthquake slip by inversion of GNSS and InSAR data assuming homogeneous elastic medium, *Zenodo*. http://doi.org/10.5281/zenodo.1098399

Briole, P., Ganas, A., Elias, P., Dimitrov, D., 2021. The GPS velocity field of the Aegean. New observations, contribution of the earthquakes, crustal blocks model. *Geophys. J. Int.* 226, 468–492. https://doi.org/10.1093/gji/ggab089

Caputo, R. 1990. Geological and structural study of the recent and active brittle deformation of the Neogene-Quaternary basins of Thessaly (Central Greece). *Scientific Annals, 2,* Aristotle University of Thessaloniki, Thessaloniki (1990), p. 255, 5 encl.

Caputo, R. 1993. Morphotectonics and kinematics along the Tirnavos fault, northern Larissa plain, mainland Greece, *Zeits. für Geomorph*. N.F., Suppl.-Bd., 94, pp. 167-185

Caputo, R., 1995. Inference of a seismic gap from geological data: Thessaly (Central Greece) as a case study. *Ann. Geofisc*., 38 (1), pp. 1-19, 10.4401/ag-4127

Caputo, R., 1996. The active Nea Anchialos Fault System (Central Greece): comparison of geological, morphotectonic, archaeological and seismological data. *Annali di Geofisica*, 39, 3, 557-574.

Caputo, R., and Pavlides, S., 1993. Late Cenozoic geodynamic evolution of Thessaly and surroundings (Central-Northern Greece). *Tectonophysics*, 223, 3-4, 339-362.

Caputo, R., B. Helly, S. Pavlides, G. Papadopoulos, 2004. Palaeoseismological investigation of the Tyrnavos Fault (Thessaly, Central Greece). *Tectonophysics*, 394 (1), pp. 1-20, 10.1016/j.tecto.2004.07.047.

Caputo, R., and Helly, B. 2005. Archaeological evidences of past earthquakes: a contribution to the SHA of Thessaly, Central Greece. *J. Earthq. Eng*., 9 (2), 199-222, 10.1080/13632460509350539

Caputo, R., Pavlides, S. 2013. The Greek Database of Seismogenic Sources (GreDaSS), version 2.0.0: A compilation of potential seismogenic sources (Mw>5.5) in the Aegean Region, 10.15160/unife/gredass/0200

Caputo, R., B. Helly, D. Rapti, S. Valkaniotis, 2021. Late Quaternary hydrographic evolution in Thessaly (Central Greece): The crucial role of the Piniada Valley. *Quaternary International*, https://doi.org/10.1016/j.quaint.2021.02.013.

Crotwell, H.P., Owens, T.J., Ritsema, J., 1999. The TauP Toolkit: Flexible Seismic Travel-time and Ray-path Utilities. *Seismol. Res. Lett*. 70, 154–160. https://doi.org/10.1785/gssrl.70.2.154

Dalla Via, G., Crosetto, M., Crippa, B. 2012. Resolving vertical and east-west horizontal motion from differential interferometric synthetic aperture radar: The L'Aquila earthquake. *J. Geophys. Res*., 117, B02310. https://doi.org/10.1029/2011JB008689

D'Agostino, N., M. Métois, R. Koci, L. Duni, N. Kuka, A. Ganas, I. Georgiev, F. Jouanne, N. Kaludjerovic, R. Kandić, 2020. Active crustal deformation and rotations in the southwestern Balkans from continuous GPS measurements. *Earth and Planetary Science Letters*, 539, 116246, https://doi.org/10.1016/j.epsl.2020.116246

Delvaux, D. and Sperner, B. 2003. Stress tensor inversion from fault kinematic indicators and focal mechanism data: the TENSOR program. In: New Insights into Structural Interpretation and Modelling (D. Nieuwland Ed.). Geological Society, London, Special Publications, 212, 75-100.

Drakatos, G., Papanastassiou, D., Voulgaris, N., Stavrakakis, G., 1998. Observations on the 3-D crustal velocity structure in the Kozani-Grevena (NW Greece) area. *J. Geodyn*. 26, 341–351. https://doi.org/10.1016/S0264-3707(97)00061-6

Ganas, A., Salvi, S., Atzori, S., Tolomei, C., 2006a. Ground deformation in Thessaly, Central Greece, retrieved from Differential Interferometric analysis of ERS-SAR data. *11th International Symposium on Natural and Human Induced Hazards & 2nd Workshop on Earthquake Prediction Abstract Volume, June 22-25, 2006, Patras, Greece*, page 41.

Ganas, A, Sokos, E, Agalos, A, Leontakianakos, G, Pavlides S, 2006b. Coulomb stress triggering of earthquakes along the Atalanti Fault, central Greece: Two April 1894 M6+ events and stress change patterns. *Tectonophysics*, 420, 357–369.

Ganas, A., G. Drakatos, S. Rontogianni, C. Tsimi, P. Petrou, M. Papanikolaou, P. Argyrakis, K. Boukouras, N. Melis and G. Stavrakakis, 2008. NOANET: the new permanent GPS network for Geodynamics in Greece. *Geophysical Research Abstracts*, Vol. 10, EGU2008-A-04380.

Ganas, A., 2020. NOAFAULTS KMZ layer Version 3.0 (2020 update) (Version V3.0) [Data set]. *Zenodo*. http://doi.org/10.5281/zenodo.4304613

Ganas, A., Valkaniotis S., Tsironi V., Karasante I., Elias P., Kapetanidis V., Kassaras I., Papathanassiou G. and Briole, P. 2021a. The March 2021 seismic sequence in Larisa - Damasi, Thessaly (central Greece), its seismotectonic characteristics and geodynamic effects. *Zenodo*. http://doi.org/10.5281/zenodo.4617264

Ganas, A., Elias, P., Briole, P., Valkaniotis, S., Escartin, J., Tsironi, V., Karasante, I., Kosma, C., 2021b. Co-seismic and post-seismic deformation, field observations and fault model of the 30 October 2020 Mw = 7.0 Samos earthquake, Aegean Sea. *Acta Geophys.* https://doi.org/10.1007/s11600-021-00599-1

Goldstein, R. M.; Werner, C. L. 1998. Radar interferogram filtering for geophysical applications. *Geophys. Res. Lett*. 25(21), 4035-4038.

Grigoriadis, V.N., Tziavos, I.N., Tsokas, G.N., Stampolidis, A., 2016. Gravity data inversion for Moho depth modeling in the Hellenic area. *Pure Appl. Geophys*. 173, 1223–1241. https://doi.org/10.1007/s00024-015-1174-y

Hatzfeld, D., Karakostas, Vassilios, Ziazia, M., Selvaggi, G., Leborgne, S., Berge, C., Guiguet, R., Paul, Anne, Voidomatis, P., Diagourtas, Dimitris, Kassaras, Ioannis, Koutsikos, I., Makropoulos, Kostas, Azzara, Riccardo, Bona, M., Baccheschi, S., Bernard, Pascal, Papaioannou, Christos, 1997. The Kozani- Grevena (Greece) Earthquake of 13 May 1995.

Revisited from a Detailed Seismological Study. *Bulletin of the Seismological Society of America*, 87, 473-473.

Hatzfeld, D., Ziazia, M., Kementzetzidou, D., Hatzidimitriou, P., Panagiotopoulos, D., Makropoulos, K., 1999. Microseismicity and focal mechanisms at the western termination of the North Anatolian Fault and their implications for continental tectonics, *Geophysical Journal International*, Volume 137, Issue 3, pp. 891-908.

Jackson, J. A., Gagnepain, J., Houseman, G., King, G. C. P., Papadimitriou, P., Soufleris, C., & Virieux, J. 1982. Seismicity, normal faulting, and the geomorphological development of the Gulf of Corinth (Greece) the Corinth earthquakes of February and March 1981. *Earth and Planetary Science Letters*, 57(2), 377– 397. https://doi.org/10.1016/0012-821X(82)90158-3

Kapetanidis, V., 2017. Spatiotemporal patterns of microseismicity for the identification of active fault structures using seismic waveform cross-correlation and double-difference relocation, PhD Thesis, National and Kapodistrian University of Athens.

Kapetanidis, V., Kassaras, I., 2019. Contemporary crustal stress of the Greek region deduced from earthquake focal mechanisms. *J. Geodyn.* 123, 55–82. https://doi.org/10.1016/j.jog.2018.11.004

Karakostas, C., Klimis, N., Lekidis, V., Makra, K., Margaris, B., Morfidis, K., Papaioannou, C., Rovithis, E., Salonikios, T., Sotiriadis, D., Theodoulidis, N., 2021. ΟΙ ΣΕΙΣΜΟΙ ΤΗΣ ΘΕΣΣΑΛΙΑΣ - Μ6.3, 3 Μαρτίου 2021 και Μ6.1, 4 Μαρτίου 2021. Προκαταρκτική έκθεση. https://doi.org/10.5281/ZENODO.4641200

Karastathis, V., Papoulia, J., Di Fiore, B., Makris, J., Tsampas, A., Stampolidis, A., Papadopoulos, G., 2011. Deep structure investigations of the geothermal field of the North Euboean Gulf, Greece, using 3-D local earthquake tomography and Curie Point Depth analysis. *Journal of Volcanology and Geothermal Research*, 206. https://doi.org/10.1016/j.jvolgeores.2011.06.008

Kilias A., Mountrakis D., 1989. The Pelagonian nappe. Tectonics, metamorphism and magmatism. (In Greek with English abstract). Bull. Geol. Soc. Greece, 23(1), 29-46.

King, G. C. P., Stein, R. S., and Rundle, J. B. 1988. The Growth of Geological Structures by Repeated Earthquakes 1. Conceptual Framework, *J. Geophys. Res.*, 93 (B11), 13307– 13318, doi:10.1029/JB093iB11p13307.

King, G.C.P., Stein, R.S., Lin, J., 1994. Static stress changes and the triggering of earthquakes, *Bull. Seism. Soc. Am.*, 84(3), 935-953.

Kiratzi, A.A., Wagner, G.S., Langston, C.A. 1991. Source parameters of some large earthquakes in Northern Aegean determined by body waveform inversion. Pure Appl. Geophys. *PAGEOPH* 135, 515–527, https://doi.org/10.1007/BF01772403

Konstantinou, K.I, 2017. Accurate relocation of seismicity along the North Aegean Trough and its relation to active tectonics. *Tectonophysics*, 717, 372-382.

Konstantinou, K. I., V. Mouslopoulou, W.-T. Liang, O. Heidbach, O. Oncken, and J. Suppe 2016. Present-day crustal stress field in Greece inferred from regional-scale damped inversion of earthquake focal mechanisms. *J. Geophys. Res. Solid Earth*, 121, doi:10.1002/2016JB013272.

Lekkas, E.L., Mavroulis, S.D. 2016. Fault zones ruptured during the early 2014 Cephalonia Island (Ionian Sea, Western Greece) earthquakes (January 26 and February 3, Mw 6.0) based on the associated co-seismic surface ruptures. *J Seismol* 20, 63–78. https://doi.org/10.1007/s10950-015-9510-3

Lekkas, E., K. Agorastos, S. Mavroulis, Ch. Kranis, Emm. Skourtsos, P. Carydis, M. Gogou, K.-N. Katsetsiadou, G. Papadopoulos, I. Triantafyllou, A. Agalos, S. Moraitis, E. Stamati, D. Psarris, G. Kaviris, V. Kapetanidis, P. Papadimitriou, A. Karakonstantis, I. Spingos, V. Kouskouna, I. Kassaras, K. Pavlou, N. Voulgaris, M. Mavrouli, S. Pavlides, A. Chatzipetros, S. Sboras, E. Kremastas, A. Chatziioannou, A. Kiratzi, C. Papazachos, N. Chatzis, V. Karakostas, E. Papadimitriou, I. Koukouvelas, K. Nikolakopoulos, A. Kyriou, D. Apostolopoulos, V. Zygouri, S. Verroios, A. Belesis, I. Tsentzos, P. Krassakis, K. Lymperopoulos, A. Karavias, D. Bafi, T. Gatsios, M. Karatzia, I. Gkougkoustamos, T. Falaras, I. Parcharidis, G. Papathanassiou, C.P. Evangelidis, V. Karastathis, G-A. Tselentis, A. Ganas, V. Tsironi, I. Karasante, S. Valkaniotis, D. Galanakis, G. Kostantopoulou, N. Theodoulidis, Ch. Karakostas, V. Lekidis, K. Makra, V. Margaris, K. Morfidis, Ch. Papaioannou, M. Rovithis, Th. Salonikios, N. Papadopoulos, A. Kourou, M. Manousaki, T. Thoma 2021. The early March 2021 Thessaly earthquake sequence. *Newsletter of Environmental, Disaster and Crises Management Strategies*, 22, ISSN 2653-9454.

Lomax, A., 2014. Seisgram2K, Seismogram visualization and analysis software version 7.0, http://alomax.free.fr/seisgram/SeisGram2K.html

Mantovani, A., Valkaniotis, S., Rapti, D. et al. 2018. Mapping the Palaeo-Piniada Valley, Central Greece, Based on Systematic Microtremor Analyses. *Pure Appl. Geophys*. 175, 865–881. https://doi.org/10.1007/s00024-017-1731-7

Migiros, G. 1985. Geological map of Greece in 1:50,000 scale, map sheet Gonnoi. Institute of Geological & Mineralogical Exploration, Athens.

Mountrakis, D., 1984. Structural evolution of the Pelagonian Zone in Northwestern Macedonia, Greece. *Geological Society, London, Special Publications*, 17, 581-590, https://doi.org/10.1144/GSL.SP.1984.017.01.45

Mountrakis, D., Kilias, A., Pavlides, S., Zouros, N., Spyropoulos, N, Tranos, M., and Soulakelis, N. 1993. Field study of the southern Thessaly highly active fault zone, in Proc. *2nd Congress Hellenic Geophys. Union*, 2, 603-614.

Müller, M.D., A. Geiger, H.G. Kahle, G. Veis, H. Billiris, D. Paradissis, S. Felekis, 2013. Velocity and deformation fields in the North Aegean domain, Greece, and implications for fault kinematics, derived from GPS data 1993–2009. *Tectonophysics*, 597, pp. 34-49.

Novotný, O., Zahradník, J., Tselentis, G.-A. 2001. Northwestern Turkey Earthquakes and the Crustal Structure Inferred from Surface Waves Observed in Western Greece. *Bulletin of the Seismological Society of America*, 91(4), 875–879. https://doi.org/10.1785/0120000116

Okada Y., 1992. Internal deformation due to shear and tensile faults in a half space, *Bull. Seism. Soc. America*, 82, 1018–1040.

Palyvos, N., Pavlopoulos, K., Froussou, E., Kranis, H., Pustovoytov, K., Forman, S.L., Minos-Minopoulos, D., 2010. Paleoseismological investigation of the oblique-normal Ekkara ground rupture zone accompanying the M 6.7–7.0 earthquake on 30 April 1954 in Thessaly, Greece: Archaeological and geochronological constraints on ground rupture recurrence. *J. Geophys. Res*. 115, B06301. https://doi.org/10.1029/2009JB006374

Papadimitriou, E.E, Karakostas, VG., 2003. Episodic occurrence of strong ($Mw \geq 6.2$) earthquakes in Thessalia area (central Greece), *Earth and Planetary Science Letters*, Volume 215, Issues 3–4, 395-409, https://doi.org/10.1016/S0012-821X(03)00456-4.

Papastamatiou, D., Mouyaris, N., 1986. The earthquake of April 30, 1954, in Sophades (Central Greece). *Geophys. J. R. astr. Soc.*, 87, 885-895.

Papazachos, B.C., Panagiotopoulos, D.G., Tsapanos, T.M., Mountrakis, D.M., Dimopoulos, G.C., 1983. A study of the 1980 summer seismic sequence in the Magnesia region of Central Greece. *Geophys. Jour. R. astron. Soc. London*, 75, 155-168.

Papazachos, B.C., P.M. Hatzidimitriou, G.F. Karakaisis, C.B. Papazachos, G.N. Tsokas, 1993. Rupture zones and active crustal deformation in southern Thessalia, central Greece, *Boll. Geof. Teor. Appl*. 139, 363-374.

Pavlides S., 1993. Active faulting in multi-fractured seismogenic areas; examples from Greece. *Z. Geomorph*. N. E., 94, 57-72.

Pavlides, S., Kouskouna, V., Ganas, A., Caputo, R., Karastathis, V., Sokos, E., 2004. The Gonnoi (NE Thessaly - Greece) Earthquake (June 2003, Ms=5.5) and the Neotectonic Regime of Lower Olympus. *5th International Symposium on Eastern Mediterranean Geology, Thessaloniki, Greece, 14-20 April 2004*, 627-630.

Plastiras, V. 1985. Geological map of Greece in 1:50,000 scale, map sheet Larissa. Institute of Geological & Mineralogical Exploration, Athens.

Rigo, A., Chabalier, J.-B. de, Meyer, B., Armijo, R., 2004. The 1995 Kozani-Grevena (northern Greece) earthquake revisited: an improved faulting model from synthetic aperture radar interferometry. *Geophys. J. Int*. 157, 727–736. https://doi.org/10.1111/j.1365-246X.2004.02220.x

Salvi, S., Ganas, A., Stramondo, S., Atzori, S., Tolomei, C., Pepe, A., Manzo, M., Casu, F., Berardino, P., Lanari, R., 2004. Monitoring Long-Term Ground Deformation by SAR Interferometry: Examples from the Abruzzi, Central Italy, and Thessaly, Greece. *5th International Symposium on Eastern Mediterranean Geology, Thessaloniki, Greece, 14-20 April 2004*, Reference T7-17.

Soufleris, C., J.A Jackson, G.C.P King, C Spencer, C Scholz, 1982. The 1978 earthquake sequence near Thessaloniki (northern Greece). *Geophysical Journal of the Royal Astronomical Society*, 68 (1982), pp. 429-458.

Stamatis, A. 1987. Geological map of Greece in 1:50,000 scale, map sheet Deskati. Institute of Geological & Mineralogical Exploration, Athens.

Taymaz, T., Jackson, J.A., McKenzie, D., 1991. Active tectonics of the north and central Aegean Sea, *Geophys. J. Int*., 106, 433-490.

Taymaz, T., Ganas, A., Yolsal-Çevikbilen, S., Vera, F., Eken, T., Erman, C., Keleş, D., Kapetanidis, V., Valkaniotis, S., Karasante, I., Tsironi, V., Gaebler, P., Melgar, D., Ocalan, T., 2021. Source Mechanism and Rupture Process of the 24 January 2020 Mw 6.7 Doğanyol-Sivrice Earthquake obtained from Seismological Waveform Analysis and Space Geodetic Observations on the East Anatolian Fault Zone (Turkey), *Tectonophysics*, https://doi.org/10.1016/j.tecto.2021.228745

Toda, S., Stein, R.S., Sevilgen, V., Lin, J., 2011. Coulomb 3.3 Graphic-rich deformation and stress-change software for earthquake, tectonic, and volcano research and teaching-user guide. U.S. Geological Survey Open-File Report 2011-1060, 63, http://pubs.usgs.gov/of/2011/1060/

Tolomei C., Caputo R., Polcari M., Famiglietti NA., Maggini M., Stramondo S., 2021. The Use of Interferometric Synthetic Aperture Radar for Isolating the Contribution of Major Shocks: The Case of the March 2021 Thessaly, Greece, Seismic Sequence. *Geosciences*. 11(5):191. https://doi.org/10.3390/geosciences11050191

Tranos, M., E. Papadimitriou, A. Kilias, 2003. Thessaloniki-Gerakarou Fault Zone (TGFZ): the western extension of the 1978 Thessaloniki earthquake fault (northern Greece) and seismic hazard assessment. *J. Struct. Geol*., 25, pp. 2109-2123

Triantafillis, E. 1987. Geological map of Greece in 1:50,000 scale, map sheet Elassona. Institute of Geological & Mineralogical Exploration, Athens.

Tsodoulos, I.M., K. Stamoulis, R. Caputo, I. Koukouvelas, A. Chatzipetros, S. Pavlides, C. Gallousi, C. Papachristodoulou, K. Ioannides, 2016. Middle-Late Holocene earthquake history of the Gyrtoni Fault, Central Greece: insight from optically stimulated luminescence (OSL) dating and paleoseismology, *Tectonophysics*, 687, 14-27, 10.1016/j.tecto.2016.08.015

Valkaniotis S., Ganas A., Papathanassiou, G., and Papanikolaou M., 2014. Field observations of geological effects triggered by the January-February 2014 Cephalonia (Ionian Sea, Greece) earthquakes, *Tectonophysics*, 630, 150-157, DOI:10.1016/j.tecto.2014.05.012

Valkaniotis, S., Papathanassiou, G., Ganas, A., Kremastas, E., Caputo, R., 2021. Preliminary report of liquefaction phenomena triggered by the March 2021 earthquakes in Central Thessaly, Greece. https://doi.org/10.5281/ZENODO.4608365 released (2021, March 16).

Veci, L., Lu, J., Prats-Iraola, P., Scheiber, R., Collard, F., Fomferra, N., Engdahl, M., 2014. The Sentinel-1 toolbox. In: *Proceedings of the IEEE International Geoscience and Remote Sensing Symposium (IGARSS). IEEE*, pp. 1–3.

Vidakis, M. 1998. Geological map of Greece in 1:50,000 scale, map sheet Farkadona. Institute of Geological & Mineralogical Exploration, Athens.

Waldhauser, F., 2001. hypoDD—A Program to Compute Double-Difference Hypocenter Locations: U.S. Geological Survey Open-File Report 01-113, 25 pp., https://pubs.usgs.gov/of/2001/0113/ .

Waldhauser, F., Ellsworth, W. L. 2000. A Double-difference Earthquake location algorithm: Method and application to the Northern Hayward Fault, California. *Bulletin of the Seismological Society of America*, 90(6), 1353–1368. https://doi.org/10.1785/0120000006

Wessel, P., Luis, J. F., Uieda, L., Scharroo, R., Wobbe, F., Smith, W. H. F., Tian, D. 2019. The Generic Mapping Tools version 6. *Geochemistry*, *Geophysics*, *Geosystems*, 20, 5556–5564.

Wright, T.J., Parsons, B., Lu, Z. 2004. Toward mapping surface deformation in three dimensions using InSAR. *Geophysical Research Letters*, 31 (1), L01607. https://doi.org/10.1029/2003GL018827

Table S1. List with relocation data for the three main events of the March 2021 northern Thessaly sequence. Time is UTC.

Event	LAT (°)	LON (°)	DEPTH (km)	YEAR	MO DAY Hr Min SS.SS	M_L (NOA)
1	39.7495	22.1791	10.7	2021	3 3 10 16 7.400	6.0
2	39.8227	22.1261	13.0	2021	3 4 18 38 16.600	5.9
3	39.8152	21.9738	7.1	2021	3 12 12 57 49.060	5.2

Table S2. Focal mechanisms of 22 aftershocks with M≥4.0.

Year	Mo	Day	Hr	Mn	Sec	Latitude	Longitude	Dep	Mag	Strike1	Dip1	Rake1	Strike2	Dip2	Rake2
2021	3	3	10	20	45.93	39.694	22.174	9.4	4.7	178.8	49.5	-43.8	300.7	58.2	-130.2
2021	3	3	10	23	8.12	39.692	22.154	10.4	4.1	267.5	47.0	-139.7	147.5	61.8	-50.7
2021	3	3	10	26	18.33	39.641	22.218	9.7	4.1	2.8	52.9	-37.8	117.9	60.7	-136.3
2021	3	3	10	34	7.54	39.707	22.232	11.7	4.9	283.0	56.1	-148.8	174.3	64.5	-38.2
2021	3	3	11	12	23.08	39.707	22.150	10.3	4.3	327.1	50.8	-41.6	86.4	59.0	-132.5
2021	3	3	11	35	56.66	39.691	22.208	10.2	4.8	344.4	44.7	-87.5	160.9	45.4	-92.5
2021	3	3	18	24	8.06	39.723	22.087	11.6	5.2	328.6	54.0	-34.7	80.7	62.6	-138.5
2021	3	3	18	49	48.25	39.734	22.101	12.4	4.2	77.7	33.7	-92.0	260.1	56.3	-88.7
2021	3	3	21	0	54.67	39.748	22.127	10.2	4.0	278.3	43.7	-145.3	161.7	66.8	-51.8
2021	3	4	2	43	37.77	39.719	22.221	11.6	4.0	349.1	36.7	-71.0	145.9	55.6	-103.6
2021	3	4	9	36	15.37	39.782	22.123	13.2	4.4	130.9	48.0	-35.9	246.7	64.2	-132.0
2021	3	4	18	45	26.58	39.828	22.000	11.9	4.1	242.0	51.4	-150.8	132.8	67.6	-42.4
2021	3	4	19	23	50.99	39.829	21.927	11.6	5.0	248.8	41.9	-101.6	84.2	49.1	-79.8
2021	3	4	19	31	31.96	39.801	22.039	11.5	4.2	125.0	52.7	-38.4	240.7	60.4	-135.8
2021	3	4	20	3	8.11	39.729	22.115	11.1	4.2	331.7	53.5	-29.4	80.2	66.8	-139.7
2021	3	5	9	59	58.96	39.825	22.021	15.1	4.2	86.0	41.7	-85.4	259.8	48.5	-94.1
2021	3	5	10	1	14.49	39.768	22.076	10.3	4.2	294.8	36.0	-84.3	107.8	54.2	-94.1
2021	3	6	16	36	17.51	39.659	22.243	11.6	4.1	356.0	65.3	-22.9	96.0	69.3	-153.5
2021	3	6	19	47	39.76	39.829	22.064	9.6	4.1	3.7	47.9	-34.6	118.5	65.1	-132.3
2021	3	11	14	19	40.40	39.768	22.076	6.3	4.0	124.4	46.9	-42.0	246.0	60.8	-128.5
2021	3	15	15	43	37.71	39.762	22.149	8.0	4.3	263.2	24.5	-86.2	79.0	65.6	-91.7
2021	3	21	17	15	54.04	39.771	22.102	8.8	4.1	287.5	42.3	-69.4	80.6	51.0	-107.8

Fig. S1: Magnitude distribution histogram of the relocated events (M_L after National Observatory of Athens manual measurements).

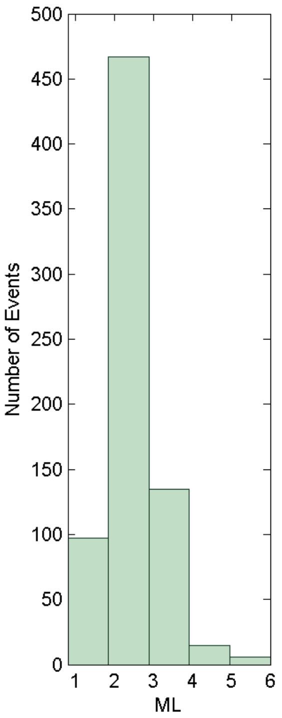

Fig. S2: Graph showing East, North, Up position time series of station KLOK during the period of the 2^{nd} event (March 4, 2021 18:38 UTC).

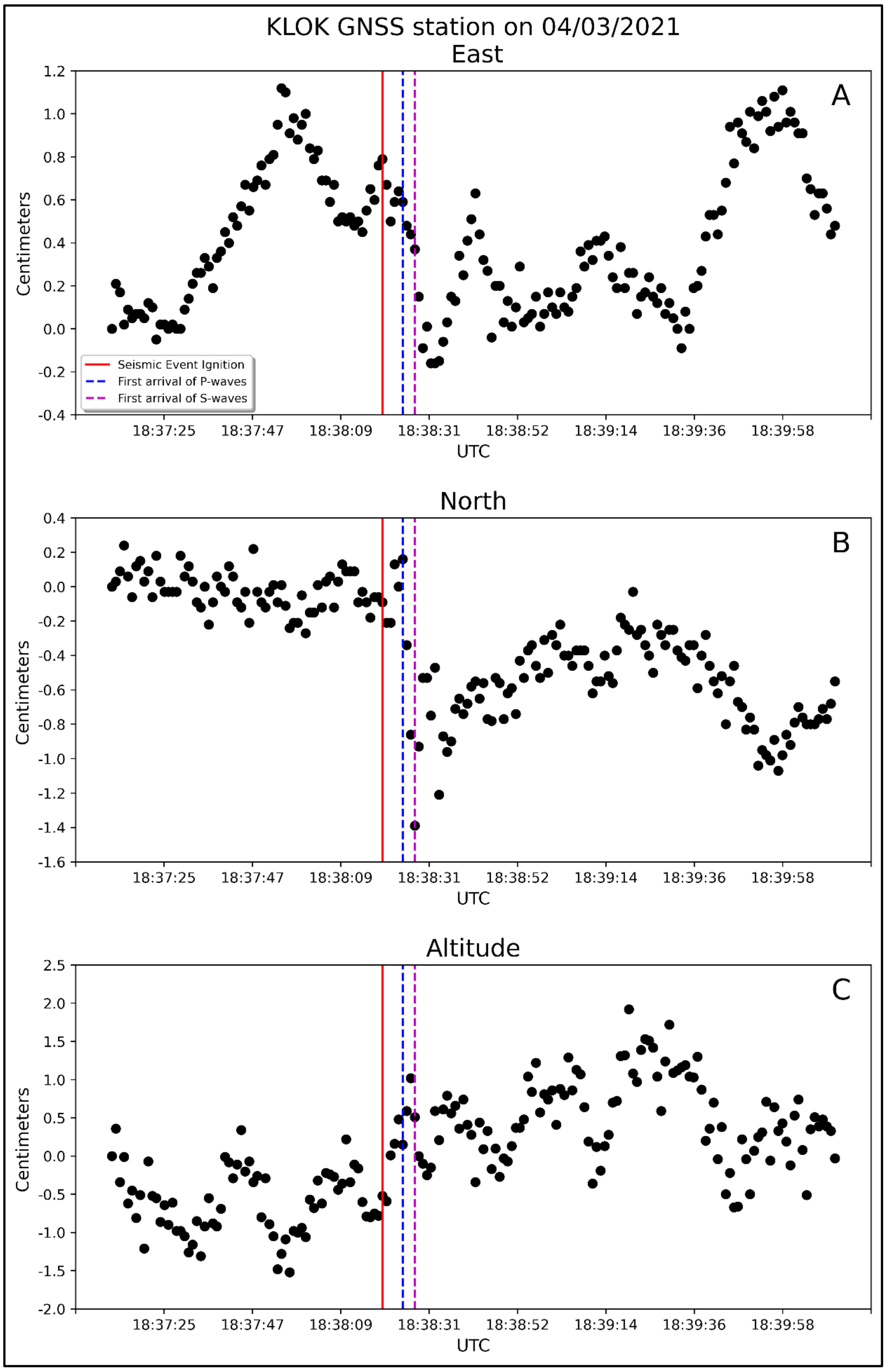

Fig. S3: Coulomb stress transfer on optimally-oriented planes to regional extension (N183.9°E). Calculation at a depth of 9 km.

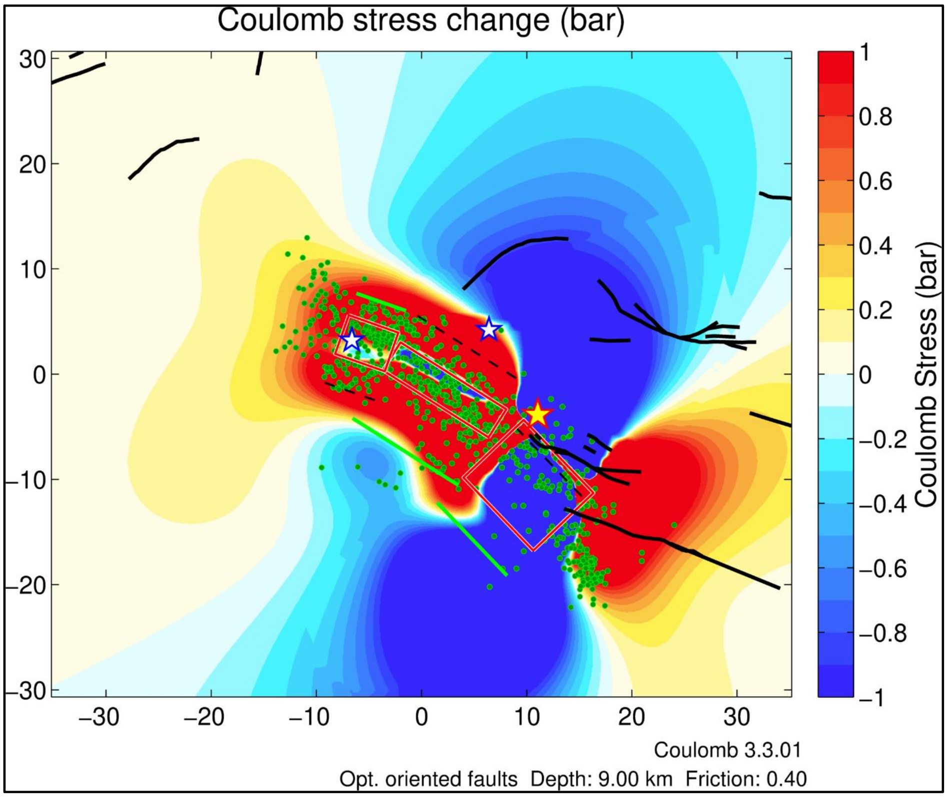

Fig. S4: Vertical cross-sections of Coulomb stress transfer through the fault planes of Fig. 14. The green line shows the respective fault plane. Stars denote the hypocentre of the respective major earthquake, while green circles represent smaller aftershocks. Horizontal dashed line shows the depth of 9 km where map slices are shown in Fig. 14.

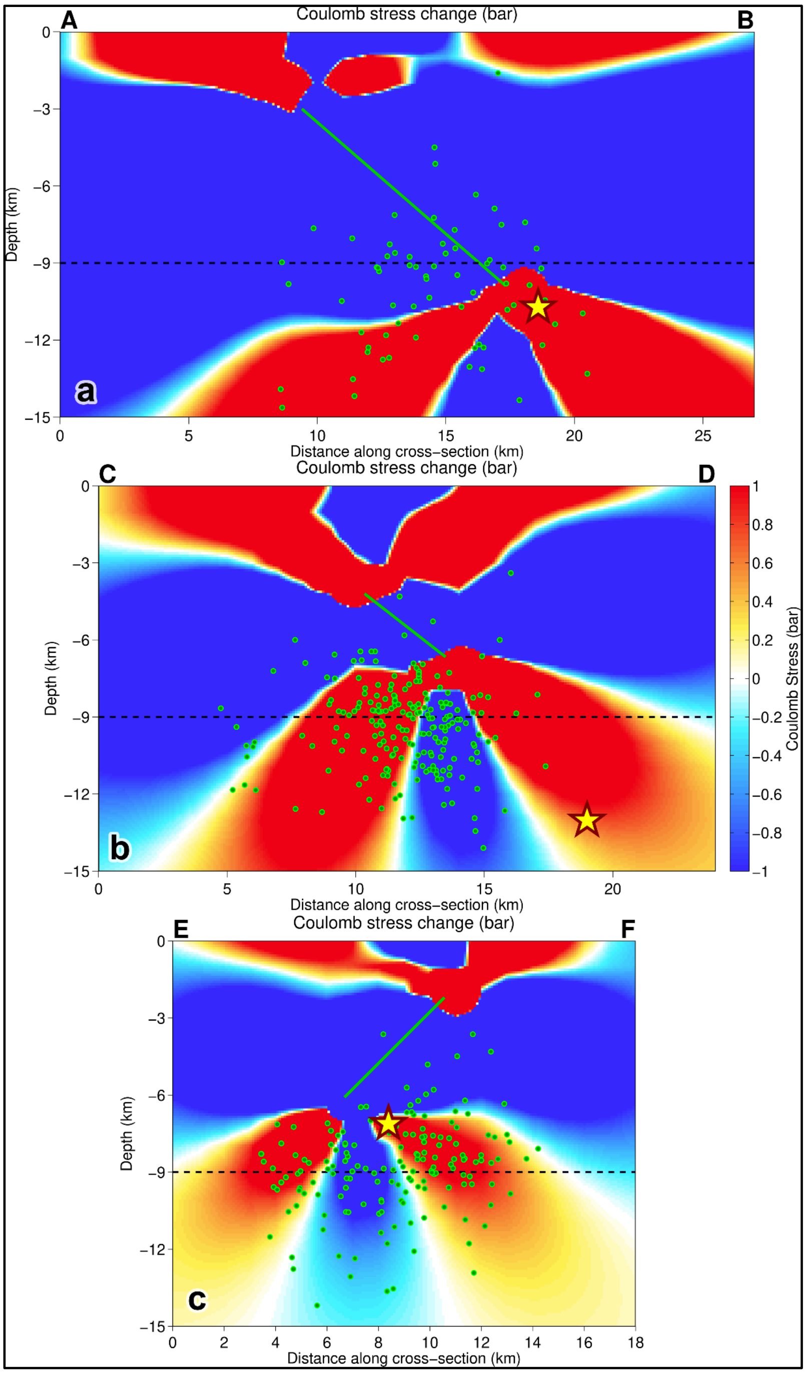

BGSG

Volume 58

Research Paper

ACCELERATING DEFORMATION SEISMICITY PATTERNS BEFORE THE MARCH 3, 2021 THESSALY M_W 6.3 STRONG EARTHQUAKE. FIRST RESULTS.

Georgios Chatzopoulos[1]

[1]**Section of Geophysics – Geothermics, Department of Geology and Geoenvironment, National and Kapodistrian University of Athens, 15784 Panepistimiopolis, Athens, Greece,**
ggh1983@hotmail.com.

Abstract

A widely felt strong shallow earthquake with Mw 6.3 magnitude occurred in Thessaly (Central Greece) on March 3, 2021. This recent strong event attracted our interest to apply and evaluate the capabilities of the Accelerating Deformation method. Based on the recently proposed generalized Benioff strain idea which could be justified by the terms of Non-Extensive Statistical Physics (NESP), the common critical exponent was calculated in order to define the critical stage before a strong event. The present analysis comprised a complex spatiotemporal iterative procedure to examine the possible seismicity patterns at a broad region and identify the best one associated with the preparation process before the strong event. The starting time of the accelerating period, the size and location of the critical area are unknown parameters to be determined. Furthermore, although, the time of failure is already known, in the present research it was not set as a fixed value in the algorithm to define the other unknown parameters but instead different catalogue ending dates have been tried out to be with an objective way. The broad region to be investigated was divided with a square mesh and the search of events around a point has been carried on with different size circular and elliptical shapes. Among the obtained results, the solution which exhibits the most dominant scaling law behavior as well as the one which exhibits the smallest spatial area and yet the more dominant scaling law behavior are presented.

***Keywords**: Accelerating deformation, Thessaly, earthquake, Benioff strain.*

Correspondence to:
Georgios Chatzopoulos
ggh1983@hotmail.com

DOI number:
http://dx.doi.org/10.12681/bgsg.27155

Keywords:
Accelerating deformation, Thessaly, earthquake, Benioff strain

Citation:
Chatzopoulos, G. (2021), Accelerating Deformation Seismicity Patterns Before the March 3, 2021 Thessaly M_w 6.3 Strong Earthquake. First Results. Bulletin Geological Society of Greece, 58, 87-104.

Publication History:
Received: 01/06/2021
Accepted: 26/07/2021
Accepted article online: 29/07/2021

The Editor wishes to thank two anonymous reviewers for their work with the scientific reviewing of the manuscript and Ms Emmanouela Konstantakopoulou for editorial assistance.

Περίληψη

Ο πρόσφατος ισχυρός σεισμός μεγέθους ροπής Mw 6.3, την 3η Μαρτίου 2021, στην περιοχή της Θεσσαλίας αποτελεί μια ενδιαφέρουσα περίπτωση για την εφαρμογή της μεθόδου της επιταχυνόμενης παραμόρφωσης. Σύμφωνα με πρόσφατα ερευνητικά αποτελέσματα, η ερμηνεία της γενικευμένης παραμόρφωσης Benioff είναι δυνατό να τεκμηριωθεί με όρους Μη-Εκτατικής Στατιστικής Φυσικής και υποδεικνύει ένα κοινό κρίσιμο εκθέτη ο οποίος συμβάλει στον καθορισμό της κρίσιμης κατάστασης πριν από ένα ισχυρό σεισμό. Στην παρούσα εργασία εξετάστηκαν οι χωροχρονικές ιδιότητες της σεισμικότητας της ευρύτερης περιοχής με σκοπό να ανιχνευτούν πιθανά προσεισμικά πρότυπα, λαμβάνοντας ως παραμέτρους το χρόνο έναρξης της επιταχυνόμενης παραμόρφωσης καθώς και τη γεωμετρία και την έκταση της πιθανά κρίσιμης περιοχής. Για τον καθορισμό των σεισμών που πιθανά σχετίζονται με την υπό εξέταση σεισμική διέγερση, η περιοχή μελέτης χωρίστηκε σε τετραγωνικό πλέγμα και εξετάσθηκε η χρονική εξέλιξη της παραμόρφωσης Benioff σε κυκλικά και ελλειπτικά σχήματα στους κόμβους του πλέγματος. Παρά το ότι ο χρόνος γένεσης του σεισμού είναι γνωστός, η μελέτη πραγματοποιείται θεωρώντας τον ως μια υπό προσδιορισμό μεταβλητή. Από τα αποτελέσματα που προκύπτουν, παρουσιάζονται αυτά που έχουν την πιο σημαντική συμπεριφορά επιταχυνόμενης παραμόρφωσης καθώς και τα αποτελέσματα για μια μικρότερη σε διάμετρο κρίσιμη περιοχή τα οποία παρουσιάζουν εξίσου έντονη επιταχυνόμενη παραμόρφωση.

Λέξεις – Κλειδιά: *Επιταχυνόμενη παραμόρφωση, Θεσσαλία, σεισμός, παραμόρφωση Benioff.*

1. INTRODUCTION

A widely felt strong shallow earthquake with magnitude Mw 6.3 occurred in Thessaly (Central Greece) on March 3, 2021. This event rose scientific awareness due to the structural damages and the aftershock sequence with the several moderate and strong events during the first 48 hours. The Thessaly region exhibits faults capable for strong events up to M7.0 as that occurred in Sofades in 1954 (Papazachos and Papazachou, 2003). In this region and the surrounding areas, the dominant tectonic features are the normal faults with a NW-SE strike. According to the moment tensors of the mainshock and the two largest aftershocks occurred on 04/03/2021 and 12/03/2021 with M_w=6.0 and 5.6 respectively illustrated in Fig.1, the activated fault follows the same extensional stress regime of Thessaly region. This is also verified by the recent work of Ganas et al. (2021) where a detailed examination of the aftershock focal mechanism based on source parameters from all the available reporting agencies is presented. The moment tensors in Fig.1 since 2003 with Mw equal or larger than 4.0 are from the revised database published by the National Observatory of Athens seismic network (NOA): doi.org/10.7914/SN/HL (accessed on 02/5/2021) as well as from the Global Centroid-Moment-Tensor (GCMT) (Ekström et al., 2012).

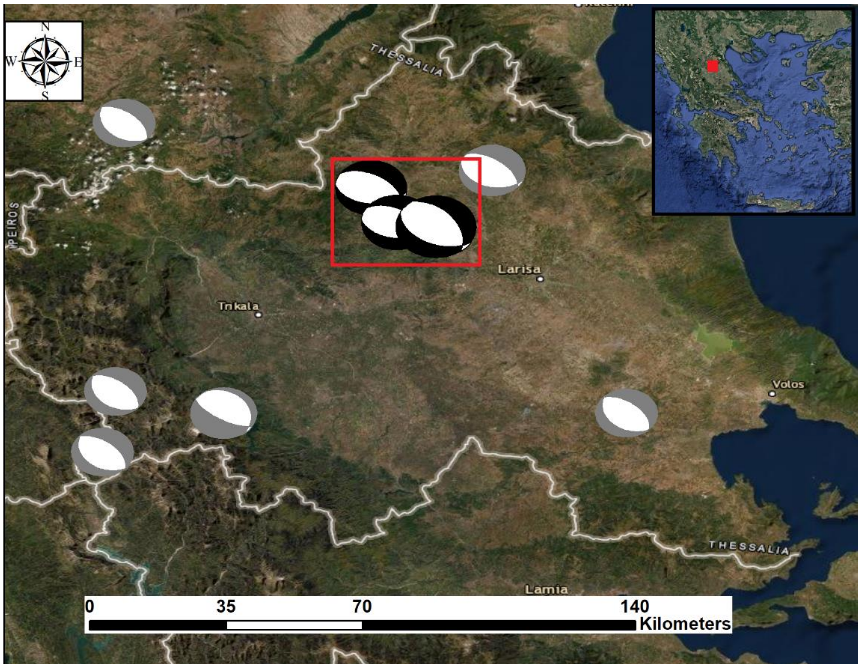

Fig.1: The moment tensors of the mainshock and the two strongest aftershocks (inside the red box) as well as of past events (noted with gray color in the surrounding region). Image from ArcGIS (www.arcgis.com, accessed on 11/07/2021), moment tensor illustration from Mirone software (Luis, 2007).

The recent large event in this area attracts our interest to apply and evaluate the applicability of the Accelerating Deformation method which is a widely used method based on the seismicity pattern observed before large events (Bufe and Varnes, 1993; Bowman et al., 1998; Papadopoulos et al 2000; Papazachos and Papazachos, 2000; Papazachos et al., 2005; Mignan and Di Giovambattista, 2008; De Santis et al., 2010 and references therein). Understanding the evolution of preseismic patterns related to the large earthquake parameters estimation and the seismic hazard mitigation is a scientific challenge. The hazard associated with large earthquakes, is attracting a vast number of researchers to study the preseismic indicators. Aiming to explain the observed seismicity patterns during the preparatory phase, theories that consider the large mainshocks as a critical point have been proposed. According to these ideas, in the deformed region, as the time progresses there is an increase in the number of events usually with moderate magnitudes, which leads to a critical point, which is the completion of this preparation process (Sornette and Sornette, 1990; Jaume, S.C., Sykes, L.R., 1999; Rundle et al., 2000). Several studies have been focused on the fractal structure and properties of the faults and the fracture process have been correlated with hierarchical scaling laws (Lapenna et al., 2000; Di Giovambattista and Tyupkin, 2001; Scholz and Aviles 2013; Vallianatos and Chatzopoulos, 2018). An innovative approach to study the collective properties of earthquakes based on *Tsallis entropy* (Tsallis, 2009; Vallianatos et al., 2016) who used a generalized concept of the Boltzmann-Gibbs statistical mechanics. Tsallis used this concept to study the seismicity as dynamical systems that exhibit memory effects, long range correlations and multifractality. Based on the Tsallis non-extensive statical physics, a theoretical model to address the scaling laws as that of Benioff strain evolution for large earthquake preparation mechanisms was proposed (Vallianatos and Chatzopoulos, 2018 and references therein). In the present work, an effort to investigate the possible seismicity patterns before the Thessaly first strong event (M_w=6.3) with the ideas of Accelerating Deformation as recently formulated in Vallianatos and Chatzopoulos (2018) is presented.

2. METHODS AND DATA

In the Accelerating Crustal Deformation method, the energy release during the preparation phase of a large earthquake expressed by an accelerating – decelerating seismic crustal deformation scalar equation (Bufe and Varnes, 1993):

$$\Omega(t) = \Omega_f - B(t_f - t)^m, \qquad \textbf{(1)}$$

where t is the preparation time before the origin time (t_f) of the termination event i.e., the mainshock, Ω_f is the cumulative strain energy at t_f while B, and m are model parameters. The critical exponent m takes values close to 0.3 for accelerating energy according to several theoretical and laboratory results (Brehm and Braile 1999; Ben-Zion and Lyakhovsky, 2002), close to 1 for background seismicity while values larger than 1 characterize deceleration seismicity patterns.

A considerable number of researchers (Bufe and Varnes, 1993; Bowman, et al., 1998; Brehm and Braile, 1999; Papazachos and Papazachos, 2000; Rundle, et al., 2000; Scordilis et al., 2004; Di Giovambattista and Tyupkin, 2004; Mignan and Di Giovambattista, 2008; De Santis et al., 2010; Papadopoulos and Minadakis, 2016 and references therein) studied the preshock seismicity patterns with the most common measuring quantity the cumulative square root of seismic energy known as Benioff strain. The cumulative Benioff strain, $\Omega(t)$ for n events at the time t:

$$\Omega(t) = \sum_{i=1}^{n(t)} E_i^{1/2}(t), \quad \textbf{(2)}$$

where E_i is the seismic energy of the to ith event. The energy can be estimated from the magnitude. The validated empirical relation energy (E) versus moment magnitude (M) for the Greek region proposed by Papazachos and Papazachos (2000), was applied:

$$\log E = 1.5 * M + 4.7. \quad \textbf{(3)}$$

To define the beginning of the acceleration period, (the time when the power law scaling starts and express the deviation from linearity which characterizes the background seismicity pattern) the Curvature parameter (Cp) have been proposed by Bowman et al. (1998):

$$Cp = (Power\ law\ fit\ RMS)/(Linear\ fit\ RMS). \quad \textbf{(4)}$$

As the Cp becomes smaller approaching to zero, the scaling law behavior becomes dominant and a typical value less than 0.70 have been suggested by Bowman et al. (1998) as a robust indication of accelerating seismicity.

In the recent work of Vallianatos and Chatzopoulos (2018), analytical expressions with terms of Non-Extensive Statistical Physics (NESP) have been formulated to propound a theoretical framework that describes the physical processes of the energy flow and accumulation inside a crustal volume. The NESP ideas considered as a suitable approach as they can explain the long-range temporal dependence of seismicity in a fault system that obeys a hierarchical distribution (Scholz and Aviles, 2013; Michas et al., 2015). Vallianatos and Chatzopoulos (2018) introduced the generalized cumulative Benioff deformation,

$$\Omega_\xi(t) = \sum_{i=1}^{n(t)} E_i^{\xi}(t), \quad \textbf{(5)}$$

where $0 \leq \xi \leq 1$. When the energy exponent ξ is equal to 0, then the quantity $\Omega_0(t)$ is the cumulative number of earthquakes till the time t. For ξ equal to 0.5, the $\Omega_{0.5}(t)$ is the well-known cumulative Benioff strain while for ξ equal to 1, the quantity $\Omega_1(t)$

represents the cumulative energy released. They applied a non-extensive statistical physics approach and concluded to the equivalent power law equation:

$$\Omega_{\xi}(t) = \Omega_{\xi f} - B(t_f - t)^{m_{\xi}}, \qquad \textbf{(6)}$$

where t is the time before the time of failure t_f and when $t = t_f$ the Ω_{ξ} is equal to $\Omega_{\xi}(t_f)$, B is a model parameter and m_{ξ} is the critical exponent. This approach suggests that during the accelerating seismic pattern for $0 \leq \xi \leq 1$ there is a common critical exponent $m_{\xi} \approx 0.30$ which is independent of the ξ-value of the generalized Benioff strain $\Omega_{\xi}(t)$.

According to Vallianatos and Chatzopoulos (2018), the entropy parameter q determines the cumulative fractal distribution of seismic subvolumes of preshocks inside a stressed crustal volume V, with fractal dimension $d = d_e \frac{2-q}{q-1}$, where d_e the Euclidean dimension. Following the equation 10c of Vallianatos and Chatzopoulos, (2018):

$$m_{\xi} = \alpha(d_e - 1 - d) + 1 \qquad \textbf{(7)}$$

the m_{ξ} depends on the Euclidean dimension d_e of the stressed crustal volume V of the earthquake preparation region and the NESP entropy parameter q. By considering a 3D spatial distribution $(d_e = 3)$ of EQs during the preparation phase $\left(t < t_f\right)$ the entropy parameter is constrained to take values between $\frac{7}{4}$ and 2 whereas for the 2D case (e.g., a very shallow seismogenic layer) the entropy parameter is constrained to values $\frac{5}{3} < q < 2$ (Vallianatos and Chatzopoulos, 2018). In any case, the earthquake source region is a complex, sub-additivity seismic system characterized by long-range temporal correlations among earthquakes.

Based on the remark that there is common critical exponent m_{ξ}, which is independent of the ξ, the M_w=6.3 (March 3, 2021) mainshock occurred in Thessaly has been examined for the existence of accelerating seismicity patterns. Although, this analysis has been carried out in a retrospective manner and the time of failure (t_f) is already known, the latter did not take a fixed value, and it has been estimated from the algorithm along with the other power law relation parameters. The aim was to examine all the possible variables such as the starting time of the accelerating seismicity pattern as well as the size and the location of the critical area in order to evaluate them along with the estimated t_f.

Since no recent large earthquakes occurred in the broad region under investigation, to pursuit the starting time and define the acceleration period, it was necessary to use an earthquake catalogue with long time history. Based on the previous published work for the Accelerating Deformation method (Papazachos and Papazachos, 2000; Di Giovambattista and Tyupkin, 2004; Papazachos et al., 2005), a few years to a couple of decades is reported as a typical duration of the preparatory phase for an event of such a magnitude. To this end, as time, t elapses since 2005, a cumulative procedure with a monthly iteration step was implemented to study the recent strong event in Thessaly. The generalized Benioff strain analyses were conducted on the earthquake catalogue provided by the Permanent Regional Seismological Network operated by the Aristotle University of Thessaloniki, registered in the International Federation of Digital Seismograph Networks with doi:10.7914/SN/HT (accessed on 02/05/2021). This is an open access manually revised catalogue, and it has been adopted for this research. The earthquake catalogue is the input data for the Accelerating Deformation method. Its quality relies on the data completeness and its accuracy on the of the earthquake parameters (epicenter, origin time, depth).

The data completeness of the catalogue has been carried out by examining the Magnitude of completeness, M_c which is based on Gutenberg-Richer law and defines the lowest magnitude value of a dataset in which all earthquakes were detected (Mignan and Woessner, 2012). The spatial variation of M_c for the examined period (since 2005) and region (descripted in the next paragraph) is much less than 3.0, calculated using geographical coordinates with grid size 0.1 degrees with 50 events and 50 bootstraps method with the “best combination” option in ZMAP software (Wiemer, 2001) which uses the Max Curvature, Goodness of Fit 90 and 95% confidence techniques (Wyss et al., 2001). The temporal variations of M_c for the research area present a peak close to 3.1 in the end of 2008. Considering the M_c examination results, a range cut-off for the earthquake magnitudes, Mcut with values from 4.9 down to 3.2 was applied to investigate the possible seismicity patterns based on the Mcut changes. Furthermore, due to inherent significant uncertainty of earthquakes depths, posing a depth parameter limit to refine the earthquake catalogue may have negative impact to the identification of the accelerated crustal volume. Thus, different depth cut-off values (Dcut) were tested, starting from 25 km down to 40 km, with an iteration mode, initially with a 5 km step and afterwards with a 2.5 km.

Towards identifying the location of the deformed crustal volume that presents critical point characteristics, the broader region around the epicenter of the mainshock (from

N38.50° to N41.0° and from E21.00° to E23.50°) was initially divided in a square mesh with 0.05 degrees size as a first approximation search to point out the locations with a possible result. Subsequently the search was repeated with a denser square mesh (0.02 degrees size) around these locations with a preliminary seismic pattern identification. In this way, the processing time as well as the computing power needed for algorithm to carry out the whole iterative procedure, were dramatically reduced. At every mesh point, an iterative expanding circular area was shaped with the use of the Euclidean distance to find the surrounding events. The circle varies in diameter from 40 to 300 km with an initial step 4 km which was reduced to 2 km for a more comprehensive second scan. Earth's shape was considered in the calculations of distances. In an attempt to reveal directional (strike) properties of the critical area, resulted from the above circular (symmetrical) approximation, the iterative algorithm continues using elliptical shapes. Around the center of the identified circular critical area, an ellipse is tried out, using the same parameters such as time window, magnitude and depth cut-offs values. The size of the ellipses axes has been set to take values from 40 km up to 300 km with a 4 km step and the primary axis is rotated in the horizontal plane from 0 to 180 degrees with a 15 degrees step.

Regarding the application of Curvature parameter criterion, the seismic pattern solutions were initially screened with $C_p \leq 0.55$, which is a rational value based on the experience built-up by examining other case studies, and on-going analysis to narrow down the results led to $C_p \leq 0.50$, as lower Cp-values indicate higher degree of deviation from the background seismicity. To achieve a valid regression analysis, both for power law and linear fittings, the minimum number of events in a possible seismic pattern solution was set to 30. During the mesh scan, when the latter statistical threshold was satisfied for the events around a point, then the algorithm performed three individual sets of power law and linear fitting, one for each ξ generalized Benioff strain function exponent 0, 0.5 and 1. Preliminary identifications were considered those who exhibited critical exponents, m_ξ with values 0.30±0.05 for the same time-window, circle size and number of events. Among these solutions, to retrieve those with the more accurate regression analysis, and since the algorithm delivers three sets of power law - linear fittings and three Cp-values, the results that did not demonstrate the smallest Curvature parameter mean value were filtered out. Furthermore, adopting the reasonable seismological hypothesis that the seismicity associated with the critical phenomenon is expected to be spatially concentrated, between the results with the same Cp mean-value, the ones delivering the smallest critical areas have been selected. Lastly, to examine the quality and robustness of the power law fitting, the square of the Pearson correlation coefficient (r) was used between each cumulative quantity ($\Omega_\xi(t)$)

and the corresponding power law fitting and accepted results were considered the ones that presented $r \geq 0.977$.

3. RESULTS

The first approach to identify the stressed critical volume with circular areas around a mesh point demonstrated values for Mcut from 3.2 up to 3.6. The analysis showed that all the circle centers with a possible solution form two clusters and are located north of the mainshock's epicenter while the majority of the associated events are North-Westerly from the epicenter. The possible solutions produced, present circles with diameter ranging from 190 to 280 km. The best two (with the lowest mean Cp value) circular seismic pattern solutions for the largest Mcut available (Mcut=3.6) are comparatively presented and discussed here.

The first one, (named hereafter as CAA) focuses on the overall smallest Cp mean-value while the other one (named hereafter as CAB) is aftermath of constraining circle diameter up to 200 km. The circular critical area A achieved $m_\xi = 0.30 \pm 0.05$ with the lowest Cp mean-value along with its generalized Benioff strain power law and linear fitting with ξ-values 1, 0.5 and 0 are presented in Fig. 2. The circle center has geographical coordinates N40.40°, E22.00° and the circle diameter is 252 km, the latter to be perceived as an indicative numerical result and not an exact value of a seismotectonic feature or behavior. The determined time window of accelerating seismicity (the main earthquake preparation period) for this solution includes events since the second half of 2009. The circular critical area CAB resulted by posing upper limit to its size, again along with its generalized Benioff strain power law and linear fitting for ξ values 1, 0.5 and 0 respectively and critical exponent $m_\xi = 0.30 \pm 0.05$ are illustrated in Fig. 3. The circle center has now geographical coordinates N40.74°, E21.64°, moved ~48 km away and heading NW 320° from that of CAA solution, the circle diameter is 192 km and the time window includes events since the second quarter of 2008. For the shake of completeness, the seismicity in the investigated broad region around the main event which has not been correlated with the critical area since 2008, is also presented in both figures (illustrated with black circles). It comprises events with local magnitude equal to or greater than Mcut =3.6 up to 5.0. Based on the n extensive experimentation and trials on other studied cases, the generalized Benioff strain with ξ=1 (the release of cumulative of seismic energy) usually achieves a better estimation for the occurrence time of failure (t_f). This consistency concept appears also in this research, where for the solution CAA the cumulative energy release has the more accurate estimation of failure time (08-Mar-2021) (Fig. 2b) just a few days after the actual occurrence time of the strong earthquake while for CAB solution provides an estimation of t_f a few weeks ahead (23-Mar-2021) (Fig. 3b).

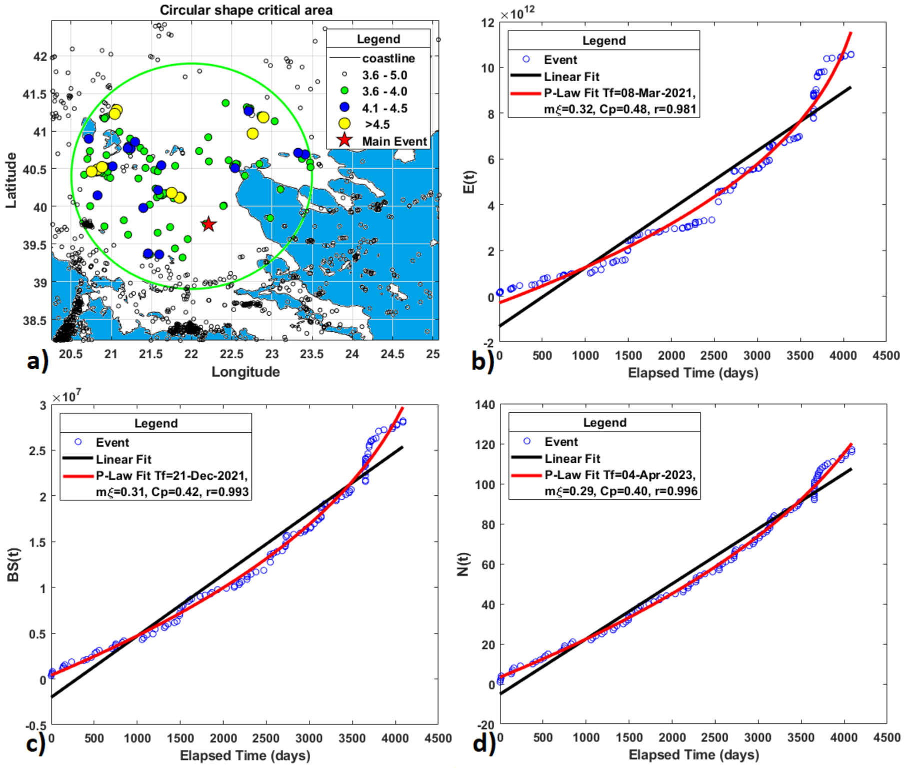

Fig. 2: a) Map with the circular critical area approach based on mean Cp criterion as well as the rest seismicity (see text for details). The first strong earthquake is denoted with a red star while the magnitudes of the events associated with the critical area are represented with circles with different color and size. The generalized Benioff strain (red curve) and the linear fitting (black line) for: b) the cumulative energy released (ξ=1); c) the cumulative Benioff strain (ξ=0.5); d) cumulative number of earthquakes (ξ=0).

The robustness of the solution CAA is justified by the results acquired by selecting Mcut equal to 3.5, thus more earthquakes are included. A similar seismic pattern solution was produced with the same geographical coordinates and size of circular critical area but the estimation of failure time (19-02-2021) is almost two weeks before of that of the CAA solution. By selecting Mcut equal to 3.4, the solution is compatible to CAA, the circle center has geographical coordinates N40.54, E21.74, circle diameter 198 km while the estimation of failure time is just a week before of that of CAA. The application of the depth cut off filter on the studied earthquake catalogue proved to have no influence on the CAA and CAB solutions as all the events associated with their determined critical areas are featured by shallower hypocenters.

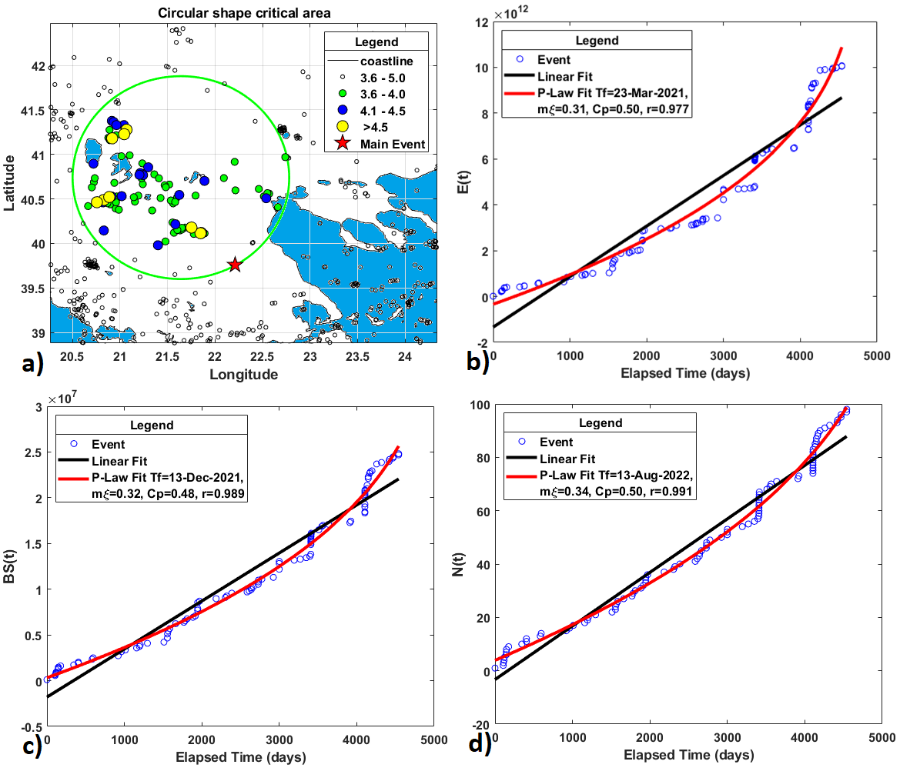

Fig. 3: a) Map with the circular critical area approach with the small radius as well as the rest seismicity (see text for details). The first strong earthquake is denoted with a red star while the magnitudes of the events associated with the critical area are represented with circles with different color and size. The generalized Benioff strain (red curve) and the linear fitting (black line) for: b) the cumulative energy released (ξ=1); c) the cumulative Benioff strain (ξ=0.5); d) cumulative number of earthquakes (ξ=0).

An additional alternative effort to evaluate the validity of the obtained results and yet more to reveal the long-range correlations in seismicity of a critical crustal volume under accelerating deformation was exercised by searching the area for seismicity patterns with different, earlier than the main event, ending dates. The earthquake catalogue was shrunk from its bottom (events backward in time were progressively removed) as the ending date of the catalogue was successively sent to the past with an iterative 10-day step. This method pushes artificially the seismic pattern identification iterative procedure in a previous date. At every iteration, a monthly iteration step since 2005 was implemented to point out the starting point for the accelerating deformation period but this time with a "new" ending point moved further in the past of the main event's actual occurrence time. This iterative catalogue reduction test showed that the obtained results were the same since 10-Aug-2020 signifying that after that date there were no new events with magnitude equal or larger than Mcut in the identified critical area.

Taking the aforesaid iteratively optimized results for the circular critical area approximation into account, the same algorithmic procedure with an elliptical (asymmetric) approximation was applied. This approach aims to investigate probable striking properties of the critical seismic area subjected by a non-uniform stress regime, as in the case of Thessaly basin being under a regional extensional stress with N-S direction (Caputo, and Pavlides, 1993). To this end, the critical area search with the elliptical shape approximation, was executed in a region limited around the previous solutions using the same time-window and criteria (m_{ξ} = 0.30±0.05, Cp ≤0.50, D_{cut}, M_{min} = 3.6, and r ≥0.977). Again, the results obtained by applying the smallest Curvature Parameter mean-value criterion. The elliptical critical area identified, adopting the CAA solution parameters, along with the generalized Benioff strain power law and linear fittings with ξ-values 1, 0.5 and 0 respectively, are depicted in Fig. 4. The elliptical area center has geographical coordinates N40.44° and E22.08° (compatible with those of CAA), the principal axes have lengths 268 km and 244 km respectively, and the ellipse azimuth is 0 degrees. The estimated time of failure (01-04-2021) based on the cumulative energy release (ξ=1) (Fig. 4b) is almost a month later than the actual, so much less successful than of CAA. The results from this analysis do not significantly improve the image of the critical area and they do not point out any prominent striking as the output ellipse is practically a circle (flattening value 0.09).

The elliptical critical area identified, adopting the CAB solution parameters, along with the generalized Benioff strain power law and linear fittings with ξ-values 1, 0.5 and 0 respectively, are depicted in Fig. 5. The elliptical area center has geographical coordinates N40.40°, E21.64° (moved ~33 km to the south from that of CAB south and surprisingly matching the geographical latitude of the center of both the circle and ellipsis from CAA), the principal axes have lengths 256 km and 164 km, respectively, and the ellipsis azimuth is 165 degrees. The estimated time of failure (02-03-2021) is the most accurate one among the all the results, always coming out from the generalized Benioff strain with ξ=1 (Fig. 5b).

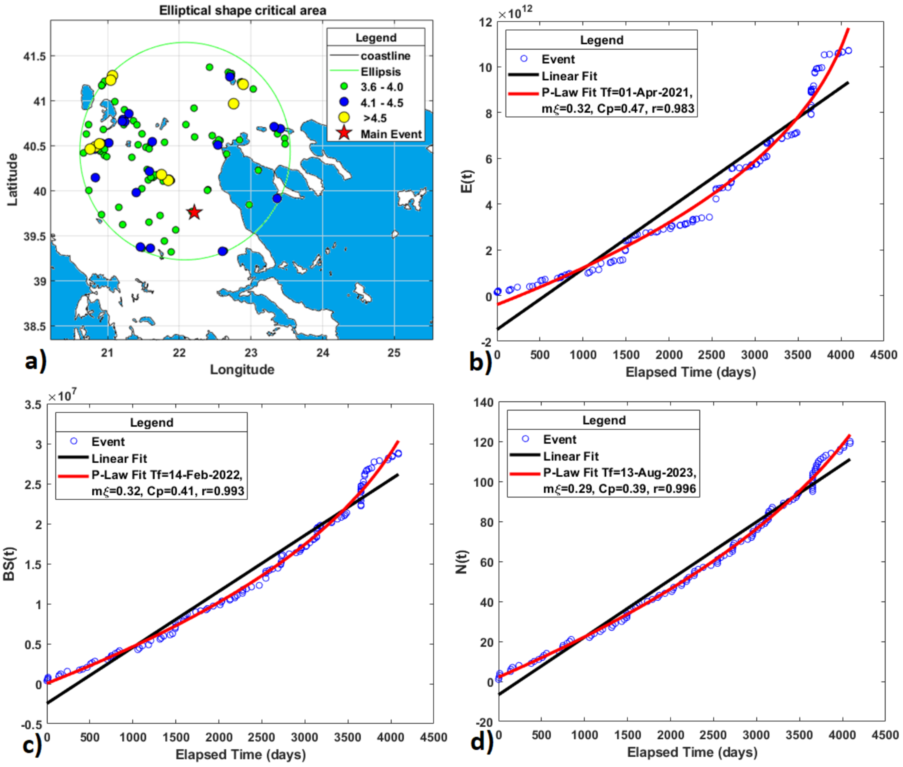

Fig. 4: a) Map with the elliptical critical area approach based on 'CAA' solution. The first strong earthquake is denoted with a red star while the magnitudes of the events associated with the critical area are represented with circles with different color and size. The generalized Benioff strain (red curve) and the linear fitting (black line) for: b) the cumulative energy released (ξ=1); c) the cumulative Benioff strain (ξ=0.5); d) cumulative number of earthquakes (ξ=0).

4. CONCLUDING REMARKS

Following a complex spatiotemporal iterative procedure to examine the possible seismicity patterns, it is shown that the recently proposed ideas for the generalized Benioff strain can explain and identify accelerating seismicity patterns before the M_w=6.3 strong Thessaly earthquake. The generalized Benioff strain with the common critical exponent criterion $m_\xi = 0.30 \pm 0.05$ can provide results for different earthquake magnitude cut-off values. The Mcut investigation for the possible seismicity patterns shown that small changes in the Mcut value will present results with similar identified critical area spatial properties but the larger Mcut values appear to have more accurate results in terms of time of failure estimation. Thus, setting the Mcut value to allow smaller magnitudes then it is necessary to enhance the searching resolution details and in this case the quality of the catalogue has to be considered.

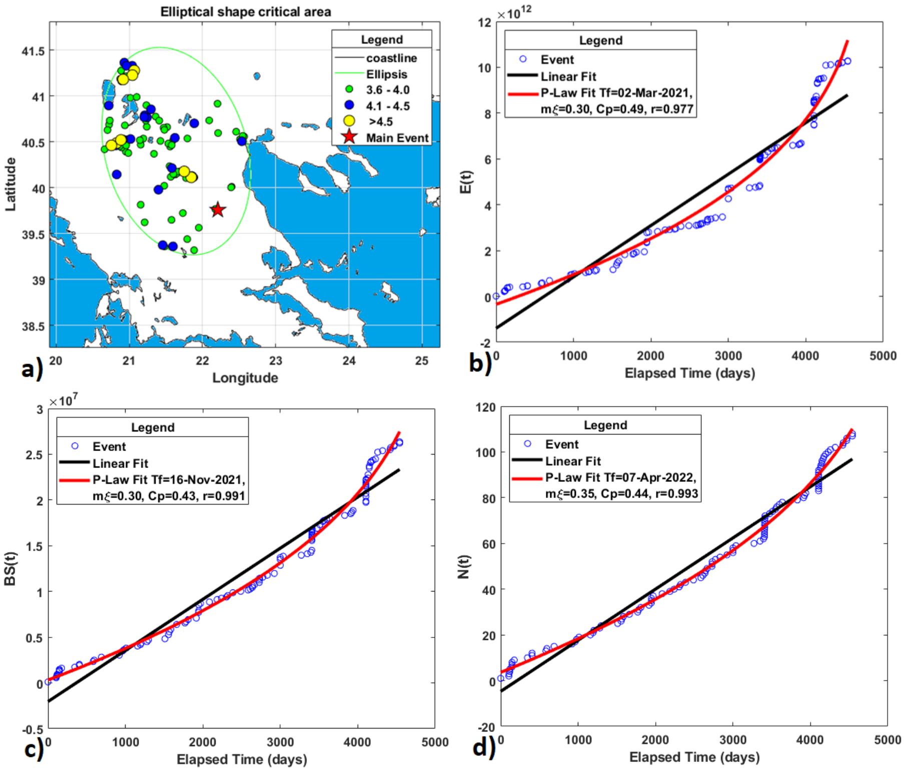

Fig. 5: a) Map with the elliptical critical area approach based on 'CAB' solution. The first strong earthquake is denoted with a red star while the magnitudes of the events associated with the critical area are represented with circles with different color and size. The generalized Benioff strain (red curve) and the linear fitting (black line) for: b) the cumulative energy released (ξ=1); c) the cumulative Benioff strain (ξ=0.5); d) cumulative number of earthquakes (ξ=0).

A number of criteria have been applied to improve the solutions robustness. The mean-value Curvature parameter criterion Cp $\leq$0.50 defines a critical area dominant scaling law behavior while the square of the Pearson correlation coefficient ($r \geq$0.977) helps to have accurate fittings. The successive stage procedure to search first for circular and then for elliptical shape critical areas aims to reduce the processing time and increase the computing power efficiency.

The time of failure estimation obtained from the power law fitting for the present Accelerating Deformation study case, is better for ξ=1 (cumulative seismic energy) as it is closer to the actual occurrence time of the mainshock. The rest ξ exponents (ξ=0.5 and 0) provide a not so accurate time of failure estimation. Based on the experience built-up by examining other case studies, the rest ξ exponents usually estimate the time of failure in the more distant future, but for this case the difference between estimations is significant. This is a matter that will be addressed again in a future work with more examples.

Both approaches (symmetrical and non-symmetrical), applied successively, produce compatible results. The CAA and CBB best solutions for circular (symmetrical) critical areas provide results with similar spatiotemporal properties. As the elliptical (non-symmetrical) approximation is subsequently applied on the outputs of the best circular areas, the constrained circle size of CBB favors the asymmetric approach results. The results for the asymmetrical (elliptical) approximation for CAA solution point out as the best option an ellipsis with small flattening (0.09) which has an estimation for failure time almost a month later than the actual origin time. On the contrary, the elliptical approach for CAB solution appears to provide the most promising result. The majority of the events associated with the critical area and the mainshock are concentrated in a narrow area with NW-SE strike and North-Westerly of the mainshock's epicenter. The ellipse for CAB solution follows the Thessaly basin regional extensional stress regime and has the most accurate estimated time of failure.

5. ACKNOWLEDGMENTS

This research is co-financed by Greece and the European Union (European Social Fund-ESF) through the Operational Programme «Human Resources Development, Education and Lifelong Learning» in the context of the project "Reinforcement of Postdoctoral Researchers - 2nd Cycle" (MIS-5033021), implemented by the State Scholarships Foundation (IKY).

6. REFERENCES

Ben-Zion, Y. and Lyakhovsky, V., 2002. Accelerated Seismic Release and Related Aspects of Seismicity Patterns on Earthquake Faults. *Pure and Applied Geophysics*, 159, 2385–2412 https://doi.org/10.1007/s00024-002-8740-9

Bowman, D. D., Quillon, G., Sammis, C.G., Sornette, A. and Sornette, D., 1998. An observational test of the critical earthquake concept. *Journal of Geophysical Research*, 103, 24359 – 24372 doi:10.1029/98JB00792.

Brehm, D.J., and Braile, L.W., 1999. Refinement of the modified time-to-failure method for intermediate-term earthquake prediction. *Journal of Seismology*, 3, 121 – 138. https://doi.org/10.1023/A:1009859431834

Bufe, C.G. and Varnes, J.D., 1993. Predictive Modeling of the Seismic Cycle of the Greater San Francisco Bay Region. *Journal of Geophysical Research*, 10, 9871–9883.

Caputo, R. and Pavlides, S., 1993. Late Cainozoic geodynamic evolution of Thessaly and surroundings (central-northern Greece). *Tectonophysics*, 223, 3–4, 339-362.

Di Giovambattista, R. and Tyupkin, Y., 2001. An analysis of the process of acceleration of seismic energy emission in laboratory experiments on destruction of rocks and before strong earthquakes on Kamchatka and in Italy. *Tectonophysics*, 338, 339–351.

Di Giovambattista, R. and Tyupkin, Y., 2004. Seismicity patterns before the M=5.8 2002, Palermo (Italy) earthquake: seismic quiescence and accelerating seismicity. *Tectonophysics*, 384, 243 - 255.

De Santis, A., Cianchini, G., Qamili, E. and Frepoli, A., 2010. The 2009 L'Aquila (Central Italy) seismic sequence as a chaotic process. *Tectonophysics*, 496, 44–52.

Ekström, G., Nettles, M. and Dziewonski, A.M., 2012. The global CMT project 2004-2010: Centroid-moment tensors for 13,017 earthquakes. *Physics of the Earth and Planetary Interiors,* 200-201, 1-9, doi: 10.1016/j.pepi.2012.04.00

Ganas, A., Valkaniotis, S., Briole, P., Serpetsidaki, A., Kapetanidis, V., Karasante, I., Kassaras, I., Papathanassiou, G., Karamitros, I., Tsironi, V., Elias, P., Sarhosis, V., Karakonstantis, A., Konstantakopoulou, E., Papadimitriou, P., & Sokos, E.,2021. Domino-style earthquakes along blind normal faults in Northern Thessaly (Greece): kinematic evidence from field observations, seismology, SAR interferometry and GNSS. *Bulletin Geological Society of Greece*, 58, 37-86. https://doi.org/10.12681/bgsg.27102

Jaumé S.C., Sykes L.R. 1999. Evolving Towards a Critical Point: A Review of Accelerating Seismic Moment/Energy Release Prior to Large and Great Earthquakes. In: Wyss M., Shimazaki K., Ito A. (eds) Seismicity Patterns, their Statistical Significance and Physical Meaning. Pageoph Topical Volumes. Birkhäuser, Basel. https://doi.org/10.1007/978-3-0348-8677-2_5

Lapenna V., Macchiato M., Piscitelli S., Telesca L. 2000. Scale-invariance Properties in Seismicity of Southern Apennine Chain (Italy). In: Blenkinsop T.G., Kruhl J.H., Kupková M. (eds) Fractals and Dynamic Systems in Geoscience. Pageoph Topical Volumes. Birkhäuser, Basel. https://doi.org/10.1007/978-3-0348-8430-3_7

Luis, J., 2007. Mirone: A multi-purpose tool for exploring grid data. Computers & Geosciences, 33, 31-41.

Michas, G., Vallianatos, F., Sammonds, P., 2015. Statistical Mechanics and scaling of fault population with increasing strain in the Corinth Rift. *Earth Planetary Science Letters*, 431, 150–163 https://doi.org/10.1016/j.epsl.2015.09.014 .

Mignan, A. and Di Giovambattista, R., 2008. Relationship between accelerating seismicity and quiescence, two precursors to large earthquakes. *Geophysical Research Letters*, 35, L15306 doi:10.1029/2008GL035024.

Mignan, A. and Woessner, J., 2012. Estimating the magnitude of completeness for earthquake catalogs. *Community Online Resource for Statistical Seismicity Analysis*, Version: 1.0, pp. 1 – 45.

Papadopoulos, G.A., Drakatos, G. & Plessa, A., 2000. Foreshock activity as a precursor of strong earthquakes in Corinthos Gulf, Central Greece. *Physics and Chemistry of the Earth, Part A: Solid Earth and Geodesy*, 25(3), 239 - 245.

Papadopoulos, G.A. and Minadakis, G., 2016. Foreshock Patterns Preceding Great Earthquakes in the Subduction Zone of Chile. *Pure and Applied Geophysics*, 173, 3247–3271. https://doi.org/10.1007/s00024-016-1337-5

Papazachos, B. and Papazachos, C., 2000. Accelerated Preshock Deformation of Broad Regions in the Aegean. *Pure and Applied Geophysics*, 157, 1663–1681.

Papazachos, B. and Papazachou, K. 2003. The earthquakes of Greece. Ziti Publications, Thessaloniki, Greece, 286 pp.

Papazachos, C. B., Karakaisis , G. F., Scordilis, E. M. & Papazachos, B. C., 2005. Global observational properties of the critical earthquake model. *Bulletin of the Seismological Society of America*, 95(10), 1841 – 1855.

Rundle, J.B., Klein, W., Turcotte, D.L. and Malamud, B.D., 2000. Precursory Seismic Activation and Critical-point Phenomena. *Pure and Applied Geophysics*, 157, 2165–2182. https://doi.org/10.1007/PL00001079

Scholz, C.H. and Aviles, C.A. 2013. The Fractal Geometry of Faults and Faulting. In: Earthquake Source Mechanics AGU Geophysical Monograph Series, Das, S., Boatwright, J., Scholz, C.H., (Eds.), AGU 100: Washington, DC, USA, 37, 147–155.

Scordilis, E.M., Papazachos, C.B., Karakaisis, G.F. and Karakostas, V.G., 2004. Accelerating seismic crustal deformation before strong mainshocks in Adriatic and its importance for earthquake prediction. *Journal of Seismology*, 8, 57 – 70.

Sornette, A. and Sornette, D., 1990. Earthquake rupture as a critical point: consequences for telluric precursors. *Tectonophysics*, 179, 327 - 334.

Tsallis, C., 2009. Introduction to Nonextensive Statistical Mechanics - Approaching a Complex World. Springer- Verlag, New York, 382 pp., doi: 10.1007/978-0-387-85359-8

Vallianatos F., Michas G., Papadakis G. 2016. A Description of Seismicity Based on Non-extensive Statistical Physics: A Review. In: D'Amico S. (eds) Earthquakes and Their Impact on Society. Springer Natural Hazards. Springer, Cham. https://doi.org/10.1007/978-3-319-21753-6_1

Vallianatos, F. and Chatzopoulos, G., 2018. A Complexity View into the Physics of the Accelerating Seismic Release Hypothesis: Theoretical Principles. *Entropy*, 20(10):754, doi.org/10.3390/e20100754

Wiemer, S., 2001. A software package to analyze seismicity: ZMAP. *Seismological Research Letters*, 72(3), pp.373-382 https://doi.org/10.1785/gssrl.72.3.373

Wyss, M., Wiemer, S. and Zuniga, R., 2001. ZMAP A tool for analyses of seismicity patterns, Typical Applications and Uses: A Cookbook.

BGSG

Volume 58

Research Paper

Correspondence to:
Maria Kouli
mkouli@hmu.gr

DOI number:
http://dx.doi.org/10.12681/bgsg.27058

Keywords:
Thessaly earthquake; Land Surface Temperature; RETIRA; thermal anomalies

Citation:
Kouli, M., Peleli,S., Saltas, V., Makris, J.P. and Valianatos, F. (2021), Robust Satellite Techniques for Mapping Thermal Anomalies Possibly Related to Seismic Activity of March 2021, Thessaly Earthquakes. Bulletin Geological Society Greece, 58, 105-130.

Publication History:
Received: 18/05/2021
Accepted: 05/08/2021
Accepted article online: 07/08/2021

The Editor wishes to thank two anonymous reviewers for their work with the scientific reviewing of the manuscript and Ms Emmanouela Konstantakopoulou for editorial assistance.

ROBUST SATELLITE TECHNIQUES FOR MAPPING THERMAL ANOMALIES POSSIBLY RELATED TO SEISMIC ACTIVITY OF MARCH 2021, THESSALY EARTHQUAKES

Maria Kouli [1,2*], Sofia Peleli [1,2], Vassilis Saltas [1,2], John P. Makris [1,2], Filippos Vallianatos [1,3]

[1] Institute of Physics of the Earth’s Interior & Geohazards, UNESCO Chair on Solid Earth Physics and Geohazards Risk Reduction, Hellenic Mediterranean University Research Center, Romanou 3, 73133 Chania, Crete, Greece; saltas@hmu.gr, jpmakris@hmu.gr, sofia.peleli@gmail.com,fvallian@hmu.gr

[2] Hellenic Mediterranean University, Faculty of Electronic Engineering, Romanou 3, Chania, Crete, Greece

[3] National and Kapodistrian University of Athens, Faculty of Geology and Geoenvironment, Department of Geophysics and Geothermics, Athens, 15784 Panepistimiopolis fvallian@geol.uoa.gr

*Correspondence: mkouli@hmu.gr; Tel.: +302821023016

Abstract

In recent years, there is a growing interest concerning the development of a multi-parametric system for earthquakes’ short term forecast identifying those parameters whose anomalous variations can be associated to the complex process of such events. In this context, the Robust Satellite Technique (RST) has been adopted herein with the aim to detect and map thermal anomalies probably related with the strong earthquake of M6.3 occurred near the city of Larissa, Thessaly on March 3rd 2021 10:16:07 UTC. For this purpose, 10 years (2012-2021) of daily Night-time Land Surface Temperature (LST) remotely sensed data from Moderate Resolution Imaging Spectroradiometer (MODIS), were analyzed. Pixels characterized by statistically significant LST variations on a daily scale were interpreted as an indicator of variations in seismic activity. Quite intense (Signal/Noise ratio > 2.5) and rare, spatially extensive and time persistent, TIR signal transients were identified, appearing twenty five days before the Thessaly main shock (pre-seismic anomalies: February 6th, February 11th March 1st), the day of the main earthquake (co-seismic anomaly) and after the main shock (post-seismic anomalies: March 4th, 10th and 17th). The final dataset of thermal anomalies *was combined with geological and structural data of the area of interest, such as active faults, composite seismogenic sources, earthquake epicenter and topography in order to perform preliminary spatial analysis.*

Keywords: *Thessaly earthquake; Land Surface Temperature; RETIRA; thermal anomalies.*

Περίληψη

Τα τελευταία χρόνια, υπάρχει ένα αυξανόμενο ενδιαφέρον σχετικά με την ανάπτυξη ενός πολυπαραμετρικού συστήματος βραχυπρόθεσμων προβλέψεων σεισμικών γεγονότων συσχετίζοντας τα τελευταία με ανώμαλες μεταβολές παραμέτρων όπως είναι η θερμοκρασία. Σε αυτό το πλαίσιο, η Εύρωστη Δορυφορική Τεχνική (Robust Satellite Technique-RST) έχει υιοθετηθεί εδώ με σκοπό την ανίχνευση και χαρτογράφηση πιθανών θερμικών ανωμαλιών που σχετίζονται χωροχρονικά με τον ισχυρό σεισμό μεγέθους M6.3 που συνέβη 20 km ΒΔ της πόλης της Λάρισας, στις 3 Μαρτίου 2021 και ώρα 10:16:07 UTC. Το σύνολο των δεδομένων που αναλύθηκε καλύπτει μια χρονική περίοδο δέκα ετών (2012-2021) νυχτερινών καταγραφών LST (Land Surface Temperature) του φασματοραδιόμετρου MODIS (Moderate Resolution Imaging Spectroradiometer). Τα εικονοστοιχεία που χαρακτηρίζονται από στατιστικά σημαντικές μεταβολές LST σε καθημερινή κλίμακα ερμηνεύθηκαν ως πιθανοί δείκτες διακυμάνσεων της σεισμικής δραστηριότητας. Αρκετά έντονες θερμικές ανωμαλίες με λόγο σήματος προς θόρυβο μεγαλύτερο του 2.5 και σπάνιες, χωρικά εκτεταμένες και χρονικά ανθεκτικές θερμικές μεταβολές εμφανίζονται 25 ημέρες πριν από το κύριο σεισμό της Θεσσαλίας και συγκεκριμένα την 6η Φεβρουαρίου, 11η Φεβρουαρίου και 1η Μαρτίου, την ημέρα του κύριου σεισμού καθώς και έως και 14 ημέρες μετά τον κύριο σεισμό (μετασεισμικές ανωμαλίες την 4η, 10η και 17η Μαρτίου). Το σύνολο των θερμικών ανωμαλιών συνδυάστηκε με άλλα δεδομένα, όπως η γεωλογία, η τοπογραφία, τα ενεργά ρήγματα και οι σύνθετες σεισμικές πηγές της περιοχής ενδιαφέροντος προκειμένου να πραγματοποιηθεί μια προκαταρκτική χωρική ανάλυση.

Λέξεις-κλειδιά: *Σεισμός Θεσσαλίας; Θερμοκρασία Εδάφους; Εύρωστη Δορυφορική Τεχνική (Robust Satellite Technique-RST); δείκτης RETIRA; θερμικές ανωμαλίες.*

1. INTRODUCTION

Looking toward the assessment of a multi-parametric system for tectonic deformations’ short term (from days to weeks) forecast, a preliminary step is to identify those parameters (chemical, physical, biological, etc.) whose anomalous variations can be, to some extent, associated to the complex process of preparation of such a tectonic event (Genzano et. al., 2020). A candidate parameter for integration in such a multiparametric system should: i) be selected on the basis of experimental observations, ii) be measurable with sufficient space-time continuity, iii) exhibit space-time transients (potentially related to earthquakes) identifiable through clear, scientifically founded and repeatable data analysis techniques and iv) exhibits a non-occasional relation between space-time transients and earthquake characteristics (e.g. time, position, magnitude) (Genzano et al., 2020).

Among the different parameters, the fluctuations of Earth's thermally emitted radiation, as measured by sensors on board of satellite systems operating in the Thermal Infra-Red (TIR) spectral range has been proposed since long time as a potential precursor. Satellite remote sensing enables the estimation of Land Surface Temperature (LST) over wide areas and especially in sites with different land surface characteristics such as vegetation cover, topography, lithology, tectonic structure and geomorphometry, with a variable spatio-temporal resolution depending on the selected satellite/sensor system (Li et al., 2013). Satellite sensors, as MODIS (Moderate Resolution Imaging Spectroradiometer), having channels in the infrared region of the electromagnetic spectrum, enable the monitoring of the Earth’s thermal field at a moderate spatial resolution (Lillesand et al., 1987; Anderson et al., 2012; Vollmer and Möllmann, 2017). As a result, LST can greatly contribute to the understanding of land surface processes in various scales (from local to global) (Brunsell and Gillies, 2003; Anderson and Kustas, 2008; Kustas and Anderson, 2009; Karnieli et al., 2010; Ganas et al., 2010; Keramitsoglou et al., 2011; Zhang et al., 2014; Christman et al., 2016; Scambos et al., 2018; Eleftheriou et al., 2016b; Aguilar-Lome et al., 2019; Athanasiadou et al.,2020; Peleli et al., 2021).

Since 2001, a general approach called Robust Satellite Techniques (RST) (Tramutoli et al., 2001; 2005; 2007) has been used to discriminate anomalous thermal signals, possibly associated to tectonic activity from normal fluctuations of Earth's thermal emission related to other causes. The RST considers each anomaly in the space-time domain as a deviation from a normal state that can be defined by processing multi-year time series of homogeneous (e.g., same month, same spectral channel/s; same overpass times) cloud-free satellite records. As shown in several papers (e.g., Tramutoli et al., 2001, 2005, 2009, 2015b, 2018b; Filizzola et al., 2004; Eleftheriou et al., 2016a; Genzano et., 2020; Peleli et al., 2021), differently from other approaches, the RST methodology is able to isolate residual TIR variations which are potentially related to seismic events. During the last 20 years, the RST technique has been applied to four different continents and many geo-tectonic contexts, in several earthquakes with magnitudes ranging from 4.0 to 7.9, using both polar (NOAA-AVHRR, EOS-MODIS) and geostationary (MFG-MVIRI, MSG-SEVIRI, GOES-IMAGER, MTSAT-IMAGER) satellite data, revealing correlations between TIR anomalies and tectonic deformation, in a time window ranging from 30 days before to 15 days after a seismic event (Genzano et al., 2020 and references therein). Nevertheless, remote sensing techniques for several reasons cannot perform identically well everywhere, every time (e.g. due to the presence of clouds). For this reason, sometimes the satellite-based research approaches have been the object of criticism (e.g. Pavlidou et al., 2019). From the other hand, a quite solid study performed by a group with a multi-decade experience in this specific field suggests that TIR variations have a non-casual relation with earthquakes' occurrence. For instance, Filizzola et al. (2004) reported TIR anomalies related to the M~5.9 Athens earthquake of 7 September 1999. Similarly, Tramutoli et al. (2005) applied the RST methodology for the M7.8 Izmit earthquake on 17 August 1999. Pergola et al. (2010) detected thermal anomalies a few days before the Abruzzo (Italy) earthquake occurred on 6 April 2009 (M5.8). Moreover, the long-term analysis (10 years of continuous data over Greece, with a false positive rate of 7%) performed by Eleftheriou et al. (2016a) revealed the generic correlation among earthquakes and RST calculated thermal anomalies.

In the current study, RST has been adopted with the aim to detect and map thermal anomalies probably related with one of the most significant earthquake sequences recorded in northern Thessaly, near the city of Larissa during March of 2021 (for details about Thessaly sequence and its impact please refer to Ganas et al., 2021 and Mavroulis et al., 2021). The sequence included a M6.3 main event on March 3rd 2021, 10:16:07 UTC which was followed by a M6.0 event after 32 hours and a M5.6 event on March 12 and thousands of smaller aftershocks. For this purpose, 10 years (2012-2021) of daily Night-time Land Surface Temperature (LST) remotely sensed data from Moderate Resolution Imaging Spectroradiometer (MODIS), were analyzed.

2. GEOTECTONIC SETTING

The Province of Thessaly comprises the most extended plain in the Greek peninsula. Its terrain is divided into the Plain of Trikala-Karditsa to the west and the Plain of Larisa to the east. The Pinios River drains the entire Basin of Thessaly (Fig.1a). On March

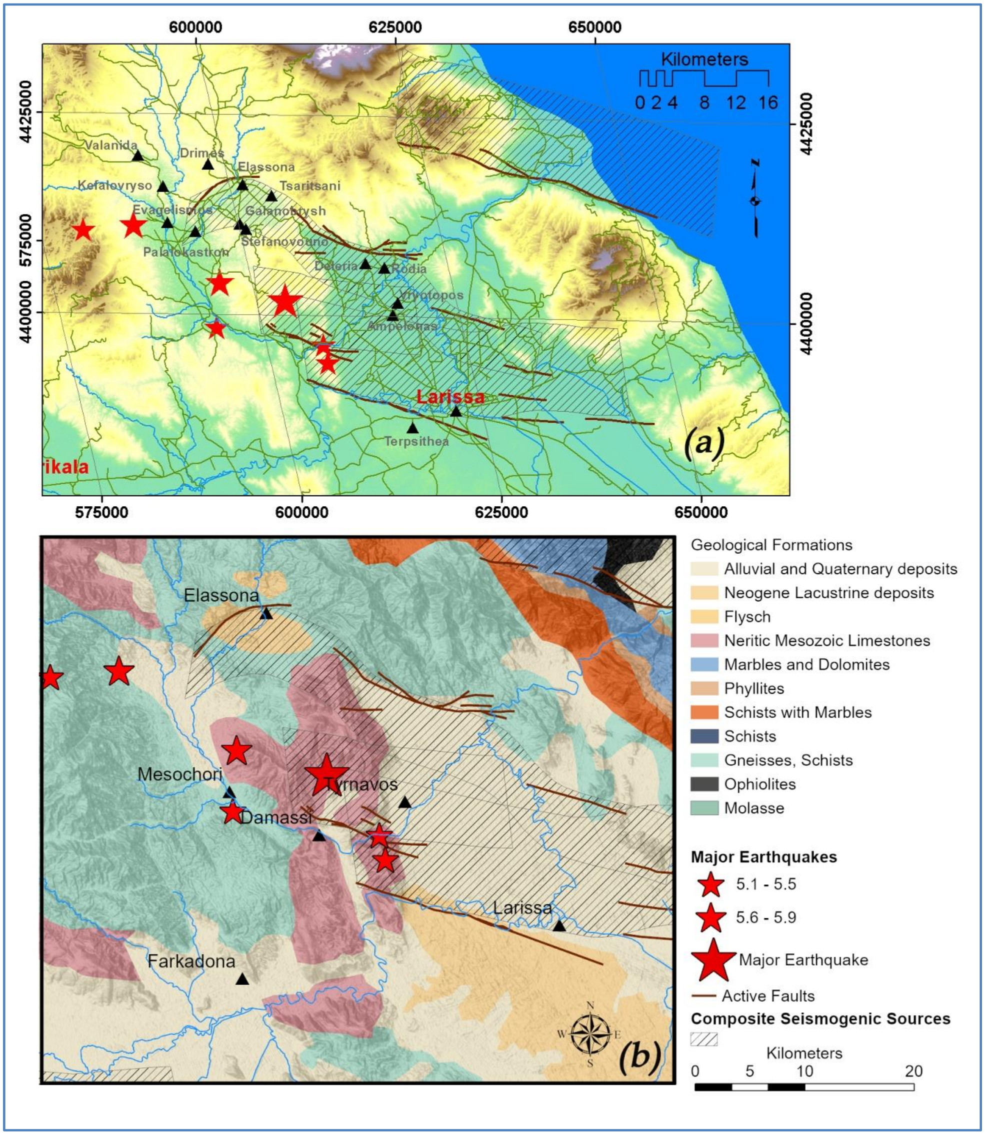

Fig. 1: (a) The SRTM elevation model (Shuttle Radar Topography Mission Void Filled (DOI: /10.5066/F7F76B1X downloaded from https://earthexplorer.usgs.gov/) and (b) the geological map of the study area, with overlay of the major earthquakes obtained from European Mediterranean Seismological Centre, the major active faults (adopted from Ganas et al., 2013) and the seismogenic sources (adopted from Caputo and Pavlides, 2013) located in the area.

3rd 2021 10:16:07 UTC, a strong earthquake (M 6.3) occurred 20 km NW of the city of Larissa. Another strong earthquake occurred on March 4th 18:38:19 UTC (M 5.8) in the same area. Consequently, many damages were caused by the seismic activity affecting thousands of people (Fig.1a). The most serious damages occurred near Damassi and other villages located along the banks of Titarissios river. The broader area exhibits geological complexity and intense tectonic deformation (Athanassiou,

2002) (Fig. 1b). The plain is covered by a thick alluvium layer which represents a significant mantle of beds in the rivers and the streams (Athanassiou, 2002; Vassilopoulou et al., 2013). The Quaternary deposits can be classified to: alluvial sediments that cover the plain of Larissa, fluvial terraces (Penios river) and lacustrine deposits. Mesozoic carbonates (karstic limestones and marbles) and Paleozoic Metamorphic formations (gneiss, schists and amphibolites) are underlain the Neogene deposits. The simplified geology of the area is given in Fig. 1, after Athanassiou, 2002. After the Alpine orogenesis, Eastern Thessaly, was affected by a NE–SW extensional regime. As a result, NW–SE elongated horsts and grabens bounded by large normal faults were formed. This tectonic regime is responsible for the NW–SE trending Larissa Basin that dominates the morphology of the region (Caputo et al., 1994). From Middle-Late Pleistocene until now, Thessaly is affected by a N–S lithospheric extension creating a new system of normal faults mainly trending E–W to ESE–WNW (Caputo, 1990, Caputo and Pavlides, 1993). The major consequence of the structural rearrangement was the creation of the Tyrnavos Basin within the Larissa Plain (Caputo et al., 1994). The Tyrnavos Basin has a general E(SE)–W(NW) orientation and it is bordered by two antithetic sets of normal faults, both showing a partial overlapping right-stepping geometry (Caputo, 1995).

3. MATERIALS AND METHODS

The RST (Robust Satellite Techniques; Tramutoli et al., 2005; 2007) technique is a known multi-temporal procedure of satellite data analysis. Its main advantage compared to other methods is the “natural noise” reduction. The source of this “natural noise” can be the water vapor content of the atmosphere or several spatio-temporal changes in land cover, topography and weather conditions. This methodological approach assumes that each spatio-temporal anomaly constitutes a deviation from normality. This deviation/anomaly can be computed by analyzing multiple cloud-free satellite images that meet the same homogeneous characteristics (i.e., same spatial location, same spectral channels, same overpass hours and same day / month for each year) to be comparable to each other. The RETIRA-index, used in this work, is defined as:

$$\otimes_{\Delta T}(r,t') = \frac{\Delta T(r,t') - \mu_{\Delta T}(r)}{\sigma_{\Delta T}(r)}$$

(1)

where:

$r = (x,y)$ defines the exact location of each pixel (x,y) on the satellite image,

t' refers to the acquisition time of the satellite image, with $t' \in \tau$, where τ characterizes the homogenous domain of satellite image acquired in the same hour of the day and the same month of the year.

(i) $\Delta T(r,t')$ represents the difference $(T(r,t') - T(t'))$ of the observed TIR signal value $T(x,y,t)$ with the spatial average $T(t)$ of all the pixels of the satellite image. $T(x,y,t)$ is measured for each pixel of the satellite image (r), while $T(t)$ is calculated in place on the satellite image, without considering the cloudy pixels, all representing the same class of the study area (land or sea) according to where the r is located,

(ii) $\mu_{\Delta T}(r)$ represents the time average and $\sigma_{\Delta T}(r)$ the standard deviation of $\Delta T(r,t')$ measured at site r, computed only on cloud-free pixels from satellite images of the homogenous datasets ($t' \in \tau$).

The RETIRA index provides an estimation of the local (spatial-temporal) excess of the current $\Delta T(r,t')$ signal with its historical computed mean value, weighted by its variability $\sigma_V(x,y)$ at the given location. The latter includes all the possible noise sources, including also the ones that do not have any relationship to the monitored event. The use of $\Delta T(r,t)$ instead of $T(r,t)$ reduces the possible contributions due to daily or yearly meteorological variations (e.g., occasional warming) and/or season time-drifts. The signal (S) is evaluated by comparison with the standard deviation, $\sigma_{\Delta T}(r)$. In this way, the signal to noise ratio *(S/N)* can be used to evaluate the intensity of anomalous TIR transients. Tramutoli et al., (2001) showed that the RETIRA index emphasizes low-level thermal anomalies regardless of sources of natural/observational noise.

In many cases, the measurements of TIR anomalies are affected by unexpected natural and/or observational changes such as climatological (e.g., extremely warm days), wildfires, cloud coverage or inaccurate image navigation/co-location. Based on previous literature, (e.g., Filizzola et al., 2004; Tramutoli et al., 2005; Eleftheriou et al., 2016a), one can conclude that RETIRA index (which is based on time-averaged quantities), is sensitive to the abrupt occurrence of signal outliers due to these natural (Aliano et al., 2008a) or observational (see Filizzola et al., 2004; Aliano et al., 2008b) phenomena. However, the specific spatiotemporal characteristics of these signal variations (small duration, often known date of occurrence and typical spatial distribution) help RETIRA index to define, isolate and highlight the presence of spatiotemporally persistent thermal anomalies even in very low intensity (Tramutoli et al. 2005) and therefore eliminate false alarms.

In this study the MODIS Land Surface Temperature and Emissivity Daily L3 Global 1km (MOD11_A1) product (https://modis.gsfc.nasa.gov/)(i.e., the version 006 (V5)) available from February 24, 2000 was used for the RETIRA index computation. The daily level 3 LST product at 1km spatial resolution is a tile of daily LST product gridded in the Sinusoidal projection. A tile contains 1200 x 1200 grids in 1200 rows and 1200 columns. The exact grid size at 1km spatial resolution is 0.928km by 0.928km (Wan, 2013). This product's spatial resolution guarantees an accuracy of 1 K under cloud-free conditions (e.g., Wan and Dozier, 1996; Wan, 2013). The retrieved MODIS Land Surface Temperature has only non-cloudy pixels due to the use of the MODIS cloud mask product (MOD35_L2 from Terra MODIS or MYD35_L2 from Aqua MODIS) (Wan, 2013). The Scientific Data Sets (SDSs) in the MOD11A1 product are shown in Table 1. The overpass times provided by MODIS LST product are in local solar time, which is defined as the MODIS observation time in coordinated universal time (UTC) plus longitude in degrees divided by 15 (Williamson et al., 2013). MODIS overpass times are converted from local solar time to local standard time or UTC. Night-time LST images (with approximately 00:00 local time of land surface observation in Thessaly) were preferably used because they are affected by soil–air temperature differences to a smaller extent than those acquired a different hour of the day. Moreover, night-time thermal images are less sensitive to local variations of solar illumination and shadows which could be a significant source of land surface temperature variability.

10 years of satellite records (every day of February and March from 2012 to 2021) were incorporated to the RETIRA index computation. The use of long time series satellite data (usually more than 6 years of observations) is absolutely necessary in order to create the thermal background of the region of interest. In detail, during the pre-processing phase, we isolated the "Night-time and Surface Temperature" layer dataset for the ten years' time period and all the images were spatially clipped over the broader earthquake affected area. In this way, 283 images were obtained for the month of February and 310 images for the month of March. Each image contains 5921 non cloudy pixels. The existence of clouds in the images is given as no data value and consequently the number of available pixels reduces as the cloud coverage increases. The images after being spatially subset to the region of interest were checked one by one for the percentage of cloud cover in the specific area as it has been proved that in cases where

the cloudy fraction of the scene exceeds the 80% of the land portion, the remaining values of image constitute the considered signal not representing the real conditions at that given time (Eleftheriou et al., 2016a). Consequently, all the images with a cloud fraction more than 80% were excluded from the final reference field computation. A total of 343 images with a cloud cover of less than 80% were used to calculate the monthly reference fields $\mu_{\Delta T}(x,y)$ and $\sigma_{\Delta T}(x,y)$; 173 images for February and 170 images for March (Figs. 2 and 3 respectively). Subsequently the RETIRA index was calculated for 34 images. Of these, 16 images belong to February while 18 belong to March 2021. The remaining 25 images for the two months of 2021 had a cloud cover of over 80% and as a result were excluded from the procedure. The next step was the on-screen examination of the 34 calculated indices in order to check for the presence of imprinted thermal anomalies. RETIRA is assumed to be a Gaussian standardized variable and the choice of its relative threshold value quantitatively qualifies how much rare (and significant) are the identified anomalies. Anomalous pixels (i.e., pixels of thermal anomaly) were considered those having values of the RETIRA index higher than 2.5. The daily analysis revealed that 9 over the 34 images included anomalous pixels with RETIRA values higher than 2.5.

As already mentioned, the main advantage of RETIRA method over other methods is the reduction of "natural noise". The last one may be due to changes in vegetation, topography and weather conditions. Since these noise sources are eliminated, the extracted thermal anomalies may be associated with intense and rare phenomena such as earthquakes, wildfires and extremely warm days. The time period (February and March) in which we applied this technique helps us to reject the last two phenomena (wildfires and extremely warm days). RETIRA anomalies may be also induced by cloud-coverage and inaccurate image navigation/co-location. Therefore, an assessment of achieved results was performed in order to discriminate true from false thermal anomalies. As a result, 2 out of the 9 images with RETIRA values higher than 2.5 were characterized as false thermal anomalies due to clouds existence. These false thermal anomalies are artifacts characterized from high RETIRA values located along the boundaries of cloudy pixels (violet areas) with the land pixels (Fig. 4). No thermal anomaly image with inaccurate image navigation/co-location was found.

Table 1. The Scientific Data Sets (SDSs) in the MOD11A1 product. (https://icess.eri.ucsb.edu/modis/LstUsrGuide/usrguide.html)

SDS Name	**Long Name**	**Number Type**	**Unit**	**Valid Range**	**Fill Value**	**Scale factor**	**Offset**
LST_Day_1km	Daily daytime 1km grid	uint16	K	7500-65535	0	0.02	0.0
QC_Day	Quality control for daytime LST and emissivity	uint8	none	0-255	0	NA	NA
Day_view_time	(local solar) Time of daytime Land-surface Temperature observation	uint8	hrs	0-240	0	0.1	0
Day_view_angle	View zenith angle of daytime Land-surface Temperature	uint8	deg	0-130	255	1.0	-65.0
LST_Night_1km	Daily nighttime 1km grid Land-surface Temperature	uint16	K	7500-65535	0	0.02	0.0
QC_Night	Quality control for nighttime LST and emissivity	uint8	none	0-255	0	NA	NA
Night_view_time	(local solar) Time of nighttime Land-surface Temperature observation	uint8	hrs	0-240	0	0.1	0
Night_view_angle	View zenith angle of nighttime Land-surface Temperature	uint8	deg	0-130	255	1.0	-65.0
Emis_31	Band 31 emissivity	uint8	none	1-255	0	0.002	0.49
Emis_32	Band 32 emissivity	uint8	none	1-255	0	0.002	0.49
Clear_day_cov	day clear-sky coverage	uint16	none	0-65535	0	0.0005	0.
Clear_night_cov	night clear-sky coverage	uint16	none	0-65535	0	0.0005	0.

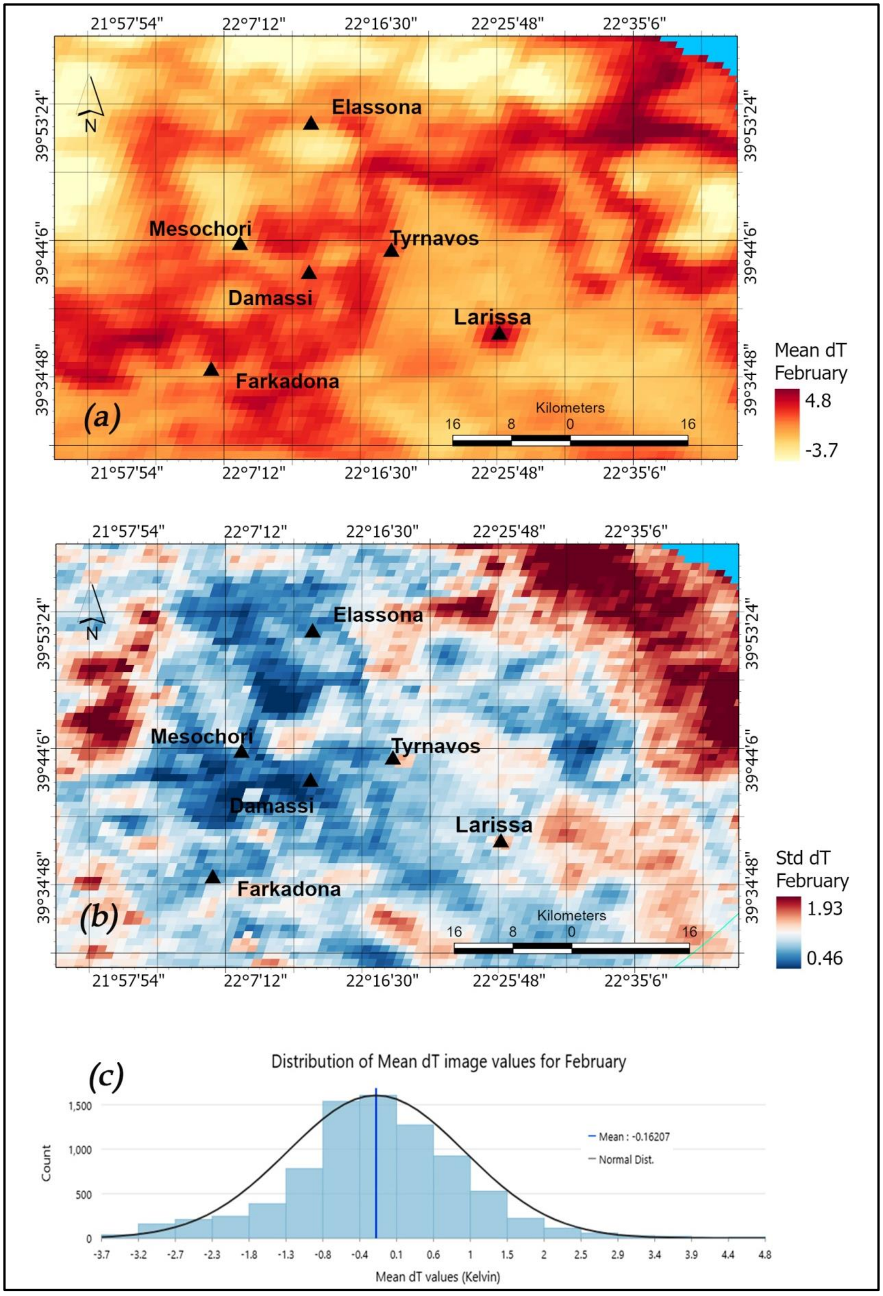

Fig. 2: Monthly Reference fields $\mu_{\Delta T}(x,y)$ and $\sigma_{\Delta T}(x,y)$ calculated for February using MODIS LST images acquired over the broader Larissa area from 2012 to 2021. The histogram showing the frequency distribution of the $\mu_{\Delta T}(x,y)$ (in Kelvin) is also given.

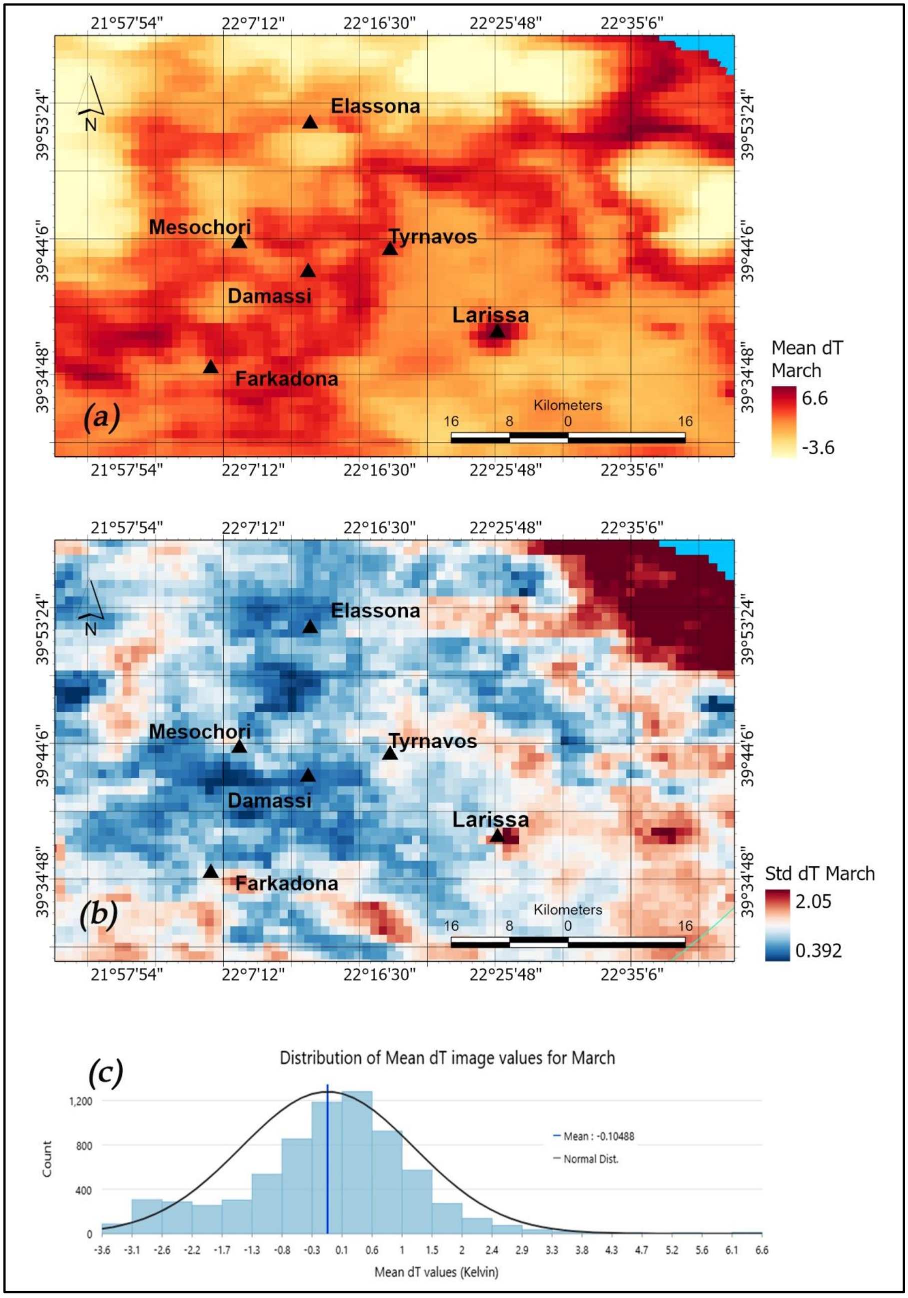

Fig. 3: Monthly Reference fields $\mu_{\Delta T}(x,y)$ and $\sigma_{\Delta T}(x,y)$ calculated for March using MODIS LST images acquired over the broader Larissa area from 2012 to 2021. The histogram showing the frequency distribution of the $\mu_{\Delta T}(x,y)$ (in Kelvin) is also given.

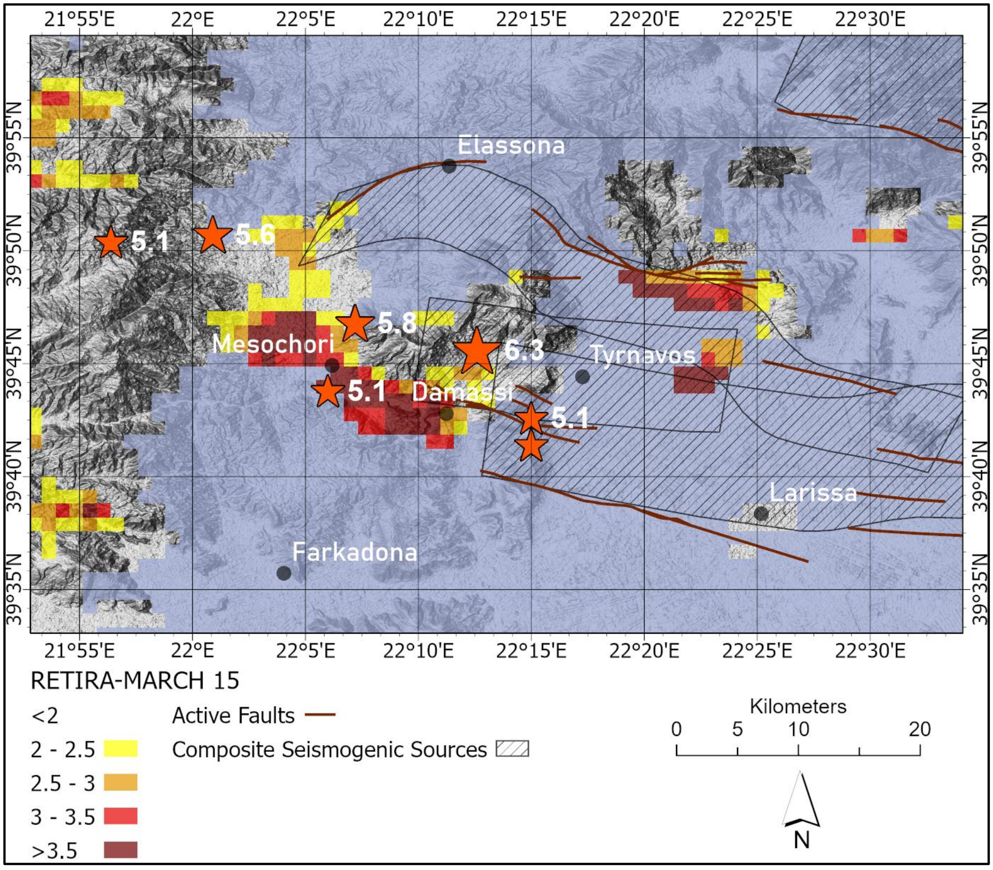

Fig. 4: Example of a false RETIRA thermal anomaly map. This pattern of artifacts is characterized from high RETIRA values located along the boundaries of cloudy pixels (violet areas) with the land pixels. Such images were excluded for further analysis.

4. RESULTS AND DISCUSSION

In this section, results achieved using the RETIRA index are presented and discussed. As we have already mention, the daily analysis revealed that 9 over 34 images included anomalous pixels with RETIRA values higher than 2.5. It is worth mentioning that 2 out of the 9 images were characterized as false thermal anomalies due to clouds. For instance, Fig. 4 shows a false thermal anomaly mapped on 15 March 2021 and excluded from further analysis since the anomalous pixels are induced due to cloud coverage. The 2 images were identified with on-screen interpretation and were immediately excluded. In this case we cannot talk about a false alarm. We consider a false alarm to exist when the index shows abnormal values that are not due or induced by a known cause and within a period of 15 days before them or 30 days after them there has been no earthquake occurrence with M> 4 in the research area (Eleftheriou et al., 2016a).

Unfortunately, due to the bad meteorological conditions we were not able to depict in detail the time persistence of thermal anomalies. This is the case of missing values and depends directly on the time of observations. In our case the sequence of the 7 thermal anomalies, 3 before the main earthquake, 1 on the day of the earthquake and another 3 after it, constitutes a successful application of the RETIRA index. Quite intense (Signal/Noise > 2.5) and rare, spatially extensive and time persistent, TIR signal transients were identified, appearing twenty-five, twenty and two days before the Thessaly main shock (pre-seismic anomalies: February 6th, February 11th March 1st), the day of the main earthquake (co-seismic anomaly) and one day, seven days and fourteen days after the main shock (post-seismic anomalies: March 4th, 10th and 17th) (Figs 5, 6 and 7). As shown in Figs. 5, 6 and 7, in some cases there are pixels with values up to 5 and this fact is an indication of the intensity of the anomalies (see dark brown pixels). Hence, we introduced the seven mapped thermal anomalies along with several geological elements, such as active faults and seismogenic sources in a Geographic Information System (GIS) (Figs 5, 6 and 7).

Regarding the preseismic thermal activity of the region of interest, on the 6th of February the thermal anomalies appear East of Elassona, near the village of Farkadona while there are few pixels in the western part of the area of interest (Fig 5). On February 11 (20 days before the main earthquake), the thermal anomalies are oriented ESE–WNW and are concentrated within the composite seismogenic zone located in the Tyrnavos basin. Near the village Damassi, almost at the point where the main earthquake occurred, they cross a second, NE-SW oriented zone defined by thermal anomalies (Fig 5). On March 1, the clouds allow us to see only scattered thermal anomalies. In many cases these anomalies are spatially limited by the existence of faults as in the case south of Farkadona (Fig. 5). On the day of the earthquake, the thermal anomalies appear in 3 areas: in the area between the epicenters of the main earthquake and the main aftershock that followed a day later, northeast of the village of Farkadona and in a N-W oriented zone east of the village of Mesochori (Fig.6). Finally, regarding the post-seismic thermal anomalies, on March 4 they are concentrated exclusively NE of Elassona (Fig. 7), on March 10 they present a spatial distribution similar to the distribution of February 11 and are controlled spatially by the ruptured zones as in the case north of Damassi village (Fig. 7). On March 17, the thermal anomalies occupy an extended area defined by the villages of Damassi, Farkadona Tyrnavos and reach very close to Larissa (Fig. 7).

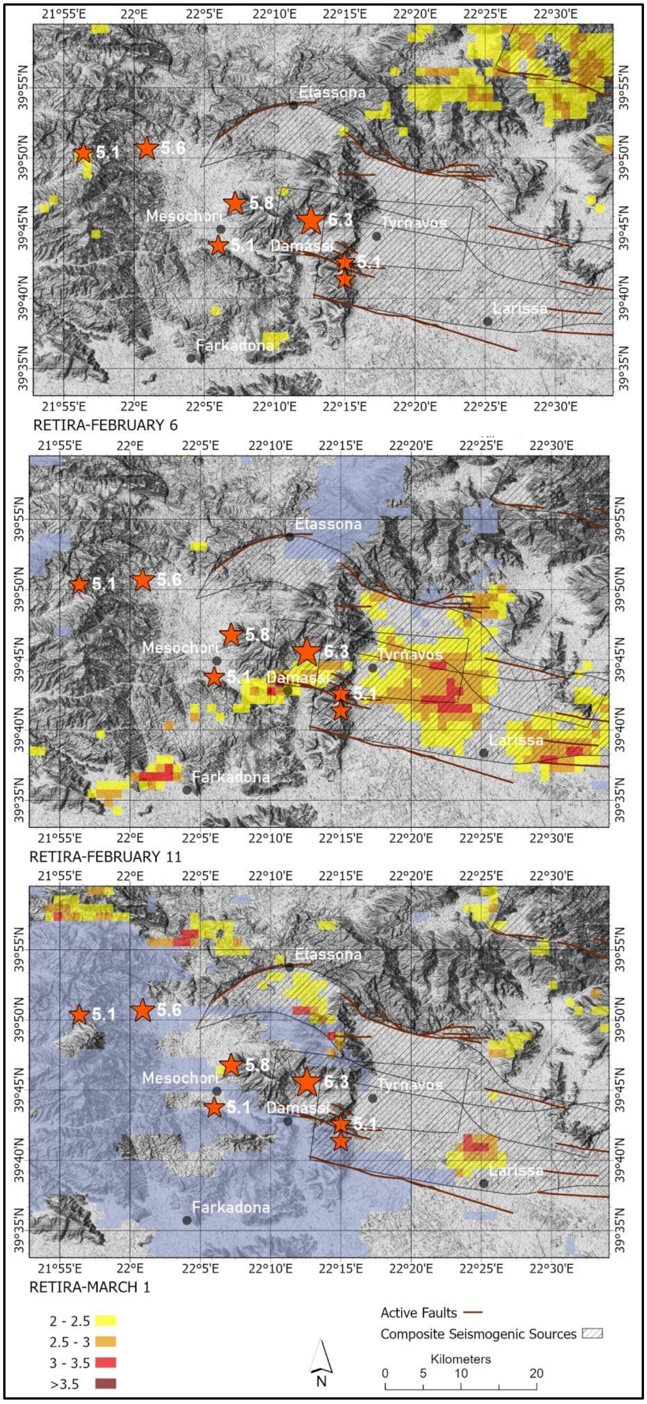

Fig. 5 Preseismic RETIRA thermal anomaly maps of the broader earthquake area combined with the active faults and seismogenic sources. Significant thermal anomalies were identified 25 (February 6th), 20 (February 11th) and 2 (March 1st) days before the main shock and are presented with different colors depending on their RETIRA value. The maps are draped over shaded relief. Cloud coverage is given with violet color.

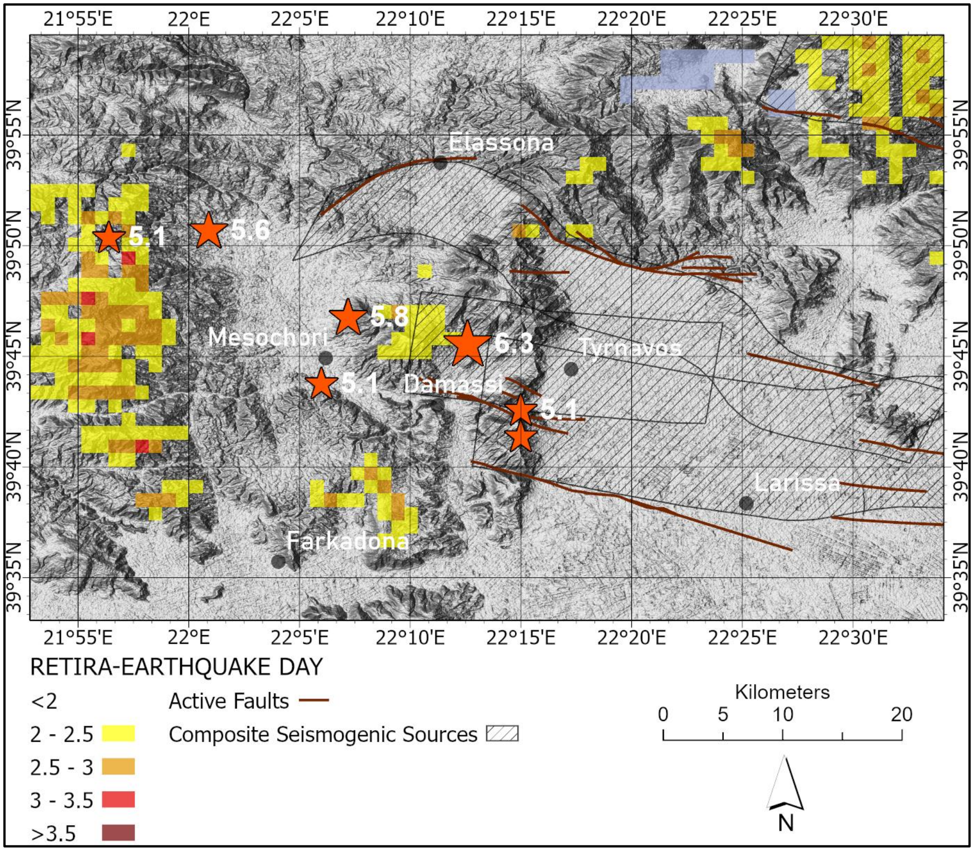

Fig. 6: Coseismic RETIRA thermal anomaly map of the broader earthquake area combined with the active faults and seismogenic sources. Significant thermal anomalies are presented with different colors depending on their RETIRA value. The map is draped over shaded relief. Cloud coverage is given with violet color. The MODIS scene has been acquired the night of March 3, 2021.

The total number of pixels characterized as thermally anomalous at least in one out of the seven RETIRA maps is 744. Moreover, the cumulative maps of Fig. 8 show the frequency of occurrence of thermal anomalies (i.e., the number of times over-threshold values are reached) during the 7 days represented by the RETIRA index maps for each pixel with RETIRA value greater than 2.5 (Fig. 8a) and for RETIRA value greater than 2.0 (Fig. 8b). In the aforementioned images, pixels characterized anomalous only once are not presented. In this way, we were able to define the areas in which the thermal anomalies are space-time persistent.

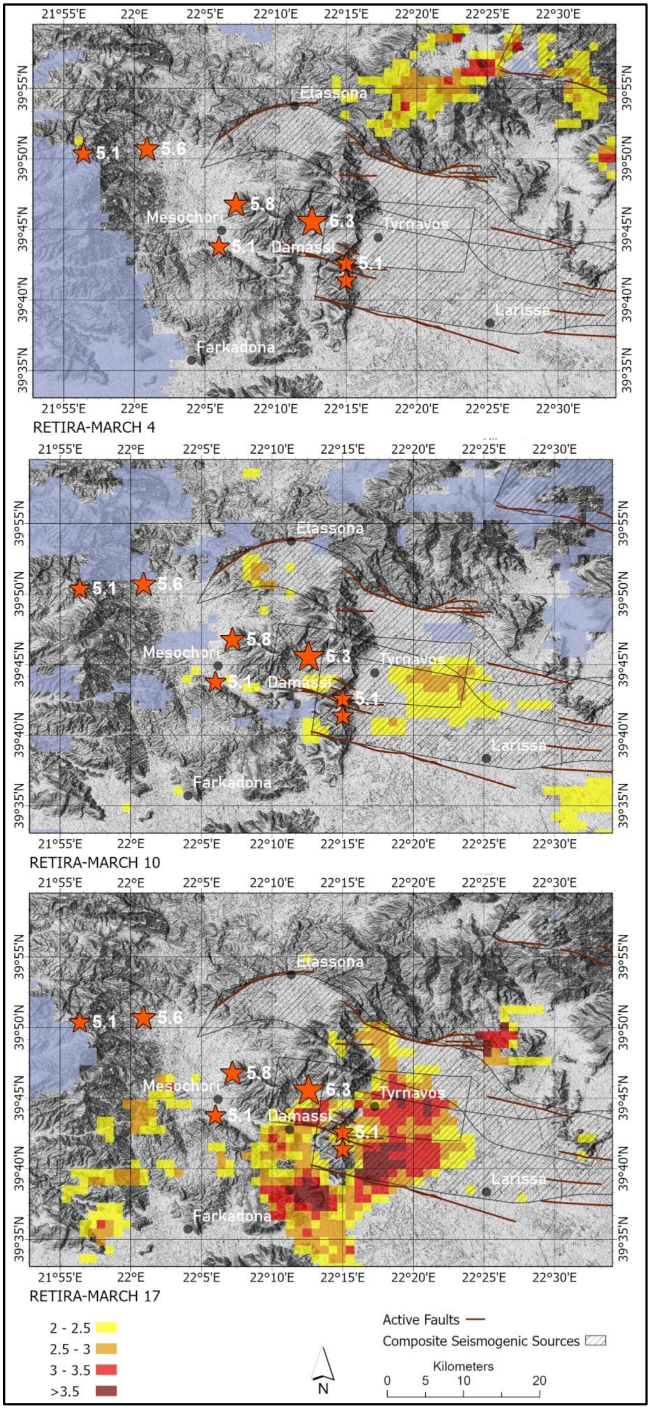

RETIRA-MARCH 4

RETIRA-MARCH 10

RETIRA-MARCH 17

Fig. 7: Postseismic RETIRA thermal anomaly maps of the broader earthquake area combined with the active faults and seismogenic sources. Significant thermal anomalies were identified on March 4th, 10th and 17th and are presented with different colors depending on their RETIRA value. Cloud coverage is given with violet color. The maps are draped over shaded relief.

In the first case, 84 pixels with values 2 (75 pixels) and 3 (9 pixels) have been isolated; regarding the pixels equal to 2, two of them are located west of village Damassi, 5 in the area between Damassi and Tyrnavos, 54 in the area between Tyrnavos and Larissa, while the rest 14 are mainly located to the northeast of Tyrnavos basin. The nine pixels with value equal to 3 **(**i.e., these pixels were characterized as thermally anomalous the 3 out of the 7 days) are located east of Tyrnavos and they are surrounded from an extended area with value equal to 2 (Fig. 8a). The Fig. 8b shows the cumulative map when the RETIRA index threshold decreases to 2 instead of 2.5. As expected, the area covered by thermally anomalous pixels is more extended, as less intense anomalies are taken into account but the general spatial distribution pattern remains the same.

Preferential spatial distribution of anomalies over time seems to be concentrated inside the composite seismogenic sources and to be controlled by the existence of the active faults. In some cases, thermally anomalous pixels are located in the junction of two faults. A probable explanation could be the uplifting of the fluids and/or gasses through the tectonic faults due to changes of the sub-surface physicochemical processes. For instance, micro-fracturing can lead to permeability changes and gas diffusion, which supported by their high mobility (Conti et al., 2021; Martinelli, 2021). As stated by Pulinets and Ouzounov (2011), increase of stress can cause release of CO_2, CH_4, N_2O (greenhouse gases) that are trapped in the pores of rock, this can cause a local greenhouse effect). In addition, we note that the opening of microfractures has been suggested as a source of electrical precursors which some of the cases are related with the observations of gas emissions (see Vallianatos et al., 2004 and references therein).

Finally, preliminary spatial analysis of the number of times over-threshold values are reached, shows that the thermally anomalous pixels are hosted mainly by Quaternary deposits (Fig. 9), probably due to their high permeability. Taking into account all the pixels which showed thermally anomalous behavior at least in one out of the seven RETIRA maps (744 pixels in total)**,** the majority of them is detected in elevations lower than 350 m (Fig. 10a) and within a distance of 4 km from the faults (Fig. 10b).

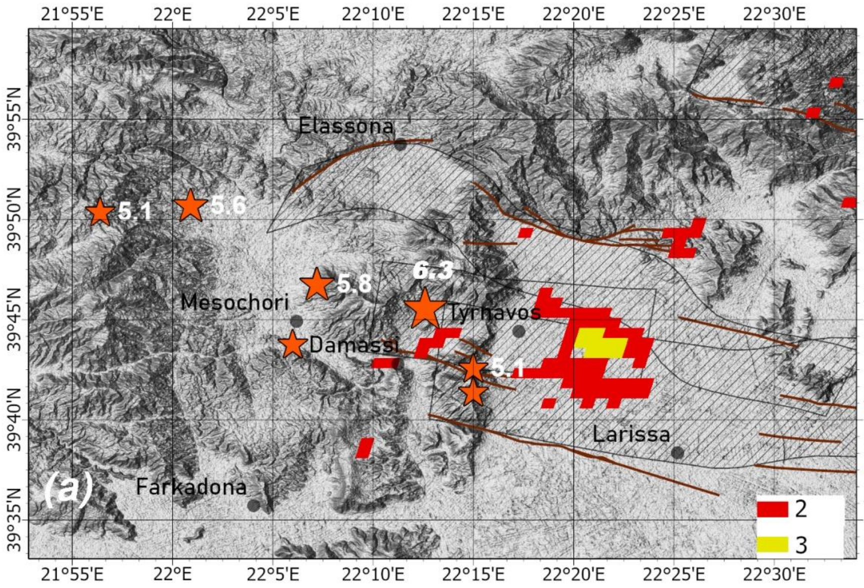

Cumulative Thermal Anomaly (N pixels with RETIRA > 2.5)

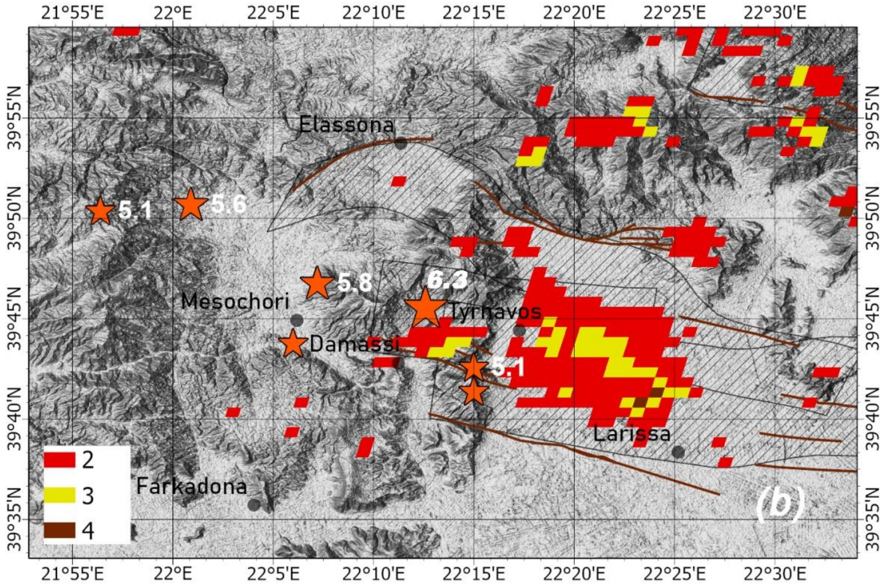

Cumulative Thermal Anomaly (N pixels with RETIRA > 2)

Fig. 8: Cumulative maps counting for each pixel the number of times over-threshold values (i.e., RETIRA index greater than 2.5 and 2.0) are reached for the seven days of thermal anomalies. These products cover a period of time from February 6 to March 17.

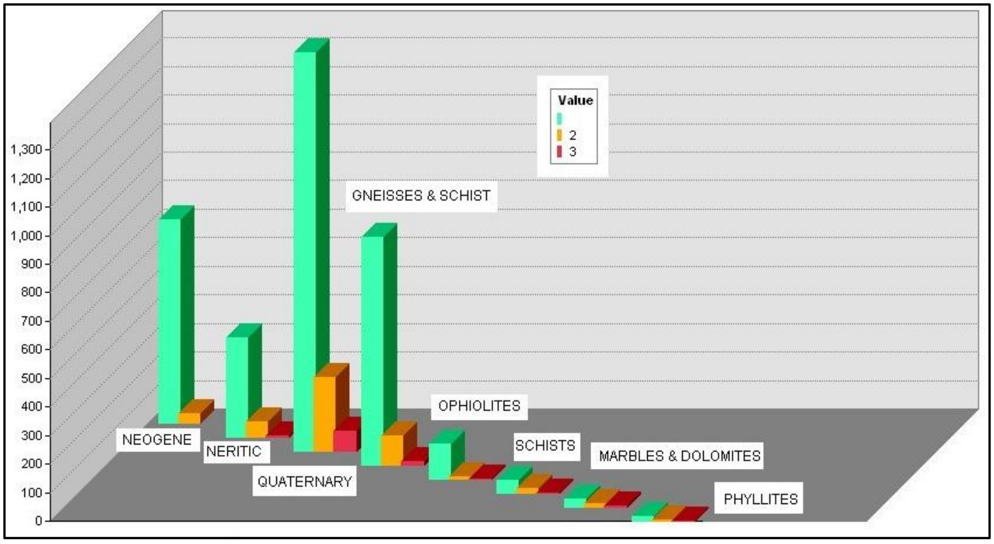

Fig. 9: The frequency distribution of cumulative thermal anomalies (based on Fig. 8b) within the different geological formations of the study area. With the green color is shown the total number of pixels in the geological formations.

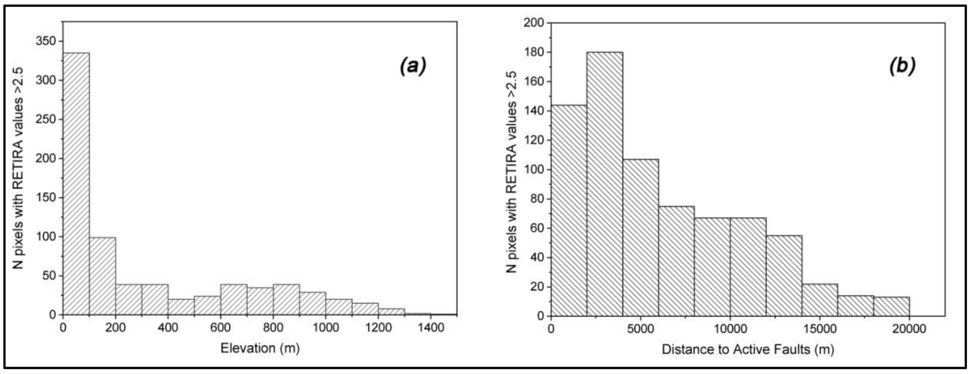

Fig. 10: The frequency distribution of all the thermally anomalous pixels (y-axis, 744 pixels in total) with respect to (a) the elevation and (b) the distance to active faults.

5. CONCLUSIONS

In the present work, MODIS (LST) data from a time-period of 10 years (2012-2021) were coupled with robust satellite technique and especially RETIRA index, with the aim to detect anomalous signal variations ascribable to Thessaly's earthquake sequence. We managed to detect preseismic, coseismic and post seismic thermal anomalies. The detected anomalies show a close spatial relation with the previously known seismogenic sources and the tectonic lineaments located in the area. Building up a system based on continuously updated observations, provided that they are adequately selected and analyzed, may represent a hopeful research line to actually exploit accumulated knowledge of seismic hazard. In this direction, the RST technique and the long-term satellite thermal imagery processing combined with geological data can be proved a valuable tool.

6. ACKNOWLEDGMENTS

We acknowledge support of this study by the project "HELPOS - Hellenic Plate Observing System" (MIS 5002697) which is implemented under the Action "Reinforcement of the Research and Innovation Infrastructure", funded by the Operational Programme "Competitiveness, Entrepreneurship and Innovation" (NSRF 2014-2020) and co-financed by Greece and the European Union (European Regional Development Fund).

7. REFERENCES

Aguilar-Lome J., Espinoza-Villar R., J.C. Espinoza, J. Rojas-Acuña, B.L. Willems & W.M. Leyva-Molina, 2019. Elevation-dependent warming of land surface temperatures in the Andes assessed using MODIS LST time series (2000–2017). *Int J Appl Earth Obs*., 77, pp 119-128 https://doi.org/10.1016/j.jag.2018.12.013

Aliano C., Corrado R., Filizzola C., Genzano N., Pergola N. & V. Tramutoli, 2008a. Robust TIR satellite techniques for monitoring earthquake active regions: limits, main achievements and perspectives. *Ann Geophys.*, 51, 303-317 https://doi.org/10.4401/ag-3050

Aliano C., Corrado R., Filizzola C., Pergola N. & Tramutoli V., 2008b. Robust satellite techniques (RST) for the thermal monitoring of earthquake prone areas: the case of Umbria-Marche October, 1997 seismic events. *Ann Geophys.*, 51, 451-459 https://doi.org/10.4401/ag-3025

Anderson M. & Kustas W., 2008. Thermal remote sensing of drought and evapotranspiration. *EOS T Am Geophys Un*., 89 pp. 233-234 https://doi.org/10.1029/2008EO260001

Anderson M.C., Allen R.G., Morse A., Kustas W.P., 2012. Use of Landsat thermal imagery in monitoring evapotranspiration and managing water resources. *Remote Sens. Environ*, 122, pp 50-65 https://doi.org/10.1016/j.rse.2011.08.025

Athanasiadou, L., Psomiadis, E., & Stamatis, G. 2020. Thermal Remote Sensing for Water Outflows Detection and Determination of the Role of Lineaments in Underground Hydrodynamics of Evia Island, Central Greece. *Bulletin of the Geological Society of Greece*, *56*(1), 100-132. https://doi.org/10.12681/bgsg.20948

Athanassiou A., 2002. Neogene and Quaternary mammal faunas of Thessaly. *Annales Géologiques des PaysHelléniques*, XXXIX (A), 279–293.

Brunsell N.A. & Gillies R.R., 2003. Determination of scaling characteristics of AVHRR data with wavelets: Application to SGP97. *Int. J. Remote Sens*., 24, pp 2945-2957 https://doi.org/10.1080/01431160210155983

Caputo R. and Pavlides S., 2013. The Greek Database of Seismogenic Sources (GreDaSS), version 2.0.0: A compilation of potential seismogenic sources (Mw > 5.5) in the Aegean Region. *doi: 10.15160/unife/gredass/0200*.

Caputo R., Bravard J.-P., Helly B., 1994. The Pliocene-Quaternary tecto-sedimentary evolution of the Larissa Plain (Eastern Thessaly, Greece). *Geodinamica Acta*, 7, pp. 57-85 https://doi.org/10.1080/09853111.1994.11105267

Caputo R., Pavlides S., 1993. Late Cainozoic geodynamic evolution of Thessaly and surroundings (central-northern Greece). *Tectonophysics*, 223, pp. 339-362 https://doi.org/10.1016/0040-1951(93)90144-9

Caputo R., Piscitelli S., Oliveto A., Rizzo E., Lapenna V., 2003. The use of electrical resistivity tomography in active tectonics. Examples from the Tyrnavos Basin, Greece. *J. Geodyn*., 36 (1–2), pp. 19-35 10.1016/S0264-3707(03)00036-X

Caputo, R. 1990. Geological and structural study of the recent and active brittle deformation of the Neogene-Quaternary basins of Thessaly (Greece). In: *Scientific Annals, Vol. 12, Aristotle University of Thessaloniki, Thessaloniki.*

Christman Z., Rogan J., Eastman J.R. & Turner B.L., 2016. Distinguishing Land Change from Natural Variability and Uncertainty in Central Mexico with MODIS EVI, TRMM Precipitation, and MODIS LST Data. *Remote Sens*., 8, pp 478 https://doi.org/10.3390/rs8060478

Conti L., Picozza P. and Sotgiu A., 2021. A Critical Review of Ground Based Observations of Earthquake Precursors, Front. Earth Sci., 06 July 2021, https://doi.org/10.3389/feart.2021.676766

Eleftheriou A., Filizzola C., Genzano N., Lacava T., Lisi M., Paciello R., Pergola N., Vallianatos F. & Tramutoli V., 2016a. Long-term RST analysis of anomalous TIR sequences in relation with earthquakes occurred in Greece in the period 2004–2013. *Pure Appl. Geophys.*, 173, pp 285-303 https://doi.org/10.1007/s00024-015-1116-8

Eleftheriou D., Kiaghidis K., Kalmintzis G., Kalea A., Bantasis C., Koumadoraki P., Spathara M.E., Tsolaki A., Tzampazidou M.I., Gemitzi A., 2016b. Determination of annual and seasonal daytime and nighttime trends of MODIS LST over Greece-climate change implications. *Sci. Total Environ.*, 616, pp 937-947 doi: 10.1016/j.scitotenv.2017.10.226

Filizzola C., Pergola N., Pietrapertosa C. & Tramutoli V., 2004. Robust satellite techniques for seismically active areas monitoring: a sensitivity analysis on September 7, 1999 Athens's earthquake. *Phys. Chem. Earth*, PT A/B/C, 29, pp 517-527 DOI: 10.1016/j.pce.2003.11.019

Ganas, A., Lagios, E., Petropoulos, G. and Psiloglou, B., 2010. Thermal imaging of Nisyros volcano (Aegean Sea) using ASTER data: estimation of radiative heat flux, *International Journal of Remote Sensing*, 31: 15, 4033 — 4047 https://doi.org/10.1080/01431160903140837

Ganas, A., Oikonomou, I. & Tsimi, C., 2013. NOAfaults: a digital database for active faults in Greece, Bulletin of the Geological Society of Greece, 47: 2, 518 – 530 https://doi.org/10.12681/bgsg.11079

Ganas, A., Valkaniotis, S., Briole, P., Serpetsidaki, A., Kapetanidis, V., Karasante, I., Kassaras, I., Papathanassiou, G., Karamitros, I., Tsironi, V., Elias, P., Sarhosis, V., Karakonstantis, A., Konstantakopoulou, E., Papadimitriou, P., & Sokos, E., 2021. Domino-style earthquakes along blind normal faults in Northern Thessaly (Greece): kinematic evidence from field observations, seismology, SAR interferometry and GNSS. *Bulletin of the Geological Society of Greece,* 58, 37-86. https://doi.org/10.12681/bgsg.27102

Genzano N., Filizzola C., Lisi M., Pergola N., Tramutoli V., 2020. Toward the development of a multi parametric system for a short-term assessment of the seismic hazard in Italy. *Annals of Geophysics*, 63-5, PA550 https://doi.org/10.4401/ag-8227

Karnieli A., Agam N., Pinker R.T., Anderson M., Imhoff M.L., Gutman G.G., Panof N. & Goldberg A., 2010. Use of NDVI and land surface temperature for drought assessment: Merits and limitations. *J. Climate*, 23, pp 618-633. https://doi.org/10.1175/2009JCLI2900.1

Keramitsoglou I., Chris T., Kiranoudis C.T., Ceriola G., Weng Q., Rajasekar U., 2011. Identification and analysis of urban surface temperature patterns in Greater Athens, Greece, using MODIS imagery. *Remote Sens. Environ.*, 115, pp 3080-3090. https://doi.org/10.1016/j.rse.2011.06.014

Kustas W. & Anderson M., 2009. Advances in thermal infrared remote sensing for land surface modeling. *Agr. Forest Meteorol.*, 149, pp 2071-2081. https://doi.org/10.1016/j.agrformet.2009.05.016

Li Z.L., Tang B.H., Wu H., Ren H., Yan G., Wan Z. & Sobrino J.A., 2013. Satellite-derived land surface temperature: Current status and perspectives. *Remote Sens. Environ.*, 131, pp 14-37 https://doi.org/10.1016/j.rse.2012.12.008

Lillesand T. M., Kiefer R. W. & Chipman J. W.,1987. *Remote sensing and image interpretation.* John Wiley & Sons, New York.

Martinelli G., 2020. Previous, Current, and Future Trends in Research into Earthquake Precursors in Geofluids, *Geosciences*, 10, 189; https://doi.org/10.3390/geosciences10050189

Mavroulis, S., Mavrouli, M., Carydis, P., Agorastos, K., & Lekkas, E., 2021. The March 2021 Thessaly earthquakes and their impact through the prism of a multi-hazard approach in disaster management. *Bulletin of the Geological Society of Greece*, 58, 1-36. https://doi.org/10.12681/bgsg.26852

Pavlidou E., van der Meijde M., van der Werff H. and Hecker C., 2019, Time Series Analysis of Land Surface Temperatures in 20 Earthquake Cases Worldwide, *Remote Sensing*, 11, 61; doi:10.3390/rs11010061

Peleli, S., Kouli, M., Marchese, F., Lacava, T., Vallianatos, F., Tramutoli, V., 2021. Monitoring temporal variations in the geothermal activity of Miocene Lesvos volcanic field using remote sensing techniques and MODIS – LST imagery. *International Journal of Applied Earth Observation and Geoinformation*, 95, 102251. https://doi.org/10.1016/j.jag.2020.102251

Pulinets S. & Ouzounov D., 2011. Lithosphere–atmosphere–ionosphere coupling (LAIC) model–an unified concept for earthquake precursors validation *J. Asian Earth Sci.* 41 371–82. https://doi.org/10.1016/j.jseaes.2010.03.005

Scambos T. A., Campbell G. G., Pope A., Haran T., Muto A., Lazzara M., Reijmer C.H. and van den Broeke M.R., 2018. Ultralow surface temperatures in East Antarctica from satellite thermal infrared mapping: The coldest places on Earth *Geophys Res Lett.*, 45, pp 6124–6133 https://doi.org/10.1029/2018GL078133

Tramutoli V., 2007. Robust Satellite Techniques (RST) for Natural and Environmental Hazards Monitoring and Mitigation: Theory and Applications. *Int. Work. Anal. Multi-temporal Remote Sens. Images. IEEE*, pp 1–6 10.1109/MULTITEMP.2007.4293057

Tramutoli V., Di Bello G., Pergola N. & Piscitelli S., 2001. Robust satellite techniques for remote sensing of seismically active areas. *Ann di Geofis*., 44, pp 295–312 https://doi.org/10.4401/ag-3596

Tramutoli V., Cuomo V., Filizzola C., Pergola N. & Pietrapertosa C., 2005. Assessing the potential of thermal infrared satellite surveys for monitoring seismically active areas: The case of Kocaeli (Izmit) earthquake, August 17, 1999. *Remote Sens Environ*., 96, pp 409-426 10.1016/j.rse.2005.04.006

Vallianatos F., Triantis D., Tzanis A., Anastasiadis C., Stavrakas I., 2004. Electric earthquake precursors: from laboratory results to field observations, *Physics & Chemistry of the Earth*, 29, 339-351. DOI: 10.1016/j.pce.2003.12.003

Vassilopoulou S., Sakkas V., Wegmuller U., Capes R. 2013. Long Term and Seasonal Ground Deformation Monitoring of Larissa Plain (Central Greece) by Persistent Scattering Interferometry, *Cent. Eur. J. Geosci.*, 5(1), pp 61-76. https://doi.org/10.2478/s13533-012-0115-x

Vollmer M., Möllmann K.P., 2017. Infrared thermal imaging: fundamentals, research and applications, *John Wiley & Sons, 2nd Edition*. ISBN: 978-3-527-41351-5

Wan Z., 2013. MODIS Land Surface Temperature products user's guide. *https://icess.eri.ucsb.edu/modis/LstUsrGuide/usrguide.html*

Williamson S. N., Hik D. S., Gamon J. A., Kavanaugh J. L. and Koh S., 2013. Evaluating cloud contamination in clear-sky MODIS Terra daytime land surface temperatures using ground-based meteorology station observations, *J. Clim.*, 26(5), 1551–1560. https://doi.org/10.1175/JCLI-D-12-00250.1

Zhang Y., Jiang Z., Huang H., FanG Y., Mu X. and Cheng X., 2014. Thermal Anomalies Detection before 2013 Songyuan earthquake using MODIS LST data, *IGARSS 2014, doi: 10.1109/IGARSS.2014.6947110*

BGSG

Volume 58

Research Paper

Correspondence to:
Vasileios Karakostas
vkarak@geo.auth.gr

DOI number:
http://dx.doi.org/10.12681/bgsg.27237

Keywords:
seismic sequence; finite–fault slip model; seismological geodesy; stress transfer and triggering

Citation:
Karakostas, V., Papazachos, C., Papadimitriou, E., Foumelis, M., Kiratzi, A., Pikridas, C., Kostoglou, A., Kkallas, C., Chatzis, N., Bitharis, S., Chatzipetros, A., et al. (2021), The March 2021 Tyrnavos, Central Greece, Doublet (M_w6.3 and M_w6.0): Aftershock Relocation, Faulting Details, Coseismic Slip and Deformation. Bulletin Geological Society of Greece, 58, 131-178.

Publication History:
Received: 09/06/2021
Accepted: 18/08/2021
Accepted article online: 24/08/2021

The Editor wishes to thank two anonymous reviewers for their work with the scientific reviewing of the manuscript and Ms Emmanouela Konstantakopoulou for editorial assistance.

THE MARCH 2021 TYRNAVOS, CENTRAL GREECE, DOUBLET (M_W6.3 and M_W6.0): AFTERSHOCK RELOCATION, FAULTING DETAILS, COSEISMIC SLIP and DEFORMATION

Vasileios Karakostas[1], Constantinos Papazachos[1], Eleftheria Papadimitriou[1], Michael Foumelis[2], Anastasia Kiratzi[1], Christos Pikridas[3], Anastasios Kostoglou[1], Charalambos Kkallas[1], Nikolaos Chatzis[1], Stylianos Bitharis[3], Alexandros Chatzipetros[4], Aristidis Fotiou[3], Chrisanthi Ventouzi[1], Eleni Karagianni[1], Pavlos Bonatis[1], Christos Kourouklas[1], Parthena Paradisopoulou[1], Emmanouil Scordilis[1], Domenikos Vamvakaris[1], Ioannis Grendas[1], Despoina Kementzetzidou[1], Areti Panou[1], George Karakaisis[1], Ioanna Karagianni[1], Panagiotis Hatzidimitriou[1], Odysseas Galanis[1]

[1]Geophysics Department, School of Geology, Aristotle University of Thessaloniki, Greece
vkarak@geo.auth.gr, kpapaza@geo.auth.gr, ritsa@geo.auth.gr, kiratzi@geo.auth.gr, akostogl@geo.auth.gr, chkkalla@geo.auth.gr, chatniko@geo.auth.gr, xrusven@geo.auth.gr, elkarag@geo.auth.gr, mponatis@geo.auth.gr, ckouroukl@geo.auth.gr, ppara@geo.auth.gr, manolis@geo.auth.gr, dom@geo.auth.gr, igrendas@geo.auth.gr, dkementz@auth.gr, arpanou@geo.auth.gr, karakaisis@geo.auth.gr, ikara@geo.auth.gr, chdimitr@geo.auth.gr, ogalanis@geo.auth.gr

[2]Department of Physical and Environmental Geography, School of Geology, Aristotle University of Thessaloniki, Greece,
mfoumelis@geo.auth.gr

[3]Department of Geodesy and Surveying, School of Rural and Surveying Engineering, Aristotle University of Thessaloniki, Greece,
cpik@topo.auth.gr, stylbith@gmail.com, afotiou@topo.auth.gr

[4]Department of Geology, School of Geology, Aristotle University of Thessaloniki, Greece,
ac@geo.auth.gr

Abstract

On 3 March 2021, the M_w6.3 Tyrnavos earthquake shook much of the Thessalia region, leading to extensive damage in many small towns and villages in the activated area. The first main shock was followed in the next day, on 4th of March 2021, by an "equivalent" main shock with M_w6.0 in the adjacent fault segment. These are the largest earthquakes to strike the northeastern part of Thessalia since the M6.3, 1941

Larissa earthquake. The main shocks triggered extensive liquefaction mainly along the banks of the Titarisios tributary where alluvial flood deposits most probably amplified the ground motions. Our seismic monitoring efforts, with the use of recordings of the regional seismological network along with a dense local network that was installed three days after the seismic excitation initiation, led to the improved understanding the geometry and kinematics of the activated faults. The aftershocks form a north–northwest–trending, east–northeast–dipping, ~40 km long distribution, encompassing the two main ruptures along with minor activated structures, consistent with the rupture length estimated from analysis of regional waveform data and InSAR modeling. The first rupture was expanded bilaterally, the second main shock nucleated at its northern tip, where from this second rupture propagated unilaterally to the north–northwest. The focal mechanisms of the two main shocks support an almost pure normal faulting, similar to the aftershocks fault plane solution determined in this study. The strong ground motion of the March 3 main shock was computed with a stochastic simulation of finite fault model. Coseismic displacements that were detected using a dense GPS / GNSS network of five permanent stations located the Thessaly region, have shown an NNE–SSW extension as expected from the nature and location of the causative fault. Coulomb stress changes due to the coseismic slip of the first main shock, revealed that the hypocentral region of the second main shock was brought closer to failure by more than 10 bars.

Key words: *seismic sequence; finite–fault slip model; seismological geodesy; stress transfer and triggering*

Περίληψη

Στις 3 Μαρτίου 2021 ένας ισχυρός σεισμός μεγέθους M_w*6.3 έπληξε την περιοχή της βόρειας Θεσσαλίας προκαλώντας εκτεταμένες βλάβες σε πόλεις και χωριά στην περιοχή όπου έλαβε χώρα η σεισμική δραστηριότητα. Ο σεισμός αυτός ακολουθήθηκε από μεγάλο πλήθος μετασεισμών, οι περισσότεροι από τους οποίους ήταν αισθητοί από τους κατοίκους της περιοχής, και την επόμενη μέρα, την 4 Μαρτίου 2021, από έναν δεύτερο ισχυρό σεισμό μεγέθους* M_w*6.0 ο οποίος συνδέεται με την ενεργοποίηση γειτονικού ρήγματος. Οι δύο σεισμοί είναι οι ισχυρότεροι που έγιναν στην περιοχή από το 1941, όταν ένας σεισμός μεγέθους M=6.3 έγινε πολύ κοντά στην πόλη της Λάρισας. Οι κύριοι σεισμοί προκάλεσαν εκτεταμένες ρευστοποιήσεις κυρίως στις όχθες του Τιταρίσιου, παραποτάμου του Πηνειού ποταμού, όπου οι αλλουβιακές αποθέσεις πιθανόν ενίσχυσαν τις εδαφικές κινήσεις. Οι ερευνητικές μας προσπάθειες για την παρακολούθηση και την διερεύνηση της σεισμικής δραστηριότητας, οι οποίες βασίστηκαν στην χρήση των* *δεδομένων που λήφθηκαν από τους σταθμούς του Εθνικού Δικτύου Σεισμολογικών Σταθμών καθώς και τους σταθμούς ενός φορητού τοπικού σεισμολογικού δικτύου που εγκαταστάθηκε και άρχισε να παρέχει δεδομένα τρεις μέρες μετά την έναρξη της σεισμικής έξαρσης, οδήγησαν στον καθορισμό και την κατανόηση των γεωμετρικών και κινηματικών ιδιοτήτων των ρηγμάτων που ενεργοποιήθηκαν. Οι μετασεισμοί κατανέμονται σε μία ζώνη μήκους ~40 km, η οποία περιλαμβάνει τις ζώνες διάρρηξης των δύο κύριων σεισμών καθώς και δευτερεύουσες δομές οι οποίες δραστηριοποιήθηκαν αυτό το χρονικό διάστημα, σε συμφωνία με τα αποτελέσματα μοντελοποίησης κυματομορφών και InSAR. Η πρώτη διάρρηξη επεκτάθηκε δικατευθυντικά, με τη δεύτερη κύρια διάρρηξη να αρχίζει στο βορειοδυτικό της άκρο και να αναπτύσσεται μονοκατευθυντικά βόρεια–βορειοδυτικά. Οι μηχανισμοί γένεσης των δύο κύριων σεισμών δείχνουν σχεδόν καθαρά κανονικές διαρρήξεις, σε συμφωνία με την πλειονότητα των μηχανισμών γένεσης των ισχυρότερων μετασεισμών που καθορίσθηκαν στα πλαίσια της εργασίας. Η ισχυρή εδαφική κίνηση του πρώτου κύριου σεισμού υπολογίσθηκε με στοχαστική προσομοίωση μοντέλου ρήγματος πεπερασμένων διαστάσεων. Οι σεισμικές μεταθέσεις που καθορίσθηκαν από τις καταγραφές ενός πυκνού δικτύου πέντε μόνιμων σταθμών GPS / GNSS στην περιοχή της Θεσσαλίας, έδειξαν ΒΒΔ–ΝΝΑ εφελκυσμό όπως αναμένεται από τις ιδιότητες και τη θέση της κύριας διάρρηξης. Ο υπολογισμός των μεταβολών των τάσεων Coulomb λόγω της σεισμικής ολίσθησης του πρώτου κύριου σεισμού, έδειξε αύξηση των θετικών μεταβολών των στατικών τάσεων κατά 10 bar στην εστία του δεύτερου κύριου σεισμού.*

Λέξεις–κλειδιά: *σεισμική ακολουθία, μοντελοποίηση ρήγματος πεπερασμένων διαστάσεων, σεισμολογική γεωδαισία, μεταφορά τάσεων*

1. INTRODUCTION

A strong M_w6.3 earthquake struck a fault segment ~20 km bounding the west flank of Tyrnavos basin, in Thessalia area, central Greece, on the 3rd of March 2021, at 10:16:08.58 UTC (Fig. 1). The main shock is the largest to have struck the area since 1941 when an M6.0 earthquake caused severe damage in the city of Larissa, already bombarded as a battlefield of the Second World War. The epicenter (39.7349°N, 22.1908°E) was about 15 km to the northwest of the city of Larissa, and to the northwest of the Tyrnavos fault, which is the closest fault segment known to be associated with strong earthquakes. This main shock may have initiated onto a fault segment laying to the continuation of Larissa fault and subparallel to Tyrnavos fault segment. The lack of surface ruptures along with the characteristics of the aftershocks distribution, suggest a complex interplay between known active faults with surface expressions and unknown faults with lack of surface expression. The main shock caused extensive damage and due to its position in both a populated urban area and in a fault population that seems to include several active fault segments, its seismological characteristics are expected to shed more light on the development and physics of normal fault systems.

The 3rd of March main shock with M_w6.3 was strongly felt throughout most of the central and north Greek mainland, with severe structural damage in the villages very close to its epicenter. Extensive liquefaction was documented mostly close to the banks along the Titarisios tributary, associated with unconsolidated sediments and shoreline deposits. Many tension cracks were observed and documented from an initial field reconnaissance, mainly to sites located on the hanging wall. Numerous aftershocks followed with a plethora of them being felt by the population of the several small towns and villages located both inside and close to the aftershock area. In the first hours several strong aftershocks ($M \geq 4.0$) followed, distributed to an area longer than the causative fault of the 3rd of March main shock, beyond to both its edges. The off–fault activity that was northwesterly expanded, was longer and denser and encompassed M5 aftershocks as well. At the northwest tip of the first main rupture, the second main shock, with M_w6.0, nucleated in the next day, on the 4th of March, at 18:38:17.46 UTC.

The intense aftershock activity with $M \geq 4.0$ aftershocks continued for a couple of days and then with smaller magnitude but high aftershock occurrence rate. The teleseismic fault plane solutions (https://www.globalcmt.org/CMTsearch.html http://geophysics.geo.auth.gr/ss/) indicated that both earthquakes and the largest aftershocks involved normal slip accommodated on northeast dipping faults, as evidenced by the preliminary aftershock spatial distribution. The vigorous aftershock activity was recorded by the Hellenic Unified Seismological Network (HUSN, https://doi.org/10.7914/SN/HT) and analyzed in the course of routine analysis at the central Seismological Station of the Aristotle University of Thessaloniki. The aftershocks outline a pattern that favors a model of slip on a northeast dipping fault. However, several aftershocks lie off this trend and could be associated with secondary faults of the local fault population. With these possibilities, we aim to resolve the causative faults associated with this seismic excitation. The importance of resolving the faults activated by the two main shocks lies in their domination on the regional seismic hazard.

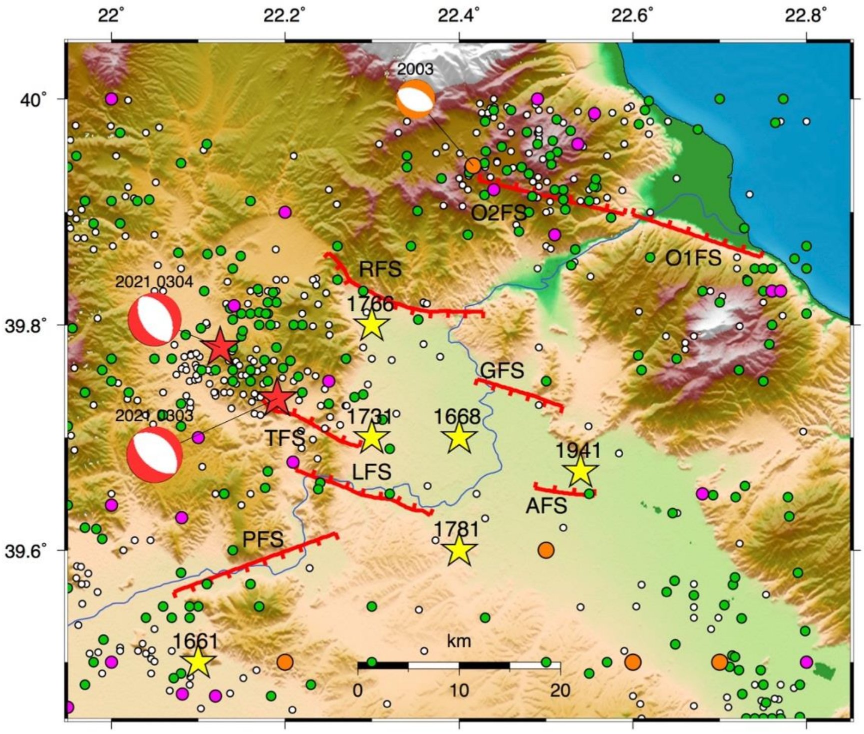

Fig. 1: Seismicity and the major fault segments of the Northern Thessaly Fault System. The white, green, magenta, and orange circles depict the earthquakes with magnitudes between 2.0≤Mw<3.0 since 1984, the 3.0≤Mw<4.0 since 1965, the 4.0≤Mw<5.0 since 1951 and the 5.0≤Mw<6.0 since 1941, respectively. The epicenters of all known strong earthquakes with Mw≥6.0 are shown as yellow stars. The epicenters of the two Mw≥6.0 main shocks are shown by the red stars. Their fault plane solutions, as estimated by the Geophysics Department of Aristotle University of Thessaloniki, are shown as equal area lower hemisphere projections with the compression quadrants colored in red. The available fault plane solution of a moderate (M_w=5.2) earthquake, taken from Global Centroid Moment Tensor (GCMT) database is also plotted. The major segments of the Northern Thessaly Fault System, Omolio 1 (O1FS), Omolio 2 (O2FS), Rodia (RFS), Gyrtoni (GFS), Asmaki (AFS), Larisa (LFS), Tyrnavos (TFS) and Pineias (PFS) are represented with the red solid lines and are taken from Caputo and Pavlides (1993) and the 2020 updated version (v3.0) of NOA Faults database (https://zenodo.org/record/4304613#.YOhi7kxRWEs).

As far as the regional stress pattern concerns, the area of Thessaly shown in Figure 1, accommodates assorted inherited structures and is currently under the influence of an extensional deformation field. The NE–SW extension (Late Miocene – Early Pleistocene) generated the so–called basin–and–range–like system (Caputo, 1990) consisting of a series of horsts and grabens bordered by NW–SE trending faults. The maximum dimensions of the seismogenic structures rarely exceed 20 – 25 km alike in the vast majority of the Greek mainland (Goldsworthy et al., 2002), comprising part of the back arc Aegean area. The activated structures constitute the northwest continuation of the Larissa and Tyrnavos faults (Fig. 1), composing a fault zone that bounds from the eastern Thessaly basin to the west. The general N–S extension in the back arc area on E–W normal faults changes to the NE–SW slip vectors on NW–SE striking normal faults, which might be attributed to the relative block rotation, although it is uncertain how the blocks can be identified and their boundaries to be defined. An inherited fault network might also support the strike differentiation. From a palaeoseismological investigation along the Tyrnavos normal fault, striking ESE–WNW, dipping to north and bounding the Tyrnavos basin, Caputo et al. (2004) suggest vertical coseismic displacements of 20–40 cm and possible recurrence time of 2–2.5 ka.

Seismicity in the 2021 rupture zone is relatively low in the instrumental era (Fig. 1) in comparison with other areas in Greece where known active fault networks control and accommodate the current seismic activity. Historical information is not adequate to support reactivation of the fault segments that accommodate the aftershock activity. The current activity provides an excellent opportunity to investigate the details of the faulting and seismotectonic properties. High quality geodetic observations from continuous Global Positioning System (GNSS) network in the study area, as well as Interferometric Synthetic Aperture Radar (InSAR), were collected in the days immediately following the inception of the seismic excitation. The contribution of satellite geodetic observations can provide a critical advantage for the estimation of earthquake magnitude and mechanism, in conjunction with the traditional seismic measurements. These observations recorded ground–to–satellite distances at successive acquisitions that correspond to surface displacements generated by the three major earthquakes of the sequence, including both the coseismic surface displacement field and early postseismic deformation. We process these geodetic observations and discuss their outcome in combination with relocated aftershock spatial distribution, to constrain the activated fault segments. Static stress change calculations show increased Coulomb stress on the second main shock focus as well as to the vast majority of aftershocks.

2. GEOTECTONIC SETTING

2.1 Geological and structural characteristics

The study area consists of crystalline rocks of the Pelagonian zone, which are unconformably overlain by younger lacustrine and fluvial Neogene and Quaternary deposit. The final configuration of the basement is an aggregate of multiple deformation episodes, both compressional and extensional, which produced brittle and semi–brittle structures of various sense of displacement. The post–orogenic collapse of the Pelagonian zone formed low-angle normal detachment faults, which in turn caused the exhumation of lower tectonostratigraphic units and the formation of characteristic tectonic windows.

This extensional tectonic deformation went on during the neotectonic period, with two main phases:

1. During Upper Miocene – Pliocene, the extensional stress field had a NE–SW direction, causing the deformation of large normal fault zones of NW–SE strike. These fault zones formed long, complex grabens of the same strike throughout central and northern Greece. In the area of Larisa plain, these zones mark its eastern and western margins.

2. During the Quaternary, the extension direction switched slightly to NNE–SSW, causing the formation of younger faults of WNW–ESE strike. These faults define the northern margin of Larisa plain, and they can be classified into two main groups:

    a. Faults dipping to SSW. These are mainly the Rodia and Gyrtoni faults, and they are generally delineating the boundary between the marginal formations to the North and the Larisa plain to the South.

    b. Faults dipping to N and NNW. Those faults (Tyrnavos, Larisa and Asmaki) are antithetic to the ones of the first group. They do not have as intense morphotectonic signature, neither their cumulative deformation is as large. They are considered secondary structures in relation to the ones marking the northern Larisa plain boundary; however, they are of particular interest as they are considered active and are closer to the large population centers of the area, increasing thus the inherent seismic hazard.

Paleoseismological studies in the area (Caputo et al., 2004, 2006; Tsodoulos et al., 2016a, b) showed that there are several faults of low slip rate (up to 0.2 mm/yr) and surface displacement of *ca.*20-40 cm per event. Despite being "slow" faults (i.e. associated with long recurrence interval), they pose a significant risk due to the fact that they can produce events of up to M ~6.5, based on their geological, geometrical and paleoseismological characteristics.

2.2 Seismic faults and surface effects

Based on field work and the available seismological information (from http://geophysics.geo.auth.ss/; doi:10.7914/SN/HT), the causative seismic fault belongs to a low–angle normal fault zone, which is considered blind, as it does not reach the surface (Pavlides et al., 2021). Its dip angle of 36º is in good agreement with the attitudes of bedrock detachment faults that were caused by the collapse of the Pelagonian orogene (Kilias et al., 2010, 2016). This is of particular importance, as it is a non typical behavior of an older, inherited alpine structure with no surface expression. The earthquake sequence of March 2021 formed various secondary effects, which are shown in Figure 2. They can generally be classified into the following groups (Ganas et al., 2021; Pavlides et al., 2021; Valkaniotis et al., 2021):

1. Liquefaction: they were mainly formed in the area close to the northern banks of Pinios river, near Piniada village, while a smaller liquefied area was formed near Vlachogianni village in the alluvial plain of Titarisios river. In both areas, the liquefied material consists of fine-grained alluvial deposits, while in the main liquefied area of Piniada the vast majority of liquefaction structures was concentrated in paleobeds of Pinios River. They were particularly susceptible to liquefaction, because they were filled with fine-grained sediments after their abandonment, and they are mechanically weaker zones.

2. Surface ruptures. Surface ruptures were localized, generally of short length and they are interpreted as secondary structures. Although small ruptures were scattered throughout the area (interpreted as local effects of gravitational slope failure), significant linear structures were observed in mainly two sites:

2.1. SE of Mesochori. They are small–scale (~1 km) ruptures with displacement of a few cm to the SW and occasional heave of 2–3 cm. They coincide with a morphotectonic NW–SE directed lineament, which is most probably associated with a normal fault that delineates Titarisios valley. Based on seismological data (epicenter location, focal mechanism etc.) it is considered that movement on this fault was triggered by the activation of the main fault. Therefore, it is considered a secondary deformation on a sympathetic supra-detachment fault.

2.2. Zarkos – Megalo Eleftherochori. They consist of a set of spaced open ruptures of NW-SE strike, with no significant vertical displacement. Their position coincides with the extrapolated projection of the top of the main blind low-angle fault. These fractures are considered secondary, although they are characteristic of the geological expression of the seismic fault.

3. Rockfalls. Rockfalls and slope failures were observed throughout the affected area (i.e. Damasi, Vlachogianni, Grizano, Damasouli, etc.), which are not associated with the activation of any of the faults, but their distribution is rather random and dependent only on the local geotechnical and morphological conditions.

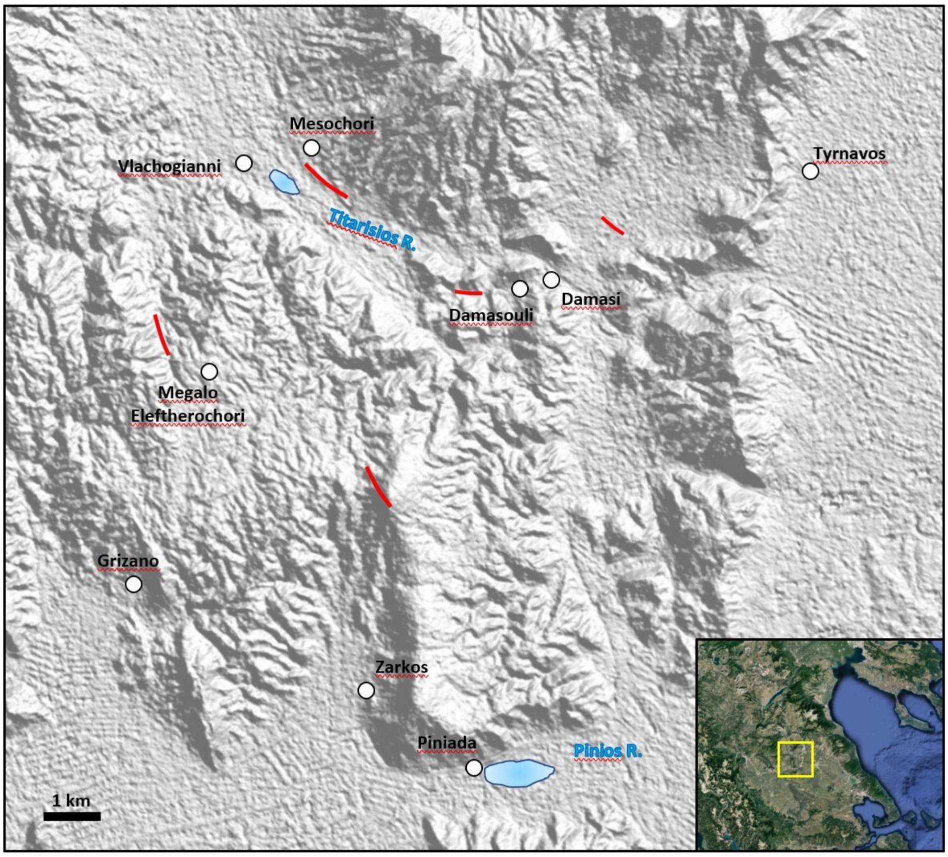

Fig. 2: Location map of the study area, the secondary effects and the sites mentioned in the text. Red lines: surface ruptures. Blue areas: liquefied areas. Inset shows the location of the area in central Greece.

3. THE AFTERSHOCK SEQUENCE

3.1 Aftershock data

To accomplish a detailed investigation of the aftershock pattern and the evolution of the aftershock sequence, we analyzed seismic data recorded between 3 of March and

03 of April 2021, by the stations of both the Hellenic Unified Seismological Network (HUSN) and the portable temporary network, and retrieved in the Seismological Station of the Geophysics Department of the Aristotle University of Thessaloniki (https://doi.org/10.7914/SN/HT), for manual phase picking and initial location. Stations up to the distance of ~150 km were selected for the relocation improvement, and are shown in Figure 3 as inverted red triangles along with the epicenters of the two main shocks, which are depicted by stars. A portable seismic network of seven (7) stations was installed in the epicentral area to enhance seismicity detectability and location improvement, also shown in Figure 3 and in larger scale in the inset map. The inverted yellow triangles depict the sites of the stations the recordings of which were used for the moment tensor inversion.

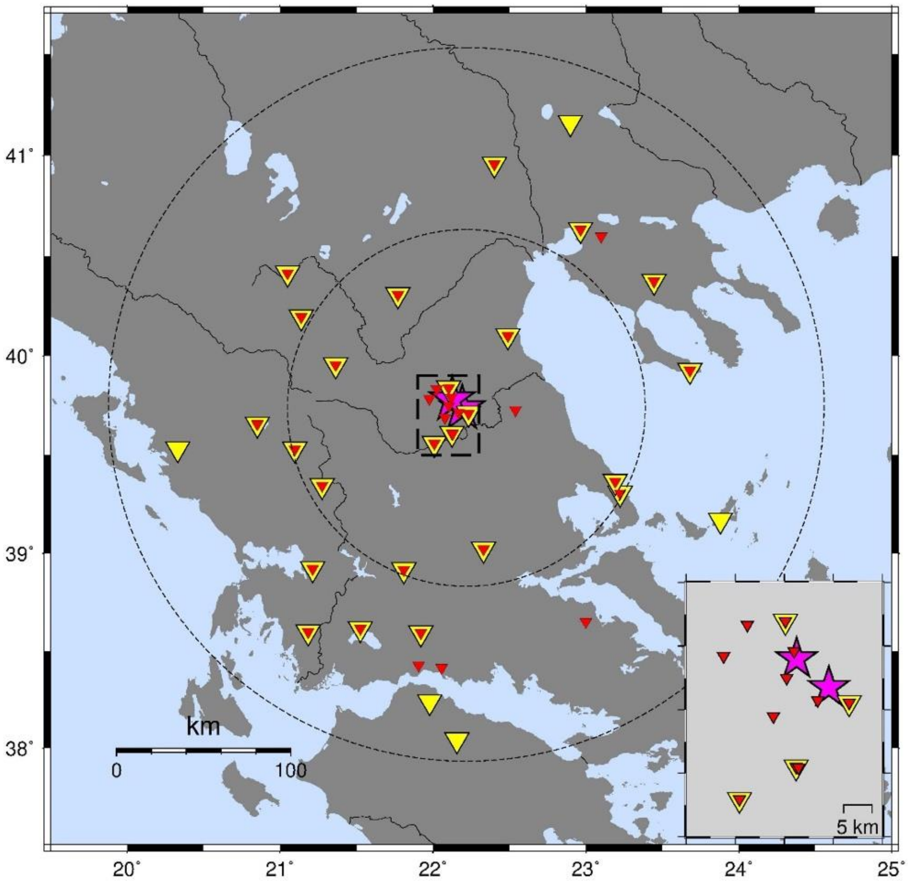

Fig. 3: Stations from the regional Hellenic Unified Seismological Network (HUSN) the recordings of which were used in earthquake relocation (red inverted triangles) and moment tensor inversions (yellow inverted triangles). Inset map shows the stations of the dense portable network. The magenta stars depict the two main shocks epicenters.

3.2 Aftershock location

A first improved location was achieved by setting a minimum number of eight (8) arrival times for each earthquake and calculating a V_p/V_s ratio that was found equal to 1.76. The velocity model given in Table 1 was defined using the *Velest* software (Kissling et al., 1994) and earthquakes that were recorder by the local network. The lateral inhomogeneities were considered by calculating and incorporating in the location process, time corrections for each seismological station.

Using the program Hypoinverse (Klein, 2002), we calculated mean 1σ error for absolute horizontal error 0.68 ± 1.02 km and vertical error 1.37 ± 2.01 km. We applied then waveform relocation process, which provided relative errors an order of magnitude smaller than the absolute errors. The relocation was accomplished with the HypoDD software (Waldhauser and Ellsworth, 2000) using catalog differential times to obtain more precise origin times for waveform preparation for the next step. Then, we used cross–correlation differential times (Schaff et al., 2004) along with catalog differential times performed by the HypoDD computer program (Waldhauser and Ellsworth, 2000) and cross correlation differential times (Schaff and Waldhauser, 2005).

Table 1. P–wave velocity model for the location of the sequence.

Depth (km)	**V_p (km/s)**
0.0–2.0	5.35
2.0–2.5	5.41
2.5–6.0	5.73
6.0–7.0	5.97
7.0–8.0	6.04
8.0–9.0	6.10
9.0–13.0	6.15
13.0–14.0	6.24
14.0–15.0	6.32
15.0–29.0	6.46
29.0–34.0	7.65
≥34.0	7.8

3.3 Aftershock fault plane solutions

Moment tensors were estimated for twenty four (24) of the strongest aftershocks while for the two mainshocks we adopted the solutions of GCMT (https://www.globalcmt.org/CMTsearch.html) and GFZ (https://geofon.gfz-potsdam.de/eqinfo/form.php) solutions, respectively. The moment tensor inversions for the aftershocks were performed with the Grond software (Heimann et al. 2018) which operates within the Pyrocko toolbox (Heimann et al. 2017), using recordings from the regional seismological stations (shown in Figure 3 with yellow triangles).

The waveforms used for the inversions were filtered in the 0.05–0.1 Hz frequency band and applying a taper fall-off factor of 1.1 [fmin/factor, fmax*factor]. The Green's functions were estimated by the QSEIS program (Wang, 1999) operated through the Pyrocko software, and using the crustal model of Table 1. The inversion was performed for a deviatoric moment tensor in the time domain assuming a point source model. A Bayessian bootstrap–based probabilistic procedure was employed for 25000 iterations, aiming to minimize the L2-norm misfit between observed and calculated waveforms with 200 parallel bootstrap chains for estimating the uncertainties.

3.4 Aftershock distribution

The aftershock seismicity catalog extends for 32 days and comprises 1476 aftershocks, which have been relocated with high accuracy. This provides the tool of detailing the properties of the two main ruptures and the secondary faults of the local fault network that have been possibly triggered by the slip redistribution and stress transfer mainly due to the coseismic slip of the two largest (M_w6.3 & 6.0) ruptures. The spatial aftershock distribution (Fig. 4) defines a narrow strip exceeding in length the 50 km and aligned in a general NW–SE direction.

The epicentral alignment agrees well with the normal faulting type of the two main shocks, the fault length is however appreciably larger than expected from their magnitudes, estimated to be of the order of 20 km each one from empirical relations for normal faults by both Wells and Coppersmith (1994) and Papazachos et al. (2004).

Table 2. Information on the fault plane solutions determined in this study along with the ones adopted from other Institutions, referred in the last column, for earthquakes occurred between 03/03/2021 to 21/03/2021.

N	Date	Time	Lat (º)	Long (º)	h (km)	M_w	M_o (Nm)	Strike (º)	Dip (º)	Rake (º)	Ref
1	**2021/03/03**	10:16:08.58	39.7349	22.1908	9.5	**6.3**	2.20e+18	314	36	-88	AUTH
2	**2021/03/03**	11:19:02.10	39.7287	22.2102	7.98	4.0	8.99e+14	283	29	-153	This study
3	**2021/03/03**	11:45:45.70	39.6909	22.2025	8.29	5.2	6.56e+16	310	47	-74	This study
4	**2021/03/03**	18:24:08.72	39.7225	22.0813	10.0	5.1	5.83e+16	319	38	-62	This study
5	**2021/03/04**	02:43:38.38	39.7111	22.2235	9.6	4.2	2.04e+15	331	54	-57	This study
6	**2021/03/04**	05:10:20.54	39.6198	22.2651	4.4	3.7	3.47e+14	312	41	-94	This study
7	**2021/03/04**	09:36:15.70	39.7803	22.1135	7.9	4.5	6.46e+15	132	53	-81	This study
8	**2021/03/04**	18:38:17.46	39.7799	22.1252	12.00	**6.0**	1.30e+18	329	41	-88	GFZ
9	**2021/03/04**	19:23:51.18	39.8224	21.9313	7.86	5.1	5.84e+16	287	30	-91	This study
10	**2021/03/05**	19:43:23.72	39.7601	21.9722	19.00	3.9	7.68e+14	282	57	-87	This study
11	**2021/03/06**	16:36:18.13	39.6709	22.2383	2.63	4.1	1.44e+15	257	35	168	This study
12	**2021/03/06**	19:47:40.21	39.8294	22.0658	2.47	4.2	2.11e+15	302	39	-105	This study
13	**2021/03/08**	18:00:45.09	39.5990	22.2724	1.85	4.0	1.17e+15	309	38	-112	This study
14	**2021/03/08**	18:07:03.14	39.6062	22.2600	2.45	3.9	7.47e+14	312	40	-105	This study
15	**2021/03/08**	18:34:20.77	39.7099	22.1062	10.88	4.0	9.63e+14	237	88	159	This study
16	**2021/03/09**	04:30:32.86	39.8735	21.9836	11.39	3.8	5.48e+14	266	47	-109	This study
17	**2021/03/11**	14:19:40.41	39.7788	22.0791	5.38	4.3	3.03e+15	267	49	-105	This study
18	**2021/03/12**	12:57:50.14	39.8281	22.0150	3.34	5.5	2.25ε+17	286	53	-92	This study
19	**2021/03/12**	14:11:35.99	39.8198	22.0421	2.78	4.0	1.16e+15	311	40	-100	This study
20	**2021/03/12**	15:00:20.09	39.8186	22.0196	5.75	4.1	1.62e+15	286	47	-80	This study
21	**2021/03/13**	15:09:12.83	39.8038	22.0045	4.48	4.3	3.29e+15	278	43	-85	This study
22	**2021/03/15**	15:43:36.39	39.7500	22.1209	5.54	4.5	6.21e+15	349	37	-44	This study
23	**2021/03/17**	03:51:32.50	39.6287	22.2657	4.70	4.0	9.57e+14	274	60	-110	This study
24	**2021/03/19**	15:50:17.16	39.8141	22.0314	6.20	4.0	9.88e+14	297	61	-101	This study
25	**2021/03/19**	20:39:19.56	39.7849	22.1073	7.90	3.8	5.86e+14	311	34	-109	This study
26	**2021/03/21**	17:15:54.00	39.7722	22.1036	8.9	4.1	1.59e+15	321	37	-52	This study

It must be noticed here that these two scaling relations are neither the only ones nor the most reliable, among others. They have been used nevertheless in a plethora of studies and are used here for the sake of comparison. The highly accurate hypocentral relocation gears the decomposition of the aftershock seismicity into components associated with distinct fault segments. Since the aftershock activity covers a larger area than expected from the causative faults of the two main shocks, the identification is seeking of both the two main ruptures dimensions and position and the "off fault" activity, connected with the activated secondary faults of the local fault network. Fault plane solutions imply almost pure normal faulting onto planes striking NW–SE and dipping to the northeast (Table 2 and Fig. 4). This strike is compatible with the observed surface expressions as described in the previous section. The fault plane solutions of the two main shocks as have been determined by other agencies also show almost pure normal faulting with comparable strike and dip angles (Table 2).

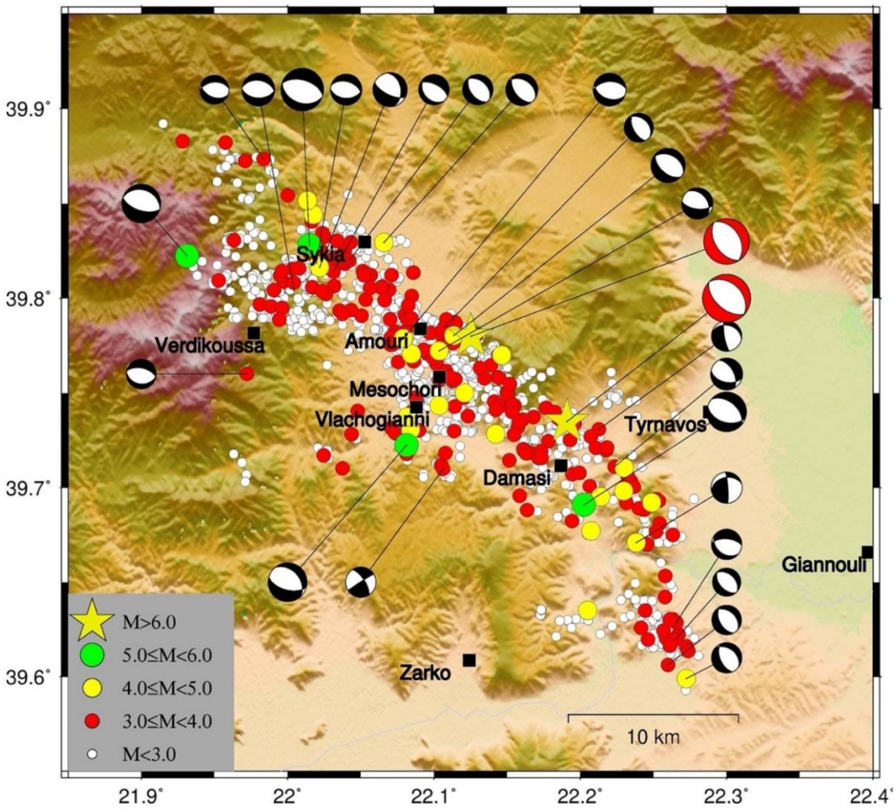

Fig. 4: Epicenters of the relocated aftershocks of the sequence for the period March 3–April 3, 2021, shown by circles with different color and size, according to their magnitude range as shown in the inset. Fault plane solutions are shown as lower hemisphere equal area projections, with the compression quadrants colored, red for the two main shocks and black for all aftershocks.

The largest ($M_w \geq 5.0$) aftershocks (green circles in Fig. 4) occurred close in time with the two main shocks but outside the main rupture areas, as detailed below in the text and shown in Figures 5 and 6, created their own aftershocks and revealing secondary fault segments of the local fault network. The northernmost part of the epicentral distribution, encompasses two strong ($M_w \geq 5.0$) aftershocks, several moderate ($M_w \geq 4.0$) ones, and dense minor magnitude seismicity forming a remarkable seismicity cloud and implying the activation of several minor fault segments, either subparallel or antithetic, an observation that needs further analysis. The southeastern distinctive cluster shown in Figure 4 is formed after a spatial gap in the activity, is closely connected in time with the first main shock, with an epicentral alignment almost at the same strike, but stepping by a few kilometers.

The first main shock relocated epicenter lies to the northwest of the Tyrnavos normal fault, revealing an adjacent activated fault segment that cannot be associated with any known earthquake. The abundant aftershocks that follow in the first hours were adequate to shed light on the causative fault geometrical parameters. Figure 5a shows the aftershock activity in the first six hours after the occurrence of the March 3, 2021, main shock. This aftershock zone outlines a ~17 km long zone, with a NW–SE orientation (~315^o), in full agreement with the strike of the focal mechanism determined by GCMT (Table 2) and the aftershocks distributed either side of the main shock epicenter. The stronger ($M \geq 4.0$) aftershocks lie between the main shock epicenter (yellow star) and the southern fault edge, where the M_w=5.2 aftershock (green circle) was also nucleated. The strike–normal cross section (Fig. 5b) indicates that the depth range of the overall seismicity was from ~4 to ~12 km. The largest aftershock occurred at the down–dip end of the main rupture, slightly dipper than the main shock. The main shock nucleated at the lower part of the seismogenic layer, consistently with the aftershocks alignment in depth that presents a dip angle of 38^o, in the least squares' sense, again in full agreement with the fault plane solution.

The duration of six hours was selected because for longer periods there is a shift of the seismicity to the NW in the area where the second main shock with M=6.0 occurred in the next day. This activity could be foreshock activity of the second strong earthquake and not aftershocks of the main shock. In addition, there is evidence that the magnitude M=5.1 earthquake which occurred in less than one hour after the main shock (Fig. 6, green symbol west of the main shock). Most of the first six hours seismicity defines the rupture dimensions (blue rectangle in the map view projection in Figure 6a), a length of 15 km and a width of 8 km, as they are given in detail in Table 3. In the cross section (Fig. 6b), we observe a noticeable fit of a dip at 46^o, a typical dip angle for normal faults in continental areas (Abers et al., 1997), and in agreement with the centroid moment tensor solution listed in Table 2.

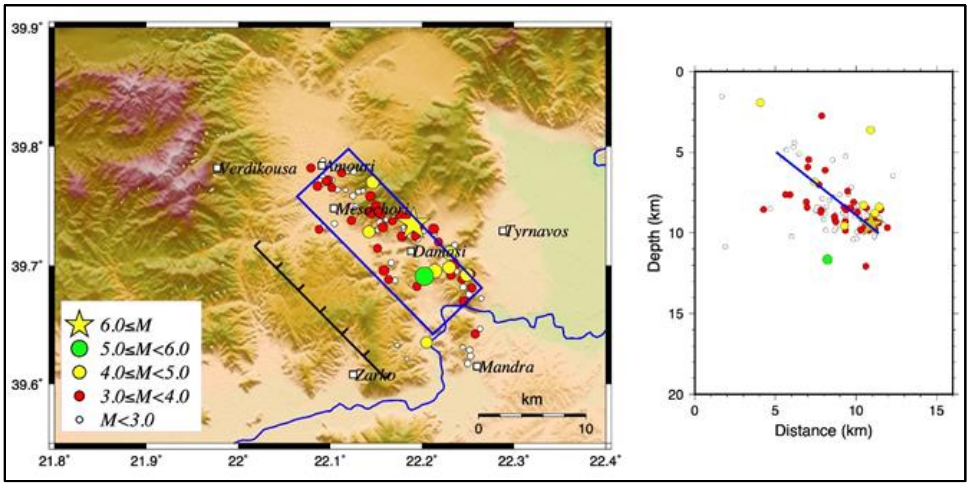

Fig. 5: (a) Relief and aftershock location map for six hours after the occurrence of the first main shock (3 March 2021). The blue rectangle indicates the surface projection of the rupture area. (b) Strike–normal cross section with the seismicity shown in (a). The blue line approximates the fault dip. Symbols are as in Figure 4.

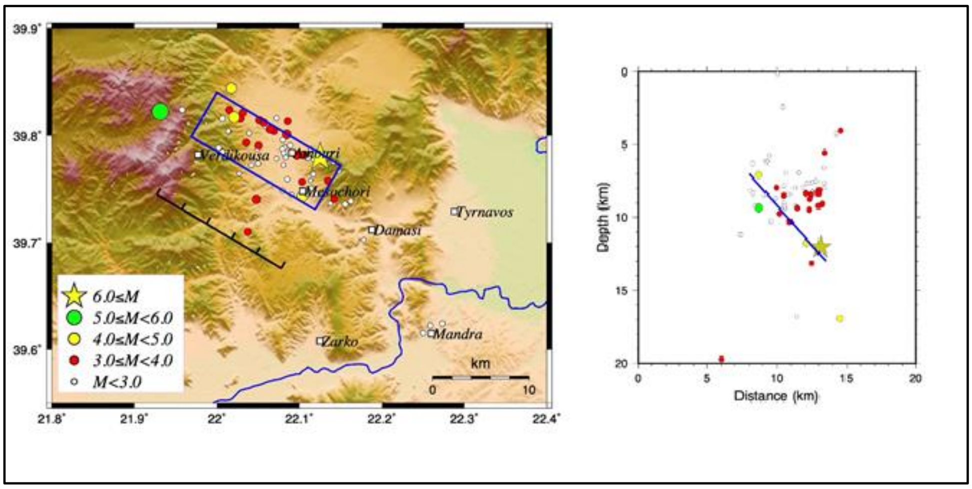

Fig. 6: (a) Same as in Figure 5a for six hours after the occurrence of the second main shock (4 March 2021). (b) Strike–normal cross section with the seismicity shown in (a). The blue line approximates the fault dip. Symbols are as in Figure 4.

Table 3. Faulting parameters of the two causative main fault segments as derived from the relocated aftershocks 3D spatial distribution. Mean slip is calculated from the seismic moment and the fault dimensions, $u=M_o/\mu S$ (considering rigidity $\mu=3.3*10^{11}$ dyn cm^{-2}).

Main shock	**1st 2021-03-03**	**2nd 2021-03-04**
Origin time	10:16:08.6	18:38:17.5
Epicenter	39.7349/22.1908	39.7799/22.1252
Depth (km)	9.5	12.0
M_w	6.3	6.0
M_o	$3.14*10^{25}$ dyn*cm	$1.12*10^{25}$dyn*cm
Strike /dip (from aftershock distribution)	315°/38°	300°/46°
Length and width from aftershocks	17 km / 8 km	15 km / 8 km
Mean slip	70 cm	28.3 cm

3.5 Temporal evolution of the sequence

The spatial and temporal characteristics of an aftershock sequence are a manifestation of internal crustal dynamics involving the redistribution of stress and displacement fields. To seek for these characteristics the spatio–temporal evolution of the sequence is investigated (Fig. 7), by detailing the pattern of the aftershock locations over time. The duration of the plot equals to 12 days, starting from the first main shock (3 March 2021, M_w6.3) occurrence. The distances are measured along an SE–NW trending axis, running parallel to the epicentral alignment shown in Figure 3. Three ellipses are drawn to delimit three distinctive spatiotemporal clusters. The southern ellipse encloses a dense cluster beyond the southern edge of the fault segment associated with the first main shock, commenced synchronously with the beginning of the seismic excitation, and located to the south of Pinios River. The first main shock is associated with a fault segment 17 km long, defined with the first hours' aftershocks that are enclosed in the second ellipse. All the $M\geq4.0$ aftershocks are included in this set, with their spatial distribution implying bilateral rupture propagation. Beyond to both edges of the main fault two $M\geq5.0$ aftershocks (green circles in Figure 7) occurred in the first day, implying crack tip stress concentration because of the coseismic slip.

Northern more, $M\geq4.0$ aftershocks (yellow circles in Figure 7) appear densely concentrated until the occurrence of the second main shock in the evening of the next day with M_w=6.0 (the second star in Figure 7). Thereafter, aftershocks concentrate to the northwest of the second main shock epicenter, covering a zone of 15 km in length (third ellipse in Figure 7), implying unilateral rupture. To the prolongation of this rupture and in less than one hour afterwards, an M=5.1 aftershock took place, around which the activity is rather sparse. The fourth and last strong ($M \geq 5.0$) aftershock took place at the northwestern part of the activated area where the activity was rather hypotonic, on 12 March, with $M_w=5.5$ (last green circle in Figure 7). Its occurrence, however, rejuvenated the seismicity, with a dense spatiotemporal cluster of M3 aftershocks (red circles close to its position in the plot of Figure 7).

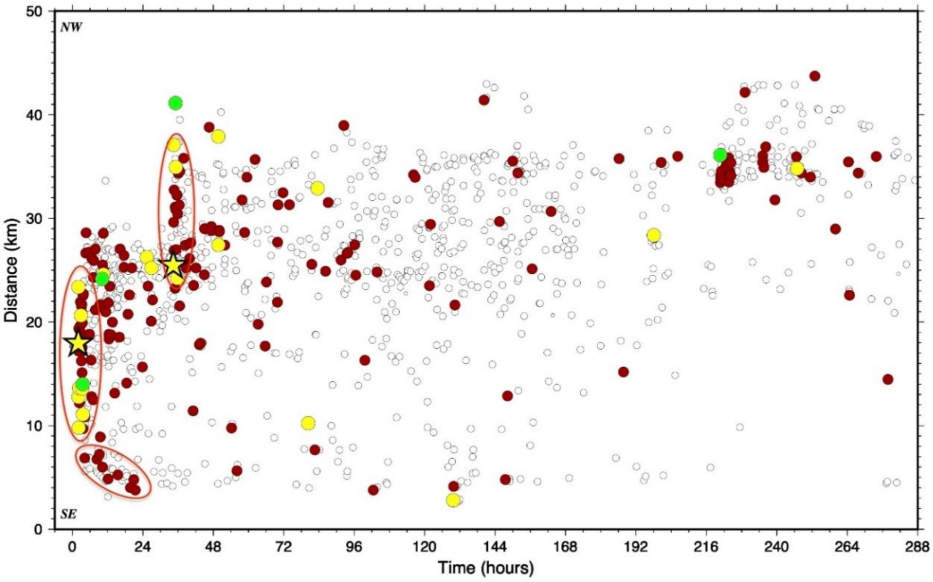

Fig. 7: Space–time plot during the first twelve days of the 2021 Tyrnavos seismic sequence. The ellipses define distinctive seismicity clustering for the two main shock and a southern activated minor fault segment. Symbols are as in Figure 4.

4. FINITE–FAULT SLIP INVERSIONS

We used inversion of regionally recorded seismic waveforms to resolve the spatial and temporal distribution of the rupture slip of the two main shocks, which occurred on 3 and 4 March 2021, respectively. Slip models describe the time history of the rupture kinematics with no specific reference to the causative stresses. Good knowledge of the detailed rupture process is essential for realistic simulations of strong ground motion, especially in the case of a complex source.

4.1 Data and methods

The seismic data consist of three–component waveforms recorded by broad band seismometers at stations located at regional distances. The location of the earthquakes is quite optimum within the seismic networks of Greece, and a good coverage in all azimuths was attained (Fig. 8a). Preprocessing of the initial waveforms includes removal of trend, downsampling to 1 sps, correction for the instrument response, and integration to displacement. Synthetic data were calculated using Green’s functions, which are the displacements at the used stations due to an impulsive force and connect data and model parameters. We calculated theoretical Green's functions calculated by a frequency–wavenumber integration method, adopting the 1-D velocity profile (Fig. 8b) of Novotny et al. (2001). The velocity model has proven to be effective in modeling regional wave propagation for earthquakes in Greece. Both the data and theoretical Green's functions were bandpass filtered using an acausal Butterworth filter with corners at 0.-2 Hz and 0.08 Hz.

To invert the data we adopt a nonnegative, least-squares inversion method with simultaneous smoothing and damping, as developed by Dreger and Kaverina (2000) and Kaverina et al. (2002). This method inverts for fault slip distributed over a grid of point sources that are triggered according to the passage of a circular rupture front. If required by the data, distortions from the constant rupture velocity and variations in the rise time can be accomplished by using the multiple–time–window technique of Hartzell and Heaton (1983). This method allows each point source to rupture in any of the time windows considered after the initial rupture trigger time. Smoothing, slip positivity, and a scalar moment minimization constraint is applied in all the inversions (see also Benetatos et al., 2007). The amount of smoothing can affect the peak value of slip but does not obscure the average distribution of slip.

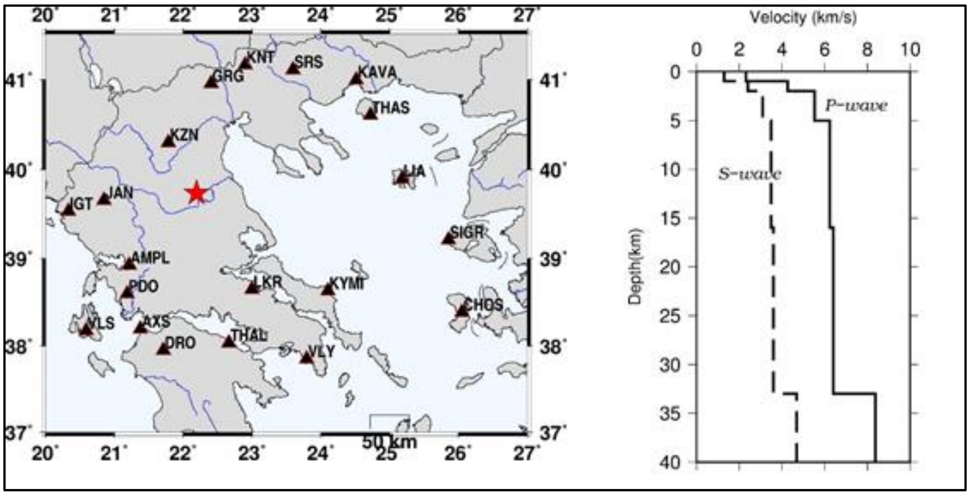

Fig. 8: (a) Broad-band stations (triangles) whose waveforms were used in the inversions. (b) 1-D velocity model adopted to calculate Green’s functions at regional distances, to perform the low–frequency inversions.

4.2 Model parameterization

To setup the fault models for the inversions, the initial fault models have at least doubled dimensions of those expected from empirical relations, for the size of the earthquakes examined, in order to corroborate unilateral rupture propagation and allow the slip to go to its preferable location. The dislocation rise time in each case is adopted using appropriate scaling relations from Somerville et al (1999). The rupture speed is grid searched and values that fit the data and provide reasonable spatial distribution of the slip are finally chosen. In both cases, the hypocenter parameters are the herein relocated ones.

4.3 Preferred Slip Models

Mainshock of 3 March 2021: We adopted the geometry of the fault plane with strike, dip, and rake angles, equal to 314°/36°/-88°, respectively, as calculated by time–domain moment tensor inversion and reported to EMSC (AUTH solution). The initial fault of 35 km × 18 km in length and width, respectively, was discretized in 1 km × 1 km, resulting in 630 subfaults where slip is determined in the model. Given the assumed depth of the hypocenter, of 9.5 km, the dip (36°) of the fault, and the subfault dimension, the top of the fault system is at 2.44 km depth (Table 1). The dislocation rise time is characterized by an isosceles triangle with a duration of 0.8s.

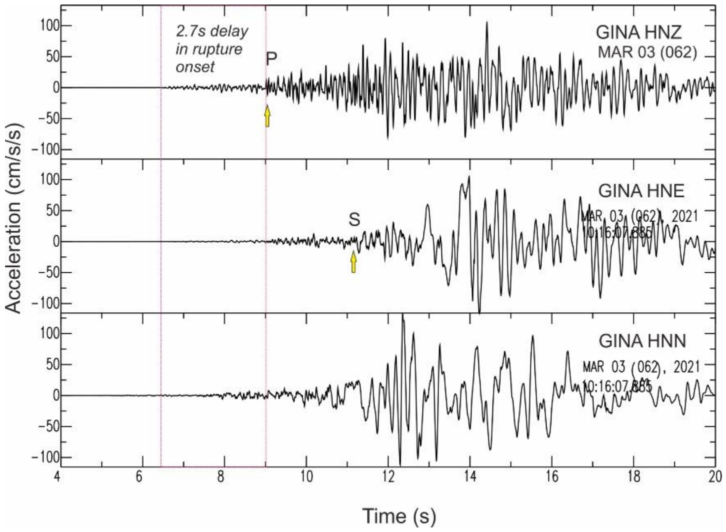

Fig. 9: Three–component acceleration recordings of the mainshock at station GINA (Giannouli in Fig. 4), located ~17 km away from the epicenter. A delay of ~2.7s is visible in rupture onset, which is corroborated in the finite-fault inversions by a rather slow rupture speed required by the data.

A series of initial inversions were performed to examine the stability of the location of the major slip patches. We started with a single fault that ruptures within a single time window. Then we applied the method of multiple time windows, again for a single fault segment that ruptures within four time–windows. Rupture speed cannot be satisfactorily resolved. A range of rupture speeds was tested, and for the single time window case, a slow rupture speed (in the range 1.2 km/s to 1.8 km/s) provides better fit to the data. This slow rupture speed was also found to corroborate the ~2.7s delay in the rupture onset as observed in the accelerograms from the closest stations (Fig. 9). For the case of multiple time-windows a rupture speed of 2.5 km/s which is 74% of the Vs velocity at the source depth, provides the same slip distribution and slightly improves the fit.

Figure 10 summarizes the slip model for the main shock. Slip is mainly confined in one major patch located updip from the hypocenter and towards ESE. The centroid is 7.5 km away from the epicenter corroborating the 6.1s difference between the centroid time and the hypocenter time as reported by GCMT, and the rupture speed considered.

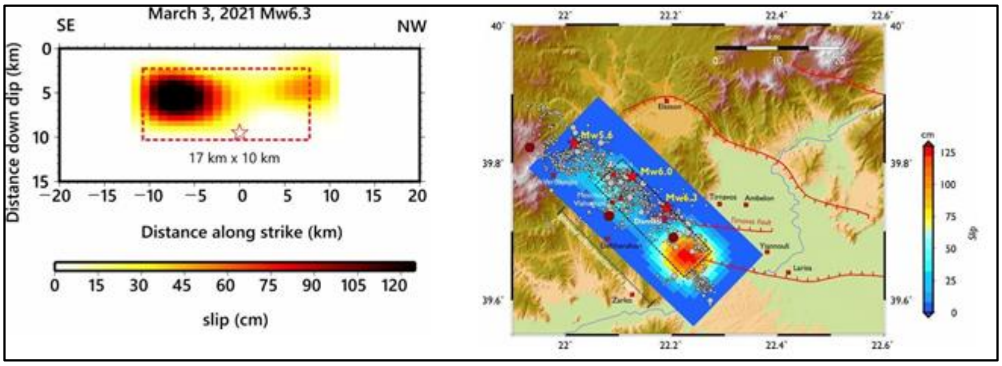

Fig. 10: Left: Spatial distribution of slip for the mainshock, along 314° fault strike direction. Slip is confined in a major slip patch (dashed rectangle) located 7.5 km SE of the hypocenter (asterisk). The rupture initiated at the bottom of the fault and propagated updip. Right: Projection to the surface of the slip distribution alongside the relocated aftershocks (circles). The dashed rectangle denotes the fault dimensions associated with the main shock, and the dashed line denotes the inferred surface projection of the fault. For this model parameterization the resolved seismic moment is $3.82 \cdot 10^{25}$ dyn·cm, resulting in $M_w=6.32$ and the average slip value is 70 cm for a shear modulus of $3.2*10^{11}$ dyn/cm².

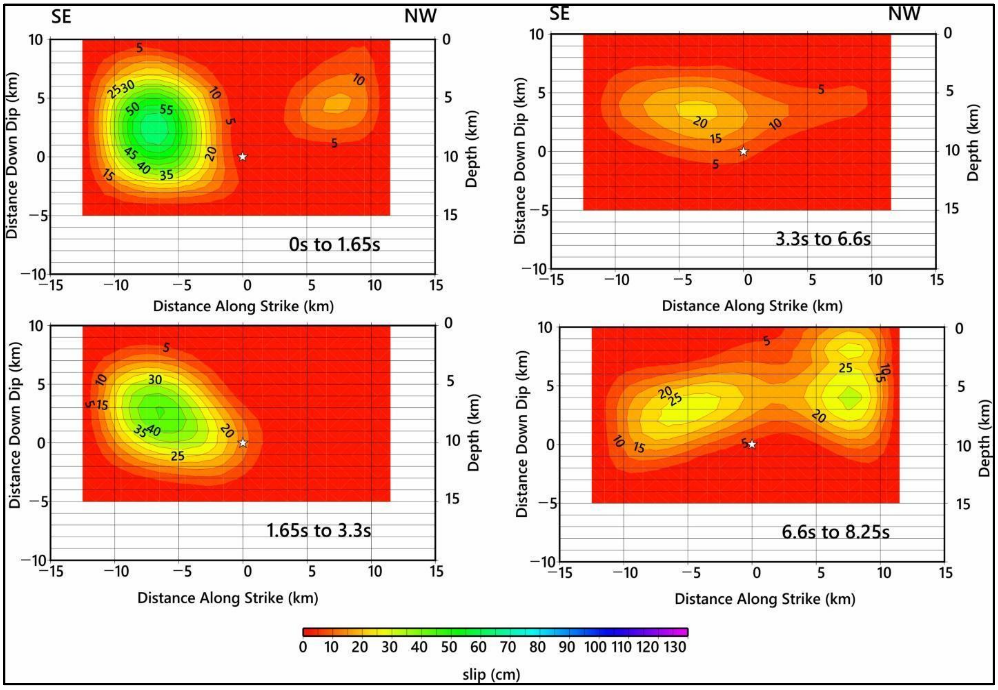

Fig. 11: Snapshots of the incremental evolution of rupture history, showing that mainly it propagated towards ESE, attaining a bilateral propagation at later stages. Contours depict slip amplitudes. Note the absolute depth scale on the right of each panel.

The rupture propagated towards ESE (Fig. 10) and persisted in that ESE direction until the later stages of the rupture process when it propagated mainly bilaterally. In all cases the updip propagation is evident. It is worth noting that the weak slip patch at the WNW corner, that is, at the westernmost edge of the fault, is clearly evident, even from the initial stage of the rupture. This area has subsequently ruptured during the 4 March second aftershock. Although the mechanism of its occurrence is not fully understood, the existence of many aftershocks surrounding the areas of large slip indicates the importance of the stress redistribution by the main shock.

Main shock of 4 March 2021: The reported focal mechanism solutions for the strongest aftershock, both by NOA and AUTH, even though determined by different methods, are remarkably compatible. Other national agencies, whose solutions are based on teleseismic modelling (GCMT for example), were not able to calculate a moment tensor, because the waveforms were obscured from another global large event that occurred at the same time. We adopted the AUTH solution and in this case, the fault plane has strike, dip, and rake angles, equal to 287°/30°/-92°, dipping to NE again, as the main shock. The rupture speed was constrained to be 1.7 km/s.

Figures 12 and 13 summarize the slip models for the aftershock. Slip is confined in a well-determined single asymmetric patch (Fig. 12) updip from the hypocenter, indicating a rather bilateral rupture propagation for this event. For this model parameterization the resolved seismic moment is 1.00E18 N m, resulting in M_w=5.97 and the average slip value is 23 cm.

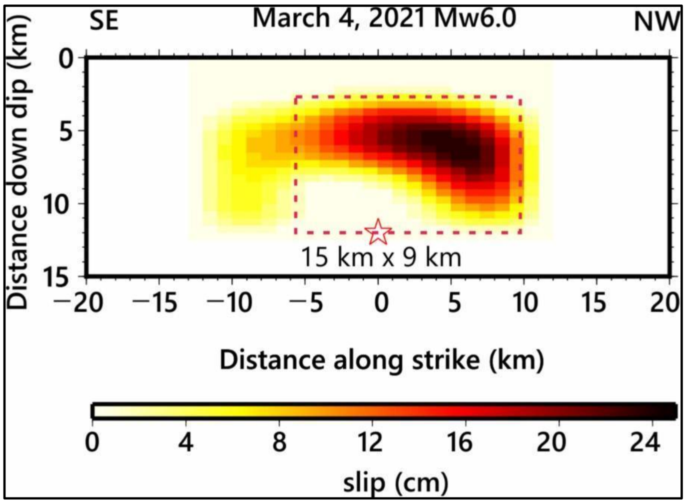

Fig. 12: Spatial distribution of slip for the March 4 main shock, along 287° fault strike direction. Slip is confined in a major slip patch (dashed rectangle) directly updip from the hypocenter (asterisk) and to its NW.

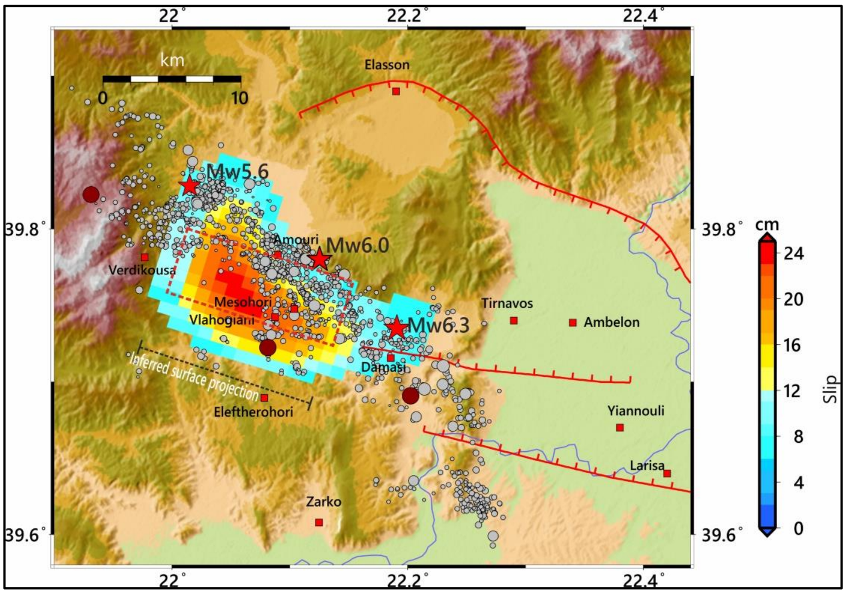

Fig. 13: Surface projection of the aftershock's slip model (Fig. 12) alongside relocated aftershocks (circles). A 30% trimming to the peak slip is imposed to the model for clarity. The dashed rectangle and line denote the fault that rupture and its inferred surface projection, respectively.

For the resolved moment and confining the ruptured area (15 km × 9 km) into a circular area, the Brune–type stress drop for the second main shock is 16 bars (1.6 MPa).

4.4 ShakeMap of the 3 March 2021 Main shock

To examine the spatial distribution of the intensity of ground motion we used the preferred slip distribution model for the first main shock, in order to perform forward modeling and calculate synthetic velocity records. We used a grid covering the broader region (Fig. 14) and in each node we calculated two horizontal velocity records. Using the modules of SAC we depict the maximum values of each component, and we contour their arithmetic average (Fig. 14a). The synthetic values do not take into account any site–effect, as a detailed profile for the epicentral region is not available, yet.

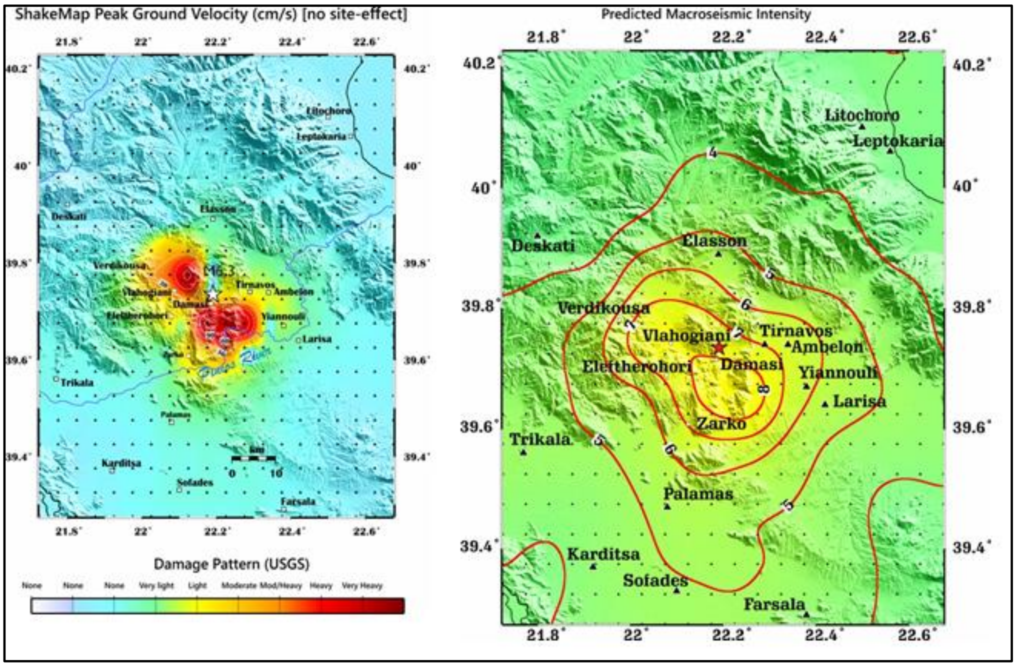

Fig. 14: (a) ShakeMap calculated using forward modeling and the slip model for the first main shock. (b) Predicted distribution of macroseismic intensities using suitable scaling relations for Greece (Caprio et al., 2015).

We used global scaling relations, which were obtained using extensive data from the Mediterranean (Caprio et al., 2015) to calculated predicted macroseismic intensities (Fig. 14b). We checked these predictions with reported intensities based on citizens information or calculated from observed records using scaling relations, as they are reported at the NOA website. In all cases, we found very good agreement. For example, at the close station GINA (Giannouli), the reported intensity from NOA is VI, in accordance with our predictions. Overall, intensity 6, encloses the region which was most affected by the earthquake.

The results of Figures 14 and 15 suggest that the reliable estimation of the expected strong seismic motion level in the epicentral area requires the correct assessment of the effect of both the position of the fault and the slip model (Figure 11), but also the effect of local geology. Considering that the simulations presented in Figure 11 concern synthetic recordings of velocity up to the frequency of 2Hz, an attempt was made to calculate the strong seismic motion of the first main shock (2021-03-03, M_w=6.3) using the stochastic finite–fault simulation approach (EXSIM algorithm, Motazedian and Atkinson, 2005; Boore, 2009). For this purpose, the geometric and kinematic characteristics of the fault of the main earthquake were employed, as they are presented in Table 3.

Initially the strong ground motion was calculated for all locations for which acceleration records were available, as well as for a dense grid (~1200 points) which covers the broader focal area, as shown in Figure 15a (area with limits 39.0–40.5° N and 21.2–23.0° E, with a step of 0.02^o (~2 km) in the meizoseismal area, and a step of 0.1^o in the broader area]. For these grid points, synthetic acceleration records were calculated for three soil categories, namely B, C and D according to UBC/NEHRP (practically equivalent to categories A, B and C according to EN1998-1), depending on the soil category of each simulation site (grid point). These categories were calculated from the values of the topographic slope of each grid point, since this slope has been shown to be empirically correlated to Vs30 (Wald and Allen, 2007; Stewart et al., 2014). The slope was calculated using the digital terrain model (SRTM30), which is an updated version of the digital terrestrial model (GTOPO30), with a resolution of 30 arcsec (average spacing of ~900 m). Figure 15b shows the final distribution of the spatial variation of Vs30, as determined for the area of interest by the previous procedure. For each soil class, generalized amplification factors were used for soil categories B, C and D (according to UBC/NEHRP) according to Margaris and Boore (1998) and Klimis et al. (1999), which were appropriately introduced in the stochastic simulation of each simulated seismic record.

To study the effect of the slip model of Figure 10 on the results, we initially employed only the geometry of the main rupture, i.e., a normal fault with a dip of ~36°, and a strike of 315^o. For this geometry, multiple rupture scenarios were considered and the average values of various parameters of the strong ground motion were calculated.

These multiple scenarios corresponded to different locations of the rupture starting point and different random models for the slip distribution along the seismic fault. Therefore, for these initial simulations, any information about the slip distribution on the fault was ignored. In this approach and for all simulation grid points, several calculations of time histories of ground acceleration have been performed, allowing the calculation of the average values of various strong ground motion parameters (e.g. PGA, PGV, etc.) for each point of the grid shown in Figure 15a.

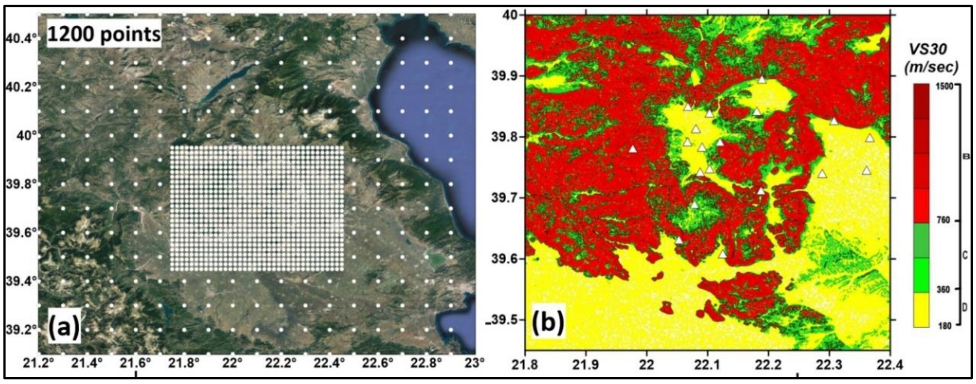

Fig. 15: a) Grid employed for the simulation of strong ground motion for the mainshock of the Tyrnavos sequence (M_w6.3, 2021/03/03). b) Spatial variation of the estimated V_s30 values in the broader Tyrnavos sequence area, as determined from the topographic slope proxy approach of Wald and Allen (2007).

Figure 16 shows the comparison between the values of the peak ground velocity (PGV) and peak ground acceleration (PGA) from accelerograph recordings with those obtained from the use of the EXSIM algorithm for the main earthquake for distances up to 100km. The comparison suggests that the stochastic simulation adequately captures the spatial distribution and the characteristics of the strong ground motion for the Tyrnavos mainshock, although in this simulation we have employed information only for the geometry of the seismic fault and a very generic approximation for the contribution of local geology site effects. It should be noted that some differences are observed between observed and predicted values, especially for peak ground acceleration (PGA), with the real (observed) values being lower (up to a factor of ~2) than the synthetic ones for the random slip model. These differences, especially in the PGA values, can be attributed to several factors. However, it should be noted that most recording sites are located in basins, with a significant thickness of sedimentary deposits (e.g., Larisa, Karditsa, Volos, etc.). This increased thickness is expected to significantly affect (increase) the high–frequency attenuation factor, κ_o, resulting in a significant attenuation of the high–frequency energy. As a result, the predicted PGA values are systematically overestimated, since we have relied on the average (and lower) UBC/NERHP soil class

κ_o values, as these were determined by Margaris and Boore (1998) and Klimis et al. (1999).

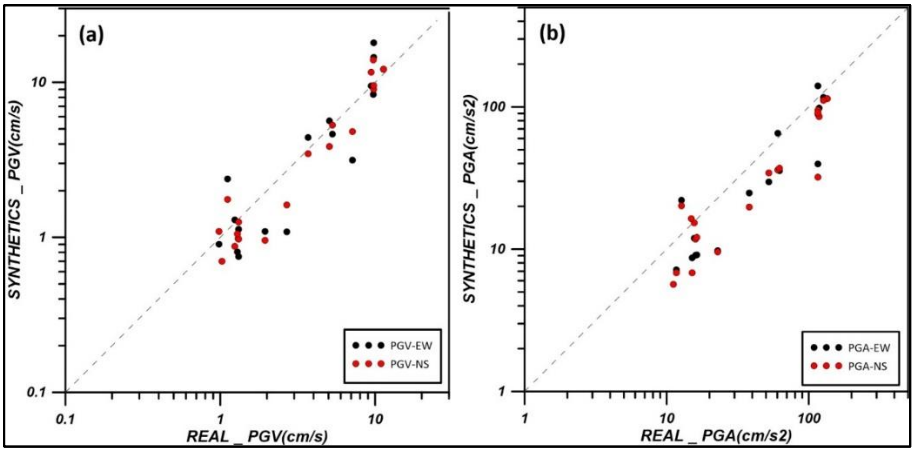

Fig. 16: Graphs showing the comparison of the PGV (a) and PGA (b) values, as these were determined from acceleration records (PGV_{Obs} και PGA_{Obs}) and EXSIM results (PGV_Syn and PGA_Syn) from the finite–fault simulation of the 3 March 2021 main shock (M_w6.3) using a random slip rupture scenario.

Given the adequate correlation of observed and simulated peak ground motion values (especially for peak ground velocity, PGV) at the accelerograph sites, despite of the use of a random slip rupture model, we estimated the spatial distribution of the expected PGA and PGV values in the meizoseismal area (Figures 17 and 18). In the results, we observe particularly large values of the peak ground acceleration (up to 0.7g) along the seismogenic fault, especially close to its surface projection, while large values are also observed in the area where the heaviest damage from the main earthquake was observed (e.g., Damasi village). PGA values along the area of the Titarisios river valley also reach values of the order of 0.35-0.45g (e.g., in the villages of Mesochori, Vlachogianni and Amouri) which, in combination with the influence of local soil conditions (Figure 15b), can partially explain the heavy damage observed in these settlements. Of particular interest is the area of increased PGA values near the southeastern end of the fault extension (northeast of the village of Zarko), as in the same area the highest surface subsidence values (~ 35cm) were observed from the InSAR data. In the city of Larissa, the stochastic simulation yields PGA values of ~100–150 cm/sec^2, in good agreement with the values observed in the installed accelerometers (LAR1, LAR4, S4, S5).

Regarding the values of the peak ground velocities (PGV) in the same area, we observe that in the meizoseismal area they range between 35–45 cm/sec. At the borders of the surface fault projection (villages Pretorio, Domeniko, Verdikousa, etc.) these values drop to 20–30 cm/sec, while at larger distances (>20 km) from the epicentral area the PGV values reach up to ~15 cm/sec (e.g., in the city of Larissa), in good agreement with the observed values.

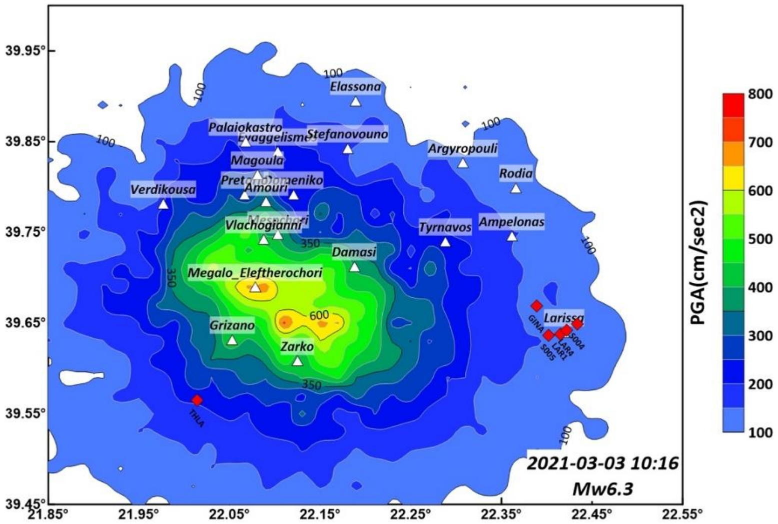

Fig. 17: Spatial distribution of the simulated peak ground acceleration (PGA) values in the broader Tyrnavos main shock area (M_w6.3) for the random slip rupture model. Accelerographs for which records were available (LAR1, LAR4, S4, S5, GINA και THLA) are depicted with red diamonds.

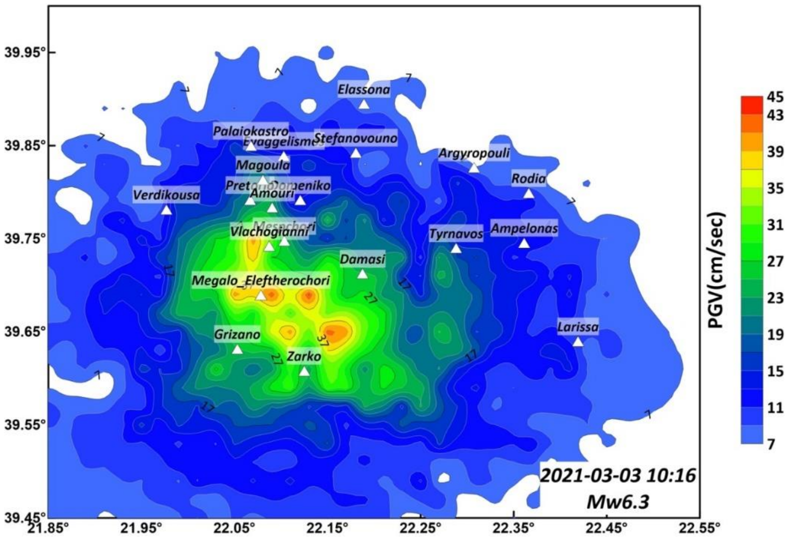

Fig. 18: Similar to Figure 17, for the peak ground velocity (PGV) distribution.

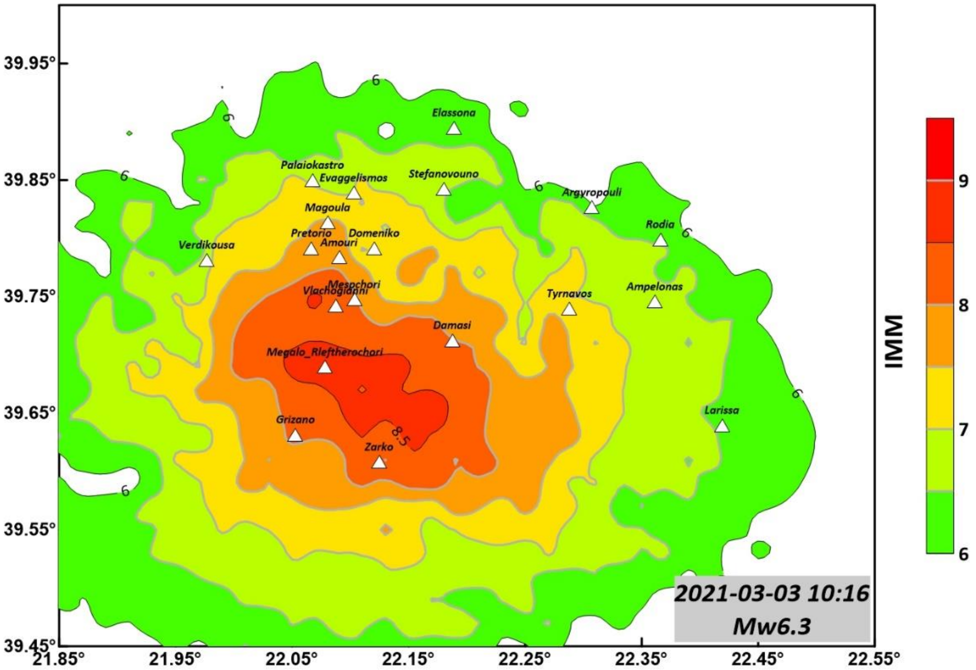

Fig. 19: Spatial distribution of the synthetic (simulated) macroseismic intensity values in the Modified Mercalli (IMM) scale, as determined from the PGA and PGV values from the finite-fault stochastic simulation approach for the 2021/03/03, M_w6.3 main shock, using a random–slip rupture model.

To estimate the predicted distribution of damage for the main earthquakes of the Tyrnavos sequence ($M_w 6.3$), we calculated the synthetic values of macroseismic intensities in the Modified Mercalli scale (IMM) by converting and averaging the synthetic values of PGA and PGV (shown in Figures 17 and 18) into macroseismic intensity values. For the conversion we used the relationship of Wald et al. (1999), appropriately corrected for the Greek version of Modified Mercalli, according to the suggestion of Kkallas et al. (2018). The spatial distribution of the predicted (simulated) macroseismic intensities for the random slip rupture model is shown in Figure 19. It is evident that the results suffer from the same problems seen in Figures 17 and 18. More specifically, while the predicted IMM values show a general consistency with the observed damage level, the actual distribution shows particularly large values close to the surface projection of the fault, leading to very high intensity values (IMM~8.5-9) in Megalo Eleftherochori, and slightly smaller values (IMM~8-8.5) for the villages of Zarko and Grizano in the prefecture of Trikala. These values are not in agreement with the observed damages, which were significant in Zarko, but relatively limited for Grizano and especially Megalo Eleftherochori, for which the highest peak ground acceleration and velocity values are predicted (Figures 17 and 18) for the random slip rupture model.

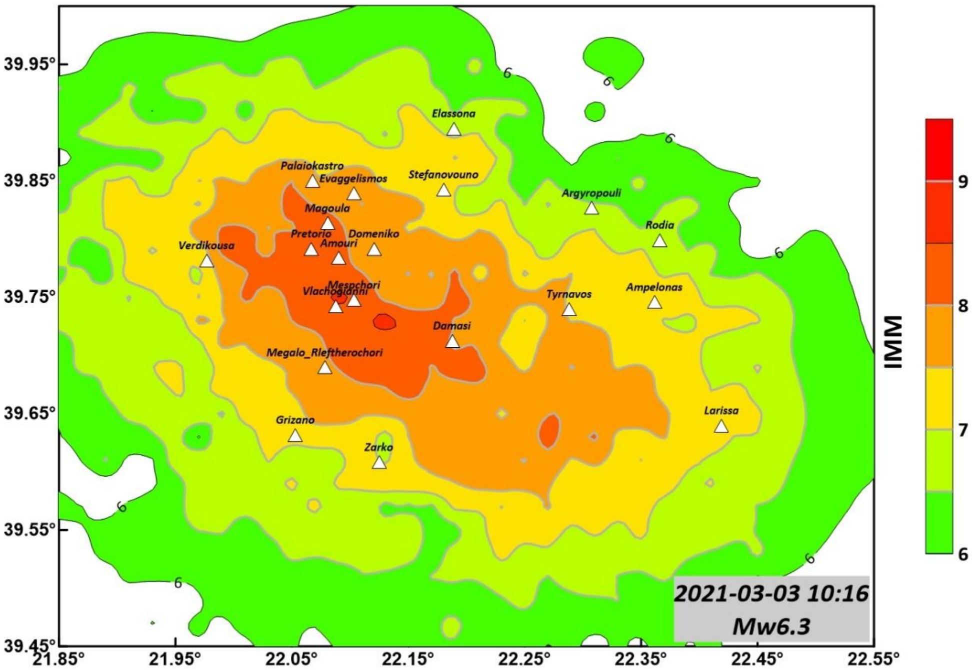

Fig. 20: Same as Figure 19 for the slip rupture model determined from broadband waveform inversion (see Figure 10).

For this reason, the calculations of the peak ground acceleration (PGA) and velocity (PGV) were repeated using the slip distribution model calculated from the inversion broad–band waveform data (Fig. 10), and the results were employed to calculate an updated IMM distribution. The results are presented for this new assessment of macroseismic intensity in Figure 19, leading to a much more realistic spatial distribution of the expected damage. In particular, we observe that the new slip rupture model has led to the concentration of heavy damage (IMM>8) values along the settlements of the Titarisios river valley, especially the villages of Damasi, Vlachogianni, Mesochori, Amouri, Pretorio and Magoula. On the contrary, a lower level of macroseismic intensity is observed for the cities of Tyrnavos and Larissa (IMM ~7.5 and 7, respectively), in very good agreement with the damage observations in these areas.

The results presented in Figures 19 and 20, and the significant differences observed depending on the rupture (slip) model adopted, suggest that the combination of the site effects from local geology along the Titarisios river basin, together with the specific pattern of rupture (slip model of Figure 11), have led to the high damage level in the specific area, as suggested by the predicted very high peak ground motion levels (PGA~0.45-0.6g and PGV~25-40cm/sec). On the contrary, for the villages south of the surface projection of the fault (Megalo Eleftherochori, Zarko and Grizano) the values of the peak strong ground motion (as expressed by PGA and PGV) for the determined slip model (Figure 10) are significantly smaller (PGA<0.35g and PGV<25 cm/s), in comparison to the results from the random slip model, in very good agreement with the observed damage pattern in this region. In summary, the previously presented simulations confirm the suggestion that the observed distribution of damage (Figure 20) of the first main shock ($M_w 6.3$) is due to the combination of three different factors that acted simultaneously:

A) The geometry of the fault, i.e., a low angle normal fault, extending significantly over a relatively large area, hence affecting a large number of settlements

B) The specific distribution of slip in the fault, as this is presented in the rupture model of Figure 10 and,

C) The contribution of the local site (geology) effects, in particular the soft soil sediments with low Vs30 values along the Titarisios river valley (Figure 15b).

While the results of Figure 20 should be considered as quite realistic, since no strong motion instrument was in operation in the meizoseismal area, it is evident that the use of more reliable and local transfer functions for the settlements mostly affected can lead to improved simulations for the observed damage distribution. This is especially critical for small spatial scales, since significant differences of observed strong ground motion levels at different sections of the various settlements have been documented, on the basis of observed damage variability (e.g., lower and upper part of the village of Damasi, etc.).

5. EARTH OBSERVATION DATA & SAR INTERFEROMETRIC PROCESSING

The analysis was based on open and free Sentinel–1 C–band Synthetic Aperture Radar (SAR) data. The Sentinel–1 mission, based upon a pre–defined and conflict-free acquisition plan, is able to systematically provide a large volume of SAR imagery, typically less than 4 hours from sensing, via the Copernicus Open Access Hub (https://scihub.copernicus.eu) since October 2014. The above fact ensures global coverage in a relatively short time, a major advantage when rapid response is intended as demonstrated after various strong earthquakes (Cornou et al., 2020; Foumelis et al., 2021). For the case of 2021, March 3 main shock the broader epicentral area, as defined by initial seismological measurements, was mapped in less than 12 hours from its occurrence, facilitating the rapid mapping of the affected zones, as well as the investigation, separately, of the stronger earthquakes of the seismic sequence.

Interferometric processing was undertaken on a Virtual Machine (VM) provided by the ESA RSS–Cloud Toolbox service (Marchetti et al., 2012), having direct access to the Copernicus archives via the CREODIAS infrastructure (https://creodias.eu). For the processing, the GAMMA software packages were used (Wegmüller et al., 2016). To compensate for the topographic component, heights from the AW3D30 DSM (Takaku et al., 2018) were utilized. The applied InSAR processing scheme has been well–demonstrated in several environments for measuring ground displacements (Papanikolaou et al., 2010; Lemoine et al., 2020). Utilizing interferometric pairs of short temporal separation (between 6 and 18 days), high coherence levels are ensured, minimizing measurements uncertainties. Regions exhibiting interferometric coherence levels below 0.3 were excluded from further analysis, as being non–valid DInSAR measurements. Although often related to temporal decorrelation, in that case, and especially for the 6-days pairs, low coherence regions were collocated to secondary earthquake phenomena, mostly liquefactions, surface ruptures and regions exhibiting highly distributed deformation (i.e. nearby observed ground motion maxima).

The major advantage of the systematic availability of EO data guaranteed the successful mapping of the earthquake–induced ground displacements. The acquisition dates of the satellite for track A120 versus the occurrence of major events was the most favorable for the investigation of the displacement field as caused by each of these earthquakes (Fig. 21).

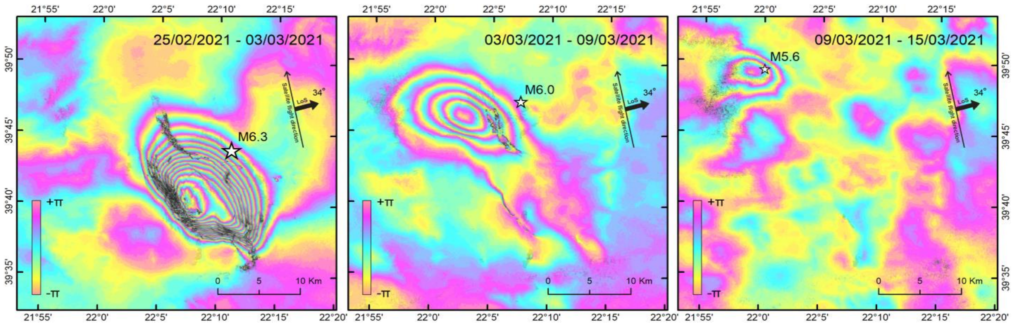

Fig. 21: Sentinel–1 6–days differential wrapped interferograms (ascending track 102) of time spans comprising the stronger earthquakes of the Tyrnavos 2021 sequence, M_w6.3 (left), M_w6.0 (center) and M_w5.6 (right). Regions of low interferometric coherence (≤0.3), non-valid DInSAR measurements, appear as black.

As observed by DInSAR, the maximum ground displacement reached -38 cm for the M6.3 mainshock (negative value indicate ground subsidence or motion away from the satellite), whereas lower values of -12 cm for the M6.0 and -9cm for the M5.6 events were calculated, representing respectively 32% and 24% of the total motion caused by the first mainshock.

The first main shock displacement field, as shown by the interferometric fringes (Fig. 21), represents an elliptical shape elongated at NW–SE direction, whereas for the second M6.0 main shock a counterclockwise rotation is observed with the ellipse being less elongated (reduced length of semi-major axis). For the M5.6 event, the interferometric fringes become more circular with elongation along a WNW–ESE direction. Common to all events is the fact that rupture zones do not seem to propagate to the surface, since no discontinuity of the interferometric fringes was recognized. This consorts with the upper limit of the seismogenic layer as defined by the relocated aftershocks.

6. GNSS DATA AND SITE DISPLACEMENT ESTIMATION

Dual frequency data were processed from five (5) permanent GNSS stations located close to the epicenter of the March 3 main shock that receive signals from the Global Satellite Navigation Satellite Systems (GNSS). The data time span cover about two weeks from March 1 to March 14, 2021. The stations belong to the HermesNet of Auth (Fotiou et.al., 2009, Fotiou and Pikridas 2012), HeXGon/SmartNet-Greece and NOANet (Chousianitis et al., 2021). The location distribution of GNSS stations is relatively optimal as they extend mainly around the epicenter area of each earthquake.

Data analysis was based on 30–sec daily GPS+Glonass observations and elevation cut–off angle 10° and therefore provided important data for depict the field of motion during the earthquakes and were included in our analysis. Four out of the five stations record GPS and Glonass data which is an advance for the impact of Satellite geometry in the process. The process was held on the current reference frame ITRF2014 using the web–based PPP platform of National Resources of Canada–Canadian Geodetic Survey (CGS). The well–known CSRS–PPP is an online application for data post–processing allowing users to compute higher accuracy positions from their GNSS raw data. Daily position coordinates are estimated on the International Terrestrial Reference Frame 2014 (ITRF2014) where positional accuracy is characterized by sub–centimeter, which fulfills the appropriate level for our study. The daily calculated displacements expressed in the topocentric system (East, North, Up) are presented in Table 4.

Table 4. Coseismic and cumulative displacements during Tyrnavos aftershock sequence between 1 and 14 March 2021.

Earthquakes	**E N Up displacement (in cm)**	**Permanent GNSS station**				
		ELAS φ=39^{0}53’32’’.7 λ=22^{0}12’22’’.1	KLOK φ=39^{0}33’53’’.3 λ=22^{0}00’51’’.4	LARM φ=39^{0}36’50’’.7 λ=22^{0}23’16’’.4	KRDI φ=39^{0}21’59’’.34 λ=21^{0}55’21’’.48	MURG φ=39^{0}44’19’’.3 λ=21^{0}33’15’’.1
March 03, 2021 10:16 AM	dE	1.0	-	0.3	-1.1	-0.2
	dN	3.3	-	0.0	0.2	-0.2
	dUp	-1.4	-	-0.2	0.3	1.2
March 03, 2021 06:24:00 PM	dE	0.5	-	0.3	-0.5	-0.6
	dN	0.7	-	0.1	-0.6	0.4
	dUp	-0.3	-	-1.1	-1.7	-1.1
March 12, 2021 12:57:00 PM	dE	0.5	-0.1	-0.5	-0.3	0.5
	dN	0.7	0.1	0.5	-0.5	0.5
	dUp	0.1	-0.2	-0.3	0.5	1.5
March 04, 2021 07:23:00 PM	dE	-0.1	-0.3	0.0	1.1	-1.0
	dN	0.1	-0.1	0.1	-2.0	1.0
	dUp	0.4	0.1	0.6	1.0	-0.6
March 04, 2021 06:38:00 PM	dE	0.4	0.0	-0.2	-0.9	-0.4
	dN	1.5	-0.7	0.5	-0.5	0.5
	dUp	0.3	-0.6	-1.6	-0.3	1.2
Cumulative Disp. **between 1 – 14 March**	dE	**2.2**	**-3.4**	**0.1**	**-0.3**	**-0.4**
	dN	**4.3**	**-4.0**	**0.5**	**-1.1**	**-0.2**
	dUp	**1.4**	**0.3**	**1.4**	**2.4**	**2.6**

After examining the effect of each earthquake in the coordinates stability, it was found out that the strongest co–seismic displacement was observed in the Elassona GPS/GNSS station (ELAS) which is located ~18 km from the first main shock epicenter (March 03, 2021, 10:16 AM), with a value of 3.3 cm on the north–south topocentric component. It must be noted that due to data availability, it was not possible to estimate co–seismic displacements for Klokotos (KLOK) site regarding the first two earthquakes. The most notable results are observed in ELAS and KLOK stations, as we may see at the cumulative displacements, which are estimated between 1 to 14 March (see Table 4). The estimated results were also confirmed from the related analysis of

Interferometric Synthetic Aperture Radar – InSAR data where similar displacements were calculated. At this point we must refer that GNSS data indicates high accuracy pinpoint displacements estimation while the InSAR technique depicts areal deformation pattern.

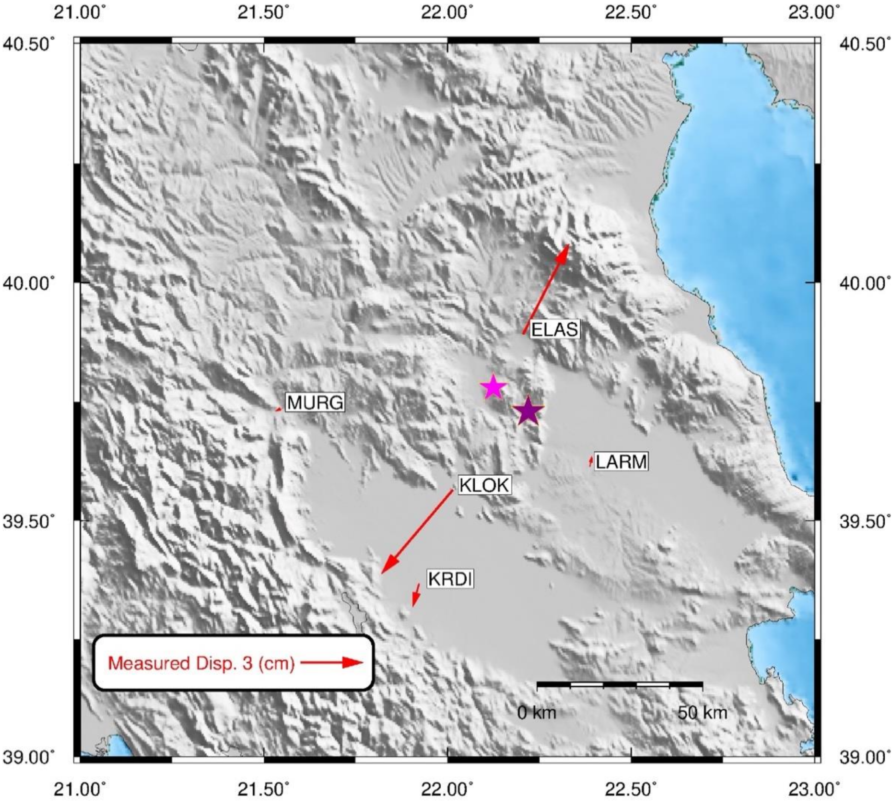

Fig. 22: *Cumulative coseismic displacements between 1 and 14 March 2021 from the GNSS network in the study area*.

7. STRESS INTERACTION OF THE SEQUENCE

There is convincing evidence, even accompanied with limited skepticism, that static Coulomb stress transfer can promote and inhibit subsequent seismicity. To unveil the cascading occurrence of the aftershock seismicity we calculate the Coulomb stress change, ΔCFF, caused by the first main shock. With simplifying assumptions to account for pore pressure effects, ΔCFF is given by (King et al., 1994):

$$\Delta CFF = \Delta\tau + \mu'\Delta\sigma_n \qquad (1)$$

where $\Delta\tau$ is the shear stress change on the target fault (positive in the direction of fault slip), $\Delta\sigma_n$ is the fault normal stress change (positive when unclamped), and μ' is the effective coefficient of friction (which implicitly includes the unknown pore pressure change on the fault).

The Coulomb hypothesis holds that earthquakes are promoted when ΔCFF is positive, and they are inhibited when ΔCFF is negative. There are numerous publications in the past 20 years, where this hypothesis has been tested and has been largely upheld for aftershock sequences (e.g., Karakostas et al., 2003; Papadimitriou et al., 2017) and sequential strong ($M \geq 6.2$ or $M \geq 7.0$) earthquake occurrence (e.g., Papadimitriou, 2002; Paradisopoulou et al., 2010). For the study area in particular, it has been shown that the episodic occurrence of $M \geq 6.2$ earthquakes, in remarkably active periods alternated with long lasting relative quiescence periods, is well supported by stress transfer among adjacent or closely located fault segments (Papadimitriou and Karakostas, 2003). The closeness in space and time of the two mainshocks evidence possible triggering through stress transfer. This observation along with the off–fault aftershocks that imply the activation of multiple minor fault segments, invites the comparison of spatial aftershock distribution with Coulomb stress changes. We seek to understand earthquake interaction on the 30 hours between the two main shocks and then the aftershocks, in a three dimensional stress changes pattern.

Figure 23 shows on a map view the Coulomb stress changes due to the coseismic slip of the March 3 main shock, calculated at a depth of 9 km (a little bit shallower than the nominal depth of the $M_w6.3$ earthquake, which equals to 9.5 km). Planar rectangular surface was assumed for the causative fault, and the source parameters for the first mainshock as defined in the previous sections (L=17 km, w=8 km, mean coseismic slip=0.70 m). The aftershock epicenters are depicted by circles with size proportional to the event magnitude, alike the representation in the map depicting the aftershock epicentral distribution. Yellow and blue colors were selected to signify positive and negative ΔCFF values that are calculated at the focus of each aftershock. The epicenters of the March 4 main shock and all following aftershocks are located inside stress enhanced areas. Perhaps the 30 hr delay is in some sense a product of a cascade of aftershocks, and not strictly the stress transfer from the first mainshock to the second. The fact that some epicenters colored as receiving positive stress changes (colored in yellow) are located in stress inhibited areas and vice versa, happens because these epicenters are projected at the depth of 9 km. Earthquakes with focal depths quite different than 9 km, might be assigned different ΔCFF value than the one calculated at this position onto the horizontal plane at the depth of 9 km.

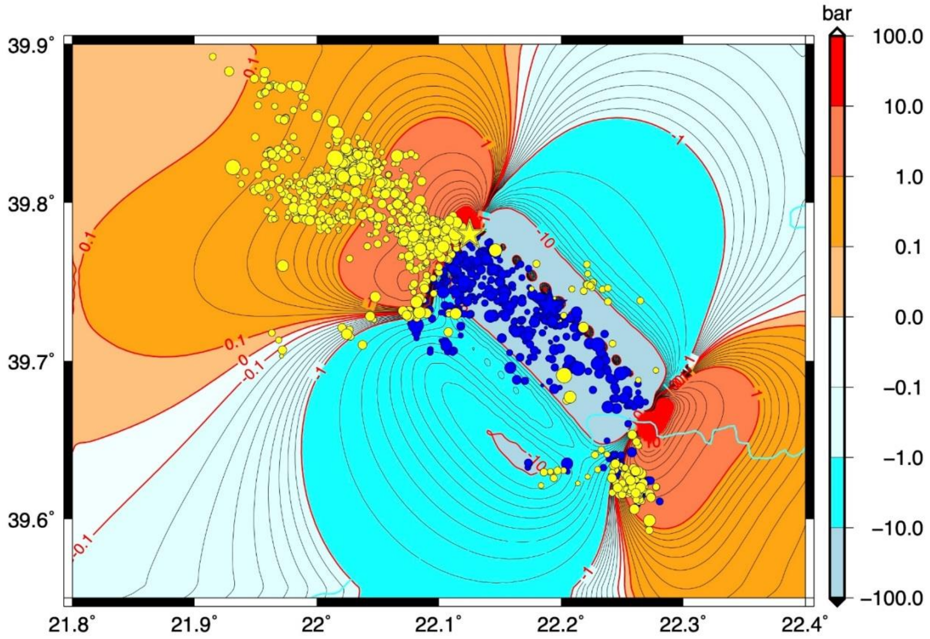

Fig. 23: Coulomb stress changes due to the coseismic slip of the March 3 (M_w6.3) main shock, resolved according to its faulting type (strike/dip/rake=314º/36º/-88º) onto a horizontal plane at a depth of 9 km. Circles of different size depict the relocated aftershocks in the first 30 hrs. between the two main shocks. The start shows the epicenter of the March 4 (M_w6.0) main shock, which is located at a site where the positive ΔCFF attain their largest value.

Figure 24 shows the Coulomb stress changes onto a plane parallel to the first rupture plane, according to the same color scale as in Figure 23. The cross–section direction is NW–SE, and the first main shock area coincides with the area where the negative ΔCFF changes attain values as small as –10 bar. The color of the projected hypocenters has been selected with the same criteria as before (Fig. 23). It is impressive that the vast majority of aftershocks occurred in stress enhanced areas. The negative ΔCFF values that are calculated at some aftershocks foci might be attributed to the simplified slip model with a uniform slip onto a planar surface, diverse of fault orientation even for the small aftershocks, relocation errors, or combination of the above. Figure 24 shows that not only was the site of the M_w6.0 hypocenter promoted by stress transfer, but aftershock seismicity in areas of negative ΔCFF was inhibited. The southern distinctive cluster that was noticed and mentioned in the spatial and temporal aftershock distribution, is clearly shown here that is entirely located in stress enhanced areas and is shallower than the other aftershock concentrations. This offers one more clue that it concerns an independent minor fault segment.

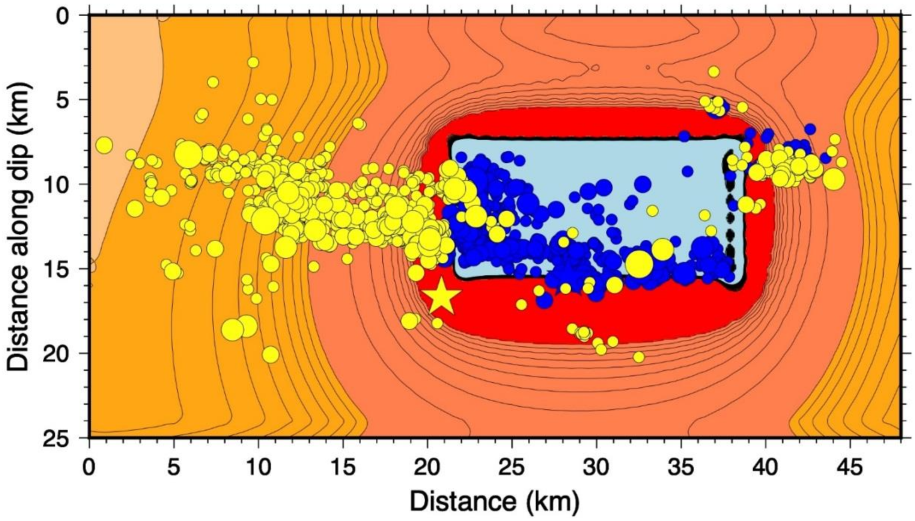

Fig. 24: Stress imparted by the first main shock (M_w6.3, 3 March 2021, white star), resolved onto a plane parallel its rupture plane and for its faulting parameters (strike/dip/rake=314°/36°/-88°). All earthquakes are projected onto this plane (after considering their focal depths and dip angle of the projection plane). Aftershocks in the first 30 hours (before the second main shock of M_w6.0, 4 March 2021) are plotted in white, whereas after that time in yellow. The second main shock (yellow star) is nucleated at an area where the positive Coulomb stress exceeds 10.0 bars.

8. DISCUSSION AND CONCLUSIONS

Our results suggest that the 2021 doublet ruptured previously unmapped fault segments with the majority of slip in the two main shocks to the west of the town of Tyrnavos. The activity mainly propagated northward from the first main shock epicenter, rupturing a crustal volume roughly between 4 and 15 km and shallower off–fault seismicity. The predominantly normal mechanism of the two main shocks, the stronger ($M \geq 5.0$) aftershocks and the overall sequence, all suggest a style of faulting controlled by extensional mechanism. Although there is little evidence for historic seismicity along these fault segments that turned up capable of hosting strong ($M \geq 6.0$) earthquakes, they exhibit similar faulting style and along with the neighboring mapped faults they appear rupturing members of a fault system that bounds the western margin of the eastern Thessalia basin, composing an extensional fault population alike in other areas in back arc Aegean region.

This seismic excitation signifies that M_w6.0 earthquakes can occur on relatively minor fault systems throughout the Greek territory and that often these minor fault systems have not been well characterized. Additionally, one more conclusion is that earthquakes of this magnitude can cause substantial ground motions resulting in significant damage to constructions that were not built according to the current building code standards.

The relocation of the two main shocks and more than~1450 aftershocks, extending from 4 to 15 km depth, outline the spatiotemporal evolution of the seismic sequence and the geometry of the ruptured fault network. Improved understanding of the aftershock sequence has become possible with the inclusion of data from the temporary monitoring network. The expansion of the aftershock spatial distribution far beyond the edges of the two main ruptures, supports the idea of a volumetric strain release process. The focal mechanisms and the aftershock spatial distribution agreed and documented the NW–SE striking and northeast dipping fault planes, of moderate dip. Additional distinctive seismicity clusters and seismicity clouds may give clues for the origin of other seismicity streaks implying minor conjugate faults activation, most probably triggered by stress transfer of the major events of the sequence.

The kinematic finite–fault rupture models calculated for the mainshock and the strongest aftershock, showed that the major slip is well–confined in slip patches (asperities). In both cases, the rupture initiated from the bottom of the fault and propagated updip. For the mainshock, if any directivity is present, then it should mainly be towards SE, towards the town of Zarko. For the aftershock, the models support rather bilateral propagation. An interesting feature observed in both models is the fact that the major slip is confined in the upper crust and in the middle of the seismogenic layer approximately between 3 and 7 km, whereas the slip in the uppermost few kilometers is systematically less compared to greater depths. This was also observed in several recent earthquakes in the Aegean area (Kiratzi, 2018; Karakostas et al., 2021; among others). Keeping in mind that this may be an artifact of the smoothing and regularization imposed to stabilize the inversion, nevertheless this observation is also supported by the cross-sections of the relocated aftershocks, pointing to different elastic properties of the uppermost part of the crust. Another observation, regarding the kinematic models of the mainshock and the strongest aftershock, is the relatively slow velocities (< 2.5 km/s) required to fit the data (which is less than 70% of the Vs velocity at the source depths). Such slow rupture speeds have been observed elsewhere (Wang et al., 2020) and they are mainly interpreted due to rupture on relatively immature fault systems (Liu et al., 2019 and references therein).

Coulomb stress changes due to the coseismic slip of the first main shock, are resolved at the focus of each aftershock. The results are projected on a map view also depicting the ΔCFF calculated at a depth of 9 km, along with onto a plane almost parallel to the planar surfaces approximated the fault planes of the two main shocks, for more detailing the vertical aftershock spatial distribution and comparing with the respective areas of positive and negative stress changes. It is derived that the onto fault aftershocks are limited to the lower southern part of the fault surface of the first main shock, whereas, in general the aftershocks occupy the entire seismogenic layer. This observation is attributed to the maximum slip fault patch (Fig. 10) at the southern upper part of the fault. The off–fault aftershocks are all well correlated with the larger positive values of Coulomb stress changes. For the distinctive clusters in particular, it became now more evident in these projections that they are associated with triggered minor faults located in different depths.

9. ACKNOWLEDGMENTS

The critical review and editorial assistance of Dr. A. Ganas along with one anonymous reviewer are greatly appreciated. The software Generic Mapping Tools was used to plot some of the maps (Wessel et al. 2013). The authors affiliated with the Department of Geophysics, of the Aristotle University of Thessaloniki, acknowledge support of this work by the project “HELPOS–Hellenic System for Lithosphere Monitoring” (MIS 5002697) which is implemented under the Action “Reinforcement of the Research and Innovation Infrastructure”, funded by the Operational Programme "Competitiveness, Entrepreneurship and Innovation" (NSRF 2014–2020) and co–financed by Greece and the European Union (European Regional Development Fund). Geophysics Department Contribution 953.

10. DATA AND RESOURCES

The seismic waveforms from broad–band and strong motion stations of the Greek network were downloaded from the ORFEUS EIDA nodes. The macroseismic data and the ShakeMap, and the other products were retrieved download from NOA, from the site https://accelnet.gein.noa.gr/noa_sites/noa.shakemaps.gr/public/index/126579.

11. REFERENCES

Abers, G. A., Mutter, C. Z. and Fang, J., 1997. Shallow dips of normal faults during rapid extension: Earthquakes in the Woodlark – D' Entrecasteaux rift system, Papua New Guinea. *Journal Geophysical Research,* 102, 15,301–15,317.

Aristotle University of Thessaloniki, 1981. Aristotle University of Thessaloniki seismological network. *Inter. Fed. Dig. Seis. Net.* doi:10.7914/SN/HT

Benetatos, C., Dreger, D. and Kiratzi, A., 2007. Complex and segmented rupture associated with the 14 August 2003 M_w6.2 Lefkada, Ionian Islands, earthquake. *Bulletin of the Seismological Society of America*, 97, 35–51.

Boore, D. M., 2009. Comparing Stochastic Point-Source and Finite-Source Ground-Motion Simulations: SMSIM and EXSIM. *Bulletin of the Seismological Society of America*, 99(6), 3202-3216, doi:10.1785/0120090056.

Caprio, M., Tarigan, B., Worden, B., Wiemer, S., and Wald, D., 2015. Ground Motion to Intensity Conversion Equations (GMICEs): A Global Relationship and Evaluation of Regional Dependency. *Bulletin of the Seismological Society of America*, 105, doi: 10.1785/0120140286

Caputo, R., 1990. Geological and structural study of the recent and active brittle deformation of the Neogene–Quaternary basins of Thessaly (Greece). *Scientific Annals*, 12, Aristotle University of Thessaloniki, Thessaloniki. 2 vols., 5 encl. 252 pp.

Caputo, R., and Pavlides, S., 1993. Late Caenozoic geodynamic evolution of Thessaly and surroundings (central–northern Greece). *Tectonophysics* 223, 339–362. doi:10.1016/0040-1951(93)90144-9

Caputo, R., Helly, B., Pavlides, S. and Papadopoulos, G., 2004. Palaeoseismological investigation of the Tyrnavos Fault (Thessaly, Central Greece). *Tectonophysics*, 394, 1–20. https://doi.org/10.1016/j.tecto.2004.07.047

Caputo, R., Helly, B., Pavlides, S., Papadopoulos, G., 2006. Archaeo- and palaeoseismological investigations in Northern Thessaly (Greece): Insights for the seismic potential of the region. *Natural Hazards*, 39, 195–212, https://doi.org/10.1007/s11069-006-0023-9

Chousianitis, K., Papanikolaou X., Drakatos G., and Tselentis, G.–A., 2021. NOANET: A Continuously Operating GNSS Network for Solid–Earth Sciences in Greece. *Seismological Research Letters*, XX, 1–15, doi: 10.1785/0220200340.

Cornou, C., Aubert, C., Audin, L., Ampuero, J-P., Baize, S., Brenguier, F., Causse, M., Chlieh, M., Combey, A., Delouis, B., Deschamps, A., Ferry, M., Foumelis, M. et al. (83 authors), 2020. Rapid response to the M_w4.9 earthquake of November 11, 2019 in Le Teil, Lower Rhône Valley, France. *Comptes Rendus Géosciences*, doi: 10.31219/osf.io/3afs5.

Dreger, D. and Kaverina, A., 2000. Seismic remote sensing for the earthquake source process and near-source strong shaking: a case study of the October 16, 1999 Hector Mine earthquake, *Geophysical Research Letters*, 27, 1941–1944.

Fotiou, A. and Pikridas, C., 2012. GPS and Geodetic Applications, Editions Ziti, Thessaloniki. ISBN:978-960-456-346-3.

Fotiou, A., Pikridas, C., Rossikopoulos, D., Spatalas, S., Tsioukas, V., Katsougiannopoulos, S., 2009. The Hermes GNSS NtripCaster of AUTh., *Bulletin Geodesy Geophysics*, 69, https://doi.org/refwid:18241

Foumelis, M., Papazachos, C., Papadimitriou, E., Karakostas, V., Ampatzidis, D., Moschopoulos, G., Kostoglou, A., Ilieva, M., Minos-Minopoulos, D., Mouratidis, A., Kkallas, C., Chatzipetros, A., 2021. On Rapid Multidisciplinary Response Aspects for Samos 2020 M7.0 Earthquake. *Acta Geophysica*, https://doi.org/10.1007/s11600-021-00578-6

Ganas, A., 2020. NOAFAULTS KMZ layer Version 3.0 (2020 update) (Version V3.0) [Data set]. Zenodo. http://doi.org/10.5281/zenodo.4304613

Ganas, A., Valkaniotis, S., Tsironi, V., Karasante, I., Elias, P., Kapetanidis, V., Kasssaras, I., Papathanassiou, G., Briole, P., 2021. The March 2021 seismic sequence in Larisa – Damasi, Thessaly (central Greece), its seismotectonic characteristics and geodynamic effects. https://doi.org/10.5281/ZENODO.4617264.

Goldsworthy, M., Jackson, J., Haines, J., 2002. The continuity of active fault systems in Greece, *Geophysical Journal International*, 148, 596–618.

Hartzell, S. H., and Heaton, T. H., 1983. Inversion of strong ground motion and teleseismic waveform data for the fault rupture history of the 1979 Imperial Valley, California, earthquake, *Bulletin of the Seismological Society of America*, 73, 1553–1583.

Heimann, S., Kriegerowski, M., Isken, M., Cesca, S., Daout, S., Grigoli, F., Juretzek, C., Megies, T., Nooshiri, N., Steinberg, A., Sudhaus, H., Vasyura-Bathke, H., Willey, T., Dahm, T. 2017. Pyrocko – An open-source seismology toolbox and library. V. 0.3. GFZ Data Serv. http://doi.org/10.5880/GFZ.2.1.2017.001

Heimann, S., Isken, M., Kühn, D., Sudhaus, H., Steinberg, A., Vasyura-Bathke, H., Daout, S., Cesca, S., Dahm, T., 2018. Grond – A probabilistic earthquake source inversion framework. V. 1.0. *GFZ Data Serv.* https://doi.org/10.5880/GFZ.2.1.2018.003

Kaverina, A., D. Dreger, and Price, E., 2002. The combined inversion of seismic and geodetic data for the source process of the 16 October 1999 M_w7.1 Hector Mine, California, Earthquake, *Bulletin of the Seismological Society of America*, 92, 1266–1280.

Karakostas, V. G., Papadimitriou, E. E., Karakaisis, G. F., Papazachos, C. B., Scordilis, E. M., Vargemezis, G., and Aidona, E., 2003. The 2001 Skyros, northern Aegean, Greece, earthquake sequence: Off–fault aftershocks, tectonic implications, and seismicity triggering. *Geophysical Research Letters*, *30*(1), 1012, doi:10.1029/2002GL015814

Karakostas, V., Tan, O., Kostoglou, A., Papadimitriou, E. and Bonatis, P., 2021. Seismotectonic implications of the 2020 Samos, Greece, M_w7.0 mainshock based on high–relocation and source slip model. *Acta Geophysica,* https://doi.org/10.1007/s11600-021-00580-y

Kilias, A., Frisch, W., Avgerinas, A., Dunkl, I., Falalakis, G., Gawlick, H.-J., 2010. Alpine architecture and kinematics of deformation of the northern Pelagonian nappe pile in the Hellenides. *Austrian Journal of Earth Sciences,* 103, 4–28.

Kilias, A., Thomaidou, E., Katrivanos, E., Vamvaka, A., Fassoulas, C., Pipera, K., Falalakis, G., Avgerinas, S., Sfeikos, A., 2016. A geological cross-section through

Northern Greece from Pindos to Rhodope mountain ranges: A field guide across the external and internal Hellenides. *Journal Virtual Explorer*, 50, 1–107, https://doi.org/10.3809/jvirtex.2016.08685

King, G.C.P., Stein, R.S. and Lin, J., 1994. Static stress changes and the triggering of earthquakes. *Bulletin of the Seismological Society of America*, 84, 935–953.

Kiratzi, A., 2018. The 12 June 2018 Lesvos Island (Aegean Sea) earthquake: Slip model and directivity estimated with finite–fault inversion. *Tectonophysics*, 724–725, 1–10, https://doi.org/10.1016/j.tecto.2018.01.003

Kissling, E., Ellsworth, W.L., Eberhart–Phillips, D., Kradolfer, U., 1994. Initial reference models in local earthquake tomography. *Journal Geophysical Research*, 99, doi: 10.1029/93JB03138.

Kkallas, Ch., Papazachos C.B., Boore D., Ventouzi Ch., and Margaris, B.N., 2018. Historical intermediate-depth earthquakes in the southern Aegean Sea Benioff zone: Modeling their anomalous macroseismic patterns with stochastic ground-motion simulations, *Bulletin Earthquake Engineering*, doi: 10.1007/2Fs10518-018-0342

Klein, F. W., 2002. User’s Guide to HYPOINVERSE–2000, a Fortran program to solve earthquake locations and magnitudes. *U. S. Geological Survey Open File Report* 02–171, Version 1.0.

Klimis, N., Margaris, B., and Koliopoulos, P., 1999. Site Dependent Amplification Functions and response Spectra in Greece, *Journal of Earthquake Engineering*, 3, 237–270.

Lemoine, A., Bertil, D., Roullé, A., Briole, P., Foumelis, M., Raucoules, D. and de Michele, M., 2020. The volcano tectonic crisis of 2018 east of Mayotte, Comoros Islands. *Geophysical Journal International*, ggaa273, https://doi.org/10.1093/gji/ggaa273.

Liu, C., T. Lay, E. E. Brodsky, K. Dascher-Cousineau, and Xiong, X., 2019. Coseismic rupture process of the large 2019 Ridgecrest earthquakes from joint inversion of geodetic and seismological observations. *Geophysical Research Letters*, 46, 11820–11829.

Marchetti, P.G., Rivolta, G., D' Elia, S., Farres, J., Mason, G. and Gobron, N., 2012. A Model for the Scientific Exploitation of Earth Observation Missions: The ESA Research and Service Support. *IEEE Geoscience and Remote Sensing*, 162, 10-18.

Margaris, B. N., and Boore, D. M., 1998. Determination of Δσ and ko from Response Spectra of Large Earthquakes in Greece. *Bulletin of the Seismological Society of America*, 88, 170–182.

Motazedian, D., and Atkinson, G. M., 2005. Stochastic Finite-Fault Modeling Based on a Dynamic Corner Frequency. *Bulletin of the Seismological Society of America*, 95(3), 995-1010, doi:10.1785/0120030207.

Novotny, O., Zahradnik, J., and Tselentis, G.-A., 2001. Northwestern Turkey Earthquakes and the Crustal Structure Inferred from Surface Waves Observed in Western Greece. *Bulletin of the Seismological Society of America*, 91, 875–879.

Papadimitriou, E. E., 2002. Mode of strong earthquake occurrence in central Ionian Islands (Greece). Possible triggering due to Coulomb stress changes generated by the occurrence of previous strong shocks. *Seismological Society of America, 92*, 3293–3308.

Papadimitriou, E.E., Karakostas, V.G., 2003. Episodic occurrence of strong ($M_w \geq 6.2$) earthquakes in Thessalia area (central Greece). *Earth Planetary Science Letters*, 215, 395–409.

Papadimitriou, E., Karakostas, V., Mesimeri, M., Chouliaras, G., Kourouklas, Ch., 2017. The M_w6.7 17 November 2015 Lefkada (Greece) earthquake: structural interpretation by means of aftershock analysis. *Pure Applied Geophysics*, 174, 3869–3888, DOI 10.1007/s00024–017–1601–3.

Papanikolaou, I.D., Foumelis, M., Parcharidis, I., Lekkas, E.L. and Fountoulis, I.G., 2010. Deformation pattern of the 6 and 7 of April 2009, M_w=6.3 and M_w=5.6 earthquakes in L' Aquila (Central Italy) revealed by ground and space based observations. *Natural Hazards & Earth System Science*, 10, 73-87.

Papazachos BC, Scordilis EM, Panagiotopoulos DG, Papazachos CB, Karakaisis GF (2004) Global relations between seismic fault parameters and moment magnitude of earthquakes. *10th Congress Hellenic Geological Society*, Thessaloniki, Greece, 14–17 April 2004, 539–540.

Paradisopoulou, P. M., Papadimitriou, E. E., Karakostas, V. G., Taymaz, T., Kilas, A. and Yolsal, S., 2010. Seismic hazard evaluation in western Turkey as revealed by stress transfer and time–dependent probability calculations. *Pure Applied Geophysics*, 167, 1013–1048, doi:10.1007/s00024–010–0085–1.

Pavlides, S., Chatzipetros, A., Sboras, S., Kremastas, E., Chatziioannou, A., 2021. The northern Thessaly strong earthquakes of March 3 and 4 and their neotectonic setting. https://doi.org/10.5281/ZENODO.4618188

Schaff, D. P. and Waldhauser, F., 2005. Waveform cross–correlation–based differential travel–time measurements at the northern California seismic network. *Bulletin of the Seismological Society of America*, 95, 2446–2461.

Schaff, D. P., Bokelmann, G. H. R., Ellsworth, W. L., Zanzerkia, E., Waldhauser, F. and Beroza, G., 2004. Optimizing correlation techniques for improved earthquake location. *Bulletin of the Seismological Society of America*, 95, 705–721.

Somerville, P., K. Irikura, S. Sawada, D. J. Wald, N. Abrahamson, Y. Iwasaki, T. Kagawa, N. Smith, and Kowada, A., 1999. Characterizing crustal earthquake slip models for the prediction of strong ground motion. *Seismological Research Letters*, 70, 59–80.

Stewart, J. P., Klimis, N., Savvaidis, A., Theodoulidis, N., Zargli, E., Athanasopoulos, G., Pelekis, P., Mylonakis, G., and Margaris, B., 2014. Compilation of a Local VS Profile Database and Its Application for Inference of VS30 from Geologic–and Terrain-Based Proxies. *Bulletin of the Seismological Society of America*, 104(6), 2827–2841. https://doi.org/10.1785/0120130331

Takaku, J., Tadono, T., Tsutsui, K. and Ichikawa, M., 2018. Quality Improvements of 'AW3D' Global DSM Derived from ALOS PRISM, Proc. IGARSS2018, IEEE, Valencia, Spain, 1612–1615.

Tsodoulos, I., Chatzipetros, A., Koukouvelas, I., Caputo, R., Pavlides, S., 2016a. Palaeoseismological investigation of the Gyrtoni Fault (Thessaly, Central Greece). *Bulletin of the Geological Society of Greece*, 50, 552–562.

Tsodoulos, I., Stamoulis, K., Caputo, R., Koukouvelas, I., Chatzipetros, A., Pavlides, S., Gallousi, C., Papachristodoulou, C., Ioannides, K., 2016b. Middle–Late Holocene earthquake history of the Gyrtoni Fault, Central Greece: Insight from optically stimulated luminescence (OSL) dating and palaeoseismology. *Tectonophysics*, 687, https://doi.org/10.1016/j.tecto.2016.08.015

Valkaniotis, S., Papathanassiou, G., Ganas, A., Kremastas, E., Caputo, R., 2021. Preliminary report of liquefaction phenomena triggered by the March 2021 earthquakes in Central Thessaly, Greece. https://doi.org/10.5281/ZENODO.4608365

Wang, R., 1999. A simple orthonormalization method for stable and efficient computation of Green’s functions. *Bulletin of the Seismological Society of America*, 89, 733–741.

Wang, K., Dreger, D. S., Tinti, E., Bürgmann, R., and Taira, T., 2020. Rupture Process of the 2019 Ridgecrest, California M_w6.4 Foreshock and M_w7.1 Earthquake Constrained by Seismic and Geodetic Data. *Bulletin of the Seismological Society of America*, 110, 1603–1626, doi: 10.1785/0120200108.

Wald, D. J. and Allen, T. I., 2007. Topographic slope as a proxy for seismic site conditions and amplification. *Bulletin of the Seismological Society of America*, 97(5), 1379-1395, doi: 10.1785/0120060267.

Wald, D. J., Quitoriano, V., Heaton, T. H., and Kanamori, H., 1999. Relationships between Peak Ground Acceleration, Peak Ground Velocity, and Modified Mercalli Intensity in California. *Earthquake Spectra*, 15(3), 557–564, https://doi.org/10.1193/1.1586058.

Waldhauser, F., and Ellsworth, W. L., 2000. A double–difference earthquake location algorithm: method and application to the northern Hayward fault, California. *Bulletin of the Seismological Society of America*, 90, 1353–1368.

Wegmüller, U., Werner, C., Strozzi, T., Wiesmann, A., Frey, O., and Santoro, M., 2016. Sentinel-1 Support in the GAMMA Software. *Procedia Computer Science*, 100, 1305–1312.

Wells DL, Coppersmith KJ, 1994. New empirical relationships among magnitude, rupture length, rupture width, rupture area, and surface displacement. *Bulletin of the Seismological Society of America*, 84, 974–1002.

Wessel, P., Smith, W. H. F., Scharroo, R., Luis, J. F. and Wobbe, F., 2013. Generic Mapping Tools: improved version released. *EOS Trans AGU* 94, 409-410.

BGSG

Volume 58

Research Paper

Correspondence to:
Filippos Valianatos
fvallian@geol.uoa.gr

DOI number:
http://dx.doi.org/10.12681/bgsg.27062

Keywords:
Earthquake, early warning system, on-site, Thessaly, IV2$_p$

Citation:
Spingos, I., Vallianatos, F. and Kaviris, G. (2021), The Scaling of *PGA* with *IV2$_p$* and Its Potential for Earthquake Early Warning In Thessaly (Central Greece). Bulletin Geological Society of Greece, 58, 179-199.

Publication History:
Received: 19/05/2021
Accepted: 06/09/2021
Accepted article online: 13/09/2021

The Editor wishes to thank one anonymous reviewer and Dr. Ch. Evangelidis for their work with the scientific reviewing of the manuscript and Ms Emmanouela Konstantakopoulou for editorial assistance.

THE SCALING OF *PGA* WITH *IV2$_P$* AND ITS POTENTIAL FOR EARTHQUAKE EARLY WARNING IN THESSALY (CENTRAL GREECE)

Ioannis Spingos[1,2], Filippos Vallianatos[1,2 *], and George Kaviris[1,2]

[1] Section of Geophysics–Geothermics, Department of Geology and Geoenvironment, National and Kapodistrian University of Athens, 15784 Athens, GR

[2*] Institute of Physics of the Earth's Interior and Geohazards, UNESCO Chair on Solid Earth Physics and Geohazards Risk Reduction, Hellenic Mediterranean University Research Center, Crete, GR 73133 Chania, Greece; fvallian@hmu.gr, fvallian@geol.uoa.gr, +302107274360

Abstract

The main goal of an Earthquake Early Warning System (EEWS) is to estimate the expected peak ground motion of the destructive S-waves using the first few seconds of P-waves, thus becoming an operational tool for real-time seismic risk management in a short timescale. EEWSs are based on the use of scaling relations between parameters measured on the initial portion of the seismic signal, after the arrival of the first wave. Herein, using the abundant seismicity that followed the 3 March 2021 M_w=6.3 earthquake in Thessaly we propose scaling relations for PGA, from data recorded by local permanent stations, as a function of the integral of the squared velocity ($IV2_p$). The $IV2_p$ parameter was estimated directly from the first few seconds-long signal window (t_w) after the P-wave arrival. Scaling laws are extrapolated for both individual and across sites (i.e., between a near-source reference instrument and a station located close to a target). The latter approach is newly investigated, as local site effects could have a significant impact on recorded data. Considering that further study on the behavior of $IV2_p$ is necessary, there are indications that this parameter could be used in future on-site single-station earthquake early warning operations for areas affected by earthquakes located in Thessaly, as it presents significant stability.

Keywords: *earthquake; early warning system; on-site; Thessaly; $IV2_p$*

Περίληψη

Ο κύριος στόχος ενός Συστήματος Έγκαιρης Προειδοποίησης Σεισμών (ΣΕΠΣ) είναι η εκτίμηση της μέγιστης αναμενόμενης εδαφικής κίνησης των καταστρεπτικών εγκαρσίων κυμάτων (S) χρησιμοποιώντας τα πρώτα δευτερόλεπτα των επιμήκων κυμάτων (P). Με τον τρόπο αυτόν, τα ΣΕΠΣ μπορούν να λειτουργήσουν ως εργαλείο για τη διαχείριση του σεισμικού κινδύνου σε πραγματικό χρόνο. Τα ΣΕΠΣ βασίζονται στη χρήση νόμων κλίμακας μεταξύ παραμέτρων που υπολογίζονται στην αρχή του σεισμικού σήματος, μετά την άφιξη του πρώτου κύματος και της αναμενόμενης έντασης της δόνησης. Η τελευταία προσδιορίζεται με διάφορους τρόπους, όπως το μέγεθος σεισμού και η μέγιστη εδαφική επιτάχυνση (PGA) των εγκαρσίων κυμάτων. Στη συγκεκριμένη εργασία, προτείνουμε νόμους κλίμακας για την παράμετρο PGA, συναρτήσει του ολοκληρώματος του τετραγώνου της ταχύτητας στα πρώτα δευτερόλεπτα καταγραφής ($IV2_p$)*, χρησιμοποιώντας σεισμούς από την πρόσφατη ακολουθία στη Θεσσαλία, η οποία σχετίζεται με τον κύριο σεισμό μεγέθους* M_w*=6.3 στις 3 Μαρτίου 2021. Χρησιμοποιήθηκαν καταγραφές από τοπικούς μόνιμους σταθμούς. Οι νόμοι κλίμακας των δύο παραμέτρων (*$IV2_p$ *και PGA) εξάχθηκαν τόσο στην ίδια θέση (και οι δύο προσδιορίσθηκαν από κυματομορφές του ίδιου σταθμού), όσο και μεταξύ μίας θέσης αναφοράς και του στόχου (*$IV2_p$ *στον σταθμό αναφοράς και PGA στον στόχο). Η τελευταία περίπτωση είναι μία νέα προσέγγιση της μεθόδου, με σκοπό τη διερεύνηση της πραγματικής επίδρασης των διαφορών των τοπικών εδαφικών συνθηκών. Λαμβάνοντας υπόψη ότι απαιτείται περαιτέρω μελέτη της συμπεριφοράς των παραμέτρων, υπάρχουν ενδείξεις ότι η παράμετρος* $IV2_p$ *μπορεί να χρησιμοποιηθεί σε ένα μελλοντικό ΣΕΠΣ στην περιοχή της Θεσσαλίας.*

Λέξεις-Κλειδιά: *σεισμός; σύστημα έγκαιρης προειδοποίησης; Θεσσαλία;* $IV2_p$

1. INTRODUCTION

In Thessaly (Central Greece), urban areas are located near major active faults increasing the threat of strong seismic events, with, possibly, devastating ramifications for financial and industrial activities, as well as the safety of local population. Advances in signal processing, telecommunications and seismology have gradually rendered the concept of a reliable Earthquake Early Warning System (EEWS) not only feasible, but quite reliable as well (Nakamura, 1988; Kanamori et al., 1997; Allen and Kanamori, 2003; Kanamori, 2005; Simons et al., 2006; Allen, 2007; Gasparini et al., 2011; Hloupis and Vallianatos, 2013, 2015; Parolai et al., 2015; Hsu and Nieh, 2020; Brooks et al., 2021). Damages from an impending strong motion can be reduced by taking mitigation measures suitable for the given warning time (Espinosa-Aranda et al., 1995; Wu et al., 1998; Iannacone et al., 2010; Beltramone and Gomes, 2021). Such an approach is already in operation in Japan (Nakamura, 1988), Taiwan (Wu et al., 1999, 2000), Mexico (Espinosa-Aranda et al., 1995), Italy (Zollo et al., 2006, 2009, 2010; Satriano et al., 2008) and California, USA (Chung et al., 2020). In Greece, a typical EEWS (Satriano et al., 2011) is currently active at a pilot stage (Kapetanidis et al., 2019), by the Seismological Laboratory of the National and Kapodistrian University of Athens (NKUA-SL). The University of Patras implemented an EEWS to monitor the area around the Rion-Antirion bridge (Sokos et al., 2016). The Geodynamic Institute of the National Observatory of Athens (GI-NOA) had installed an EEWS that also integrated alerts for tsunamis in Rhodes (Papadopoulos et al., 2014) and currently operates a trial system in the Eastern Gulf of Corinth, in cooperation with NKUA-SL and the Hellenic Mediterranean University.

An earthquake generates two fundamental types of body-waves: longitudinal (P) and shear (S) waves. The direct P-waves are weaker in amplitude and have a higher velocity than the S-waves. As a result, the difference in velocity can be used to retrieve information about the earthquake from the first wave arrivals and, consequently, predict the effect of the impending destructive secondary waves (Kanamori, 2005). This notion is implemented in practice by typical EEWSs through the investigation of scaling relationship among the Peak Displacement (P_d) of P-waves, the magnitude (M) and the hypocentral (H) or epicentral distance. The Peak Ground Acceleration (PGA) of the S-waves is retrieved from the expected magnitude estimated from P_d (e.g., Wu and Kanamori, 2005; Satriano et al., 2011). This regional approach introduces weaknesses in the system, as the EEWS' accuracy depends on earthquake location uncertainties and, consequently, is greatly affected by the geometry and density of the available seismological networks. This is in addition to inherent errors, such as the reliability of the regression analysis used to determine the scaling relations' coefficients; extrapolation of accurate coefficients might be difficult, considering the large variability in the level of ground motions for events of similar magnitude (Minson et al., 2019).

Another scaling law, previously explored as a proxy for the impending S-wave amplitude, is the relation between the integral of squared velocity estimated from the initial P-wave ($IV2_p$) and a metric of the anticipated shaking (e.g., PGA, M or the seismic intensity).

Specifically:

$$IV2_p = \int_{t_p}^{t_p+t_w} v^2(t)dt \qquad (1)$$

where t_p the P arrival time, t_w the considered signal window and $v(t)$ the signal in velocity terms. It is an alternative to using a P_d relationship and, therefore, leads to practical applications for early warning (Festa et al., 2008). Applications of $IV2_p$ include recordings by deployments of standard seismological instruments (e.g., Brondi et al., 2015; Spallarossa et al., 2019), as well as smartphones (Hsu and Nieh, 2020). This on-site approach has the advantage of eliminating network design factors (such as requiring multiple suitable locations for instrument installation), while being more immediate; essentially, earthquake location is no longer required. An obvious drawback is the effect of a single site and instrument on the accuracy of the EEWS. Furthermore, in the context of an operational on-site system, there is the issue of avoiding S-waves contamination in the t_w window.

On 3 March 2021 a strong M_w=6.3 earthquake struck Thessaly (Koukouvelas et al., 2021; Mavroulis et al., 2021; Papadopoulos et al., 2021). Its location close to the major city of Larisa (approximately 23 km away) and its shallow depth (~7 km) indicated a source with potential to cause extensive damages. However, the highest *PGA*, recorded at station GINA at the outskirts of the city, was ~140 cm/s^2, well below the limit given by the national building code, i.e., ~235 cm/s^2 (EAK, 2003). This event was followed by another strong earthquake with M_w=6.1 (Ganas et al., 2021), located ~10 km NW. The sequence has offered a considerable number of events so far (over 3,500, two months after the first large event), according to the catalogue of NKUA-SL. Epicenters have spread ~30 km to the NW, covering a very extensive area. Foci are generally located shallower than 15 km (Fig. 1). Even though only recent seismicity raised awareness for seismic hazard and risk in the area, there have been several strong and destructive earthquakes over the years, related to complex active faults. Seismic potential near Larisa is predominantly controlled by normal faulting, with ~15-km-long structures striking WNW-ESE (Caputo et al. 1993, 2004; Ganas et al., 2013). Focal mechanisms related to the 2021 sequence support such patterns (Fig. 1). However, the existence of past strong earthquakes indicates a consistent activation of regional fault systems. The city of Larisa itself, was the epicenter of three strong earthquakes between 1600 and 1900, while the broader area of the 2021 sequence witnessed two such events in 1735 and 1766 (Stucchi et al., 2013).

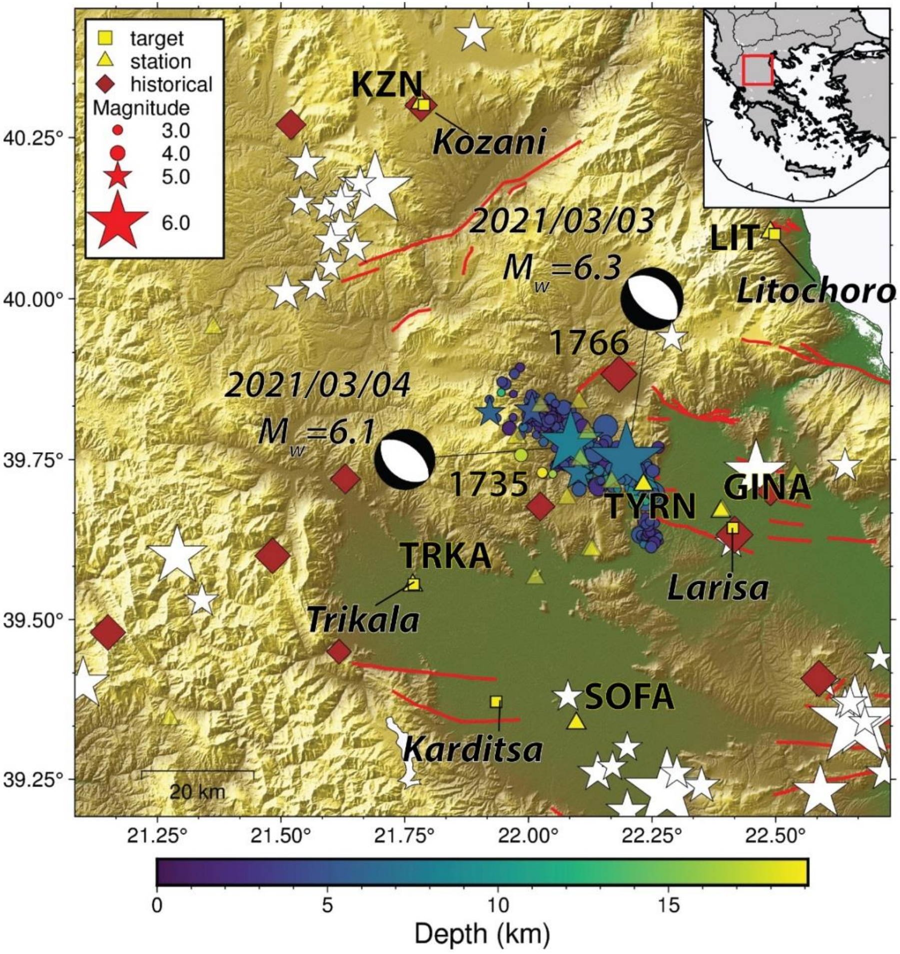

Fig. 1: Seismotectonic setting of the 2021 sequence. Recent seismicity of magnitude equal or greater than 3.0 (circles for magnitudes less than 5.0 and stars for greater) seem to be well-constrained in a ~20-km wide NW-SE linear fashion, in agreement with the strike of nodal planes. Historical earthquakes (brown diamonds) are also observed in the area (Stucchi et al., 2013). The most significant instrumental events (white stars, magnitudes greater than 5.0) is located to the SE and NW, while there is one recorded event within the city of Larisa (Makropoulos et al., 2012; NKUA-SL). Stations used in the study are shown as yellow triangles (instruments not used are faded out). Faults (solid black lines) after Ganas et al. (2013). Focal mechanism solutions from NKUA-SL. Inset: location of the study area (red box).

Considering the uncertainties in methods used for locating historical earthquakes, those earthquakes could well be correlated to the same fault system activated in 2021. Strictly referring to the activated area, there are no significant seismic events since 1766, with the possible exception of a M_w=6.1 shock in 1941 (Makropoulos et al., 2012). The area to the SE has produced a plethora of strong events, with magnitudes exceeding 6.0 (e.g., Papastamatiou and Mouyaris, 1986; Papadimitriou and Karakostas, 2003).

In this work we establish the PGA-$IV2_p$ relationship for five target cities in Thessaly: (a) Larisa, (b) Karditsa, (c) Kozani, (d) Trikala and (e) Litochoro. The first four were selected due to their urbanization level, while the last one is a hub for both winter and summer tourism, rendering it a regional financial asset. We exploited the wealth of events that belong to the recent 2021 sequence, as recorded by permanent stations of the Hellenic Unified Seismic Network (HUSN). This is a first step for exploring an on-site EEWS in the region. We explore the relationship between the two quantities both on-site and between a first-trigger station (close to the epicentral area) and each target. Multiple signal windows are investigated to investigate the stability of the laws and identify the possibility of using very short windows to avoid S arrivals within t_w.

2. DATA ACQUISITION AND PROCESSING

To investigate the behavior of $IV2_p$ and PGA in the area, we used seismic events from the recent 2021 sequence near Larisa. Earthquake information was retrieved from the NKUA-SL, which offers a comprehensive catalogue with manually picked phases. As the available number of events was large (over 2,000) in the one-month period we considered, we selected a cutoff magnitude of 3.0 to include strong signals, as identification of P arrivals could be dubious in weaker events. In total, the selected 1-month-long time period between 03/03/2021 and 03/04/2021 composed a dataset of 206 earthquakes. We then used recordings by HUSN stations that correspond to the sites of interest, i.e., TYRN (calibration near-source velocimeter), GINA (accelerometer located at the outskirts of Larisa), SOFA (accelerometer, available instrument closest to Karditsa, located in Sofades town, 15 km away), KZN (velocimeter at Kozani), TRKA (accelerometer at Trikala) and LIT (velocimeter at Litochoro). These instruments belong to the HL (National Observatory of Athens, Institute of Geodynamics, 1997) and HT (Aristotle University of Thessaloniki Seismological Network, 1981) networks. Station metadata and waveform data were retrieved through the European Integrated Data Archive (EIDA) node at GI-NOA, using the relevant international Federation of Digital Seismograph Network's (FDSN) service (Evangelidis et al., 2021). We used the ObsPy package (Beyreuther et al., 2010; Krischer et al., 2015) to acquire them and process the data.

Concerning data processing, we initially eliminated clipped waveforms, by visual inspection of event-station (velocimeters) pairs of magnitude 4.5 (or greater) and maximum epicentral distance of 30.0 km. Stations with available data, but no manually determined P arrivals, were automatically picked, after filtering the signal between 1 and 20 Hz (Baer and Kradolfer, 1987). Then, using TauP (Crotwell et al., 1999) the S-

P difference time was calculated with a regional velocity model (Karakonstantis, 2017). Finally, preprocessing concluded by removing the instrument's response from the raw data, converting amplitudes to velocity and acceleration, and applying a high-pass filter of 0.075 Hz (Wu and Kanamori, 2005, 2008).

For time windows of 1 s, 2 s and 3 s after the P arrival (t_w), $IV2_p$ was determined. We opted for this range of windows as the calibration station (TYRN) is located very close to the epicenters and, thus, S-P times are small. In any case, if t_w was larger than the theoretically estimated S-P, the event-station pair was rejected. Furthermore, we obtained *PGA* values from a time window starting at the S arrival (either manually determined, if in the initial catalogue, or theoretically by means of the S-P times) and ending 20 s later. We used vertical recordings for estimating $IV2_p$ and horizontal components for *PGA*. Finally, we regressed for the logarithms of the two quantities to estimate linear models of the form:

$$\log(PGA) = a + b * \log(IV2_p) \qquad (2)$$

It is noted that we excluded observations with $\frac{PGA}{P_a} < 2$, where P_a the peak acceleration during t_w. This was necessary to automatically identify and remove incidents of erroneous picking (whether manual or automatic) or ill-determined S-P times (for cases impacted by the uncertainties in the hypocenter, velocity model or ray-tracing algorithm).

After applying the necessary selection criteria, the final dataset consisted of 631 suitable observations for t_w=1 s, 431 for t_w=2 s and 333 for t_w=3 s, amongst the six stations. On average, 65% of the total picks were automatically determined by the Baer and Kradolfer (1987) algorithm. As our study was conducted during the evolution of the sequence, we expected a large number of unpicked (but suitable) arrivals. There seems to be a bias against accelerometers in the catalogue; GINA, SOFA and TRKA had no manually picked observations, after the selection (Fig. 2). However, we note that there were some arrivals determined from these instruments in the initial catalogue (for example, there were 22 picks at GINA that provided ineligible amplitude measurements, as the *PGA* to P_a ratio was less than 2.0). Due to its proximity to the source area, TYRN presented but a few arrivals, especially in longer signal windows (Figs 2b and 2c). LIT, the station with most eligible observations, also featured the highest number of manual picks among all t_w.

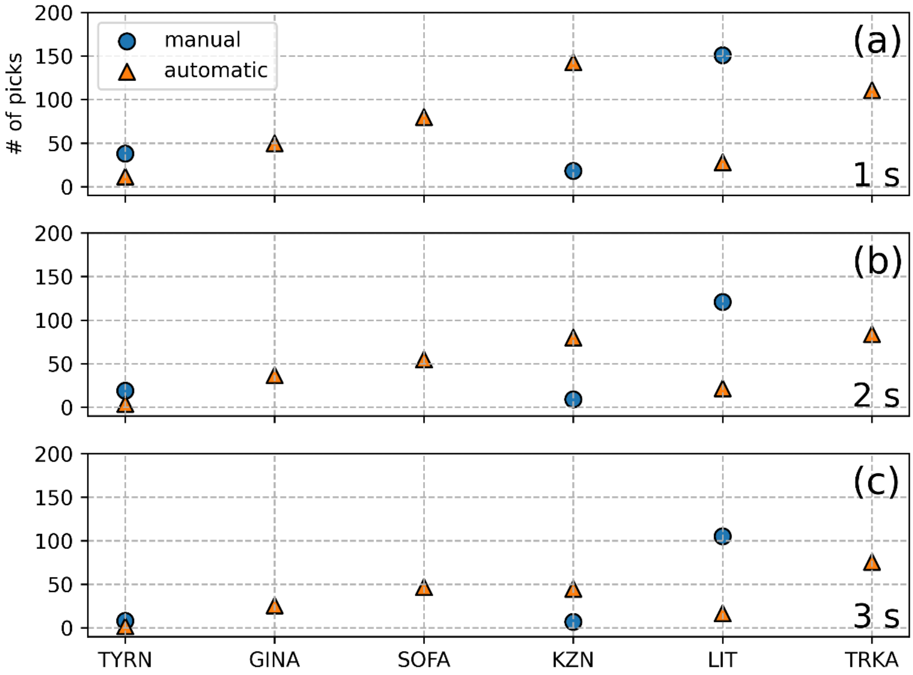

Fig. 2: Distribution of manual (circles) and automatic (triangles) picks corresponding to amplitude observations for each station and signal window, after the application of selection criteria. Each t_w, i.e., 1 s (a), 2 s (b) and 3 s (c), is noted at the bottom right of each subplot.

3. EMPIRICAL CORRELATION LAWS FOR THE AREA OF THESSALY

Determination of the strength of shaking from the initial P-wave are two important elements for earthquake early warning. This can practically be represented by *PGA*, a quantity commonly used in seismic risk and engineering (e.g. Dolce et al., 2020).

3.1. $IV2_p$ as an on-site estimator for *PGA*

As already mentioned, $IV2_p$ has been previously explored as a quantity capable of estimating the earthquake magnitude, with good correlation (Festa et al., 2008). Similarly, our analysis revealed a good correlation between $IV2_p$ and *PGA*, obtained at the same site. Following, we present coefficients of the regression models (as in Eq. 2) for on-site purposes and t_w=2 s (Table 1).

Table 1. Regression results for the on-site analysis and t_w=2 s. a is the intercept, b the slope, σ the individual standard error, N the number of observations in the regression, R^2 the correlation coefficient and SER the standard error of regression.

Station	**Site**	***a ± σa***	***b ± σb***	***N***	***R²***	***SER***
TYRN	Near source	1.720 ± 0.296	0.334 ± 0.059	23	0.60	0.216
GINA	Larisa	2.320 ± 0.275	0.390 ± 0.047	37	0.67	0.422
SOFA	Karditsa	2.098 ± 0.256	0.372 ± 0.036	55	0.67	0.308
KZN	Kozani	1.677 ± 0.229	0.329 ± 0.032	89	0.55	0.396
LIT	Litochoro	2.133 ± 0.119	0.400 ± 0.018	143	0.80	0.253
TRKA	Trikala	2.023 ± 0.169	0.346 ± 0.025	74	0.70	0.258

For a t_w of 2 s, the intercept of Eq. 2 is constrained between 1.677 and 2.320, while slopes are in the 0.329 to 0.400 range. The two quantities are well-correlated, even though results at KZN suggest a weaker connection. Regression analysis for observations in t_w=3 s offers a higher correlation (between 0.72 and 0.79) from a smaller sample across the board; for instance, suitable observations at TYRN are only 10, due to the proximity to the sources and the very small S-P times. On the other hand, adopting t_w=1 s, yields worse correlation (such as in KZN, where R^2 is 0.285), even though the number of observations is higher. Thus, we consider t_w=2 s as the most balanced window choice, accepting the tradeoff between correlation and data sample size.

Fig. 3 presents *PGA* as a function of $IV2_p$ in TYRN, used as the reference station located near the source. The proximity to most epicenters reduced the number of available observations significantly, as the difference between the arrivals of P- and S-waves was less than 2 s, in most cases. However, measurements obtained by events at the far northern side of the sequence (Fig. 1) provided valuable insight. It seems that a relation between the two quantities can be established in TYRN. In this case, we observe good regression in all time windows (even in 1 s). As seen in Fig. 3, the differences in the coefficients among the t_w are minor. Therefore, using the shortest available t_w to estimate *PGA* from a station that is virtually right above the impending earthquake is not out of the question. Moreover, even in situations such as this, with the closest target being only 23 km away, being able to estimate *PGA* 1 s after the rupture started (and has not even concluded yet) could render $IV2_p$ as the most beneficial and effective EEWS parameter.

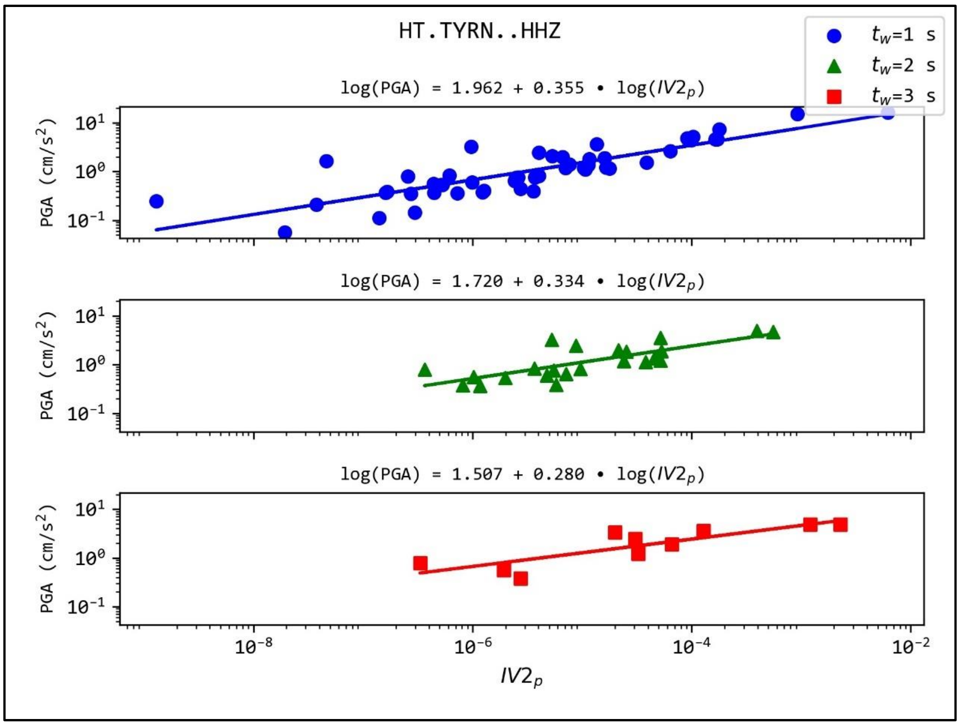

Fig. 3: Regression models of *PGA* for TYRN, in three time windows (t_w) after the P-wave arrival. *PGA* is estimated from the maximum amplitude of the two horizontals after the S-wave arrival, while $IV2_p$ is obtained from the vertical channel.

Similarly, the *PGA* – $IV2_p$ relation showcases good correlation in the target sites Larisa (GINA, Fig. 4a) and Sofades-Karditsa (SOFA, Fig. 4b). At this point, we would like to stress that SOFA was the closest available instrument to Karditsa and we consider this in our interpretation of the results. In any case, both accelerometers document a significantly correlated relation in all signal windows.

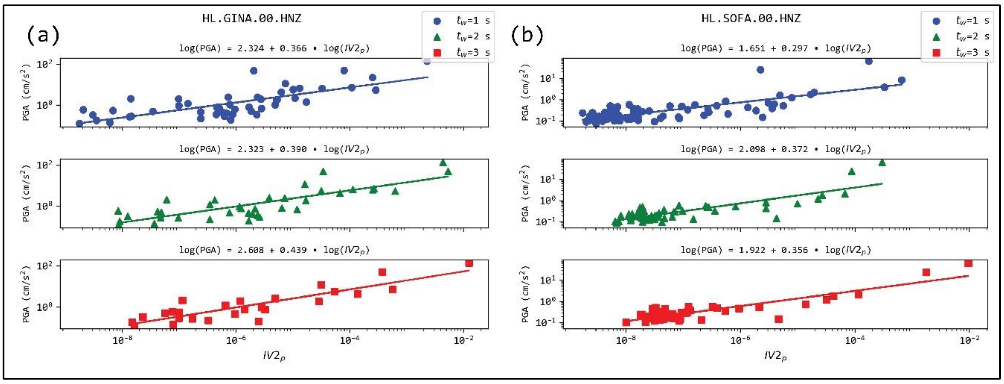

Fig. 4. Regression models of *PGA* for GINA (a) and SOFA (b). Notation as in Fig. 3.

The same behavior is present in the remaining sites, namely Kozani (KZN, Fig. 5a), Trikala (TRKA, Fig. 5b) and Litochoro (LIT, Fig. 5c). The relation between the logarithms of *PGA* and $IV2_p$ is strongly linear. Furthermore, KZN seems to be the station mostly affected by measurements in the 1 s window. There is a group of observations with low $IV2_p$ that deviates greatly from the linear model (Fig. 5a) and leads to significant skewing and low correlation. Nevertheless, the effect of this is eliminated in the 2 s and 3 s windows. Linearity is best shown in LIT (Fig. 5c), a station that, coincidentally, has the largest population of observations.

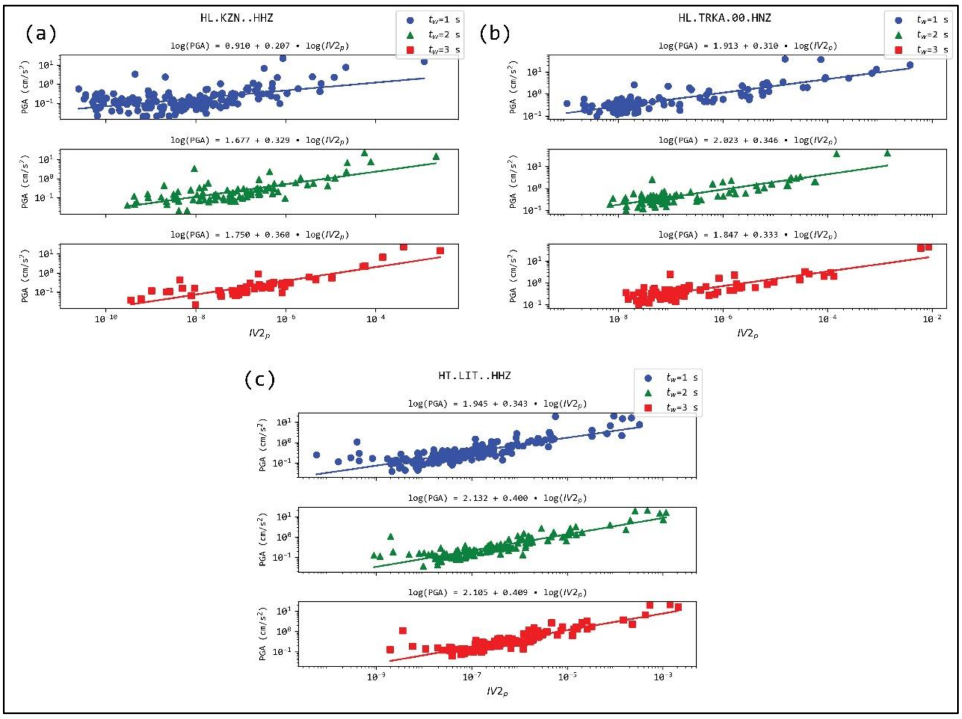

Fig. 5. Regression models of *PGA* for KZN (a), TRKA (b) and LIT (c). Notation as in Fig. 3.

3.2. *PGA* in target sites as a function of near-source $IV2_p$

The concept of using near-source stations to estimate the ferocity of the shaking has been previously explored in literature, by correlation of other parameters with the impending event's magnitude (Wu and Kanamori, 2005; Wu et al., 2007; Zollo et al., 2010). To clarify whether *IV2p* has such a potential, we related measurements of vertical velocity at the reference station located closest to the sequence (TYRN) to PGA at the five target sites (*ts*) (GINA, SOFA, KZN, TRKA and LIT). Essentially, we obtained Eq. 2 between different locations:

$$\log(PGA^{ts}) = a + b * \log\left(IV2_{p}^{TYRN}\right) \qquad (3)$$

We note that these results are a first approach in researching the feasibility of inter-site relations, between *PGA* and *IV2p*, and are preliminary. Local site effects have not been accounted for and installation sites vary. A clear logarithmic dependence exists with a slope mainly ranging between 0.30 and 0.50, with few exceptions. However, correlation is not as reliable as in the case of the same-site analysis. Inter-site laws for KZN and LIT, two stations north of the target area, presented the lower correlation. It is not yet clear whether this is coincidental or there is a cause, e.g., directivity or distance to the near-source station. In Table 2, we present the regression results for all five sites and t_w=1 s.

Table 2. Regression results for the target analysis and t_w=1 s. Notation as in Table 1.

Station	**Target**	$a \pm \sigma a$	$b \pm \sigma b$	N	R^2	SER
GINA	Larisa	1.901 ± 0.296	0.324 ± 0.054	18	0.68	0.335
SOFA	Sofades-Karditsa	1.282 ± 0.413	0.320 ± 0.078	15	0.57	0.299
KZN	Kozani	0.069 ± 0.328	0.162 ± 0.058	43	0.16	0.498
LIT	Litochoro	0.720 ± 0.305	0.226 ± 0.054	45	0.29	0.452
TRKA	Trikala	1.177 ± 0.400	0.273 ± 0.078	26	0.34	0.452

Concerning different sites, and taking into consideration the difference in epicentral distance, regression analysis for t_w equal to either 2 s or 3 s did not yield reliable results. The small number of observations for these windows at TYRN acted prohibitively. All regressions (except for LIT and a 2 s window) were carried out with less than 10 observations. Thus, and after considering that a possible connection with a 1 s window at the near-source station would be much more useful, we present regression results for the first window (Table 2). Correlations are much weaker, with only GINA (located 10 km away from TYRN, Fig. 6a) and SOFA (Fig. 6b) exhibiting a satisfactory correlation; yet, it is not as high as the on-site cases. There is no statistically supported connection between TYRN and the other three sites.

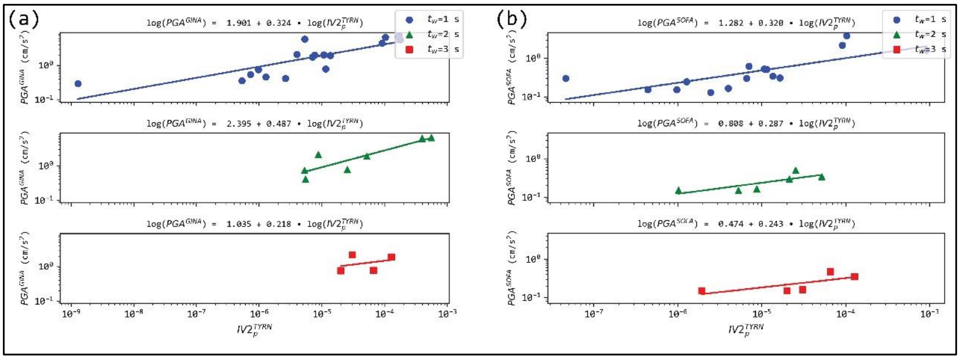

Fig. 6. Regression models of *PGA* between near-source TYRN and targets GINA (a) and SOFA (b). Notation as in Fig. 3.

4. CONCLUSIONS

We estimated empirical scaling relationships between the earthquake early warning parameter $IV2_p$ and *PGA*, using recordings of earthquakes of an extensive sequence in Thessaly which started on March 4, 2021, with the occurrence of a M_w=6.3 event. The earthquake catalogue consisted of 206 events located by NKUA-SL through means of manual phase arrival determination. Waveform data was recorded by permanent stations of HUSN, equipped with velocimeters or accelerometers. The stations were selected to azimuthally cover the area around the activated fault zone, while also correspond to sites of socioeconomic significance. These are Larisa (station GINA), Sofades-Karditsa (SOFA), Kozani (KZN), Litochoro (LIT) and Trikala (TRKA). We also selected an instrument installed at the vicinity of the seismic outburst to use as reference (TYRN). Our findings revealed a linear relationship between the logarithms of $IV2_p$ and *PGA* at single sites, with R^2 being generally greater than 0.60. Signal windows with durations of 2 s and 3 s seem to offer similar correlations, while 1 s seems to be less reliable. The very short duration of the latter renders it more sensitive to errors in phase picking. Moreover, after 1 s, the rupture might still be at a very early stage (for stronger magnitudes M≥6.0). Therefore, out of the three, a t_w of 2 s seems to be the best to estimate *IV2p* as it is long enough to provide good correlation and short enough to include more P-arrivals.

Research on the potential of $IV2_p$ is ongoing, but, if proven fruitful, it can help shape a new landscape for EEWSs, with on-site, front-end design in mind, to increase the lead time and reduce the blind zone. This will permit to grossly estimate the impeding shaking and emit an alert with the expected strong ground motion to affected partners (e.g., government agencies, local industries). The level of seismic hazard in the area makes the assessment of any developed EEWS and its capabilities extremely useful. Local industrial and other financial activity will greatly benefit from a system that broadcasts alerts, even in short notice, to the sensitive infrastructure of Thessaly. In that aspect, a system that avoids the conundrum of rapid and accurate epicenter and, more importantly, magnitude estimation could be proven invaluable for automating damage mitigation protocols.

In any case, further work is required to establish the spatial (and possibly temporal) behavior of $IV2_p$ and explore its stability both in practical (by application in other areas) and theoretical terms. A model documenting the spatial variation of $IV2_p$ is necessary for operational use. A more modern P-wave picker (e.g., Yanwei et al., 2021) would aid both optimizing the empirical laws and provide a better foundation for estimating the feasibility of the inter-site approach. As S-arrivals would not be known or be able to be estimated in real-time (due to the absence of event locations), a solution needs to be established to avoid shear-wave arrivals in the P signal window. Therefore, further investigation is required on the viability and tradeoff of using a fixed short t_w or employing a real-time S-picker at the near-source station Finally, further investigation should focus in integrating observations from events in a wider magnitude range, by assessing areas where magnitudes greater than 6.0 are present.

5. ACKNOWLEDGMENTS

The authors are grateful to the personnel of the Geodynamic Institute of the National Observatory of Athens and the Department of Geophysics of the Aristotle University of Thessaloniki involved in installing, operating and maintaining the stations used in this study, as well as all staff involved in the Hellenic Unified Seismic Network (recordings of HUSN stations were used by NKUA-SL to determine earthquake locations and focal mechanisms).

The authors would like to express their gratitude to Dr. Christos Evangelidis and an anonymous reviewer for their constructive feedback which greatly improved the manuscript.

We acknowledge support of this study by the project "HELPOS - Hellenic Plate Observing System" (MIS 5002697) which is implemented under the Action "Reinforcement of the Research and Innovation Infrastructure", funded by the Operational Programme "Competitiveness, Entrepreneurship and Innovation" (NSRF

2014-2020) and co-financed by Greece and the European Union (European Regional Development Fund).

Fig. 1 was plotted with GMT 6.0 (Wessel et al., 2019) and its Python wrapper (Uieda et al., 2021). Figs 2 through 6 were plotted with Matplotlib (Hunter, 2007).

6. REFERENCES

Allen, R. M., 2007. The ElarmS earthquake early warning methodology and its application across California in: P. Gasparini, G. Manfredi, and J. Zschau (Eds.), *Earthquake Early Warning System*, Springer, Berlin, 21– 43 pp. doi: 10.1007/978-3-540-72241-0_3

Allen, R. M., Kanamori, H., 2003. The potential for earthquake early warning in Southern California. *Science*, 300, 786– 789. doi: 10.1126/science.1080921

Aristotle University of Thessaloniki Seismological Network, 1981. Permanent regional seismological network operated by the Aristotle University of Thessaloniki, International Federation of Digital Seismograph Networks, doi: 10.7914/SN/HT.

Baer, M., Kradolfer, U., 1987. An automatic phase picker for local and teleseismic events. *Bull. Seismol. Soc. Am.*, 77, 1437–1445.

Beltramone, L., Gomes R.C., 2021. Earthquake Early Warning Systems as an Asset Risk Management Tool. *CivilEng*, 2, 120-133. doi: 10.3390/civileng2010007

Beyreuther, M., Barsch, R., Krischer, L., Megies, T., Behr, Y., Wassermann, J., 2010. ObsPy: A Python Toolbox for Seismology. *Seismol. Res. Lett*., 81, 530-533. doi: 10.1785/gssrl.81.3.530

Brondi, P., Picozzi, M., Emolo, A., Zollo, A., Mucciarelli, M. 2015. Predicting the macroseismic intensity from early radiated P wave energy for on-site earthquake early warning in Italy. *J. Geophys. Res. Solid Earth*, 120, 7174– 7189. doi: 10.1002/2015JB012367

Brooks, B.A., Protti, M., Ericksen, T., Bunn, J., Vega, F., Cochran, E.S., Duncan, C., Avery, J., Minson, S.E., Chaves, E., Baez, J.C., Foster, J., Glennie, C.L., 2021. Robust

Earthquake Early Warning at a Fraction of the Cost: ASTUTI Costa Rica. AGU Adv. 2, e2021AV000407. doi: https://doi.org/10.1029/2021AV000407

Caputo, R., Bravard, J.-P., Helly, B., 1993. The Pliocene-Quaternary tecto-sedimentary evolution of the Larisa plain (eastern Thessaly, Greece). *Geodin. Acta*, 7, 57–85.

Caputo, R., Piscitelli, S., Oliveto, A., Rizzo, E., Lapenna, V., 2004. The use of electrical resistivity tomography in active tectonics. Examples from the Tyrnavos Basin, Greece. *J. Geodyn.*, 36 (1–2), 19–35.

Chung, A.I., Meier, M.A., Andrews, J., Böse, M., Crowell, B.W., McGuire, J.J., Smith, D.E., 2020. ShakeAlert earthquake early warning system performance during the 2019 ridgecrest earthquake sequence. *Bull. Seismol. Soc. Am.*, 110, 1904–1923. doi: 10.1785/0120200032

Crotwell, H.P., Owens, T.J., Ritsema, J., 1999. The TauP Toolkit: Flexible Seismic Travel-time and Ray-path Utilities. *Seismol. Res. Lett.*, 70, 154–160. doi: 10.1785/gssrl.70.2.154

Dolce, M., Prota, A., Borzi, B., da Porto, F., Lagomarsino, S., Magenes, G., Moroni, C., Penna, A., Polese, M., Speranza, E., Verderame, G.M., Zuccaro, G., 2020. Seismic risk assessment of residential buildings in Italy. *Bull. Earthq. Eng.*, 1–34. doi: 10.1007/s10518-020-01009-5

EAK, 2003. Greek seismic code. Earthquake Planning and Protection Organization, Athens (in Greek).

Espinosa-Aranda, J., Jiménez, A., Ibarrola, G., Alcantar, F., Aguilar, A., Inostroza, M., Maldonado, S., 1995. Mexico City seismic alert system. *Seism. Res. Lett*., 66, 42–53.

Evangelidis, C., Triantafyllis, N., Samios, M., Boukouras, K., Kontakos, K., Ktenidou, O.J. , Fountoulakis, I., Kalogeras, I., Melis, N., Galanis, O., Papazachos, C.B., Hatzidimitriou, P., Scordilis, E., Sokos, E., Paraskevopoulos, P., Serpetsidaki, A., Kaviris, G., Kapetanidis, V., Papadimitriou, P., Voulgaris, N., Kassaras, I., Chatzopoulos, G., Makris, I., Vallianatos, F., Kostantinidou, K., Papaioannou, C., Theodoulidis, N., Margaris, B., Pilidou, S., Dimitriadis, I., Iosif, P., Manakou, M., Roumelioti, Z., Pitilakis, K., Riga, E., Drakatos, G., Kiratzi, A., Tselentis, G. A., 2021.

Seismic Waveform Data from Greece and Cyprus: Integration, Archival, and Open Access. Seismol. Res. Lett., 92(3), 1672-1684. doi: 10.1785/0220200408

Festa, G., Zollo, A., Lancieri, M., 2008. Earthquake magnitude estimation from early radiated energy. Geophys. Res. Lett., 35, L22307, doi: 10.1029/2008GL035576.

Ganas, A., Oikonomou, I. A., Tsimi, C., 2013. NOAfaults: a digital database for active faults in Greece. *Bul. Geol. Soc. Greece*, 47(2), 518-530. doi: 10.12681/bgsg.11079

Ganas, A., Valkaniotis, S., Briole, P., Serpetsidaki, A., Kapetanidis, V., Karasante, I., Kassaras, I., Papathanassiou, G., Karamitros, I., Tsironi, V., Elias, P., Sarhosis, V., Karakonstantis, A., Konstantakopoulou, E., Papadimitriou, P., Sokos, E., 2021. Domino-style earthquakes along blind normal faults in Northern Thessaly (Greece): kinematic evidence from field observations, seismology, SAR interferometry and GNSS. Bull. Geol. Soc. Greece, 58, 37–86. doi: 10.12681/BGSG.27102

Gasparini, P., Manfredi, G., Zschau, J., 2011. Earthquake early warning as a tool for improving society's resilience and crisis response. *Soil Dyn. Earthquake Eng*., 31(2), 267– 270, doi: 10.1016/j.soildyn.2010.09.004.

Hloupis, G., Vallianatos, F., 2013. Wavelet-based rapid estimation of earthquake magnitude oriented to early warning. *IEEE Geosci. Remote S.*, 10(1), 43-47. doi: 10.1109/LGRS.2012.2191932

Hloupis, G., Vallianatos, F., 2015. Wavelet-Based Methods for Rapid Calculations of Magnitude and Epicentral Distance: An Application to Earthquake Early Warning System. *Pure Appl. Geophys*., 172, 2371–2386. doi: 10.1007/s00024-015-1081-2

Hsu, T.-Y., Nieh, C.P., 2020. On-Site Earthquake Early Warning Using Smartphones. Sensors, 20, 2928. doi: 10.3390/s20102928

Hunter, J.D., 2007. Matplotlib: A 2D Graphics Environment. *Comput. Sci. Eng*. 9, 90–95. doi: 10.1109/MCSE.2007.55

Iannacone, G., Zollo, A., Elia, L., Convertito, V., Satriano, C., Martino, C., 2010. A prototype system for earthquake early-warning and alert management in southern Italy. *Bull. Earthquake Eng.*, 8, 1105–1129. doi:10.1007/s10518-009-9131-8.

Kanamori, H., 2005. Real-time seismology and earthquake damage mitigation. *Annu. Rev. Earth Pl. Sc.*, 33, 195–214. doi: 10.1146/annurev.earth.33.092203.122626

Kanamori, H., Hauksson, E., Heaton, T., 1997. Real-time seismology and earthquake hazard mitigation. *Nature*, 390, 461–464.

Kapetanidis, V., Papadimitriou, P., Kaviris, G., 2019. Earthquake Early Warning application in Central Greece. *Bul. Geol. Soc. Greece*, 7, 95, Ext. Abs. GSG2019-095, 277-278.

Karakonstantis, A. 2017. 3-D Simulation of Crust and Upper Mantle Structure in the Broader Hellenic Area Through Seismic Tomography. Ph.D. Thesis, Department of Geophysics-Geothermics, Faculty of Geology, University of Athens, Athens, Greece.

Krischer, L., Megies, T., Barsch, R., Beyreuther, M., Lecocq, T., Caudron, C., Wassermann, J., 2015. ObsPy: A bridge for seismology into the scientific Python ecosystem. *Comput. Sci. Discov.*, 8, 0–17. doi: 10.1088/1749-4699/8/1/014003

Koukouvelas, I.K., Nikolakopoulos, K.G., Kyriou, A., Caputo, R., Belesis, A., Zygouri, V., Verroios, S., Apostolopoulos, D., Tsentzos, I., 2021. The March 2021 Damasi Earthquake Sequence, Central Greece: Reactivation Evidence across the Westward Propagating Tyrnavos Graben. Geosci., 11(8), 328. doi: 10.3390/GEOSCIENCES11080328

Makropoulos, K., Kaviris, G., Kouskouna, V., 2012. An updated and extended earthquake catalogue for Greece and adjacent areas since 1900. *Nat. Hazards Earth Syst. Sci.*, 12, 1425–1430. doi:10.5194/nhess-12-1425-2012

Mavroulis, S., Mavrouli, M., Carydis, P., Agorastos, K., Lekkas, E., 2021. The March 2021 Thessaly earthquakes and their impact through the prism of a multi-hazard approach in disaster management. Bull. Geol. Soc. Greece 58, 1–36. doi: 10.12681/BGSG.26852

Minson, S.E., Baltay, A.S., Cochran, E.S., Hanks, T.C., Page, M.T., McBride, S.K., Milner, K.R., Meier, M.A., 2019. The Limits of Earthquake Early Warning Accuracy and Best Alerting Strategy. *Sci. Rep.*, 9, 1–13. doi: 10.1038/s41598-019-39384-y

Nakamura, Y., 1988. On the urgent earthquake detection and alarm system (UrEDAS). *Proceeding of 9th world conference on earthquake engineering, Tokyo-Kyoto, Japan.*

National Observatory of Athens, Institute of Geodynamics, 1997. National Observatory of Athens Seismic Network, International Federation of Digital Seismograph Networks, doi: 10.7914/SN/HL.

Papadimitriou, E., Karakostas, V., 2003. Episodic occurrence of strong (M_w≥6.2) earthquakes in Thessalia area (central Greece). *Earth Planetary Sc. Letters*, 215, 395-409.

Papadopoulos, G., Argyris, I., Aggelou, S., Karastathis, V., 2014. REWSET : A prototype seismic and tsunami early warning system in Rhodes island , Greece, in: Geophysical Research Abstracts, *EGU General Assembly, Vienna, Austria.*

Papadopoulos, G.A., Agalos, A., Karavias, A., Triantafyllou, I., Parcharidis, I., Lekkas, E., 2021. Seismic and Geodetic Imaging (DInSAR) Investigation of the March 2021 Strong Earthquake Sequence in Thessaly, Central Greece. Geosci., 11(8), 311. doi: 10.3390/GEOSCIENCES11080311

Papastamatiou, D., Mouyaris, N., 1986. The earthquake of April 30, 1954, in Sophades (Central Greece*). Geophys. Jour. Inter.*, 87(3), 885–895. doi: 10.1111/j.1365-246X.1986.tb01975.x

Parolai, S., Bindi, D., Boxberger, T., Milkereit, C., Fleming, K., Pittore, M., 2015. On-site early warning and rapid damage forecasting using single stations: Outcomes from the REAKT project. *Seismol. Res. Lett.*, 86(5), 1393– 1404, doi: 10.1785/0220140205.

Satriano, C., Lomax, A., Zollo, A., 2008. Real-Time Evolutionary Earthquake Location for Seismic Early Warning. *Bull. Seism. Soc. Am.*, 98 (3), 1482–1494.

Satriano, C., Elia, L., Martino, C., Lancieri, M., Zollo, A., Iannacone G., 2011. PRESTo, the earthquake early warning system for Southern Italy: Concepts, capabilities and future perspectives. *Soil Dyn. Earthquake Eng.*, 31 (2), 137-153, doi: 10.1016/j.soildyn.2010.06.008

Simons, F.J., Dando, B., Allen, R. M., 2006. Automatic detection and rapid determination of earthquake magnitude by wavelet multiscale analysis of the primary arrival. *Earth Planetary Sc. Letters*, 250, 214–223.

Sokos, E., Tselentis, G.A., Paraskevopoulos, P., Serpetsidaki, A., Stathopoulos-Vlamis, A., Panagis, A., 2016. Towards earthquake early warning for the Rion-Antirion bridge, Greece. *Bull. Earthq. Eng*., 14, 2531–2542. doi: 10.1007/s10518-016-9893-8

Spallarossa, D., Kotha, S.R., Picozzi, M., Barani, S., Bindi, B., 2019. On-site earthquake early warning: a partially non-ergodic perspective from the site effects point of view. *Geophys. Jour. Inter*., 216(2), 919–934. doi: 10.1093/gji/ggy470

Stucchi, M., Rovida, A., Gomez Capera, A.A., Alexandre, P., Camelbeeck, T., Demircioglu, M.B., Gasperini, P., Kouskouna, V., Musson, R.M.W., Radulian, M., Sesetyan, K., Vilanova, S., Baumont, D., Bungum, H., Fäh, D., Lenhardt, W., Makropoulos, K., Martinez Solares, J.M., Scotti, O., Zivcic , M., Albini, P., Batllo, J., Papaioannou, C., Tatevossian, R., Locati, M., Meletti, C., Viganò, D., Giardini, D., 2013. The SHARE European Earthquake Catalogue (SHEEC) 1000–1899. *J. Seismol*., 17 (2), 523–544. doi: 10.1007/s10950-012-9335-2.

Uieda, L., Tian, D., Leong, W.J., Toney, L., Schlitzer, W., Yao, J., Grund, M., Jones, M., Materna, K., Newton, T., Ziebarth, M., Wessel, P., 2021. PyGMT: A Python interface for the Generic Mapping Tools. doi: 10.5281/ZENODO.4592991

Wessel, P., Luis, J.F., Uieda, L., Scharroo, R., Wobbe, F., Smith, W.H.F., Tian, D., 2019. The Generic Mapping Tools Version 6. *Geochemistry, Geophys. Geosystems*, 20, 5556–5564. doi: 10.1029/2019GC008515

Wu, Y.M., Kanamori, H., 2005. Experiment of an on-site method for the Taiwan Early Warning System. *Bull. Seismol. Soc. Am.*, 95, 347– 353, doi:10.1785/0120040097.

Wu, Y.M., Kanamori, H., 2008. Development of an earthquake early warning system using real-time strong motion signals. *Sensors*, 8 (1), 1– 9.

Wu, Y.M., Shin, T.C., Tsai, Y.B., 1998. Quick and reliable determination of magnitude for seismic early warning. *Bull. Seism. Soc. Am.*, 88, 1254–1259.

Wu, Y.M., Chung, J.K., Shin, T.C., Hsiao, N.C., Tsai, Y.B., Lee, W.H.K., Teng, T.L., 1999. Development of an integrated seismic early warning system in Taiwan- case for Hualien earthquakes. *Terr. Atmospheric Ocean. Sci*., 10, 719–736.

Wu, Y.M., Lee, W.H.K., Chen, C.C., Shin, T.C., Teng, T.L., Tsai, Y.B., 2000. Performance of the Taiwan Rapid Earthquake Information Release System (RTD) during the 1999 Chi-Chi (Taiwan) earthquake. *Seismo. Res. Lett*., 71, 338–343.

Wu, Y.M., Kanamori, H., Allen, R., Hauksson, E., 2007. Determination of earthquake early warning parameters, τ_c and P_d, for southern California. *Geophys. J. Int*., 170, 711–717.

Yanwei, W., Xiaojun, L., Zifa, W., Jianping, S., Enhe, B., 2021. Deep learning for P-wave arrival picking in earthquake early warning. *Earthq. Eng. Eng. Vib*., 20, 391–402. doi: 10.1007/s11803-021-2027-6

Zollo, A., Lancieri, M., Nielsen, S., 2006. Earthquake magnitude estimation from peak amplitudes of very early seismic signals on strong motion. *Geophys. Res. Lett*., 33, L23312, doi:10.1029/2006GL027795

Zollo, A., Iannaccone, G., Convertito, V., Elia, L., Iervolino, I., Lancieri, M., 2009. Earthquake early warning system in southern Italy: Methodologies and performance evaluation. *Geophys. Res. Lett*., 36, L00B07.

Zollo, A., Amoroso, O., Lancieri, M., Wu, Y.M., Kanamori H., 2010. A threshold-based earthquake early warning using dense accelerometer networks. *Geophys. J. Int*., 183, 963– 974, doi:10.1111/j.1365-246X.2010.04765.x

BGSG

Volume 58

Research Paper

Correspondence to:
Dimitrios Galanakis
galanakis@igme.gr

DOI number:
http://dx.doi.org/10.12681/bgsg.27196

Keywords:
2021 Tyrnavos-Elassona earthquake, macroseismic observations, ground deformation phenomena, seismotectonics

Citation:
Galanakis, D., Sboras, S., Konstantopoulou, G. and Xenakis, M. (2021), Neogene-Quaternary Tectonic Regime and Macroseismic Observations in The Tyrnavos-Elassona Broader Epicentral Area of The March 2021, Intense Earthquake Sequence. Bulletin Geological Society of Greece, 58, 200-221.

Publication History:
Received: 04/06/2021
Accepted: 23/09/2021
Accepted article online: 24/09/2021

The Editor wishes to thank Christoph Gruetzner and Haralambos Kranis for their work with the scientific reviewing of the manuscript and Ms Emmanouela Konstantakopoulou for editorial assistance.

NEOGENE-QUATERNARY TECTONIC REGIME AND MACROSEISMIC OBSERVATIONS IN THE TYRNAVOS-ELASSONA BROADER EPICENTRAL AREA OF THE MARCH 2021, INTENSE EARTHQUAKE SEQUENCE

Dimitrios Galanakis [1], Sotiris Sboras [1,2], Garyfallia Konstantopoulou [1], Markos Xenakis [1]

[1]Hellenic Survey of Geological and Mineral Exploration (HSGME), Sp. Loui 1, GR136 77, Acharnae, galanakis@igme.gr kongar@igme.gr markxen@igme.gr

[2]Institute of Geodynamics, National Observatory of Athens, Lofos Nymfon, Thission, GR118 10, Athens ssboras@gmail.com

Abstract

On March 3, 2021, a strong (Mw6.3) earthquake occurred near the towns of Tyrnavos and Elassona. One day later (March 4), a second strong (Mw6.0) earthquake occurred just a few kilometres toward the WNW. The aftershock spatial distribution and the focal mechanisms revealed NW-SE-striking normal faulting. The focal mechanisms also revealed a NE-SW oriented extensional stress field, different from the orientation we knew so far (ca. N-S). The magnitude and location of the two strongest shocks, and the spatiotemporal evolution of the sequence, strongly suggest that two adjacent fault segments were ruptured respectively. The sequence was followed by several coseismic ground deformational phenomena, such as landslides/rockfalls, liquefaction and ruptures. The landslides and rockfalls were mostly associated with the ground shaking. The ruptures were observed west of the Titarissios River, near to the Quaternary faults found by bore-hole lignite investigation. In the same direction, a fault scarp separating the alpidic basement from the alluvial deposits of the Titarissios valley implies the occurrence of a well-developed fault system. Some of the ground ruptures were accompanied by extensive liquefaction phenomena. Others cross-cut reinforced concrete irrigation channels without changing their direction. We suggest that this fault system was partially reactivated, as a secondary surface rupture, during the sequence as a steeper splay of a deeper low-to-moderate angle normal fault.

Περίληψη

Στις 3 Μαρτίου 2021 ισχυρός (M_w=6.3) σεισμός καταγράφηκε κοντά στις πόλεις του Τυρνάβου και της Ελασσόνας. Την επόμενη ημέρα, δεύτερος ισχυρός (M_w=6.0) σεισμός χτύπησε την περιοχή, μόλις λίγα χιλιόμετρα προς τα ΔΒΔ. Η χωρική κατανομή της μετασεισμικής ακολουθίας και οι μηχανισμοί γένεσης αποκάλυψαν την ύπαρξη κανονικούς ρήγματος παράταξης ΒΔ-ΝΑ. Οι μηχανισμοί γένεσης επίσης αποκάλυψαν ένα εφελκυστικό πεδίο προσανατολισμού ΒΑ-ΝΔ, διαφορετικού απ' αυτόν που γνωρίζαμε μέχρι πρότινος (περίπου Β-Ν). Το μέγεθος και η επικεντρική θέση των δύο ισχυρών σεισμών, καθώς και η χωρο-χρονική εξέλιξη της ακολουθίας, υποστηρίζουν σθεναρά την διάρρηξη δύο διπλανών ρηξιγενών τμημάτων αντίστοιχα. Η ακολουθία συνοδεύτηκε από αρκετά φαινόμενα συν-σεισμικής εδαφικής παραμόρφωσης, όπως κατολισθήσεις/βραχοπτώσεις, ρευστοποιήσεις και εδαφικές διαρρήξεις. Οι κατολισθήσεις και βραχοπτώσεις συνδέονται κυρίως με την εδαφική κίνηση. Οι διαρρήξεις εντοπίστηκαν δυτικά του ποταμού Τιταρήσιος, πολύ κοντά σε Τεταρτογενή ρήγματα που ανακαλύφθηκαν παλαιότερα από τη διάνοιξη συστήματος γεωτρήσεων κατά την έρευνα για λιγνιτικά κοιτάσματα. Στην ίδια διεύθυνση, ένα τεκτονικό πρανές που χωρίζει το αλπικό υπόβαθρο από τις αλλουβιακές αποθέσεις της κοιλάδας του Τιταρήσιου υποδεικνύουν την ύπαρξη ενός καλά ανεπτυγμένου συστήματος ρηγμάτων. Αρκετές από τις εδαφικές διαρρήξεις συνδέονταν με φαινόμενα ρευστοποίησης. Κάποιες άλλες διέρρηξαν αρδευτικά κανάλια από οπλισμένο σκυρόδεμα χωρίς να αλλάξουν διεύθυνση. Προτείνεται ότι αυτό το σύστημα ρηγμάτων συμμετείχε μερικώς στη διάρρηξη των σεισμών του 2021 ως ένας κλάδος ενός βαθύτερου κανονικού ρήγματος μέσης έως μικρής γωνίας κλίσης.

Keywords: *2021 Tyrnavos-Elassona earthquake, macroseismic observations, ground deformation phenomena, seismotectonics*

1. INTRODUCTION

On March 3, 2021, at 10:16 UTC, a strong earthquake (M_w=6.3) occurred in northern Thessaly. One day later (March 4, 18:38 UTC), a second strong shock (M_w=6.0) occurred few kilometres WNW of the first one. Until the end of March, five (5) earthquakes greater than M_L=5.0 occurred in the epicentral area. Surprisingly, the focal mechanisms of the strongest shocks did not show E-W striking like we used to know as a typical direction of the active faults of Thessaly (*e.g.*, Caputo, 1993; Caputo and Pavlides, 1993; Caputo *et al.*, 2012); they revealed NW-SE-striking, pure normal dip-slip faulting, in a NE-SW oriented extensional field. In fact, a NE-SW oriented field was proposed for the previous tectonic phase that characterized broader Thessaly, *i.e.*, during Pliocene and Early Pleistocene (Caputo and Pavlides, 1991; 1993).

The affected area is located west of Mt Antichasia, east of Mt Trochalos and Mt Papalivado, which constitute the natural boundary from the Elassona sub-basin, and north of Mt Zarkos (Fig. 1). The stricken settlements are Domeniko, Magoula, Amourio, Evangelismos, Praitorio, Mesochori and Damasi, all situated in "Domeniko-Amourio" area. The ca. N-S-trending Neogene tectonic basin of Domeniko-Amourio (broader Elassona) is crossed by the Elassonitikos River, and further eastwards it enters the E-W-trending tectonic valley of Titarissios River. The Domeniko-Amourio Basin and the Titarissios valley are both intra-montane landforms, surrounded by the aforementioned mountains. The basins show a rather smooth terrain, at the margins of which most of the settlements are located, while the mountainous area is quite ragged considering that it consists of Mesozoic marbles and Paleozoic gneiss-schists (IGME, 1987; 1998). Drainage is dense and the main rivers are supplied by small and large torrents of continuous or seasonal flow. It is locally controlled by faults.

2. GEOLOGICAL SETTING

The Elassona Basin comprises the southern part of a larger depression starting from Florina to the north, and it is known for the rich in lignite-bearing sediments. It consists of two sub-basins: the northeastern one where the town of Elassona is situated, and the southwestern one, the Domeniko-Amourio sub-basin, where the epicentral area lies. These two sub-basins are connected through the Agioneri pass and the Elassonitikos valley. They both belong to the Pelagonian zone. The mountainous area is occupied by the alpidic basement (Fig. 1). The Neopalaeozoic – Lower-Middle Triassic schist-crystalline rocks occupy the SW and N part of the area and they are composed of gneisses and schist-gneiss with marble intercalations (lower members), and (bi)micaceous schists, quartzite, and orthogneiss. Granite and granodiorite intrusions occur in the schist-crystalline rocks that took place before the Pelagonian thrust. The schist-crystalline rocks pass into crystalline limestone of Triassic – Jurassic age. All the above formations of the Pelagonian zone are obducted upon an autochthonous thick series of marbles (Neopalaeozoic – Jurassic age). This series outcrops as a tectonic window at the NW part of the area. The alpidic presence is completed with the ophiolites.

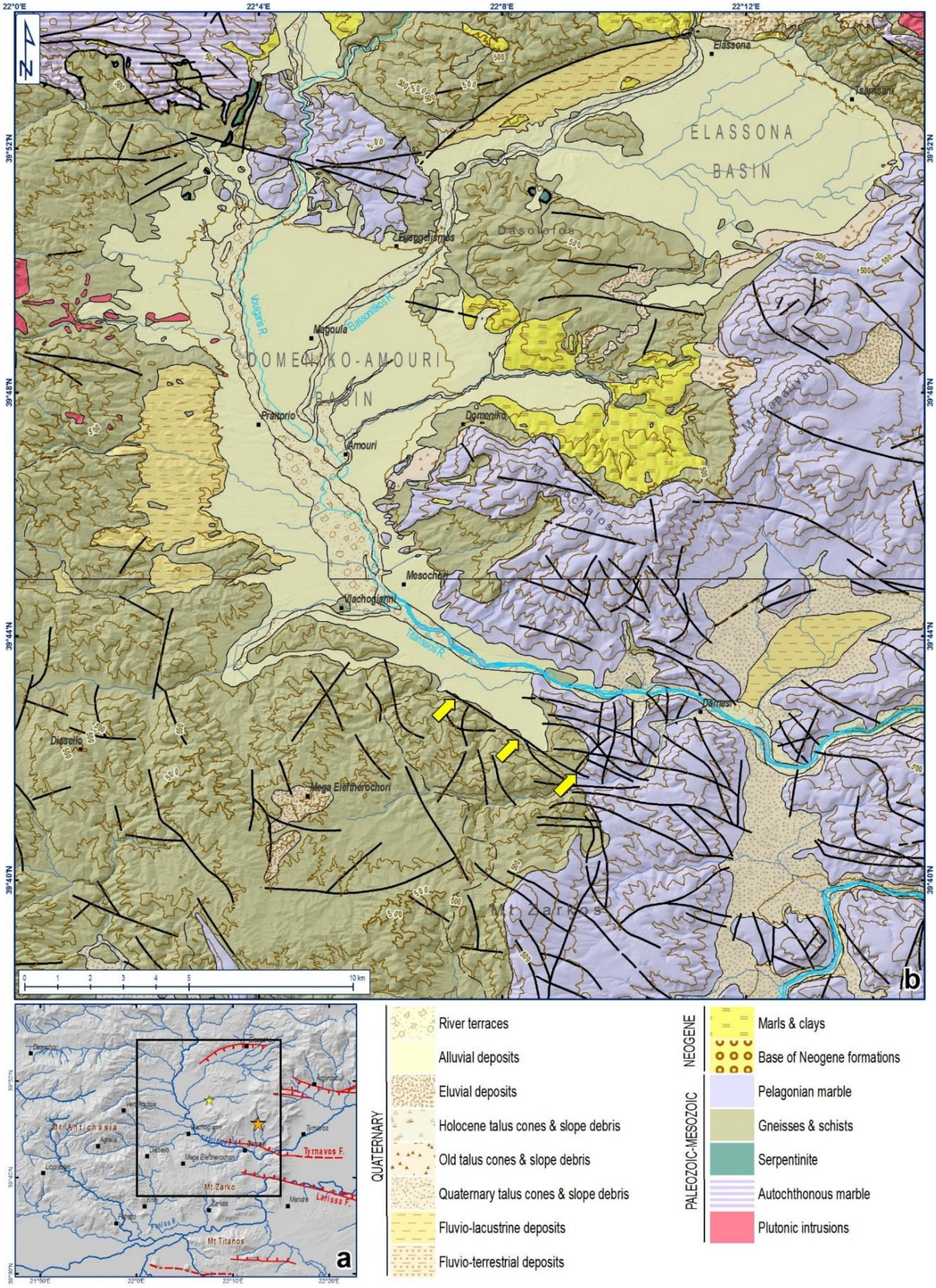

Fig. 1: Simplified geological map of the 2021 Tyrnavos-Elassona epicentral area (modified after IGME, 1987; 1998). Yellow arrows point to a fault we suggest that it partially participated in the 2021 sequence.

The neotectonic, palaeoclimatic and palaeogeographic conditions combined, facilitated the basin's formation and its fill with younger sediments. Thus, the basin is filled with Neogene and Quaternary deposits in which significant lignitic deposits are found. The Neogene (Pliocene) formations are unconformably deposited upon the schist-crystalline basement, they are significantly developed, and they mostly outcrop along the margins of Domeniko-Amourio sub-basin. In more detail, they occupy the hills at the eastern part of the sub-basin. They consist of light-coloured marl, clay and platy marly limestone with very shallow dip. In the steeper valleys, the red series of the Neogene base is observed made of sandstone and clay. The lignite-bearing layers are included in the whitish marl. The most recent deposits that overly the Neogene ones are alluvial deposits of sand, clay and unconsolidated rounded and angular gravel, river terraces, talus cones, slope debris, and deposits lying along river and torrent banks.

The slope gradient map (Fig. 2), which is based on the AW3D30 (ALOS World 3D – 30 m; Tadono *et al.*, 2014)) elevation grid, shows interesting morphological characteristics depending on the geological formations and tectonics (Fig.1). The post-alpidic sediments show a mild/smooth relief with values rarely exceeding 12° (*e.g.*, the fluvio-lacustrine deposits west of Praitorio and west of Elassona). The roughest relief belongs to the marble. Faulting has the strongest impact on the relief by forming linear steep slopes (>18°). Two characteristic examples are the several kilometres-long, ENE-WSW- to NE-SW-trending mountain-front west of Elassona, and the NW-SE-trending linear slope bounding the southern margin of the Titarissios valley. The latter has been also recognised in the 1:50,000 scale geological map ("Farkadon" sheet) of IGME (1998) (marked by yellow arrows in Fig. 1). There are also some other linear slopes, along the southeastern margin of the Elassona Basin and the southwestern margin of the Domeniko-Amourio sub-basin, which are not related to any faulting according to the literature. It is, though, an indication, but not proof, of possible (normal) fault occurrences.

During the mine research in the area by IGME (Dimitriou and Giakoupis, 1998), a dense network of boreholes was drilled revealing important tectono-stratigraphic information for the Domeniko-Amourio sub-basin (Fig. 3). Stratigraphically, the post-alpidic formations found within the basin consist of (from older to younger; Fig. 3c): i) conglomerates and clay-sandy deposits, mostly of fluvio-torrential origin, ii) the lignite-bearing formation of Upper Miocene – Pliocene, composed at its base by mud, sandy clayey and sands with thin lenses of granules and thin interbeds of pure mud, in which the lignitic deposits occur in the form of lenses and intercalations, and at its upper members by friable and rarely stiff marls alternated with clay-marly material and interbeds of marly limestone, and iii) fluviolacustrine and fluvio-torrential Quaternary deposits composed by clay-sandy materials (sandstones, clays and fine-grained conglomerates), alluvial deposits of sands, as well as river terraces, talus cones and slope debris.

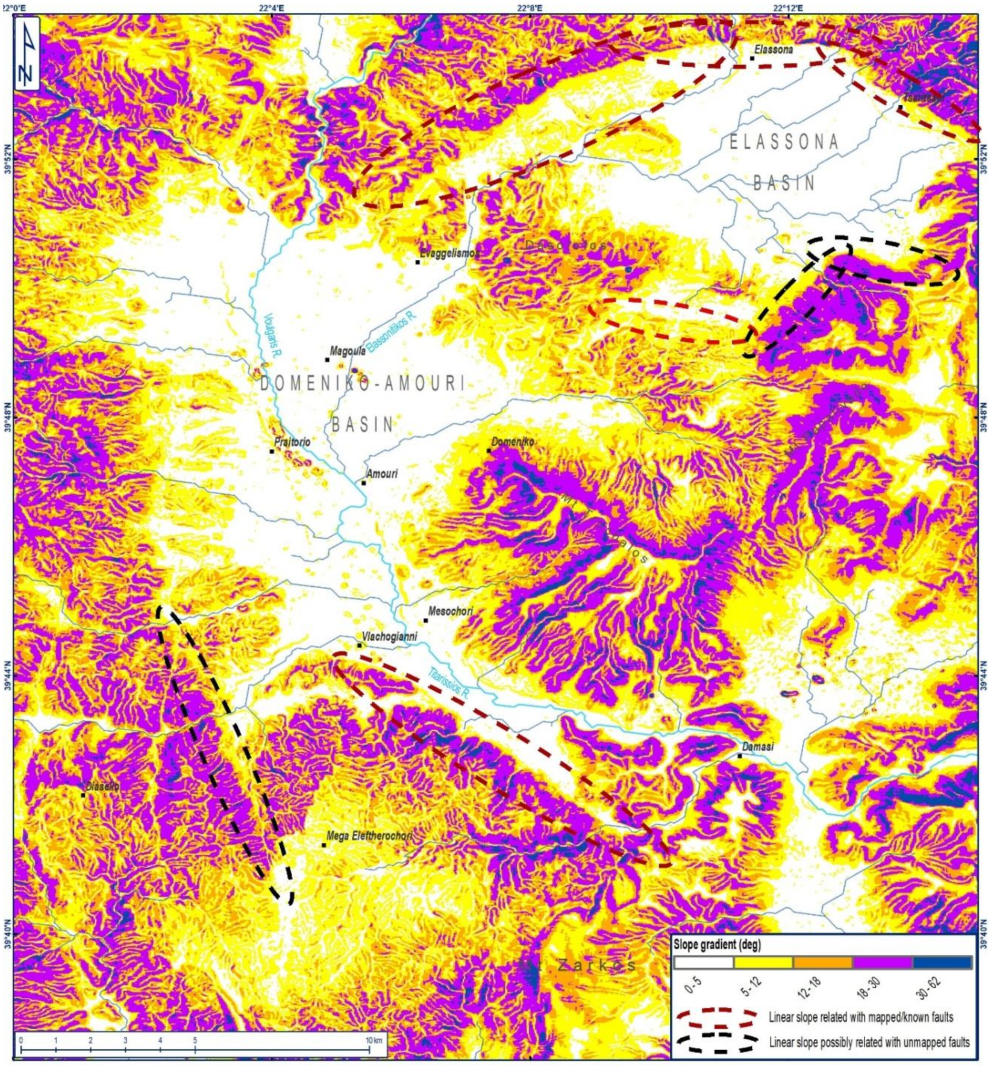

Fig. 2: Slope gradient map of the broader 2021 epicentral area based on the AW3D30 (ALOS World 3D – 30 m; Tadono *et al.*, 2014) elevation grid. The dashed ellipses mark linear slopes of mapped (or known) faults (dark red) or linear slopes implying the occurrence of normal faults (black).

3. GEODYNAMIC AND SEISMOTECTONIC SETTING

The geodynamic regime of the broader study area was under an extensional stress field of NE-SW orientation during Pliocene – Early Pleistocene and created the major faults that formed the tectonic basins of Thessaly in a NW-SE direction. During the Quaternary, the extensional stress field changed direction into N-S which is supposed to be the active one today and which formed the ca. E-W-striking normal faults (*e.g.*, Caputo and Pavlides, 1993). Based on the tectonostratigraphic interpretation of the Domeniko-Amourio sub-basin in the technical report of the lignite-deposits investigation (Dimitriou and Giakoupis, 1998), besides the topmost Holocene deposits, the rest formations that fill the sub-basin are often observed vertically displaced from borehole to borehole, implying the occurrence of normal dip-slip faulting (Fig. 3b, d). All implied faults are not of the same age since they either displace the deeper Upper Miocene formations, or they displace the base of Quaternary (Villafranchian). The younger faults, characterized as 'post-Neogene' faults, demonstrate a NW-SE direction forming bookshelf or graben-style patterns (Fig. 3b, d). Along the SW margin of Domeniko-Amourio sub-basin, a fault of similar direction, dipping to the NE, created a downthrow of several tens of metres (fault f11; Fig. 3). This fault lies in the extension of the coseismic ground ruptures and the liquefaction phenomena which were mapped south of the Titarissios river.

Historic and early instrumental records of earthquakes (*e.g.*, Papazachos and Papazachou, 2003) reveal the occurrence of few strong ($M \geq 6.0$) events in north-eastern Thessaly (Fig. 4b). Although the location and magnitude estimations are of low accuracy for old events, the proposed epicentres are mostly located in the east Thessalian Basin. In the 20th c. only one notable event of $M \geq 6.0$ occurred in this area, the magnitude of which is explicitly discussed by Caputo and Helly (2005). The recent seismic activity of the last 10 years, prior to the March 3, 2021 earthquake, reveals a cluster in the narrow epicentral area of maximum M_L=3.6 (Fig. 4c). During this period, in 2013 the cluster completely lacks any event, while in 2011, 2014 and 2017 just a few events ($M < 5$) were recorded. The surrounding area is quite poor in events, especially the biggest part of the East Thessalian Basin.

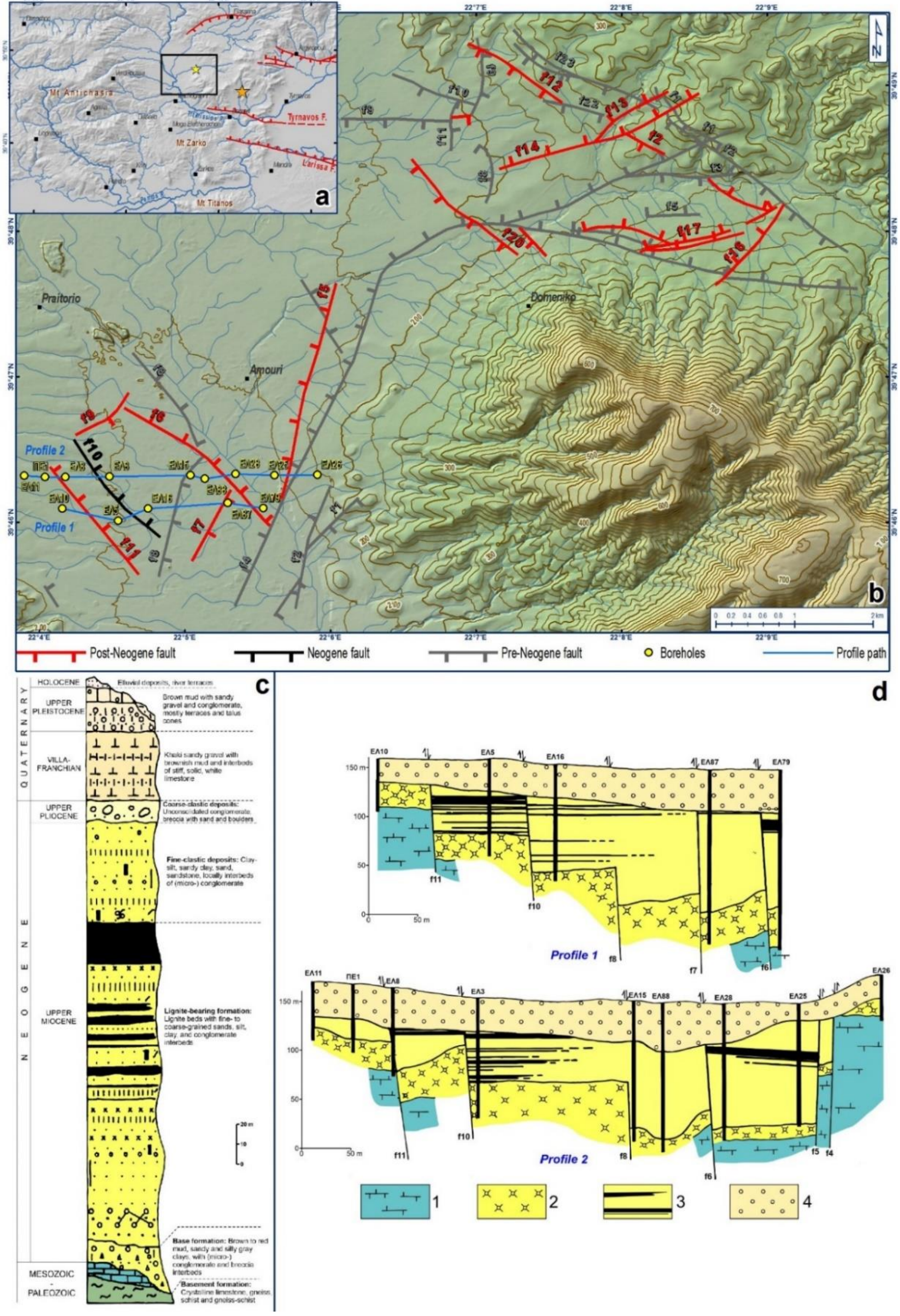

Fig. 3: a) Hillshade map of the broader 2021 epicentral area showing the epicentres of the strongest shocks (orange star = March 3, Mw=6.3, yellow star = March 4, Mw=6.0), and the neotectonic faults according to literature (for references see main text). b) Shaded relief map exported from the 5 m-DEM of Hellenic Cadastre where the fault locations suggested by IGME's study are shown (after Dimitriou and Giakoupis, 1998). The location of selected boreholes and the profile paths of inset (d) are also shown. c) Synthetic stratigraphic column of the Neogene formations of the Elassona Basin, according to the above study (after Dimitriou and Giakoupis, 1998, modified). d) Interpreted profiles based on borehole data according to Dimitriou and Giakoupis

(1998). Lithology is simplified: 1 = alpidic basement, 2 = base formation (Upper Miocene), 3 = lignite-bearing formation with the fine- and coarse-clastic deposits (Upper Miocene - Villafranchian), 4 = Quaternary deposits (Upper Pleistocene – Holocene).

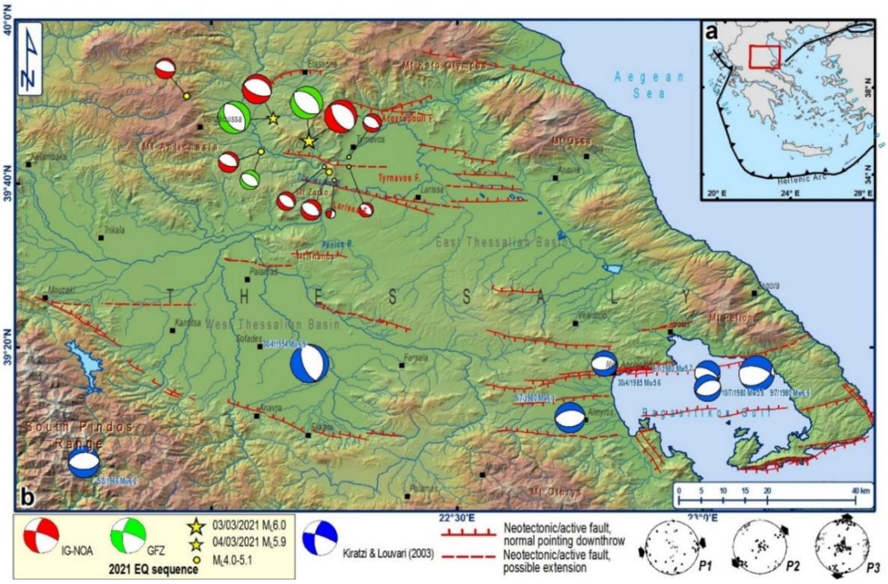

Fig. 4: (a) Map of the Aegean region showing the major crustal-scale tectonic structures (AACZ = Apulian-Aegean Collision Zone; CTFZ = Cephalonia Transform Fault Zone; NAT = North Aegean Trough) and the location of map (b). (b) Shaded relief map of Thessaly showing the major neotectonic/active faults (after Galanakis, 1997; Caputo and Pavlides, 1991; 1993; Perissoratis *et al.*, 1991; Sboras, 2011; Caputo *et al.*, 2012; GreDaSS), focal mechanisms of past significant events (Kiratzi and Louvari, 2003) and the focal mechanisms calculated by IG-NOA and GFZ for the strongest shocks of the 2021 earthquake sequence near Tyrnavos. P1, P2 and P3 (bottom right corner) are the three last tectonic phases after a meso-structural analysis in Thessaly (Caputo and Pavlides, 1993) revealing ca. E-W compression during early to middle Miocene (*P1*), NE-SW extension during Pliocene – Early Pleistocene (*P2*), and ca. N-S extension from middle Pleistocene to Today (*P3*).

4. THE MARCH 2021 SEISMIC SEQUENCE

The March 2021 sequence changed our view of what was so far known about the direction of both active faults and the extensional axis. The published moment tensor solutions revealed NW-SE-striking, almost pure normal dip-slip faulting, and consequently a NE-SW oriented extensional axis (Fig. 4b). The sequence evolved in the uppermost 25 km of the crust and was constrained west of the Tyrnavos Basin (East Thessalian Basin). The mainshock (M_W6.3) is located in the mountainous area north of Titarissios River. The second strongest shock (M_W6.0) occurred ca. 8.5 km WNW of the mainshock. The spatiotemporal evolution of the sequence (Fig. 5) shows that the strongest aftershock occurred near the north-western edge of the epicentral distribution until that time. After the M_W6.0 event, the sequence started to develop further to the WNW (Fig. 5b, c). In Fig. 5c (8 days period after the M_W6.0 event), the WNW part of the sequence was denser than the ESE one and seems to have a slight change of trend direction (towards NW-SE). Seeing all events from day 1 (March 3) until March 31 (Fig. 5d), the sequence is developed along a distance of ca. 42 km with a WNW-ESE trend. The distance between the M_W6.0 event and the WNW edge of the sequence is more than 20 km. From the preliminary seismological data, it seems that two (adjacent) fault segments were activated during the March 2021 sequence.

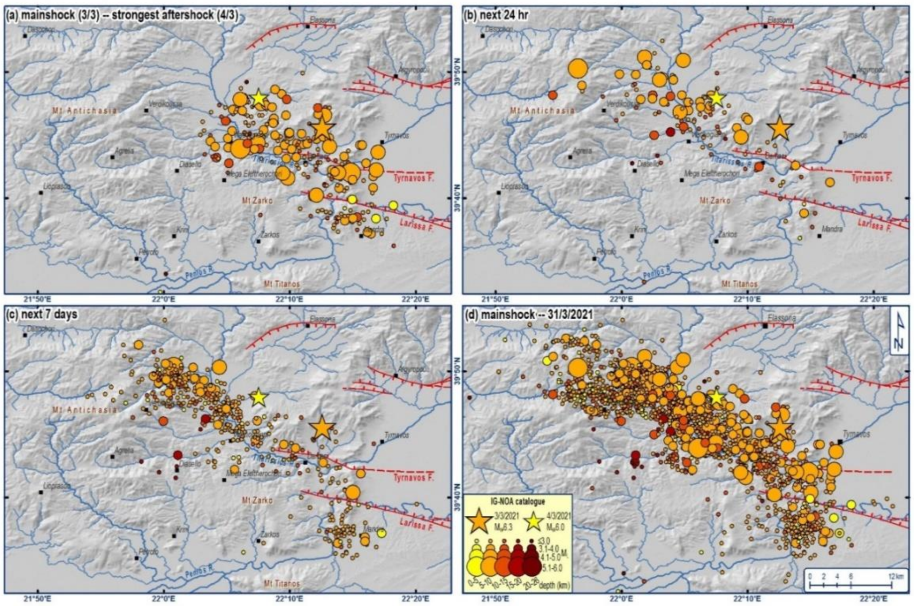

Fig. 5: Spatiotemporal evolution of the March 2021 seismic sequence in northern Thessaly: a) from the mainshock to the strongest aftershock (March 4), b) 24 hr after the strongest aftershock (March 4), c) 7 days after (c), and d) all events from the mainshock to the end of March. Epicentres obtained from the IG-NOA catalogue (http://www.gein.noa.gr/en/seismicity/earthquake-catalogs) .

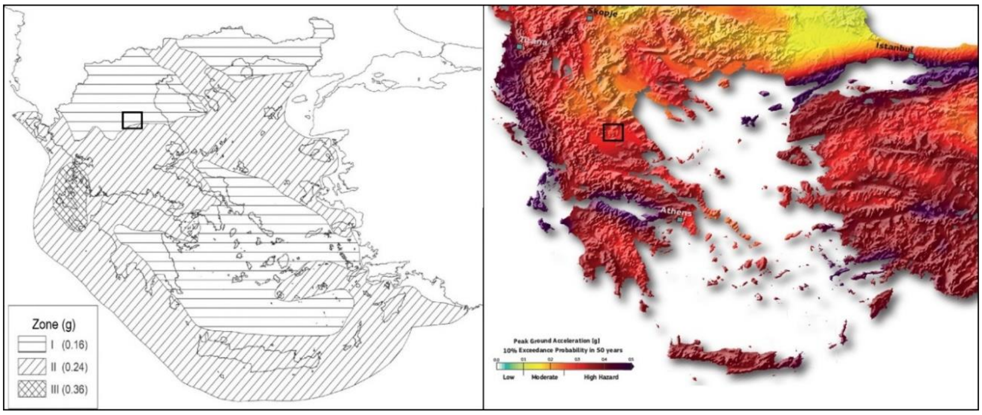

Fig. 6: *(Left)* The EPPO (2000) seismic hazard map of Greece. *(Right)* The SHARE seismic hazard map (Giardini *et al.*, 2014; Woessner *et al.*, 2015). The study area is marked by a black rectangular.

5. THE MARCH 2021 COSEISMIC (GROUND) EFFECTS

The intense earthquake activity of the March 2021 sequence caused one death, three light injuries, and heavy damages with more than 1700 buildings (houses, schools, churches, etc.) beyond repair. According to the Greek Antiseismic Regulation (EPPO, 2000) and the modified seismic hazard map (Fig. 6; Greek Government Gazette 1154B/12.8.2003), the broader Tyrnavos-Elassona region belongs to Seismic Risk Zone II (planning ground acceleration 0.24 g). The hazard map of the SHARE European project (Fig. 6; Giardini *et al.*, 2014; Woessner *et al.*, 2015) suggests 0.23 g < PGA < 0.29 g for the broader epicentral area. According to the preliminary report by the Institute of Engineering Seismology and Earthquake Engineering (ITSAK-DUTh, 2021; Fig. 7), the PGA recorded value in Larissa City is approx. 140 cm/s^2.

The seismic crisis was accompanied with several co-seismic ground deformational effects, such as secondary ground ruptures, rockfalls and liquefaction (Fig. 8; Fig. 9).

5.1. Landslides and Rockfalls

Along the Tyrnavos-Elassona highway, a 9 km-long part of the road is opened in the Mesozoic marble along the eastern mountain-front where rockfalls occurred (Fig. 9e). The artificial slope (sometimes along both sides of the road) is steep and locally significantly high, and the marble which it is made of is severely fractured, forming suitable conditions for the detachment of multi-sized rock-blocks (slide/wedging/capsizing).

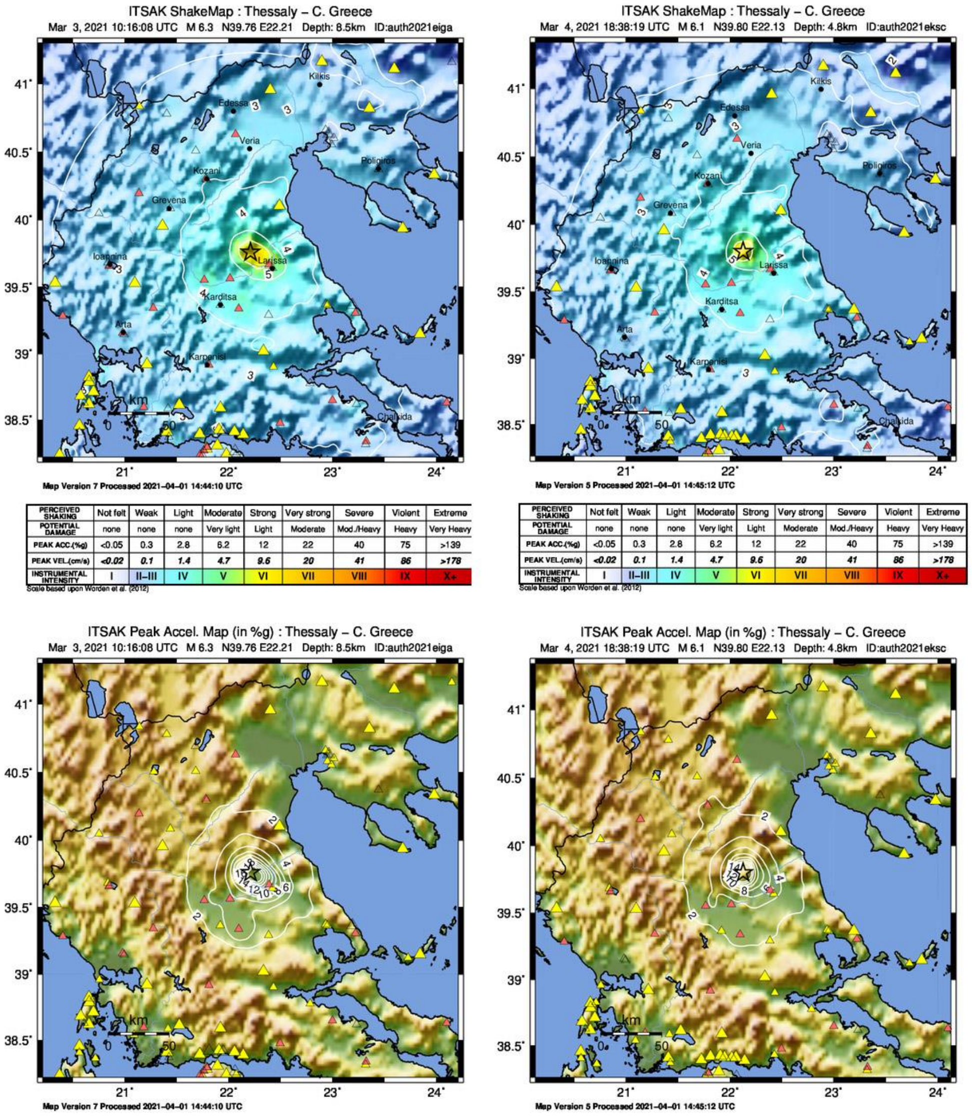

Fig. 7: Shakemaps (*Top*) and PGA maps (*Bottom*) of the March 3 (*Left*) and March 4 (*Right*) strong shocks, by the Institute of Engineering Seismology and Earthquake Engineering (ITSAK).

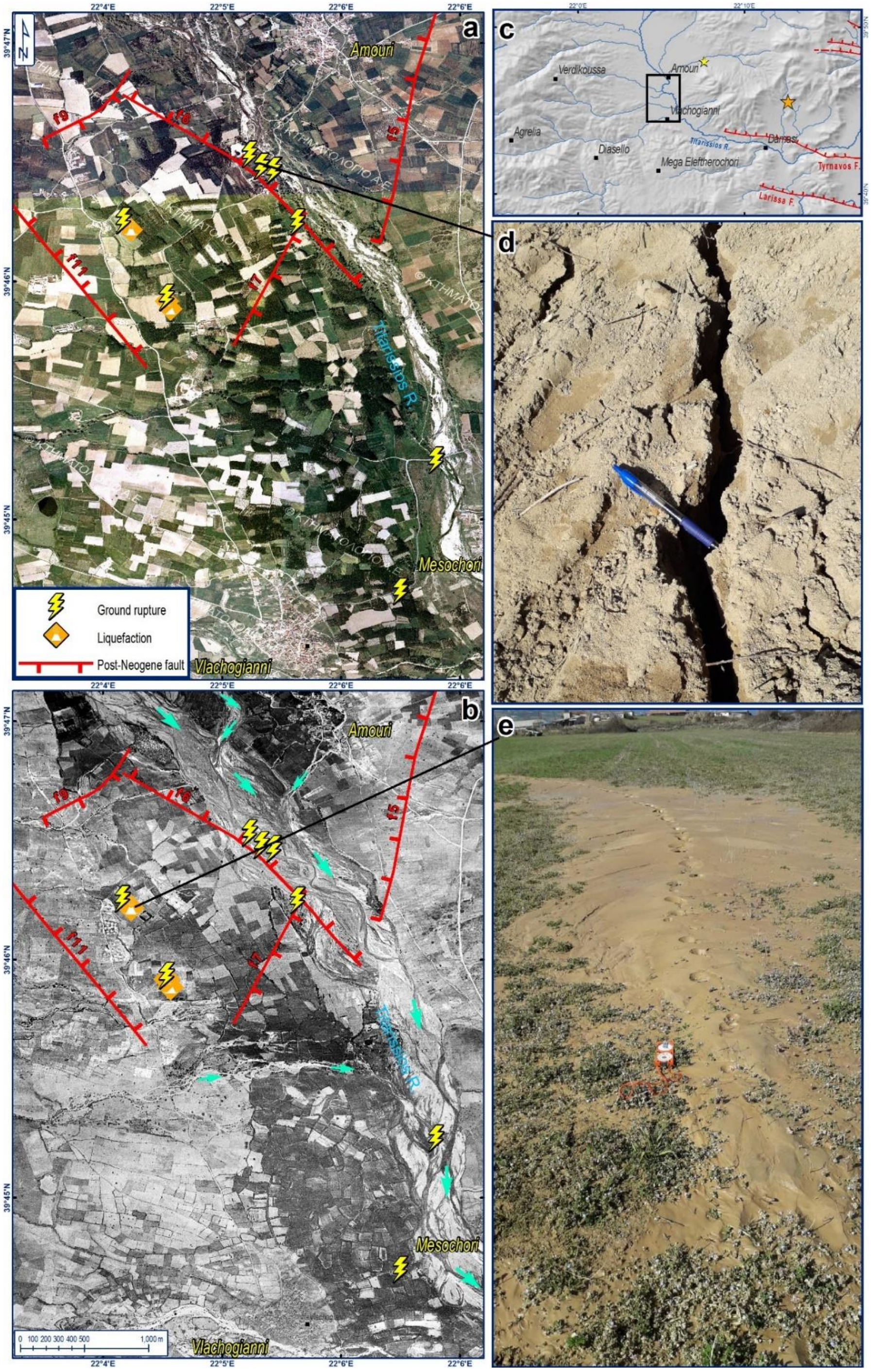

Fig. 8: Photomosaic (a, b) of the epicentral area where ground deformation phenomena were observed. The 'post-Neogene' faults of IGME's study (Dimitriou and Giakoupis, 1998) are also shown. In (b), the flow direction of the Elassonitis-Titarissios river and its tributaries is marked with light-blue arrows. Both photomosaics are obtained from the Hellenic Cadastre, dated in 2016 (a) and 1945-1946 (b); their location is shown on the hillshade map (c). Co-seismic ground ruptures (d, e), also associated with liquefaction (e). The general trend of the ruptures is NW-SE.

On the local road towards the Panagia Olympiotissa Monastery (Elassona), at the inner slope below the monastery, rockfalls of various sizes were recorded (Fig. 9g, h). The hill consists of semi-cohesive materials of a river terrace. The coarse-grained material includes rounded boulders of various sizes, rounded and angular gravel, whilst the fine-grained material is mostly sand; the matrix is of calcareous composition. Due to the progressive erosion of the fine-grained material, loose and unstable boulders are formed along the slope front, susceptible to falling after heavy rain or seismic ground shaking.

Next to the Agioi Anargyri church, in Domeniko village, the seismic ground shaking caused the detachment of a gneiss-schist boulder (ca. 5 m^3 volume), shifted only for 20-40 cm (Fig. 9d). The detachment was probably facilitated by the occurrence of a pre-existing fissure, along the length of which a root system of an adjacent tree was developed.

5.2. Ground Ruptures

In the broader area among the villages Mesochori, Vlachogianni, Varko, Praitorio and Amourio, the rivers Elassonitikos and Titarissios converge making the total thickness of the alluvial deposits and Pleistocene sediments exceed 70 m in thickness, which along with the high hydrological conditions, facilitate liquefaction phenomena and ground ruptures. It is noteworthy that the ground ruptures formed near and parallel to the Neogene and ‘post-Neogene’ faults discovered by Dimitriou and Giakoupis (1998), implying that the ruptures also prefer to follow older tectonic discontinuities as well. Several ground ruptures were observed, many times with liquefaction phenomena, along two main linear layouts: the eastern one, near the Titarissios River, has a total extent of *ca.* 3.5 km and the western one is at least 2.5 km long totally. These deformational effects were traced in farmed fields or they were crossing the road network, forming a NW-SE-striking zone, parallel to the Titarissios River and the nodal planes proposed by the focal mechanisms (Fig. 4). The ground ruptures outcrop as S-shaped extensional fissures, with a heave ranging from few millimetres up to 10 cm (locally even wider).

It is noteworthy that the ground ruptures did not stop on constructions. In two cases along the local irrigation channel network, which is made of reinforced concrete, the ruptures crossed the channels regardless of their direction (Fig. 10). In Fig. 10c, where the channel’s direction is sub-parallel to the ruptures, the fissures on the reinforced concrete only slightly diverted their direction, although the easiest way was to break the construction quasi-perpendicularly. The aligned pattern parallel to the blind faults of

Dimitriou and Giakoupis (1998), the extensional character, the soil conditions and the perseverance of the ground ruptures on any surface (either soil or construction; Fig. 8) imply that these are primary ruptures. Some scattered ruptures observed very near to the Titarissios river bank are most probably secondary ruptures due to ground shaking.

Taking into account the frequency and the size with which the ground effects appear, it is suggested that the earthquake belongs to degree VIII on the ESI-2007 scale (Michetti et al., 2007; Silva *et al.*, 2015).

6. SUMMARY AND DISCUSSION

The 2021 earthquake sequence in Tyrnavos-Elassona area revealed tectonic structures that were not concerned as active ones. Both focal mechanisms and the trend of the aftershock spatial distribution strongly suggest NW-SE-striking faulting. The focal mechanisms also revealed almost pure normal dip-slip kinematics and a NE-SW oriented extensional stress axis against the quasi-N-S one that was supposed to characterize the broader area of Thessaly. These geometry and kinematics are in agreement with the Quaternary faults that were discovered by a borehole network that was drilled during research on the lignite deposits in the Domeniko-Amourio sub-basin by Dimitriou and Giakoupis (1998). The NW-SE-striking fault mapped by IGME (1998) (Fig. 1) is considered as a south-eastern continuation of this fault system. Moreover, the spatiotemporal evolution of the sequence implies the rupture of two adjacent segments which produced the two strongest shocks, respectively.

The sequence was followed by several coseismic ground deformational phenomena, such as landslides/rockfalls, liquefaction and primary ruptures. The landslide and rockfalls were mostly associated with the ground shaking. The ruptures were observed west of the Titarissios River, near the Quaternary faults found by Dimitriou and Giakoupis (1998). Some of the ruptures were combined with extensive liquefaction phenomena. Others crossed reinforced concrete irrigation channels without changing their direction.

An emerging question is whether these ruptures represent (one of) the seismic faults that produced the strongest shocks. Although their direction fits the proposed nodal planes of the moment tensor solutions and the borehole findings, the hypocentral depths with the moderate-to-shallow dip angle, the InSAR images (Lekkas *et al.*, 2021) suggest that the rupture of the main seismic fault(s) emerged further to the south in the alpidic bedrock, which is also supported by the observations of Chatzipetros *et al.* (2021, this volume). It is noteworthy to mention that Ferrière et al. (2004; 2011) has proposed the occurrence of a bounding detachment fault along the western margin of the Meso-Hellenic Trench, part of which is the broader study area, possibly facilitating the slip during a younger reactivation as an inherited structure. Possibly imitating the seismotectonic setting of the Corinth Gulf, where a deep low-angle detachment(?) fault branches into several parallel steeper faults towards the surface with simultaneous activity (Rigo *et al.*, 1996; Hatzfeld *et al.*, 2000), the recent sequence in Tyrnavos-Elassona area probably used two slip paths along two branches: the biggest amount of slip followed a southern branch, *i.e.* the prolongation of a deeper low-angle fault towards the surface, and a small amount possibly took a different path, through steeper faults, such as the ones discovered by Dimitriou and Giakoupis (1998), creating the systematic NW-SE-striking ground fissures of a ‘secondary surface rupture’ (term after DePolo *et al.*, 1991) and producing the extensive damages in the nearby constructions.

Fig. 9 (next page: Ground deformation phenomena observed in the epicentral area of the 2021 earthquake sequence. (a) Satellite image showing the ground deformation phenomena locations, the faults detected by Dimitriou and Giakoupis (1998; see also Fig. 3), and the neotectonic faults found in the literature (see Fig. 4 for references). (b, c) Ground ruptures with liquefaction. (d) Gneiss-schist boulder detachment in Domeniko village. (e) Rockfalls along the Tyrnavos-Elassona highway. (f) Ground rupture cutting through the asphalt road. (g, h) Rockfalls near the Panagia Olympiotissa Monastery (Elassona). Locations of all photographs are shown in (a).

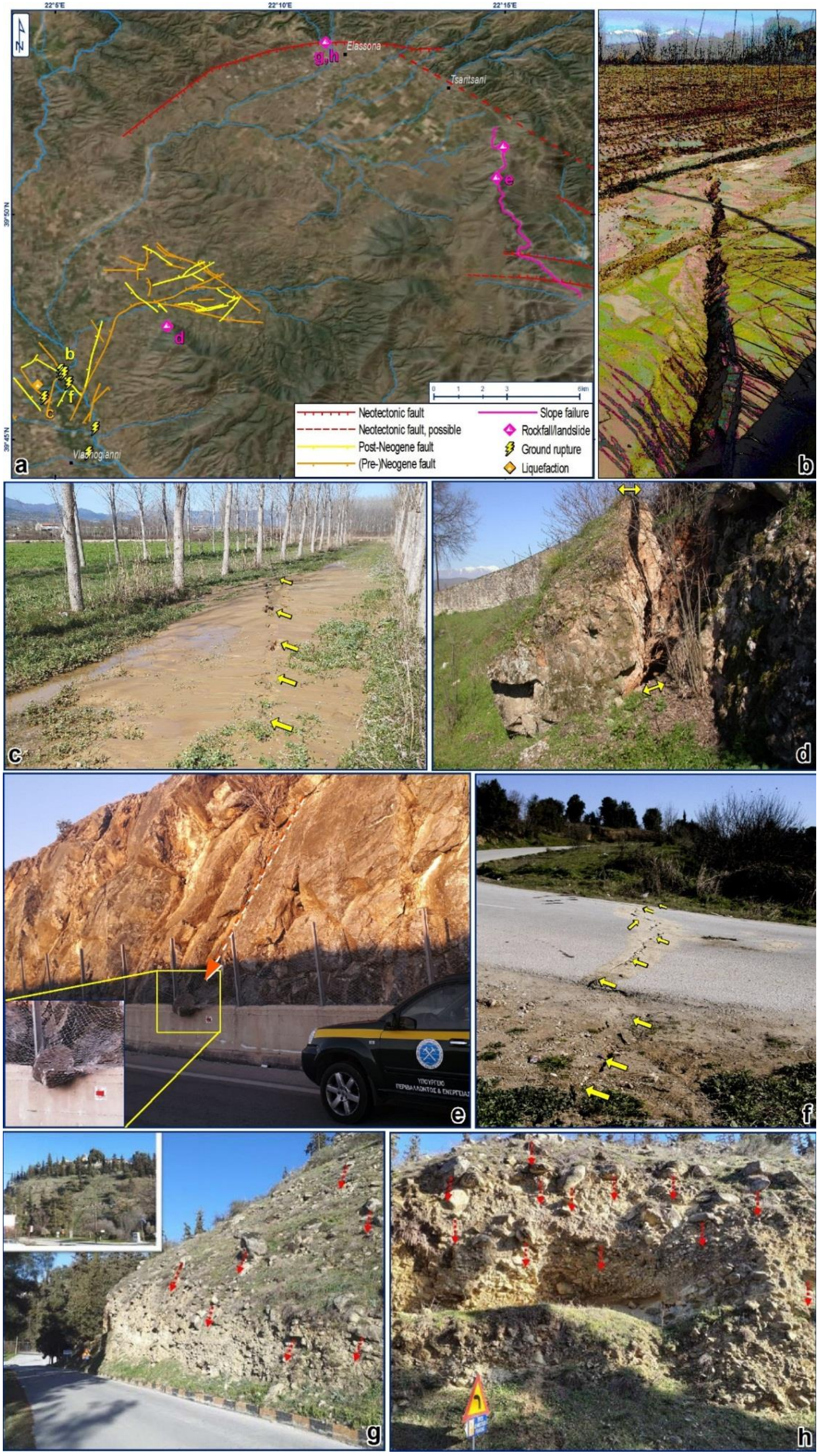
22°5'E
22°10'E
22°15'E
39°50'N
39°45'N
N
Elassona
Tsaritsani
Vlachogianni
g,h
e
d
b
c
f
0 1 2 3 6km
Neotectonic fault
Neotectonic fault, possible
Post-Neogene fault
(Pre-)Neogene fault
Slope failure
Rockfall/landslide
Ground rupture
Liquefaction
a
b
c
d
e
f
g
h

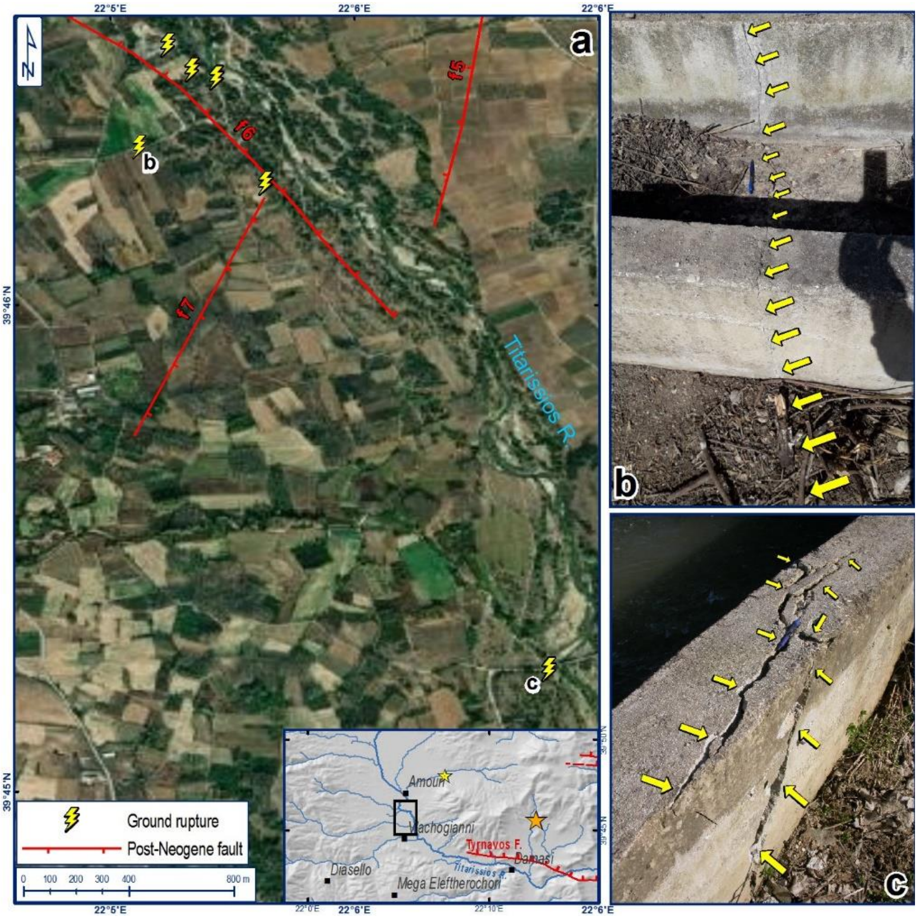

Fig. 10: Ruptures crossing irrigation channels. The construction of the channels is of reinforced concrete. The direction of the channels is (b) ENE-WSW (quasi-perpendicular to faulting), and (c) NNW-SSE (sub-parallel to faulting).

7. ACKNOWLEDGEMENTS

D.G. and S.S. would like to thank Prof. Emer. Sp. Pavlides for his insightful discussions. All authors also acknowledge the two reviewers who significantly improved the paper with their comments and suggestions.

8. REFERENCES

Caputo, R., 1993. Morphotectonics and kinematics along the Tirnavos Fault, northern Larissa Plain, mainland Greece. *Zeitsschrift für Geomorphol.*, 94, 167–185.

Caputo, R., Helly, B., 2005. Archaeological evidences of past earthquakes: a contribution to the SHA of Thessaly, Central Greece. *Journal of earthquake engineering*, 9(2), 199-222. doi: 10.1080/13632460509350539

Caputo, R., Pavlides, S. 1991. Neotectonics and structural evolution of Thessaly (Central Greece). *Bull. Geol. Soc. Greece*, 25, 119–133.

Caputo, R., Pavlides, S., 1993. Late Cainozoic geodynamic evolution of Thessaly and surroundings (central-northern Greece). *Tectonophysics*, 223, 339–362. doi: 10.1016/0040-1951(93)90144-9

Caputo, R., Chatzipetros, A., Pavlides, S., Sboras, S., 2012. The Greek database of seismogenic sources (GreDaSS): State-of-the-art for northern Greece. *Ann. Geophys*., 55, 859–894. doi: 10.4401/ag-5168

Chatzipetros, A., Pavlides, S., Foumelis, M., Sboras, S., Galanakis, D., Pikridas, C., Bitharis, S., Kremastas, E., Chatziioannou, A., Papaioannou, I., 2021. The northern Thessaly strong earthquakes of March 3 and 4 and their neotectonic setting. *Bull. Geol.Soc., Greece*, this volume.

DePolo, C.M., Clark, D.G., Slemmons, D.B. and Ramelli, A.R., 1991. Historical surface faulting in the Basin and Range province, western North America: implications for fault segmentation. *Journal of Structural Geology*, 13(2), 123-136. doi: 10.1016/0191-8141(91)90061-M

Dimitriou, D., Giakoupis, P., 1998. Mine research of coal deposit in Elassona: Domeniko sub-area. Technical report, Institute of Geological and Mineral Exploration (IGME), Athens [in Greek]

Earthquake Planning and Protection Organization – EPPO, 2000. Greek Antiseismic Regulation. EPPO, Athens.

Ferrière, J., Reynaud, J. Y., Pavlopoulos, A., Bonneau, M., Migiros, G., Chanier, F., Proust, J.N., Gardin, S., 2004. Geologic evolution and geodynamic controls of the Tertiary intramontane piggyback Meso-Hellenic basin, Greece. *Bulletin de la Société géologique de France*, 175(4), 361-381. doi: 10.2113/175.4.361

Ferriere, J., Chanier, F., Reynaud, J. Y., Pavlopoulos, A., Ditbanjong, P., Migiros, G., Coutand, I., Stais, A., Bailleul, J., 2011. Tectonic control of the Meteora conglomeratic formations (Mesohellenic basin, Greece). *Bulletin de la Société Géologique de France*, 182(5), 437-450. doi: 10.2113/gssgfbull.182.5.437

Galanakis, D., 1997. *Neotectonic structure and stratigraphy Neogene and Quaternary sediments of Almyros-Pagasitikos basin, Pilio, Oreoi-Trikeri strait and Maliakos Gulf*. PhD Thesis, Aristot. Univer. Thessaloniki, Unpub., 260 p.

Galanakis, D., Pavlides, S., Mountrakis, D., 1998. Recent Brittle Tectonic in Almyros -Pagasitikos, Maliakos, N. Euboia and Pilio. *Bull. Geol. Society of Greece*, 32(1), 263-273.

Giardini, D., Wössner, J., Danciu, L., 2014. Mapping Europe's seismic hazard. *Eos, Transactions American Geophysical Union*, 95(29), 261-262. doi: 10.1002/2014EO290001

Hatzfeld, D., Karakostas, V., Ziazia, M., Kassaras, I., Papadimitriou, E., Makropoulos, K., Voulgaris, N., Papaioannou, C., 2000. Microseismicity and faulting geometry in the Gulf of Corinth (Greece). *Geophysical Journal International*, 141(2), 438-456. doi: 10.1046/j.1365-246x.2000.00092.x

IGME – Institute of Geology and Mineral Exploration, 1987. Geological Map of Greece, “Elasson” sheet, 1:50.000 scale, IGME, Athens

IGME – Institute of Geology and Mineral Exploration, 1998. Geological Map of Greece, “Farkadon” sheet, 1:50.000 scale, IGME, Athens

ITSAK–DUTh, 2021. Thessaly Earthquakes M6.3, 03/03/2021 and M6.1, 04/03/2021. Preliminary Report. Research Unit ITSAK, EPPO and Department of Civil Engineering, DUTh. Thessaloniki. pp. 63. doi: 10.5281/zenodo.4641200

Kiratzi, A., Louvari, E., 2003. Focal mechanisms of shallow earthquakes in the Aegean Sea and the surrounding lands determined by waveform modelling: A new database. *J. Geodyn*., 36, 251–274. doi: 10.1016/S0264-3707(03)00050-4

Lekkas, E., Agorastos, K., Mavroulis, S., Kranis, C., Skourtsos, E., Carydis, P., Gogou, M., Katsetsiadou, K.-N., Papadopoulos, G., Triantafyllou, I., Agalos, A., Moraitis, S., Stamati, E., Psarris, D., Kaviris, G., Kapetanidis, V., Papadimitriou, P., Karakonstantis, A., Spingos, I., Kouskouna, V., Kassaras, I., Pavlou, K., Voulgaris, N., Mavrouli, M., Pavlides, S., Chatzipetros, A., Sboras, S., Kremastas, E., Chatziioannou, A., Kiratzi, A., Papazachos, C., Chatzis, N., Karakostas, V., Papadimitriou, E., Koukouvelas, I., Nikolakopoulos, K., Kyriou, A., Apostolopoulos, D., Zygouri, V., Verroios, S., Belesis, A., Tsentzos, I., Krassakis, P., Lymperopoulos, K., Karavias, A., Bafi, D., Gatsios, T., Karatzia, M., Gkougkoustamos, I., Falaras, T., Parcharidis, I., Papathanassiou, G., Evangelidis, C.P., Karastathis, V., Tselentis, G-A., Ganas, A., Tsironi, V., Karasante, I., Valkaniotis, S., Galanakis, D., Kostantopoulou, G., Papadopoulos, N., Kourou, A., Manousaki, M., Thoma, T., 2021. The early March 2021 Thessaly earthquake sequence*.* *Newsletter of Environmental, Disaster and Crises Management Strategies*, 22, ISSN 2653-9454.

Michetti, A.M., Esposito, E., Guerrieri, L., Porfido, S., Serva, L., Tatevossian, R., Vittori, E., Audemard, F., Azuma, T., Clague, J., Comerci, V., 2007. Intensity scale ESI 2007 (La scala di Intensità ESI 2007). In: Guerrieri, L., Vittori, E. (Eds), *Memorie Descrittive della Carta Geologica d'Italia, 74, Servizio Geologico d'Italia, Dipartimento Difesa del Suolo, APAT, Rome*, pp. 41

Papazachos, B., Papazachou, K., 2003. Earthquakes of Greece. Ziti editions, Thessaloniki.

Perissoratis, C., Angelopoulos, I., Mitropoulos, D., 1991. Surficial Sediment Map of the Aegean Sea Floor, 1:200 000 scale, "Pagasitikos" Sheet, IGME, Athens.

Rigo, A., Lyon-Caen, H., Armijo, R., Deschamps, A., Hatzfeld, D., Makropoulos, K., Papadimitriou, P., Kassaras, I., 1996. A microseismic study in the western part of the Gulf of Corinth (Greece): implications for large-scale normal faulting mechanisms. *Geophys. J. Int*., 126(3), 663-688. doi: 10.1111/j.1365-246X.1996.tb04697.x

Sboras, S., 2011. *The Greek Database of Seismogenic Sources: seismotectonic implications for North Greece*. Pubblicazioni dello IUSS, 5(1), PhD thesis, Università degli Studi di Ferrara, pp. 252.

Silva, P. G., Guerrieri, L., Michetti, A. M., 2015. Intensity scale ESI 2007 for assessing earthquake intensities. In: Beer, M. et al. (Eds), *Encyclopedia of Earthquake Engineering*, Springer-Verlag, 1219-1237.

Tadono, T., Ishida, H., Oda, F., Naito, S., Minakawa, K., Iwamoto, H., 2014. Precise global DEM generation by ALOS PRISM. ISPRS Annals of the Photogrammetry, *Remote Sensing and Spatial Information Sciences*, 2(4), 71. doi:10.5194/isprsannals-II-4-71-2014

Woessner, J., Laurentiu, D., Giardini, D., Crowley, H., Cotton, F., Grünthal, G., Valensise, G., Arvidsson, R., Basili, R., Demircioglu, M.B., Stucchi, M., 2015. The 2013 European seismic hazard model: key components and results. *Bulletin of Earthquake Engineering*, 13(12), 3553-3596. doi: 10.1007/s10518-015-9795-1

BGSG

Volume 58

Research Paper

Correspondence to:
Alexandros Chatzipetros
ac@geo.auth.gr

DOI number:
http://dx.doi.org/10.12681/bgsg.27225

Keywords:
Earthquake geology, Thessaly, interferometry, modelling, active faults

Citation:
Chatzipetros, A., Pavlides, S., Foumelis, M., Sboras, S., Galanakis, D., Pikridas, Ch., Bitharis, S., Kremastas, E., Chatziioannou, A. and Papaioannou, I. (2021), The Northern Thessaly Strong Earthquakes of March 3 and 4, 2021 and their Neotectonic Setting. Bulletin Geological Society of Greece, 58, 222-255.

Publication History:
Received: 07/06/2021
Accepted: 14/10/2021
Accepted article online: 26/10/2021

The Editor wishes to thank Assoc. Prof. Sotirios Kokkalas and Dr. Christoph Gruetzner for their work with the scientific reviewing of the manuscript and Ms Emmanouela Konstantakopoulou for editorial assistance.

THE NORTHERN THESSALY STRONG EARTHQUAKES OF MARCH 3 AND 4, 2021 AND THEIR NEOTECTONIC SETTING

Alexandros Chatzipetros [1], Spyros Pavlides [1], Michael Foumelis [1], Sotirios Sboras [2], Dimitrios Galanakis [2], Christos Pikridas [3], Stylianos Bitharis [3], Evangelos Kremastas [1], Athanassios Chatziioannou [1], Ioannis Papaioannou [4]

[1]**Department of Geology, School of Geology, Aristotle University of Thessaloniki, 54124, Thessaloniki, Greece** ac@geo.auth.gr pavlides@geo.auth.gr mfoumelis@geo.auth.gr ekremast@teemail.com ath.ch.8@gmail.com

[2]**H.S.G.M.E., Hellenic Survey of Geology and Mineral Exploration of Greece, Athens** sboras@noa.gr galanakis@igme.gr

[3]**Department of Geodesy and Surveying, School of Rural and Surveying Engineering, Aristotle University of Thessaloniki, 54124, Thessaloniki, Greece** cpik@topo.auth.gr stylbith@gmail.com

[4]**Civil Engineer- Earthquake Historian, Roidou 10, Larissa, Greece**

Abstract

A sequence of earthquakes occurred on March 3rd and 4th in Northern Thessaly, northern Greece, associated with previously unknown, blind normal faults within the crystalline Palaeozoic basement of the Pelagonian geotectonic zone. Surficial ground deformation, such as liquefaction phenomena in fluvial plains, as well as soil fissures and rock falls, have been mapped. Geological indications of the unmapped seismic fault, i.e., reactivated shear zones, open cracks, etc., have been identified within the bedrock. Based on geological indications, the main fault projection to the surface could be considered a 15 km NW-SE trending structure and average dip of 45° to the NE. The seismic source of the main shock was modelled, and the Coulomb static stress changes calculated for receiver faults similar to the source. The determination of the active tectonic regime of the region by geodetic data and the well-known faults of NE Thessaly plain are also presented, as well as the revised historical and instrumental seismicity. This earthquake raises new concerns and challenges, revising some established views, such as the status of main stress orientations, the orientation of active tectonic structures, the occurrence of a seismogenic fault in a mountainous massif of crystalline rocks without typical geomorphological expression and the role of blind faults in Seismic Hazard Assessment.

Keywords: *earthquake geology, Thessaly, interferometry, modelling, active faults*

Περίληψη

Μια σειρά σεισμών σημειώθηκε στις 3 και 4 Μαρτίου 2021 στη Βόρεια Θεσσαλία, (Βόρεια Ελλάδα), που σχετίζεται με προηγουμένως άγνωστα, τυφλά κανονικά ρήγματα στο κρυσταλλικό παλαιοζωικό υπόβαθρο της Πελαγονικής γεωτεκτονικής ζώνης. Έχουν χαρτογραφηθεί επιφανειακές παραμορφώσεις του εδάφους, όπως φαινόμενα ρευστοποίησης σε πεδιάδες του ποταμού, καθώς και ρωγμές εδάφους και καταπτώσεις βράχων. Εντοπίστηκαν γεωλογικές ενδείξεις για το μη χαρτογραφημένο σεισμικό ρήγμα, δηλαδή ζώνες διάτμησης που επανενεργοποιήθηκαν, ανοιχτές ρωγμές κ.λπ. Με βάση τις γεωλογικές ενδείξεις, η κύρια προβολή ρηγμάτων στην επιφάνεια θα μπορούσε να θεωρηθεί ως μια δομή 15 χλμ ΒΔ -ΝΑ διεύθυνσης και μέσης κλίσης 45^o στα ΒΑ. Η σεισμική πηγή του κύριου σεισμού μοντελοποιήθηκε και οι αλλαγές στατικής τάσης Coulomb υπολογίστηκαν για ρήγματα παρόμοια με την κύρια σεισμική πηγή. Παρουσιάζεται επίσης ο προσδιορισμός του ενεργού τεκτονικού πεδίου της περιοχής με γεωδαιτικά δεδομένα και τα γνωστά ρήγματα της ΒΑ Θεσσαλικής πεδιάδας, καθώς και η αναθεωρημένη ιστορική και ενόργανη σεισμικότητα. Αυτός ο σεισμός εγείρει νέους προβληματισμούς και προκλήσεις, αναθεωρώντας ορισμένες απόψεις, όπως η κατάσταση των κύριων προσανατολισμών τάσης, ο προσανατολισμός των ενεργών τεκτονικών δομών, η εμφάνιση σεισμογόνου ρήγματος σε ορεινό όγκο κρυσταλλικών πετρωμάτων χωρίς τυπική γεωμορφολογική έκφραση και ο ρόλος των τυφλών ρηγμάτων στην εκτίμηση σεισμικού κινδύνου.

Λέξεις - Κλειδιά: *γεωλογία των σεισμών, Θεσσαλία, συμβολομετρία, προσομοιώσεις ενεργά ρήγματα*

1. INTRODUCTION

The region of Thessaly lies at the central part of Greece and is characterized by an active tectonic regime, as well as by occasional destructive seismic events. The most recent geological structures of the area derive from two phases, i) the Pliocene – Lower Pleistocene phase with NW-SE-trending grabens and horsts, formed by the post-orogenic collapse which is associated with the NE–SW extensional (σ_3) pattern of the area, and ii) the Middle Pleistocene – Holocene phase with E-W- to ESE-WNW-striking normal faults, related to the N–S to NNE–SSW oriented extensional regime.

The strong earthquakes of March 3rd and 4th 2021 (Mw 6.3. and 6.0 respectively) and their aftershock sequence affected a large area of northern Thessaly. The seismogenic volume, that is the aftershock sequence, extends from the Antichasia mountain basement, up to Titarissios river valley (Fig. 1). Along the same valley, liquefaction phenomena as well as a NW-SE trending line of open fractures were observed and mapped. As suggested by all preliminary published focal mechanisms, an unknown-unmapped inherited tectonic structure represented by two low to moderate dipping fault planes was responsible for both strongest shocks respectively (Fig. 2). The Pelagonian basement which hosts this structure is a complex alpine edifice according to Kilias et al. (2013, 2016) having undergone many intense compressional phases with folding and thrusting, as well as an ultimate alpine extensional phase imprinted by low and moderate dipping normal faults.

We conducted a multidisciplinary study of the North Thessaly seismic sequence in order to define the seismic fault(s) and its (their) attributes, to track and interpret the complex primary and secondary ground deformation phenomena, to estimate the effect of the mainshock on nearby tectonic structures, and to explain the change of the active stress field orientation.

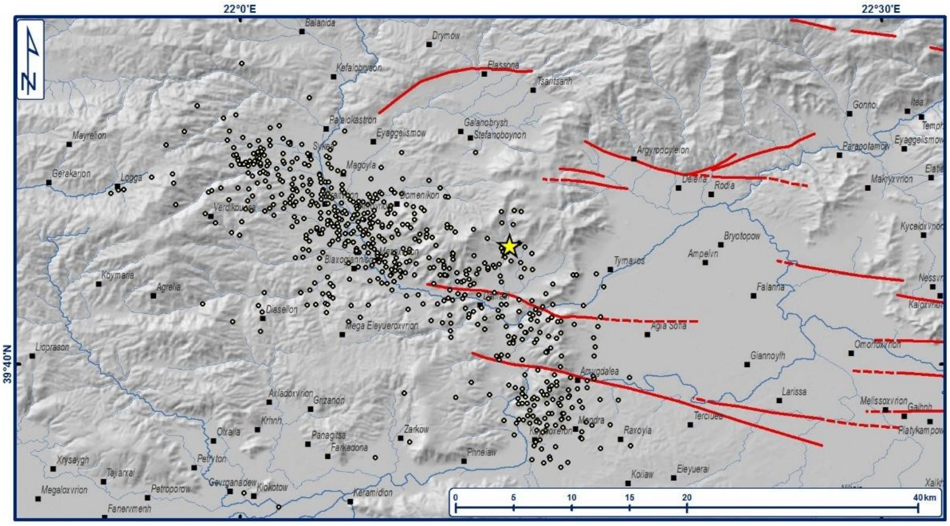

Fig. 1: The mainshock (yellow star) and the aftershock sequence (circles), aligned in a NW-SE direction. Red lines show the known active faults of the affected area (solid lines: mapped faults, dashed lines: inferred location).

Concerning the seismic history of the broader study area, during the 20th century, an earthquake of similar magnitude (M_S 6.3) occurred in Larissa on March 1, 1941, exactly 80 years ago, with severe damages and casualties for the city and the surrounding villages, mainly in the eastern Thessalian plain. This event is associated to the Asmaki fault, Fig (Caputo et al., 2004, Papaioannou, 2018).

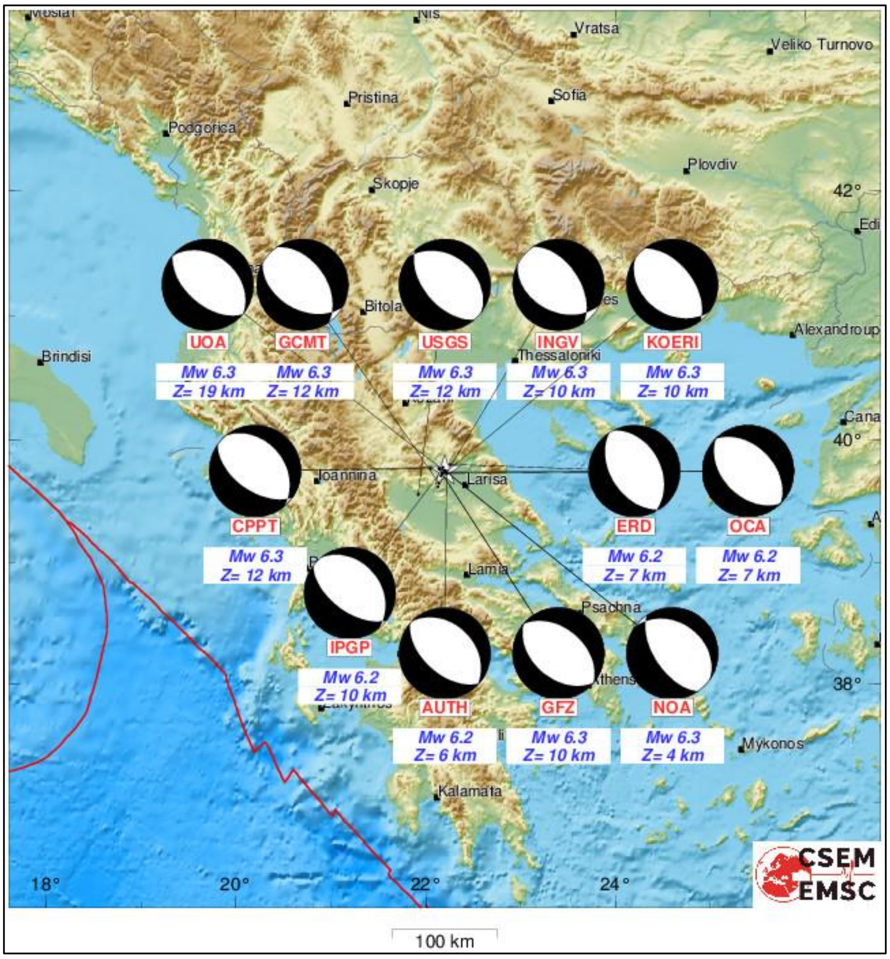

Fig. 2: Quick MT solutions, as published by various institutes (source: EMSC).

An earlier earthquake of M5.6 occurred in the northwestern area in November 1901. The epicentre of the strong historical earthquake in 1735 is possibly located in the same area and may be associated to this fault or other similar local structures. Other active geological structures of the region lie within the Larissa plain and include the Gyrtoni (GF), Rodia (RF), Elassona, Gonoi, Tempi and Omolio (OF) faults (Fig and GreDaSS http://gredass.unife.it), which are currently being studied using advanced methods (satellite imagery analysis, high resolution UAV models, geodetic, geological and paleoseimological ones; e.g. Tsodoulos et al., 2016; Kremastas et al., 2018; Lazos et al., 2021). It is worth mentioning at this point that the first author who referred to earthquakes as a possible cause of formation of Tempi valley, with the contribution of God Poseidon, was the historian Herodotus (485-425 BC).

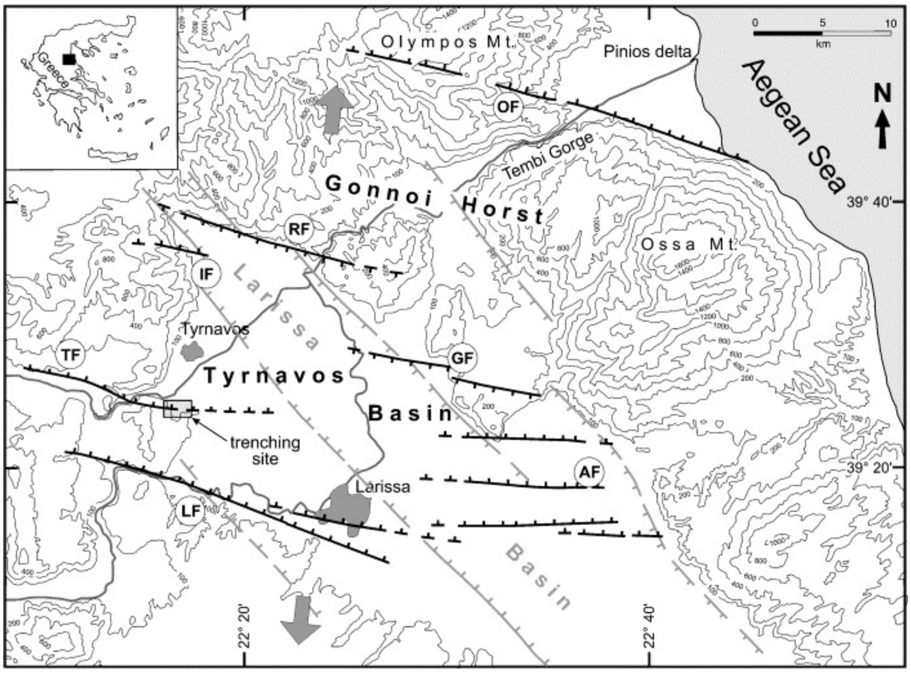

Fig. 3: Simplified tectonic map of the study area, after Caputo et al. (2004). TF: Tyrnavos fault, LF: Larissa fault, GF: Gyrtoni fault, RF: Rodia fault, AF: Asmaki fault, OF: Omolio fault.

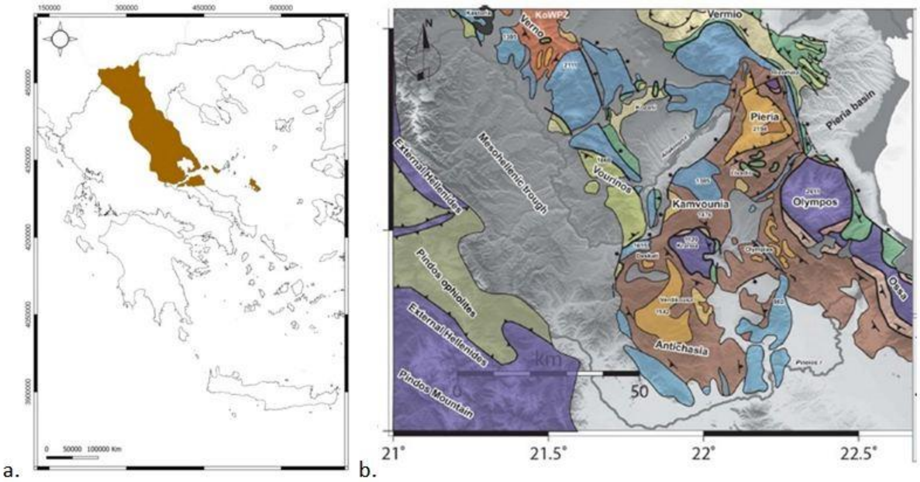

Fig. 4: a) The extend of the Pelagonian geotectonic zone in the Hellenic orogenic system. B) Geological map of part of the Pelagonian rocks in Thessaly and western Macedonia. The tectonic windows of Olympos, Krania and Rizomata are indicative of the post-orogenic collapse through low-angle normal detachment faults (Kilias and Mountrakis, 1989; Koroneos et al., 2013).

2. GEOLOGICAL SETTING

2.1. Alpine Geology-Tectonic Evolution

The study area belongs to Pelagonian geotectonic zone of Greece (Fig. 4a) and it is composed of crystalline metamorphosed Paleozoic and possibly pre-Paleozoic rocks (Fig. 4b). The accumulation of successive nappes in conjunction with the development of subducted zones, is associated with two HP/LT metamorphic stages. The extensional regime that followed the nappe tectonics led to the collapse of the orogen through large normal low angle detachment faults, and the exhumation of underlying units as tectonic windows (Lister et al., 1984; Kilias et al., 1991, 2002, 2016; Sfeikos et al., 1991; Dinter and Royden, 1993; Kilias, 1995; Forster and Lister, 1999). The extensional tectonics has played an important role from the Tertiary until today with extensive shear zones and detachment faults (Fig.). The reactivation of the inherited structures as inverse tectonics is a question under review in relation to the 2021 earthquake sequence.

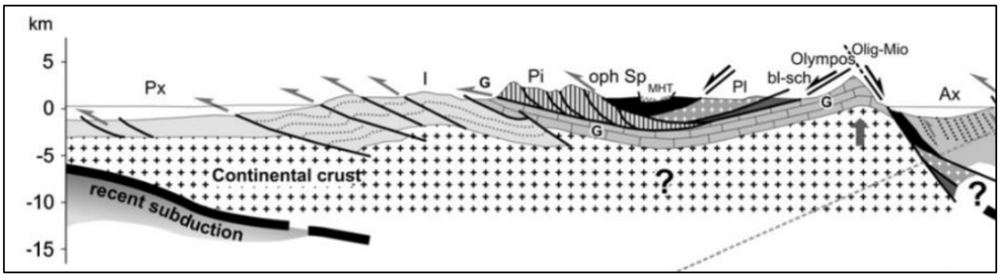

Fig. 5: Interpretation of the current geotectonic model of the broader area. SW-NE cross section, modified from Kilias et al. (2013a).

The study area has a more complex picture of tectonic deformation, as several tectonic events have affected its rocks according to Kilias et al. (1991, 2013), who give a complete picture of the deformation sequence. A dominant S1 schistosity is recognized in the wider area. It is oriented to the SW south of the tectonic window of Krania and to the NE to the north. Lineament L1 is recognized on the S1 planes, with a constant direction NE-SW to NNE-SSW. S1 and L1 are due to a deformation event (D1) associated with the overthrusting of the Pelagonian basement on the carbonate series from NE to the SW. In the last stages of D1 deformation, extensional SB shear zones are created, as well as low angle normal faults in the uppermost tectonic horizons, dipping to the SW and NE. This is followed by a second D2 compressive deformation event with very low P/T conditions, characterized by knick folds, shear zones and thrust faults.

2.2. Neotectonic regime and seismogenic sources

Since Middle Miocene, the study area is being deformed under an extensional stress field. The first post-orogenic collapse phase has a NE-SW direction of extension. This phase started in Late Miocene and lasted until Pliocene in the area. This extensional configuration has migrated to the west, following the outward migration of the orogenic front due to the roll-back of the subducting plate. It is still active in Epirus and Albania (Pavlides and Kilias, 1987; Mercier et al., 1989; Caputo and Pavlides, 1993; Mountrakis, 2006). This phase is the one that has formed the large, NW-SE trending basins of western Macedonia and Thessaly.

The active extensional field has been active since Middle Pleistocene, has a N-S general trend and affects the broader Aegean area. It caused the formation of a new generation of E-W trending normal faults, which are currently defining the northern boundary of Thessaly plain (Fig. 6).

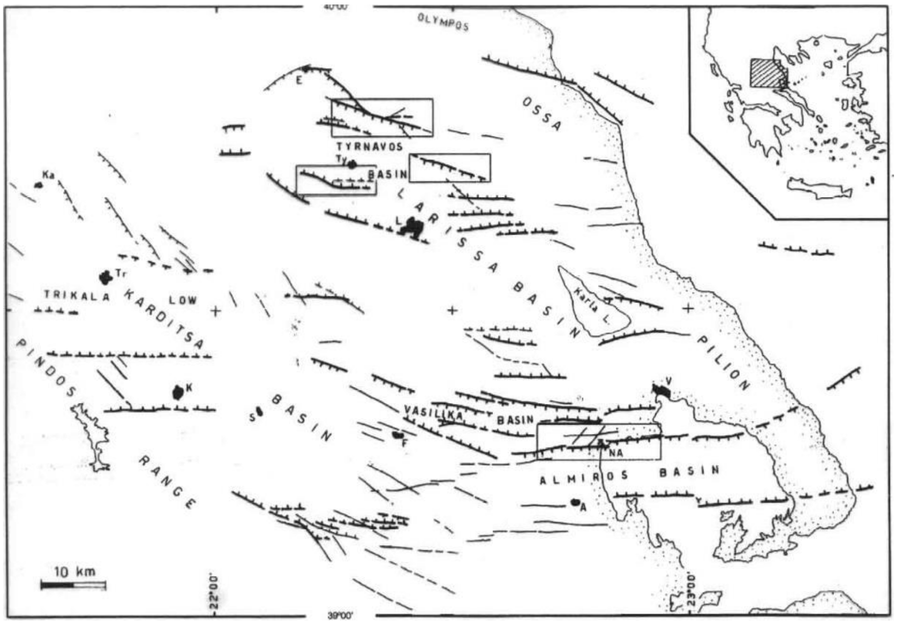

Fig. 6: Simplified tectonic map of Thessaly (Caputo and Pavlides, 1993; Caputo, 1995). The main Quaternary faults are shown in thick black lines, the teeth indicating the hangingwall.

The Tyrnavos fault is a typical tectonic structure considered as active, similar to many others in the broader area (Caputo and Pavlides, 1993; Caputo, 1995; Caputo et al., 2004). It strikes WNW-ESE and has a surficial length of 10-12 km. This fault is one of the best studied active structures in Greece for more than 30 years by the Earthquake Geology research team (AUTh) and the University of Ferrara (Italy) and is included in the Greek Database of Seismogenic Sources (GreDaSS http://gredass.unife.it, Fig. 7; Sboras, 2011; Caputo et al., 2012, 2013, 2014; Caputo and Pavlides, 2013; Sboras et al., 2014), in which it is described in detail. According to geological data, geophysical surveys and palaeoseismological excavations which study the geological history of the fault, document slow activity characterized by vertical surficial co-seismic displacements of 20-40 cm and a possible recurrence period of about 1-2.5 ka, as well as a low slip rate of 0.05-0.25 mm/year. Its earthquake potential is estimated to M 6.1 to 6.3 (Caputo et al., 2004), based on the empirical relationships Ms *versus* SRL of Pavlides and Caputo (2004) and Wells and Coppersmith (1994). The active deformation of the area is also well documented by recent satellite geodetic analysis (Chatzipetros et al., 2018; Lazos et al., 2021).

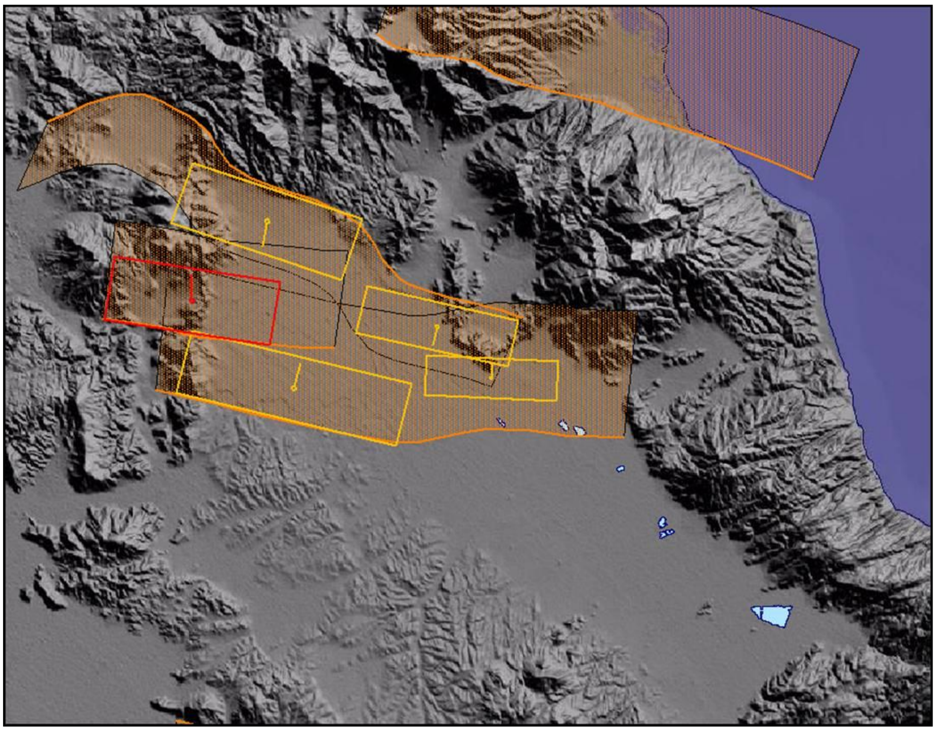

Fig. 7: The northern Thessaly fault system, as shown in the Greek Database of Seismogenic Sources (GreDaSS). Boxes are rough approximation of the vertical projection of the fault plane to the surface.

3. THE ELASSONA NEOGENE-QUATERNARY BASIN

The Elassona Basin comprises the southernmost part of the Florina-Ptolemaida-Kozani-Sarantaporo-Elassona Neogene tectonic depression, and it is known for the hosted coal deposits. The basin can be further divided into two sub-basins, the north-eastern one, where the town of Elassona lies, and the southwestern one (Potamia sub-basin), where the Domeniko, Amouri, Evangelismos and Mesochori villages are located. The latter sub-basin is located within the meisoseismal area of the March 2021 earthquake sequence. The two sub-basins are connected through the Aghioneri narrows and the Elassonitis River valley, while the Potamia sub-basin becomes narrower to the east before entering the Titarissios River valley.

The combination of neotectonic, palaeoclimatic and palaeogeographic conditions facilitated the basin formation and its filling with new sediments. Thus, the inner part of the basin is filled with Neogene and Quaternary deposits in which the lignitic deposit occurs. The Pliocene formation unconformably overlie the alpidic crystalline basement due to the intense alpidic tectonic activity that took place before the Neogene sediments deposition.

During the exploration campaign in the area by the Institute of Geology and Mineral Explration of Greece (Dimitriou & Giakoupis, 1998), a dense network of boreholes was drilled revealing important tectono-stratigraphic information for the Potamia sub-basin (see also Galanakis et al., 2021; this volume). According to this study, besides the topmost Holocene deposits, the underlying Upper Miocene to Pliocene formations are often observed vertically displaced from borehole to borehole, implying the occurrence of normal faulting. All implied faults are not of the same age since they either displace the deeper Upper Miocene formations, or the displace the base of Quaternary (Villafranchian). The younger faults, characterized as “post-Neogene” faults in the study, demonstrate a NW-SE direction forming bookshelf or graben-style patterns. Besides this study, along the SW margin of Potamia sub-basin, a fault of similar direction (dipping to the NE) is mapped, having created a downthrow of several tens of metres. This fault lies on the extension of the co-seismic ground ruptures and the liquefaction phenomena which were mapped south of the Titarissios river. Possible co-seismic ruptures or gravitational ones appeared after the earthquake on a NNW-SSE trending fault between the villages Amouri and Vlachogianni. This place is key to understanding the neotectonics of the wider area and especially the active tectonics.

4. HISTORICAL SEISMICITY

Concerning the historical seismicity of the region, important details and revisions are included in (Papaioannou, 2017a, 2017b, 2018, 2019). The epicentre distribution of the main earthquakes is given in Fig. 8. On 12/25 November 1901 according to old and new calendar respectively, at approximately 5 a.m. local time, a strong earthquake caused damage to the houses of the village Verdikoussa again, where 4-5 houses collapsed. It provoked a large landslide, as well. The information comes from a report by the Greek Consulate in Elassona (the area of Elassona was, then, under Ottoman rule), to the Greek Ministry of Foreign Affairs. Based on this macro-seismic information, it is estimated that the epicentre was reported close to Verdikoussa (geographic coordinates 39.80 ° N; 22.10 ° E) and its magnitude estimated M 5.6 +- 0.2 (possibly 5.8).

In previous seismic historical research have been referred two strong earthquakes in northern Thessaly, that of 1735 (Papazachos and Papazachou, 2003; Ambraseys, 2009) and the unknown 1901, which, most likely, occurred in the same seismogenic area of the recent earthquakes of Larissa – Tyrnavos -Elassona and in fact in northeastern part (area of Verdikoussa-Pretori villages, Fig 8 or coordinates 39.80° N; 22.00° E). The first occurred on 21 August (old calendar) / 1 September (new calendar) 1735. It was an earthquake that lasted a long time and shook Larissa city. This emerges from the following memoir written in ecclesiastical book, as follows: "On that year 1735 in the month of August 21st a great earthquake occurred". "The quake itself caused cracks in the church of Holy Monastery of Barlaam of Meteora, as well as in the dining room and in the kitchen. Earthquakes followed that lasted 15 days (aftershocks)".

From the above descriptions, it has been estimated that the earthquake probably was created from the same seismogenic area of the recent earthquakes (March 2021), which is located between Larissa and Kalambaka and strongly felt but were also slightly harmful in both cities. Intensity of the EMS-98 scale is estimated at VI in Larissa and V-VI in Kalambaka, where fallen rocks observed from the characteristic rocky monasteries of Meteora. Based on the distribution of macro-seismic information, it is estimated that the epicenter of the earthquake was located between Verdikoussa and Pretori (geographical coordinates 39.80° N; 22.00° E) and that its approximate magnitude was M 6.2, with a standard deviation of 0.2. This estimated position of the epicenter is located 18 km NW of the epicenter of the earthquake of March 3, 2021 and is 33 km away from the Varlaam Monastery of Meteora and 40 km from Larissa.

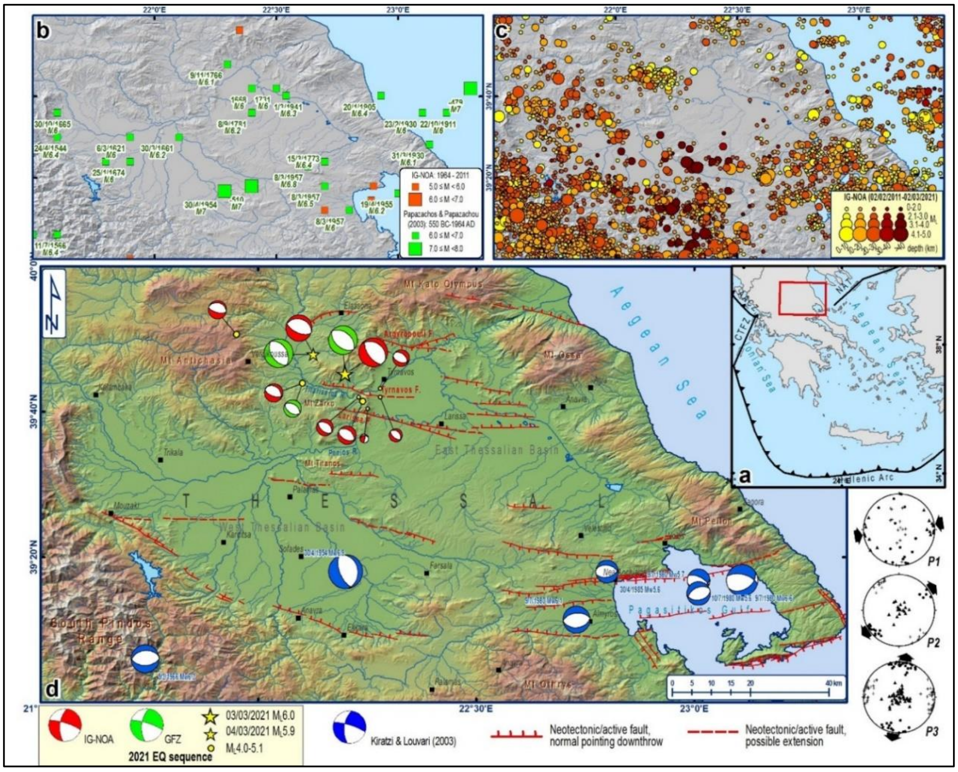

Fig. 8: Historical seismicity in the study area. The lower map shows the focal mechanisms of the main instrumentally recorded events in the area, as well as the ones of the March 2021 sequence.

Concerning the 1766 strong earthquake, which is referred in bibliography as an earthquake of the area (M 6.3; I_{max}=VIII, Elassona, 39.7^o N; 22.2^o E), we think that this is not a correct attribution. On October 28 / November 8, 1766, this strong event caused significant damage to homes and chimneys in an unnamed area, which in the current literature is considered to be Elassona town. Furthermore, the earthquake was strongly felt in Zakynthos (Zante, Ionian Sea), it had long duration and caused great concern to the inhabitants, who woke up, got out of their houses and took refuge in churches, praying. The information about this earthquake came from two sources: a) From a memoir written in a musical manuscript of Olympiotissa Monastery (Elassona), which states the following: “During 1766 October 29 in the evening of Sunday, around 4 o'clock at night, a great earthquake happened, so that many houses were shaken and damaged”. The author of the manuscript, Constantine, was the lead cantor of the church of Ioannina (Epirus). The manuscript was written in 1717, forty-nine years before earthquake, as referred to the following note, in same manuscript: “*the present was coming to an end “Asmatomelirritofthongos” book in the year of salvation, Psafiz 'ω [= 1717]: εν μηνί ιουνίω θ’η: μέρα σαββάτω. It was written by me poor, minimal and* *ignorant Constantine, and protopsalt (lead cantor) of the great church of Christ, and famous city of the metropolis of Ioannina*". Fifty years later, in January 1767, Anthimos Olympiotis became the owner of the manuscript, as is mentioned in another chronological note of the same manuscript: "*This is property of Anthimos Hieromonk of his meadow (sic) 1767 January….* " At that time Anthimos was serving as pastor and teacher in Miskolc, Hungary. Between 1717 and 1767, there is no other reference of ownership of the manuscript. It is very likely that the manuscript was purchased at Ioannina, on behalf of Anthimos, by his friend Georgios Patakis from Epirus, soul of the Greek community in Miskolc. It is well known that Anthimos, after his studies, served from the spring of 1762, as pastor and teacher in the cities of Ketskemet in Hungary and Miskolz and then as a pastor in the Austrian capital city, Vienna. In October 1777, he returned to the Olympiotissa monastery (Elassona). Upon his return he donated, besides among others, his personal library which contained 400 volumes of books, 10 of which he had compiled during fifteen years abroad. Among the books was the aforementioned manuscript, which was acquired ten years ago while in Miskolc. Therefore, the memoir was not written by Anthimos Olympiotis in Elassona, since in November 1766 he was in Hungary and had not yet become the owner of the manuscript. b) From a memory of the notary of Zakynthos Stathis Papadatos, who recorded it in a notebook stating the following: "*1776 October 28. Monday dawn 11 at 5 of the night a big earthquake happened starting slowly at first and gradually becoming stronger. The people got up and asked for forgiveness, they ran to churches*".

From the examination of the macro-seismic results described in the two memoirs, it is unlikely that the earthquake could have its epicentre in Elassona area. There was, a few years ago in Ioannina, an earthquake with epicentre in the broader area of Ioannina. This event could have caused in the city of Ioannina, the damages described by first memoir and could be strongly felt in Zakynthos, as described in the second one. In the broader area, earthquakes of magnitude 6.0 to 6.3 are rather common and have caused damages repeatedly in Ioannina city. From a similar earthquake of magnitude 6.3, which occurred on July 31, 1898, in this area, buildings and chimneys collapsed in Ioannina, while it was strongly felt in Zakynthos. Following all the above arguments, the earthquake of October 28 / November 8, 1766, must have occurred in the area of Ioannina (Epirus) and not in the area of Elassona, as previously thought. This is a revision of the catalogue of known historical earthquakes in the region. Another large earthquake in the broader area occurred on 1892 (Papazachos and Papazachou, 2003; Ambraseys, 2009; Papaioannou, 2017a, 2019), while there is information about an earthquake of 1781 of a similar magnitude.

5. GPS GEODESY AND THE TECTONICS OF THE REGION

Concerning the crustal deformation of Thessaly due to active tectonics, raw data for a seven-year period were collected from 27 permanently installed GPS/GNSS stations, and processed using by the triangulation methodology (Lazos et al., 2021). From this methodology a series of parameters was calculated including maximum horizontal extension, total velocity, maximum shear strain, area strain and rotation (Fig. 9). The maximum horizontal extension parameter shows a dominant N–S direction, which is consistent with the active fault zones of the broader Thessaly area. However, sparse distribution of E–W maximum horizontal extension vectors is documented, while it is likely to be associated with local tectonic structures; limited compressional occurrences are also observed at the western part of the study area. Regarding the total velocity, the estimated vectors are characterized by a NE–SW direction, leading to the conclusion that the broader Thessaly area show a SW motion, receiving the highest and lowest values at its southern and northern parts, respectively. Maximum shear strain is directly related to the activation of fault zones, while the highest values are observed at the eastern part of Thessaly, close to the North Aegean region.

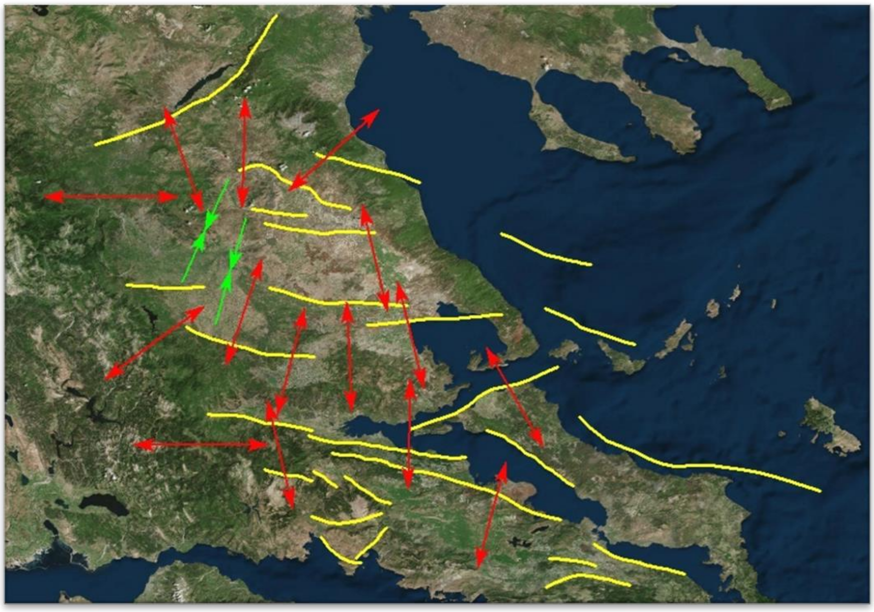

Fig. 9: Representative maximum horizontal extension (red) and contraction (green) vectors of the study.

The recent activity of the North Aegean fault zones (seismic events) was imprinted at the raw geodetic data, leading to high maximum shear strain values. Regarding the area strain parameter, it is associated with the dilatation and contraction of the study area.

The highest contraction values are documented at the western part of the study area, close to the Pindos Mountain range, where compressional tectonics occur, while the highest dilatation values are recorded at the Pagasitikos Gulf region, coexisting with high contraction values. This coexistence of dilatation and contraction indicates potential strike-slip structures, leading to the conclusion that the wider Pagasitikos Gulf area is probably affected by the North Aegean Trough fault zones activity, constituting the westward continuation of the North Anatolian fault zone. The rotation parameter shows a dominant clockwise rotation of the area, while limited and local-scale counter-clockwise rotation vectors are also documented.

6. THE MARCH 3 AND 4, 2021, EARTHQUAKES – ENVIRONMENTAL EFFECTS

The earthquake sequence produced secondary surface effects, as the seismogenic fault did not reach the surface. The surface effects were distributed throughout the affected area (Fig. 10) and have been briefly presented in preliminary publications (Ganas et al., 2021; Pavlides et al., 2021; Valkaniotis et al., 2021). The majority of the surface ruptures were observed in Titarisios river valley (Fig. 11), while the bulk of liquefaction occurred in Pinios river valley. The main features are described in the following paragraphs, based on original fieldwork and observations.

6.1. Liquefaction phenomena

Dozens of soil liquefaction occurrences, such as sand boils and flows have been mapped in areas adjacent to Pinios and Titarissios rivers. The first area is located between the villages of Koutsochero to Pineiada and Zarko (Fig: 12), while the latter is less extended and is observed mainly in the area of Vlachogianni and Varko villages. The liquefaction phenomena were mapped in great detail using UAVs (Fig. 13). Comparison with current and historical satellite images, show that in the area of Pinios river the liquefaction is clearly associated with older abandoned meanders of the river, indicating a differentiated composition, more susceptible to liquefaction (Fig. 14). A liquefaction susceptibility map of Greece and an associated database (DALO v. 1.0) have been published by Papathanassiou and Pavlides, 2009 and Papathanassiou et al., 2010), whilst an evaluation of earthquake-induced liquefaction in the urban areas and more specific in Larissa city has been published by Papathanassiou et al. (2011).

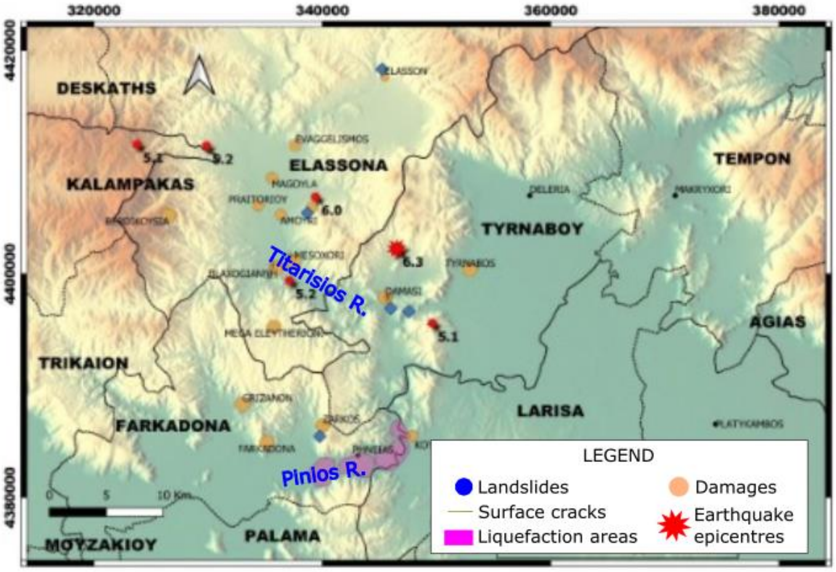

Fig. 10: Distribution map of the main surface effects that were observed in the meisoseismal area.

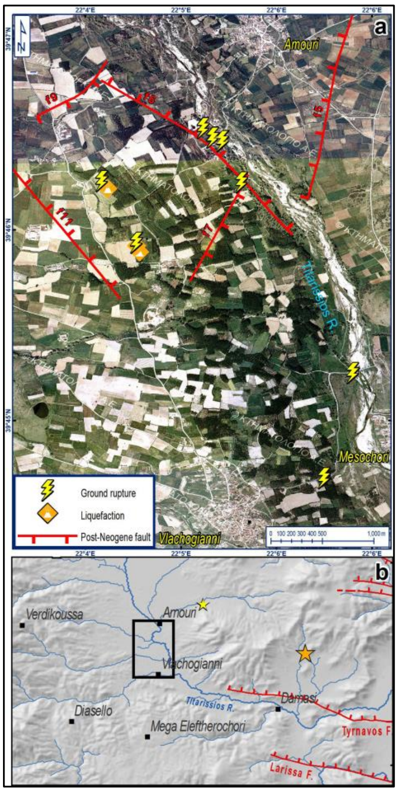

Fig. 11: Distribution of surface ruptures and liquefaction in Titarissios river valley, where the main bulk of the earthquake’s surface effect was observed.

Fig: 12: Examples of sand flows, sand boils and lateral spreading in the liquefied area SE of Pineiada village.

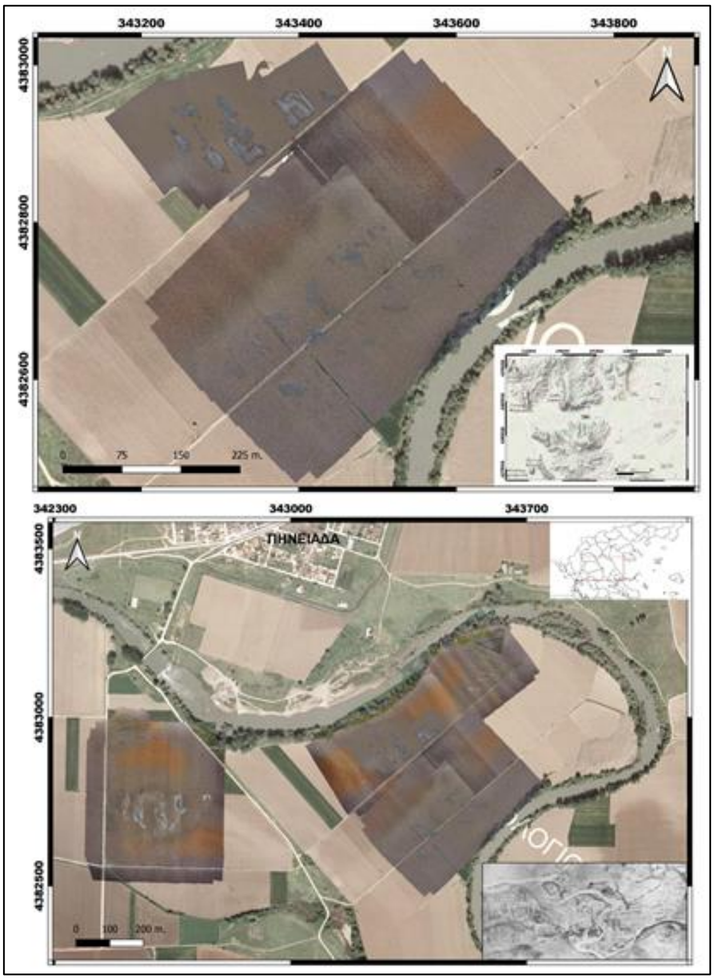

Fig. 13: Orthorectified image of the liquefied areas (gray spots). Images from a series of high-flying UAV campaigns have been combined with orthophotos from the Cadastral project of Greece.

Fig. 14: A detailed UAV composite orthophoto (yellow border) overprinted onto a satellite image, clearly shows that the distribution of individual liquefaction features (gray spots) coincides with an abandoned and filled bend of Pinios river. The current riverbed is visible at the right part of the map.

6.2. Rock falls, landslides and lateral spreading

Gravitational secondary effects, such as rock falls and landslides, were observed throughout the area (Fig. 15). Their distribution does not follow a specific pattern, but it is rather dependant of local site conditions, i.e., rock quality and slope angle. Lateral spreading was quite common in areas close to river banks, such as in Damasi, Mesochori, etc. (Fig. 16).

Fig. 15*:* Rock falls and slope failures along the country road to Vlachogianni village.

Fig. 16: Secondary cracks due to lateral spreading and associated liquefaction NW of Mesochori village.

7. GNSS DATA AND SITE DISPLACEMENT ESTIMATION

In order to estimate the influence of March 3, 2021 earthquake on site displacements a time period of fourteen days GNSS data was selected, from March 1 to March 14, 2021. Specifically, data for two days before and eleven days after the event were processed. The data extracted from five permanent GNSS stations located from 15 to 50 km away from the epicentre. GNSS stations are part of various networks such as HermesNet of Auth, HxGon SmartNet/Greece and NoaNet. Data analysis was based on 30-sec daily GPS+Glonass observations and elevation cut-off angle 10°. Four of the five stations record GPS and Glonass data which is an advance for the impact of Satellite geometry in the process. The process was held on the current reference frame ITRF2014 using the web-based PPP platform of National Resources of Canada- Canadian Geodetic Survey (CGS). The well-known CSRS-PPP is an online application for data post-processing allowing users to compute higher accuracy positions from their GNSS raw data. PPP technique uses zero-difference pseudoranges and carrier phase data utilizing precise orbits, clock values (retrieving from analysis centers) and models for account of satellite antenna offset and earth and ocean tide loading. This algorithm can potentially achieve high order positional accuracy. This is done in the present study because daily station data were processed. Also, the used platform has a modernization option which includes PPP with ambiguity resolution for data collected on or after 1 January 2018. Co-seismic displacements derived by daily processing scenarios, where the estimates of position coordinate characterized by sub-centimeter accuracy, is an appropriate level for our study. The maximum horizontal displacements were observed in ELAS (2.2 cm to the North and 4.3 cm to the East) and KLOK (3.4 cm to the South and 4 cm to the West) stations. These displacements are in accordance with the focal mechanism parameters, as well as with the long-term active extension direction, as discussed earlier. The daily calculated displacements expressed in the topocentric system (East, North, Up) are presented in the following table 1, while the timeseries of the horizontal displacements is shown in Fig 17.

Table 1. GNSS displacements.

GNSS station	Latitude	Longitude	dEast (m)	dNorth (m)	dUp (m)
ELAS	39.89243	22.20612	0.022	0.043	0.014
KLOK (GPS only)	39.56473	22.01438	-0.034	-0.040	0.003
KRDI	39.36348	21.92264	-0.003	-0.011	0.024
LARM	39.61410	22.38791	0.001	0.005	0.014
MURG	39.73871	21.55422	-0.004	-0.002	0.026

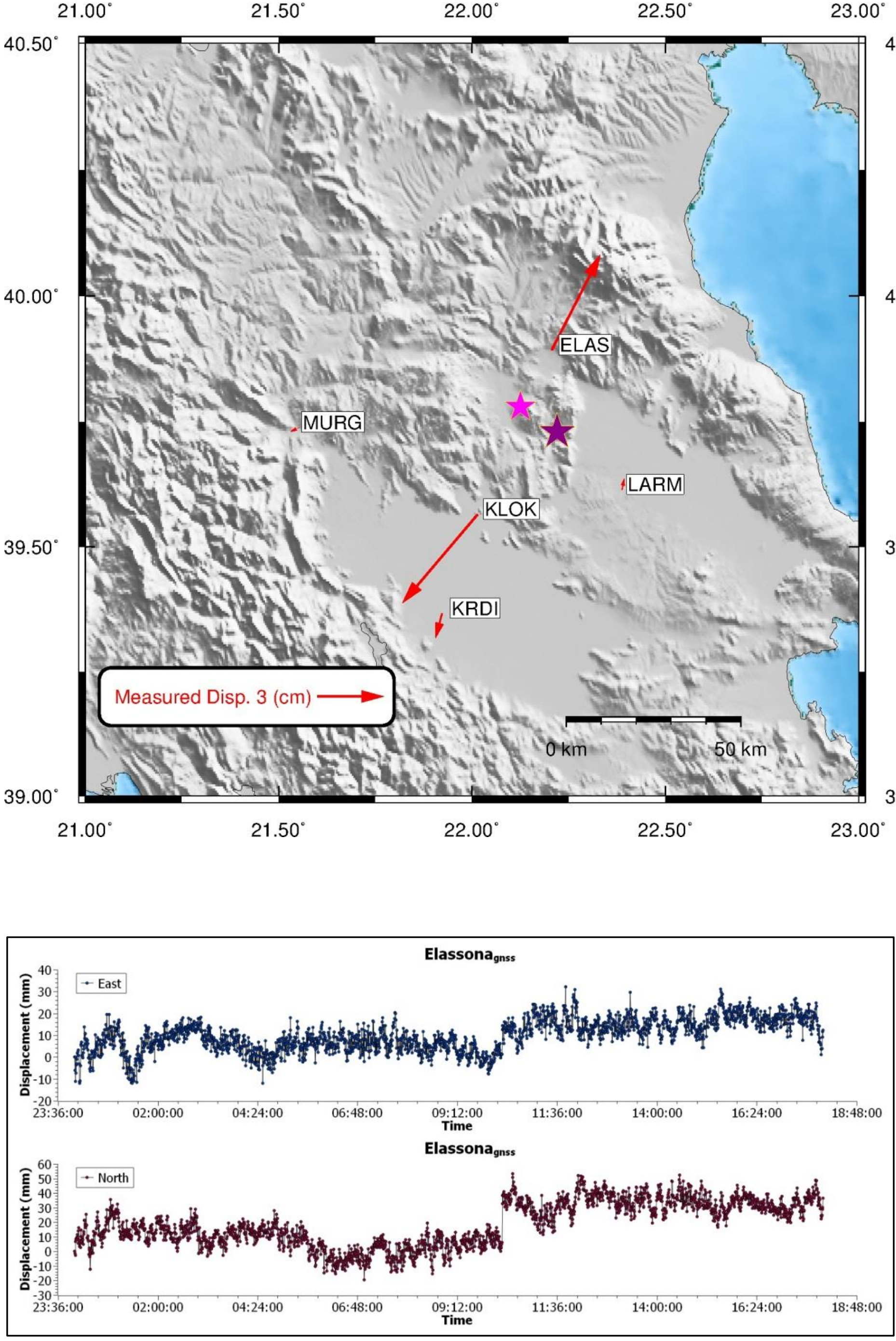

Fig. 17: Horizontal co-seismic displacements in the broader area of the earthquakes.

8. EARTH OBSERVATION MAPPING OF SECONDARY PHENOMENA

For the mapping of earthquake-induced secondary phenomena by means of Earth Observation (EO), Copernicus Sentinel-1 mission data covering the broader epicentral area were used. This comprise of Sentinel-1 imagery from four different tracks, namely two ascending (A102 & A175) and two descending (D007 & D080) satellite orbits. The imagery utilized, limited to scenes acquired immediately before and after of the mainshock, are shown in Table 2.

Table 2. Co-seismic Sentinel-1 interferometric pairs utilized in the current work.

Acquisition Geometry	**Relative Orbit**	**Incidence Angle (degrees)**	**Acquisition Time (UTC)**	**Pre-event Acquisition Date**	**Post-event Acquisition Date**	**Temporal Separation (days)**	**Perpendicular Baseline (m)**
Ascending	102	34	~16:25	25/02/2021	03/03/2021	6	-42.5
Ascending	175	44	~16:30	02/03/2021	08/03/2021	6	11.6
Descending	007	44	~04:30	03/03/2021	09/03/2021	6	47.6
Descending	080	34	~04:40	02/03/2021	08/03/2021	6	-54.2

Our approach is based on analysis and interpretation of co-seismic interferometric coherence products for the recognition of surface changes within the area of interest. Interferometric processing was undertaken on a Virtual Machine (VM) provided by the ESA RSS-Cloud Toolbox service (Marchetti et al., 2012), having direct access to the Copernicus archives via the CREODIAS infrastructure (https://creodias.eu). For the processing of the S-1 IW Single Look Complex (SLC) data, the GAMMA software packages were used (Papanikolaou et al., 2010; Foumelis et al., 2013; Wegnüller et al., 2016; Lemoine et al., 2020). To compensate for the topographic component, heights from the AW3D30 DSM (Takaku et al., 2018) were utilized. Although during the early response phase, and in order to rapidly aid in-situ observation, differential interferograms were generated using annotated orbits, for the current work we used precise orbit state vectors, with an accuracy better than 5 cm (Peter et al., 2017). The differential interferogram of the M6.3 mainshock, responsible for the majority of the secondary phenomena observed, is shown in Fig. 18.

For the estimation of coherence, the complex normalized interferogram and the two corresponding backscatter intensity images are used (Fig. 19). The applied estimator is adaptive, adjusting the window size to local coherence levels estimated in an initial non-adaptive step. Large estimation windows are applied for regions of low coherence, reducing thus the bias, while small estimator windows in regions of high coherence maintain spatial resolution. To reduce temporal decorrelation effects, only interferometric pairs of 6-day time span were utilized (Table 2). The overall obtained high coherence levels allowed the identification of local low coherence patterns (Fig. 19), that could be attributed to earthquake-induced secondary effects (i.e., liquefaction and surface ruptures).

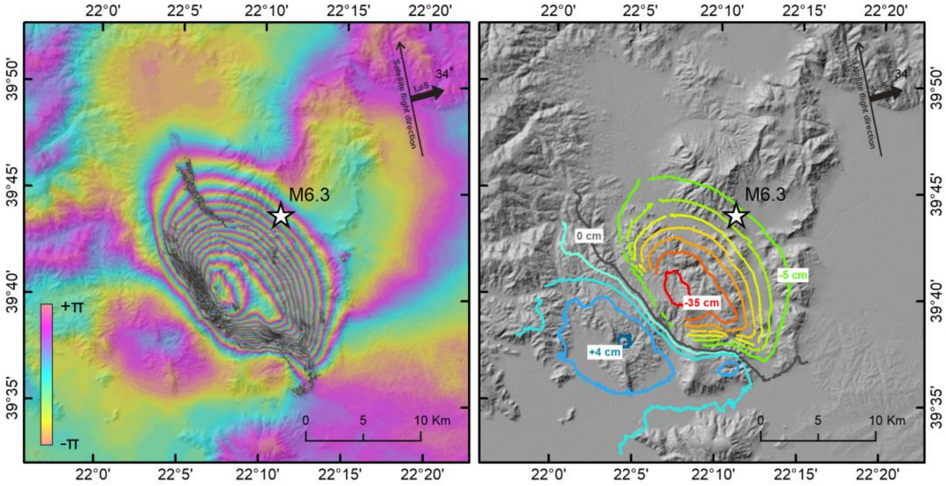

Fig. 18: Co-seismic differential interferogram of the M6.3 Tyrnavos earthquake using Sentinel-1 pre- (25/02/2021) and post-event (03/03/2021) scenes acquired along the ascending 102 orbit (left) and extracted displacement contours after phase unwrapping (right). The reference point is located outside the shown frame.

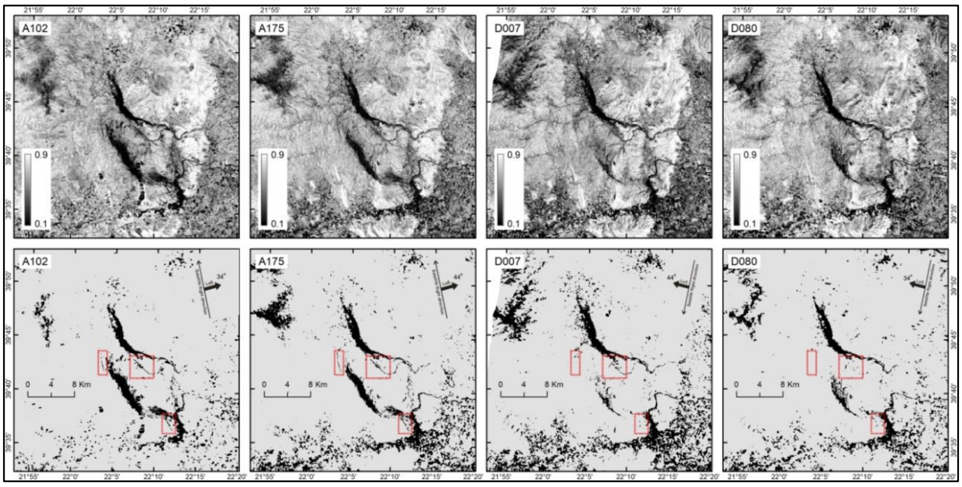

Fig. 19: Interferometric coherence of co-seismic pairs (see Table 1) acquired by different Sentinel-1 geometries (up) and extracted low coherence regions based on 0.3 thresholds (down). Note the narrow linear features in the red dotted polygons, visible only in ascending geometries due to favorable alignment between their trend and the LoS direction.

However, due to the influence of the SAR acquisition geometry as expressed by layover and shadow effects (mainly between ascending and descending orbits) as well as other short-term changes of the surface, several non-common regions of low coherence exist between the various coherence maps. Based on the assumption that secondary surficial effects caused by the earthquake should be present in all co-seismic interferometric pairs of comparable temporal coverage, only regions exhibiting low coherence values (below 0.3) in all considered pairs were accepted for further analysis. The above masking step reduced considerably the number of irrelevant (non-earthquake related) low coherence signals. Subsequent sieve filtering, as post-processing in a GIS environment, was still considered necessary to eliminate small low coherence cluster (2-3 pixels size), providing a much cleaner composite coherence output (Fig. 20).

Nevertheless, the above-mentioned procedure masked out actual linear low coherence features detectable only by single SAR geometry (see Fig. 19). This is more evident when the features, in principle narrow low coherence zones, are aligned more or less parallel to the Line-of-Sight (LoS) direction of the satellite. Developed mainly along the SW-NE direction, the north-westward looking descending orbit represents a non-favorable viewing condition. Thus, a complementary step involving visual interpretation of co-seismic differential interferograms was considered to outline discontinuities of the interferometric fringes (Fig. 21). That was proven equally valuable for the direct mapping of linear surface ruptures.

EO-detected surface ruptures seem constraint within the region affected by the M6.3 induced ground displacements, located south of the mainshock epicenter, maintaining a NW-SE trend (Fig. 21). The two major spatially continuous regions of low coherence collocate well with the Pinios and Titarissios River plains, can be attributed to extended liquefactions or other surface disturbance triggering phenomena. Finally, a decorrelated zones (coherence <0.3) of approximately 1.6 sq. km, located in the vicinity of the area where maximum ground displacements were observed (Fig. 21). This region can be associated to distributed deformation because of the propagation of motion caused by a blind seismic rupture to the surface.

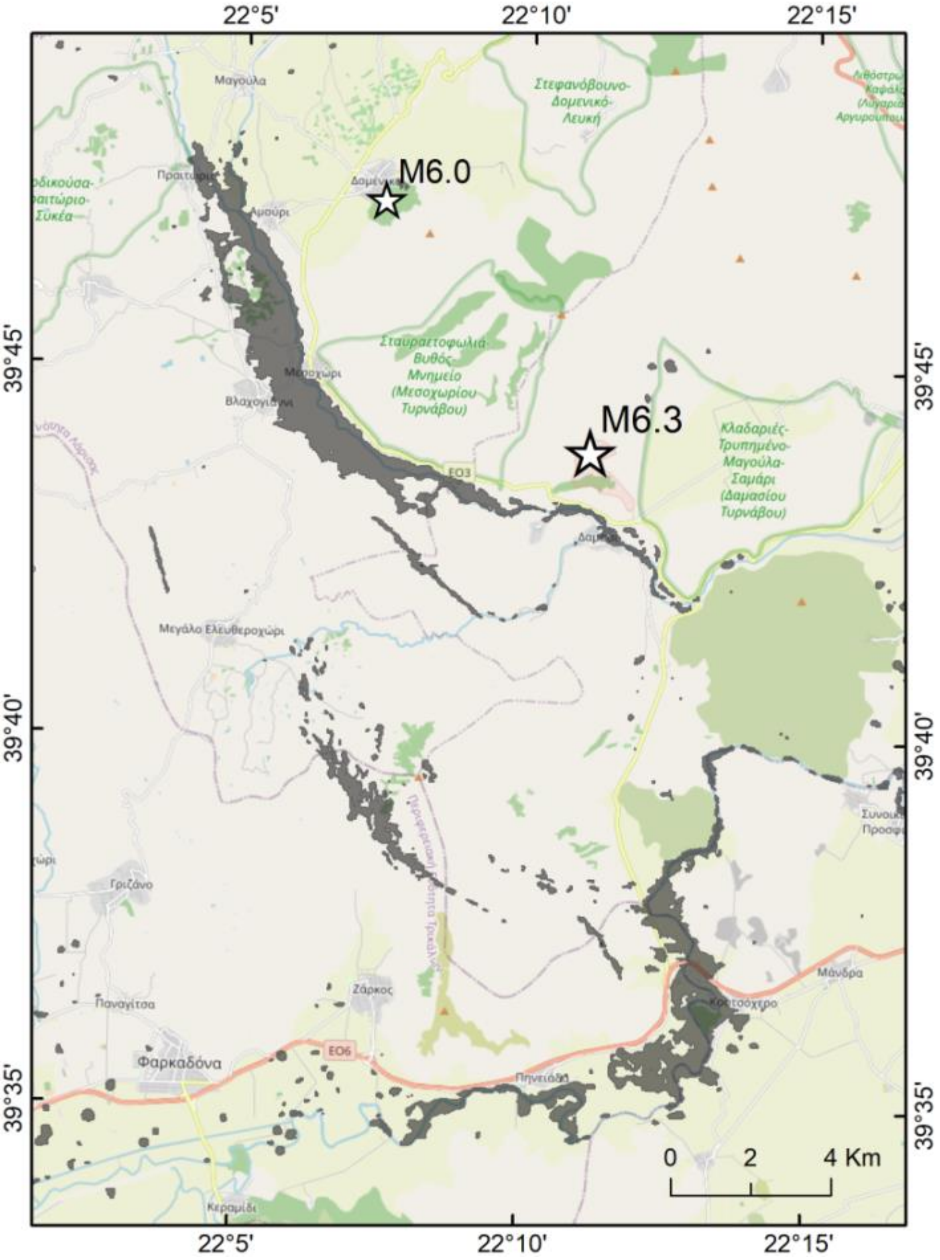

Fig. 20: Regions of low interferometric coherence (<0.3) as derived by combined analysis of independent coherence estimates from different acquisition geometries (see text for details). These low coherence regions, shown in grey, common to all examined co-seismic pairs (see Table 2), can be attributed to the secondary phenomena (i.e. liquefactions and surface ruptures) induced by the Tirnavos M6.3 mainshock.

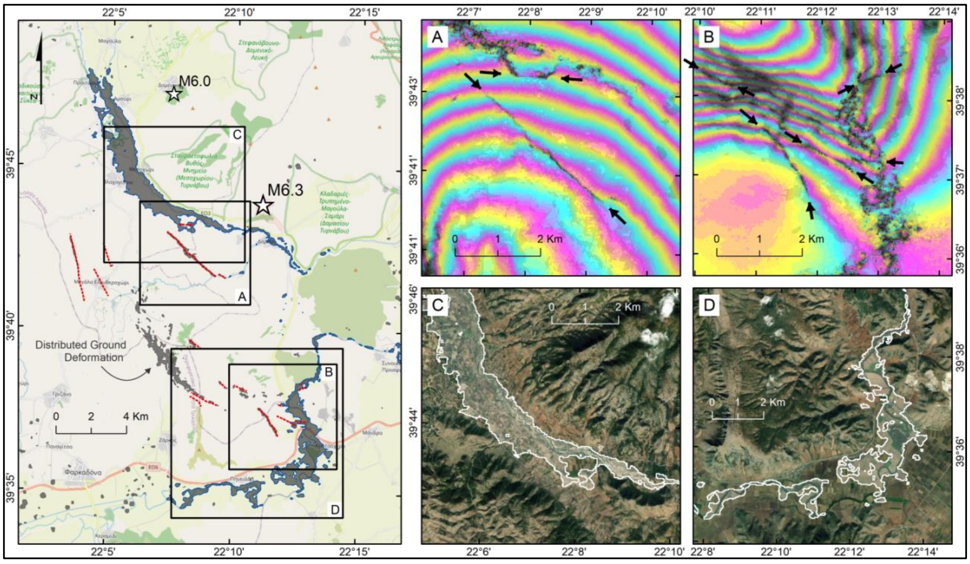

Fig. 21: Composite map of decorrelated areas (shaded polygons) as derived by analysis of co-seismic interferometric coherence estimates and surface ruptures (red dotted lines) by visual interpretation of fringes' spatial discontinuities (A and B). Regions suffered extended liquefactions (shaded polygons with blue outline) collocate with riverbeds (C and D).

9. THE NEW, PREVIOUSLY UNKNOWN, SEISMOGENIC FAUL

As far as the insofar unknown and unmapped seismic fault is concerned, fieldwork showed that there are characteristic geological indications in the Pelagonian continental basement rocks (e.g. Kilias and Mountrakis, 1987; Kilias et al., 1991), indicating that a moderate to low angle normal fault has acted as a hidden or blind fault during the earthquake. Field observations show that similar older normal faults in the basement close to the epicentre are dipping with angles ranging between 25^{o} and 50^{o}. Although the inferred dip angle of focal mechanisms 35-40^{o} seems low, it is well within the range of seismogenic normal faults, as observed in global data sets (Jackson and White, 1989). It is associated with the bedrock schistosity, as well as with small high angle reverse faults of the Pelagonian anticline. The presumed seismic fault extends in the broader area between the villages of Zarko and Megalo Eleftherochori, as an inherited shear zone (Fig. 22). Geologic indications include outcrops of the post Alpine shear zone (Fig. 22a,b,c), located along the boundary between interferometrically-indicated uplift and subsidence terrains (Fig. 23, that is 0 line of displacement), the existence of cataclasite and fault gouge in the shear zone (Fig. 22a-e), which indicates reactivation of the fault in brittle conditions during the neotectonic period and slickenlines compatible with the active stress field (Fig. 22a,c,d). Fault surfaces strike at N160^{o}E and dip at 50^{o} on average which is in good agreement to the published focal mechanisms by Greek (NOA and AUTh) and other international Institutes. Co-seismic indicators include small, ruptured fault surfaces with detached rock slabs and pieces, as well as small-scale soil fractures following the trace of the mapped fault (Fig. 22d,g), with negligible vertical displacement and small heave (up to 2 cm).

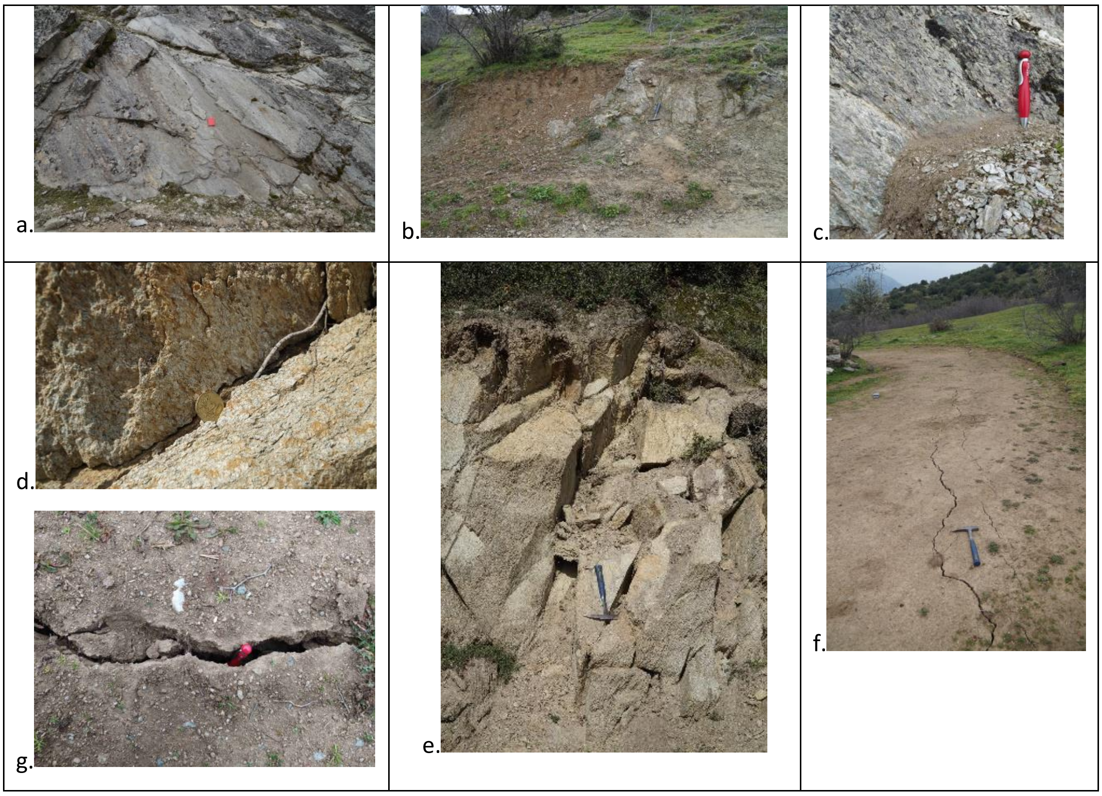

Fig. 22: a) Fault surface of the low-angle normal fault in the bedrock, believed to be a strand of the causative fault zone b) a zone of intense brittle shearing, accompanied by fault gouge and cataclasite within the low-angle normal fault zone c) fault surface d) opening along a pre-existing shear zone e) cataclasite and opening in Paleozoic crystalline rocks f & g) co-seismic surface cracks in the soil cover, following the inferred strike and location of the causative fault zone in the bedrock.

The seismic fault model (seismic source) of the mainshock is based on the GFZ's moment tensor solution (strike: 130^{o}, dip: 45^{o}, rake: -90^{o}), the scalar relationships of Wells & Coppersmith (1994; length and width), and the interferograms along with the site observations (position). We calculated the Coulomb static stress changes for receiver faults similar to the seismic source at a depth of 8 km. A vertical cross-section normal to the source's strike is also calculated. Results show stress-load beyond the tips of the fault, suggesting a triggering scenario for faults of similar geometry and kinematics located in this red area (Fig. 23). The northwestern edge of the fault (red-yellow) was activated during the second event of 4th of March. The seismic source is also used to model the vertical displacement on the ground after using the Okada formulae (Fig. 23). The maximum calculated vertical displacement is 2.93 cm. Both Coulomb and Okada calculations were performed with the Coulomb v. 3.3 application (Lin and Stein, 2004; Toda et al., 2011).

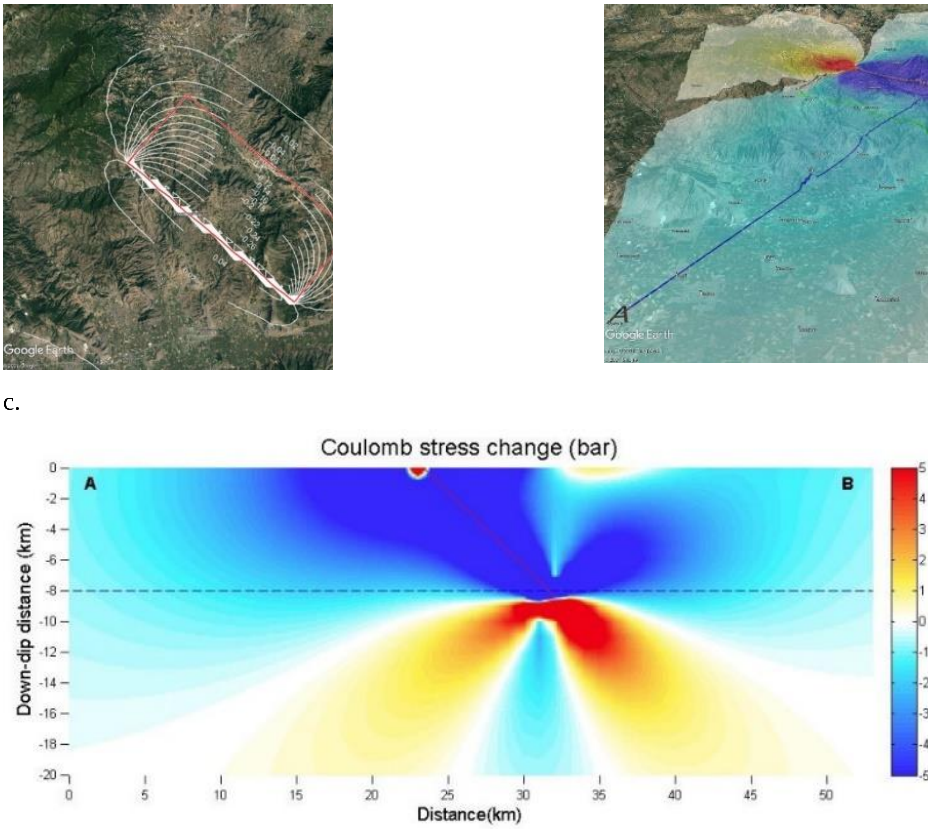
a.

b.

c.

Fig. 23: a) A preliminary model of the seismic source is showing vertical displacement on the ground b) The seismic fault model (seismic source) of the mainshock is based on the GFZ’s moment tensor solution. The Coulomb static stress changes (seismic source at a depth of 8 km). (c) Vertical cross-section normal to the source’s strike (A-B). Results show stress-load beyond the tips of the fault, suggesting a triggering scenario for faults of similar geometry and kinematics located in this red area.

10. CONCLUDING REMARKS

The fault that ruptured in 2021 cannot be associated with any of the previously known active faults in the area. Field work, seismological data and InSAR results show that the main seismogenic structure is neither the well-studied active fault of Tyrnavos, nor the extension to the NW of the also well-known fault of Larissa, although both appear to have been activated and partially affected by the main seismic fault as secondary triggered structures. A NE-dipping normal fault was activated for the main event as a blind or buried fault, following pre-existing inherited alpine structures, that does not appear to have a surficial expression. The strongest aftershock or second main earthquake of 4th of March (M_w 6.0) is within the same rupture area, but may have been produced by a secondary adjacent segment of the same fault zone in the seismic sequence site. Based on the overall results of the work performed in this paper, we propose the model of Fig. 24. The main seismogenic structure is a low-angle normal detachment fault that dips towards the NE, while the steeper dipping mapped active faults that reach the surface are interpreted as supra-detachment structures. They occasionally have been activated as triggered faults, as indicated by minor co-seismic surface ruptures along the Titarissios valley fault, the Zarkos shear zone and the presumed extension of Tyrnavos fault to the WNW. This fault configuration is compatible with the post-orogenic collapse pattern, which caused crustal thinning and exhumation of lower tectonostratigraphic units throughout the broader area.

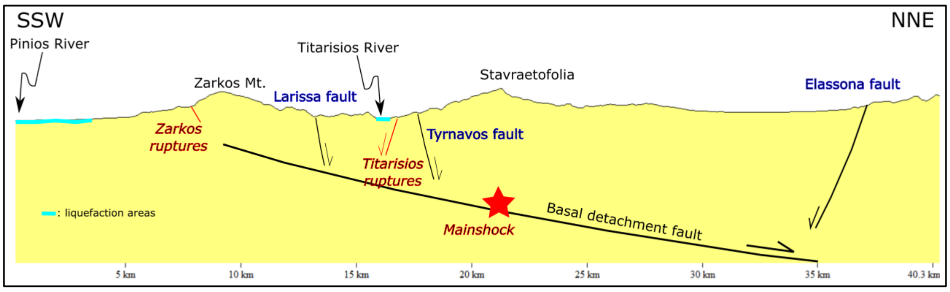

Fig. 24: Interpretive sketch of the assumed tectonic structure of the area, based on geological and seismological data.

The active stress pattern of the Thessalian upper crust in the area is characterized by extension in an NNE-SSW direction. This is based in both Quaternary neotectonic quantitative methods and focal mechanisms of recent earthquakes (Fig. 8). The older Neogene-Pliocene extensional field had a different tensile direction (NE-SW, Pavlides and Mountrakis, 1987; Mercier et al., 1989; Caputo and Pavlides, 1993). The Neogene-Quaternary Elassona-Potamia basin shows that in addition to the ESE-WNW trending faults (~110°) that are favourably oriented to the active tectonic field, inherited NW-SE directed faults can also be activated. The analysis of the focal mechanisms of the latest earthquakes seems to be related to the active field of trends and faults that tend to create new structures in the area, proving its continuous and gradual geological evolution. At the same time, however, this earthquake raises new substantive questions and concerns, while revising some established views, such as:

(a) The status of active stress trends.
(b) The direction of active tectonic structures.
(c) The existence of a seismogenic fault in a mountainous volume of crystalline rocks without typical geomorphological expression.
(d) The role of blind faults to Seismic Hazard Assessment.

11. ACKNOWLEDGEMENTS

The authors are grateful to Assoc. Prof. Sotirios Kokkalas and Dr. Christoph Gruetzner, whose valuable comments have greatly improved the manuscript. We would also like to thank the Editor-in-Chief Dr. Athanasios Ganas for his assistance in the final format of the manuscript.

12. REFERENCES

Ambraseys, N., 2009. Earthquakes in the Mediterranean and Middle East. Cambridge University Press, Cambridge. https://doi.org/10.1017/CBO9781139195430

Caputo, R., 1995. Inference of a seismic gap from geological data: Thessaly (Central Greece) as a case study. *Annals of Geophysics, 38*. https://doi.org/10.4401/ag-4127

Caputo, R., Chatzipetros, A., Pavlides, S., Sboras, S., 2013. The Greek Database of Seismogenic Sources (GreDaSS): state-of-the-art for northern Greece., *Annals of Geophysics*. https://doi.org/10.4401/ag-5168

Caputo, R., Chatzipetros, A., Pavlides, S., Sboras, S., 2012. The Greek Database of Seismogenic Sources (GreDaSS): state-of-the-art for northern Greece. *Annals of Geophysics*, 55, 859–894. https://doi.org/10.4401/ag-5168

Caputo, R., Helly, B., Pavlides, S., Papadopoulos, G., 2004. Palaeoseismological investigation of the Tyrnavos Fault (Thessaly, Central Greece). *Tectonophysics*, 394, 1–20. https://doi.org/10.1016/j.tecto.2004.07.047

Caputo, R., Pavlides, S., 2013. Greek Database of Seismogenic Sources (GreDaSS)., University of Ferrara, Italy. https://doi.org/10.15160/UNIFE/GREDASS/0200

Caputo, R., Pavlides, S., 1993. Late Cainozoic geodynamic evolution of Thessaly and surroundings (central-northern Greece). *Tectonophysics,* 223, 339–362. https://doi.org/10.1016/0040-1951(93)90144-9

Caputo, R., Pavlides, S., GreDaSS Working Group, 2014. The Greek Database of Seismogenic Sources (GreDaSS): the new version. *EGU General Assembly 2014*.

Chatzipetros, A., Lazos, I., Pavlides, S., Pikridas, C., Bitharis, S., 2018. Determination of the active tectonic regime of Thessaly, Greece: a geodetic data based approach. *XXI International Congress of the CBGA*. Salzburg, 227.

Dinter, D.A., Royden, L., 1993. Late Cenozoic extension in northeastern Greece: Strymon Valley detachment system and Rhodope metamorphic core complex. *Geology*, 21, 45–48. https://doi.org/10.1130/0091-7613(1993)021

Forster, M.A., Lister, G.S., 1999. Detachment faults in the Aegean core complex of Ios, Cyclades, Greece. *Geological Society*, *London*, *Special Publications*, 154, 305–323. https://doi.org/10.1144/GSL.SP.1999.154.01.14

Foumelis, M., Trasatti, E., Papageorgiou, E., Stramondo, S., Parcharidis, I., 2013. Monitoring Santorini volcano (Greece) breathing from space. *Geophysical Journal International*, 193, 161–170. https://doi.org/10.1093/GJI/GGS135

Galanakis, D., Sboras, S., Konstantopoulou, G., & Xenakis, M. 2021. Neogene-Quaternary tectonic regime and macroseismic observations in the Tyrnavos-Elassona broader epicentral area of the March 2021, intense earthquake sequence. Bulletin of the Geological Society of Greece, 58, 200-221. doi:https://doi.org/10.12681/bgsg.27196

Ganas, A., Valkaniotis, S., Tsironi, V., Karasante, I., Elias, P., Kapetanidis, V., Kasssaras, I., Papathanassiou, G., Briole, P., 2021. The March 2021 seismic sequence in Larisa - Damasi , Thessaly (central Greece), its seismotectonic characteristics and geodynamic effects. https://doi.org/10.5281/ZENODO.4617264

Jackson, J.A., White, N.J., 1989. Normal faulting in the upper continental crust: observations from regions of active extension. *Journal of Structural Geology*, 11, 15–36. https://doi.org/10.1016/0191-8141(89)90033-3

Kilias, A., 1995. Tectonic evolution of the Olympus - Ossa mountains : emplacement of the blueschists unit in eastern Thessaly and exhumation of Olympus - Ossa carbonate dome as a resault of tertiary extension (Central Greece). *Mineral Wealth*, 96, 7–22.

Kilias, A., Alonso-Chaves, F.M., Orozco, M., Tranos, M., Soto, J., 2002. Extensional collapse of the Hellenides: a review. . *Rev. Soc. Geol. España,* 15, 129–139.

Kilias, A., Falalakis, G., Sfeikos, A., Papadimitriou, E., Vamvaka, A., Gkarlaouni, C., 2013a. The Thrace basin in the Rhodope province of NE Greece - A Tertiary supradetachment basin and its geodynamic implications. *Tectonophysics*, 595–596, 90–105. https://doi.org/10.1016/j.tecto.2012.05.008

Kilias, A., Fasoulas, C., Priniotakis, M., Sfeikos, A., Frisch, W., 1991. Deformation and HP/LT Metamorphic Conditions at the Tectonic Window of Kranea (W -- Thessaly, Northern Greece). *Zeitschrift Der Deutschen Geologischen Gesellschaft*, 142, 87–96. https://doi.org/10.1127/zdgg/142/1991/87

Kilias, A., Mountrakis, D., 1989. The Pelagonian nappe: tectonics, metamorphism and magmatism. *Bulletin of the Geological Society of Greece*, 23, 29–46.

Kilias, A., Mountrakis, D., 1987. Structural Geology of the Central Pelagonian Zone (Kamvounia Mountains, North Greece). *Zeitschrift Der Deutschen Geologischen Gesellschaft*, 138, 211–237. https://doi.org/10.1127/zdgg/138/1987/211

Kilias, A., Thomaidou, E., Katrivanos, E., Vamvaka, A., Fassoulas, C., Pipera, K., Falalakis, G., Avgerinas, S., Sfeikos, A., 2016. A geological cross-section through Northern Greece from Pindos to Rhodope mountain ranges: A field guide across the external and internal hellenides. *Journal of the Virtual Explorer*, 50, 1–107. https://doi.org/10.3809/jvirtex.2016.08685

Kilias, A., Vamvaka, A., Falalakis, G., Sfeikos, A., Papadimitriou, E., Gkarlaouni, C., Karakostas, B., 2013b. The Mesohellenic trough and the Thrace Basin. Two Tertiary molassic Basins in Hellenides: do they really correlate? *Bulletin of the Geological Society of Greece*, 47, 551. https://doi.org/10.12681/bgsg.11082

Koroneos, A., Kilias, A., Avgerinas, A., 2013. Hercynian plutonic rocks of Voras Mountain, Macedonia, Northern Greece: Their structure, petrogenesis, and tectonic significance. *International Geology Review*, 55, 994–1016. https://doi.org/10.1080/00206814.2012.758830

Kremastas, E., Pavlides, S., Chatzipetros, A., Koukouvelas, I., Valkaniotis, S., 2018. Mapping the Gyrtoni Fault (Thessaly, Central Greece) using an Unmanned Aerial Vehicle. 9th International INQUA Meeting on Paleoseismology, *Active Tectonics and Archeoseismology (PATA)*, 126–129.

Lazos, I., Pikridas, C., Chatzipetros, A., Pavlides, S., 2021. Determination of local active tectonics regime in central and northern Greece, using primary geodetic data. *Applied Geomatics*, 13, 3–17. https://doi.org/10.1007/s12518-020-00310-x

Lemoine, A., Briole, P., Bertil, D., Roullé, A., Foumelis, M., Thinon, I., Raucoules, D., de Michele, M., Valty, P., Colomer, R.H., 2020. The 2018-2019 seismo-volcanic crisis east of Mayotte, Comoros islands: Seismicity and ground deformation markers of an exceptional submarine eruption. *Geophysical Journal International*, 223, 22–44. https://doi.org/10.1093/GJI/GGAA273

Lin, J., Stein, R.S., 2004. Stress triggering in thrust and subduction earthquakes and stress interaction between the southern San Andreas and nearby thrust and strike-slip faults. *Journal of Geophysical Research: Solid Earth*, 109, 2303. https://doi.org/10.1029/2003JB002607

Lister, G.S., Banga, G., Feenstra, A., 1984. Metamorphic core complexes of Cordilleran type in the Cyclades, Aegean Sea, Greece. *Geology*, 12, 221–225. https://doi.org/10.1130/0091-7613(1984)12<221:MCCOCT>2.0.CO;2

Marchetti, P.G., Bivolta, G., D'Elia, S., Farres, J., Mason, G., Gobron, N., 2012. A Model for the Scientific Exploitation of Earth Observation Missions: The ESA Research and Service Support. *IEEE Geoscience and Remote Sensing*, 10–18.

Mercier, J.L., Sorel, D., Vergely, P., Simeakis, K., 1989. Extensional tectonic regimes in the Aegean basins during the Cenozoic. *Basin Research*, 2, 49–71. https://doi.org/10.1111/j.1365-2117.1989.tb00026.x

Mountrakis, D.M., 2006. Tertiary and Quaternary tectonics of Greece, *Geological Society of America Special Papers*. Geological Society of America. https://doi.org/10.1130/0-8137-2409-0

Papaioannou, I., 2019. The Larisa, Tyrnavos and Agia earthquake of 1892 [in Greek].

Papaioannou, I., 2018. The Larisa earthquake of March 1, 1941 [in Greek].

Papaioannou, I., 2017a. Earthquake activity in Thessaly during 16th-18th centuries [in Greek]., *Thessaliko Imerologio*, 353–396.

Papaioannou, I., 2017b. Earthquake activity in Thessaly during the 19th century [in Greek]., *Thessaliko Imerologio*, 273–292.

Papanikolaou, I.D., Foumelis, M., Parcharidis, I., Lekkas, E.L., Fountoulis, I.G., 2010. Deformation pattern of the 6 and 7 April 2009, MW=6.3 and MW=5.6 earthquakes in L'Aquila (Central Italy) revealed by ground and space based observations. *Natural Hazards and Earth System Science*, 10, 73–87. https://doi.org/10.5194/NHESS-10-73-2010

Papathanassiou, G.., Seggis, K.., Pavlides, S.., 2011. Evaluating earthquake-induced liquefaction in the urban area of Larissa, Greece. *Bulletin of Engineering Geology and the Environment*, 70, 79–88. https://doi.org/10.1007/s10064-010-0281-3

Papathanassiou, G., Pavlides, S., 2009. GIS-based DAtabase of historical Liquefaction Occurrences in broader Aegean region, DALO v1.0. *Proceedings of the XVII International Conference on Soil Mechanics &Amp; Geotechnical Engineering, Earthquake Geotechnical Engineering Satellite Conference.* https://doi.org/refwid:13962

Papathanassiou, G., Valkaniotis, S., Chaztipetros, A., Pavlides, S., 2010. Liquefaction susceptibility map of Greece. *Bulletin of the Geological Society of Greece*, 43, 1383. https://doi.org/10.12681/bgsg.11314

Papazachos, B.C., Papazachou, C.B., 2003. The earthquakes of Greece [in Greek], Second edi. ed. Ziti Editions, Thessaloniki.

Pavlides, S., Caputo, R., 2004. Magnitude versus faults' surface parameters: quantitative relationships from the Aegean Region. *Tectonophysics*, 380, 159–188. https://doi.org/10.1016/j.tecto.2003.09.019

Pavlides, S., Chatzipetros, A., Sboras, S., Kremastas, E., Chatziioannou, A., 2021. The northern Thessaly strong earthquakes of March 3 and 4 and their neotectonic setting. https://doi.org/10.5281/ZENODO.4618188

Pavlides, S., Kilias, A., 1987. Neotectonic and active faults along the Serbomacedonian zone (SE Chalkidiki, northern Greece). *Annales Tectonicae*, 1, 97–104.

Pavlides, S.B.B., Mountrakis, D.M.M., 1987. Extensional tectonics of northwestern Macedonia, Greece, since the late Miocene. *Journal of Structural Geology*, 9, 385–392. https://doi.org/10.1016/0191-8141(87)90115-5

Peter, H., Jäggi, A., Fernández, J., Escobar, D., Ayuga, F., Arnold, D., Wermuth, M., Hackel, S., Otten, M., Simons, W., Visser, P., Hugentobler, U., Féménias, P., 2017. Sentinel-1A – First precise orbit determination results. *Advances in Space Research*, 60, 879–892. https://doi.org/10.1016/J.ASR.2017.05.034

Sboras, S., 2011. The Greek Database of Seismogenic Sources: seismotectonic implications for North Greece. Pubblicazioni Dello IUSS 5, 1–274.

Sboras, S., Pavlides, S., Caputo, R., Chatzipetros, A., Michailidou, A., Valkaniotis, S., Papathanassiou, G., 2014. The use of geological data to improve SHA estimates in Greece. *Bollettino Di Geofisica Teorica Ed Applicata*, 55. https://doi.org/10.4430/bgta0101

Sfeikos, A., Böhringer, C., Frisch, W., Kilias, A., Ratschbacher, L., 1991. Kinematics of the Pelagonian nappes in the Kranea area, N. Thessaly (Greece). *Bulletin of the Geological Society Greece*, 25, 101–115. https://doi.org/refwid:11747

Takaku, J., Tadono, T., Tsutsui, K., Ichikawa, M., 2018. Quality improvements of "AW3D" global DSM derived from ALOS PRISM. *International Geoscience and Remote Sensing Symposium (IGARSS) 2018-July*, 1612–1615. https://doi.org/10.1109/IGARSS.2018.8518360

Toda, S., Stein, R.S., Sevilgen, V., Lin, J., 2011. Coulomb 3.3 Graphic-rich deformation and stress-change software for earthquake, tectonic, and volcano research and teaching-user guide, Open-File Report. https://doi.org/10.3133/OFR20111060

Tsodoulos, I., Stamoulis, K., Caputo, R., Koukouvelas, I., Chatzipetros, A., Pavlides, S., Gallousi, C., Papachristodoulou, C., Ioannides, K., 2016. Middle–Late Holocene earthquake history of the Gyrtoni Fault, Central Greece: Insight from optically stimulated luminescence (OSL) dating and paleoseismology. *Tectonophysics*, 687. https://doi.org/10.1016/j.tecto.2016.08.015

Valkaniotis, S., Papathanassiou, G., Ganas, A., Kremastas, E., Caputo, R., 2021. Preliminary report of liquefaction phenomena triggered by the March 2021 earthquakes in Central Thessaly, Greece. https://doi.org/10.5281/ZENODO.4608365

Wegnüller, U., Werner, C., Strozzi, T., Wiesmann, A., Frey, O., Santoro, M., 2016. Sentinel-1 Support in the GAMMA Software. *Procedia Computer Science*, 100, 1305–1312. https://doi.org/10.1016/J.PROCS.2016.09.246

Wells, D.L., Coppersmith, K.J., 1994. New empirical relationships among magnitude, rupture length, rupture width, rupture area, and surface displacement. *Bulletin of the Seismological Society of America*, 84, 974–1002.